ISSN 0915-6348

NATIONAL INSTITUTE FOR FUSION SCIENCE

Proceedings of the International Seminar on Atomic Processes in Plasmas

July 29-30, 1999, Toki, Japan

(Eds.) T. Kato and I. Murakami

(Received - Jan. 20, 2000)

NIFS-PROC-44 Jan. 2000

RESEARCH REPORT
NIFS-PROC Series

NAGOYA, JAPAN

Proceedings of the International Seminar on Atomic Processes in Plasmas

July 29 - 30, 1999, Toki, Japan

edited by
Takako Kato
Izumi Murakami

Abstract

The International Seminar on Atomic Processes in Plasmas (ISAPP), a satellite meeting to the ICPEAC was held July 28-29 at the National Institute for Fusion Science in Toki, Gifu, Japan. About 110 scientists attended the ISAPP meeting and discussed atomic processes and atomic data required for fusion research. This Proceedings book includes the papers of the talks, posters and panel discussion given at the meeting.

The invited talks described the super configuration array method for complex spectra, near-LTE atomic kinetics, R-matrix calculations, the binary-encounter dipole model for electron-impact ionization of molecules, other calculations of molecular processes, the ADAS project and the NIFS atomic data-base, and a survey of the role of molecular processes in divertor plasmas. On the experimental side crossed-beam ion-ion collision-experiments for charge transfer, and storage-ring and EBIT measurements of ionization, excitation and dielectronic recombination cross-sections were presented, and atomic processes important for x-ray laser experiments and x-ray spectroscopy of astrophysical plasmas were described. The new method of plasma polarization spectroscopy was outlined. There was also a spectroscopic study of particle transport in JT-60U, new results for detached plasmas, and a sketch of the first hot plasma experiments with the Large Helical Device recently completed at NIFS.

A panel discussion on International Data Center collaboration, chaired by Dr. Janev, included representatives of atomic data centers in Japan, US, IAEA, UK (JET project), Russia, Korea and China.

Key words;
atomic processes, plasma spectroscopy, excitation, ionization, recombination, charge transfer, X-ray, polarization spectroscopy, atomic database, tokamak, divertor, LHD, EBIT

PREFACE

The "International Seminar on Atomic Processes in Plasma" was held as a satellite meeting of the XXI-ICPEAC (International Conference of Physics of Electronic and Atomic Collisions) on July 29 - 30, 1999 at the National Institute for Fusion Science, Toki, Japan. This is the second satellite meeting of ICPEAC on this subject. The first one was held twenty years ago, in 1979, at the Institute of Plasma Physics, Nagoya University, organized by Professor S. Hayakawa in Nagoya University.

The seminar was intended to bring together both atomic and plasma physicists to review and discuss atomic processes arising in various plasmas: high and low temperature and high and low density plasmas. For the first time, the people who use different terminologies in different research fields could really discuss these problems. There were 109 participants from 16 countries, among whom 42 were from outside Japan. The Seminar was opened by an address by Professor M. Fujiwara, Director of the National Institute for Fusion Science. Many participants visited the LHD (Large Helical Device) in NIFS. The conference discussions were carried out actively in a friendly atmosphere. At the end of the Seminar, we had a party in Yamagami Spa. We enjoyed nice Japanese cooking as well as the Japanese hot spa there. I hope this meeting will be a trigger to explore the new field between Atomic physics and Plasma physics.

The Proceedings includes 20 invited papers and 57 contributed papers presented at the Seminar. It also includes papers from 9 atomic data centers in the world presented in a panel discussion. The program is given at the end of the Proceedings. The list of participants is also attached for future communication, so that communication between the different fields of research will continue.

On behalf of the organizing committee, I would like to express our sincerest thanks to all participants who made active contributions not only by the formal presentation of papers but also through informal discussions. I also would like to acknowledge the organizational efforts of Drs. I. Murakami, H. Sakaue, Profs. C. Namba and N. Ohno, and sincere support by Profs. T. Fujimoto, Y. Itikawa and S. Ohtani. I also would like to thank the office people in NIFS for the support with the budget and official procedures.

I acknowledge the financial support of Yu-Kwai and a contribution of the JuRoku Bank Ltd as well as the National Institute for Fusion Science.

Takako KATO
Chairperson, Organizing Committee
International Seminar on Atomic Processes in Plasma

Contents

Atomic Processes in Plasma - Towards Plasma Atomic Processes -

Takako KATO

Data and Planning Center
National Institute for Fusion Science, Toki 509-5292, Japan

Abstract. The problems of atomic process in plasmas are reviewed briefly. We discuss recent experimental results, non equilibrium plasma, high density effects in plasma and plasma spectroscopy. Atomic processes in plasma is developing as a new research field.

1. Introduction

It is said that 99% of the Universe is made of plasma. There are many kinds of plasmas. For laboratory plasmas, we can mention magnetic confinement fusion, inertial confinement fusion, X - ray lasers, industrial plasmas, discharges and light source plasmas. When we look into space, there are many kinds of plasmas. Recently intergalactic space in clusters of galaxies is found by X-ray measurement to be a high temperature plasma. Plasma emissions are observed from supernova remnants, binary stars, neutron stars etc. in our galaxy. On the Sun we observe high temperature plasmas in the corona and in solar flares. In the solar interior a hot dense plasma exists. In interplanetary space there is low temperature plasma. There are also plasmas in the earth's atmosphere such as lightning and aurora.

When we consider these various plasmas, the plasma parameters range from low density (0.01 cm^{-3}) to high density (10^{24} cm^{-3}) and from low temperature (0.01 eV) to high temperature (50 keV). Therefore there are many kinds of atomic processes involving atoms, molecules and highly charged ions. Atomic data and atomic databases for these processes are necessary for diagnostics and modelling.

2. Various Atomic Processes and Atomic Data

To understand the various plasmas, information about atomic and molecular processes are necessary. The main electron collisional processes are excitation, ionization, dissociation and recombination (including dielectronic recombination as well as radiative and three body recombination). In ionization processes there are direct ionization and indirect ionisation like excitation autoionization. The dielectronic recombination and autoionization processes have been studied intensively during the last ten years. There are also similar processes like excitation, ionization, recombination, dissociation produced by radiation. These processes are important in hot dense matter such as laser produced plasmas and stellar atmospheres. For heavy particle collisions, charge transfer, ionization, excitation are important. In low temperature plasmas, the elastic collisions control transport processes, especially energy/momentum transfer between neutral hydrogen and ions or molecules.

In order to supply atomic data for the plasma research, we need a lot of data. These data should be evaluated for the plasma physicists. We need databases of evaluated data for cross sections and rate coefficients. However it is not so easy to make the evaluated data. In order to arrive at evaluated data, a database for individual original data is also necessary. We need to update the evaluated data. For this kind of job, international collaboration would be very useful.

3. Recent Topics

Recently interesting experimental results are obtained in plasmas. One important topic is the detached plasma in fusion reactor divertors. In divertor plasmas spectral series emission from the recombining plasma is measured and indicates a detached plasma[1]. The spectra showed much lower temperature than measured by Langmuir probes. Such a temperature lower than 1 eV was not expected two or three years ago. The atomic processes in such a low temperature suggest molecular activated recombination[2]. The radiation loss is revealed to be beneficial for edge cooling, although the radiation loss from the center of the plasma is harmful. We also have interesting results for electron and ion collisions in Storage Rings at very low electron energies. Detailed measurements of recombination rate coefficients and cross sections of highly charge ions have been performed. The results give very precise data showing dielectronic states. The dependence on energy and on plasma density, electric field and magnetic field can be studied by this method. Some measured results for recombination are not yet explained by theoretical calculations[3].

In Astrophysical plasmas the main processes are electrons and photons collisions. However recently charge exchange processes relating to X-ray production have been proposed.

4. Non equilibrium plasma

In high density and steady plasma, local thermodynamic equilibrium (LTE) is obtained. In LTE the population density is expressed by the Saha-Boltzmann formula which does not depend on the rate coefficients. It only depends on the statistical weight and energies of the levels and on the temperature. Near LTE conditions, atomic processes are described by a symmetric linear-response matrix[4]. This result makes a relation between plasma atomic processes and thermodynamics as well as offering an efficient method for radiative transfer calculation.

In the case of Non LTE, the population densities depend on the rate coefficients. There are two kinds of Non LTE; steady state ($dn/dt = 0$) and non steady state ($dn/dt \neq 0$). In steady state, when there is a flow of the material the plasma is not always in ionization equilibrium. This situation occurs in laboratory plasma such as Tokamak. Generally speaking the plasma is in an ionizing state in a Tokamak, although a recombining state occurs in the divertor. When there is no flow in a steady state, ionization equilibrium is expected, as in the solar corona. However the ionizing plasma such as solar flares and the recombining plasma

such as laser produced plasmas are considered in non steady state state which is time - dependent plasma.

We have analysed X-ray spectra from Sun and found the non equilibrium ionization in solar flares[5] as shown in Fig.1. This result can help to make a flare model. We can determine the plasma state from the time - dependent ion abundance ratios in plasmas.

5. High density effects, Microfield effects, Field effects for rate coefficients in plasma

In plasma a microfield is created by the motion of the particles. This field causes level mixing and Stark broadening of spectral lines. For dielectronic recombination process, an electron is captured in highly excited states. Therefore the recombination rate coefficients change very much due to the microfield effects in high density plasma. In order to know the density effect precisely we need the correct recombination rate for high Rydberg states. We also need to know the Stark effect and level mixing for these levels. In order to know the effective ionization and recombination rate coefficients, we have to study the collisional radiative model including dielectronic states. A systematic study of the collisional radiative model is necessary to investigate these effects.

The electrostatic field of plasma waves makes plasma satellite lines. For high Rydberg states the effect of this electrostatic field might be important[6].

It is well known that the measured transport in plasma can not be explained by neo classical transport theory. This is called anomalous transport. We consider that anomalous transport might be related to some atomic processes. For example the loss of plasmamomentum through charge exchange with neutral particles is considered to be important in the formation/destruction of transport barriers in toroidal plasma. This problem has not been studied sufficiently from the view point of atomic processes, but atomic spectroscopy already gives an important diagnostic technique for transport.

6. Plasma spectroscopy

Plasma spectroscopy is a window to learn about any plasma. We can obtain much information from spectroscopy. However the measured spectra are not always well understood. We have several mysteries in plasma spectroscopy. A famous one is the intensity ratio of the intercombination line and the resonance line for He-like ions which are measured both in solar flares and in Tokamaks. We also have intensity anomalies for the ratios of Lyα1 to Lyα2 for H-like ions[7], and the multiplet line ratios of OV[8] and of OIII lines. The obsered spectral feature produced by Zeeman splitting near the plasma periphery can not always be understood by normal magnetic field in plasmas. These mysteries should be resolved. They might be keys to open a new area of atomic plasma processes.

Polarization spectroscopy is another new window in the plasma spectroscopy especially important for non Maxwellian plasmas.

5. Plasma Atomic Processes

Atomic physics has a distance from Plasma Atomic Processes. Plasma physics has also a distance from Plasma Atomic Processes. I think Plasma Atomic Processes is not only an application of atomic data in plasma but a new research field between Atomic Physics and Plasma Physics.

We should make a systematic development of this research field for a wide range of plasma parameters.

References

[1] e.g. U. Wenzel et al, Nuclear Fusion, 39, 873 (1999)
[2] e.g. Ohno et al, Phys. Rev. Lett. 81, 818 (1999)
[3] e.g. R. Schuch, this proceedings,
S. Schippers, this proceedings, invited paper, ICPEAC (1999)
[4] R. More and T. Kato, Phys. Rev. Letters, 81, 814 (1998)
[5] T. Kato, T. Fujiwara, Y. Hanaoka, Astrophy. Journal. 492, 822-832 (1998), T. Kato and M. Kato, Proceedings of 32nd Scientific Assembly of Cospar, 12 - 19 July, 1998, Nagoya (1998)
[6] S. Hayakawa, Atomic processes in plasmas, IPPJ - AM - 13 (1979)
[7] H. Kubo et al, Phys. Rev. A, 46, 7877 (1992)
[8] T. Kato, E. Rachlew-Kallne, P. Horling and K-D. Zastrow, J. Phys. B, 29, 4241 - 4253 (1996)

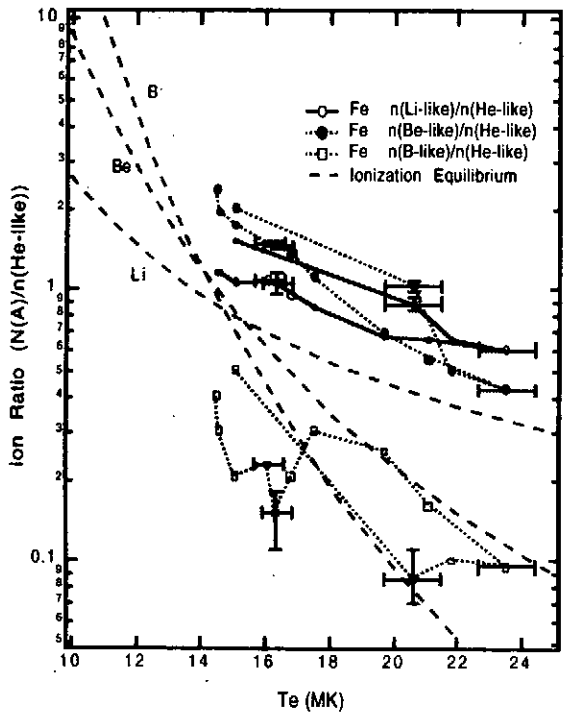

Fig.1. The derived ion density ratios from the intensity ratios of Fe ion spectra. Dashed lines are the values in ionization equilibrium [5].

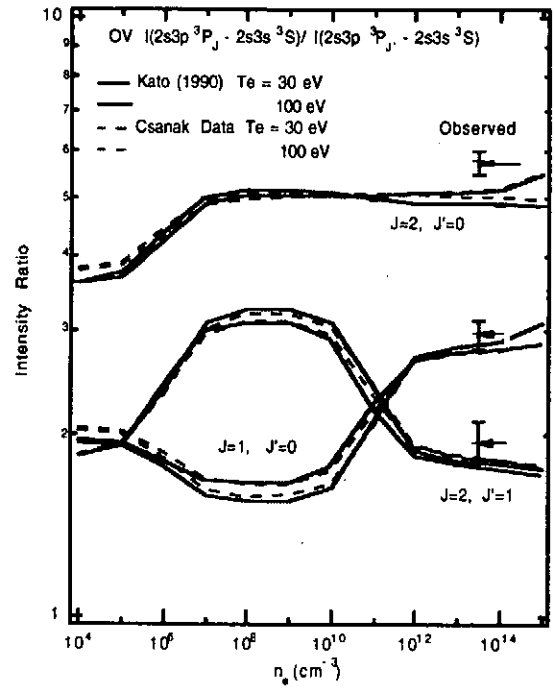

Fig.2 The intensity ratios of multiplets of OV. The observed values are shown by arrows[8].

An Atomic Data and Analysis Structure

Hugh P. Summers

[1] *Department of Physics and Applied Physics, Strathclyde University, Glasgow G4 0NG, UK*

Abstract. The Atomic Data and Analysis Structure (ADAS) Project is a shared activity of a world-wide consortium of fusion and astrophysical laboratories directed at developing and maintaining a common approach to analysing and modelling the radiating properties of plasmas. The origin and objectives of ADAS and the organisation of its codes and data collections are outlined. Current special projects in the ADAS Project work-plans are listed and an illustration given of ADAS at work.

1 Introduction

ADAS had its origins at the JET Joint Undertaking experiment of the European fusion programme. In 1984, it was decided to develop a substantial capability for modelling and analysing radiating properties of atoms and ions in plasma in support of the very powerful spectroscopic equipment to be installed at the experiment. A number of strategic decisions were taken including identifying a level of sophistication in atomic modelling sufficient for the long term future of the fusion programme, central maintenance of fundamental and derived atomic data, precise and optimised interfacing to experimental diagnostic analysis and quality control of theoretical plasma modelling data from the more testing environment of a very large experimental spectroscopy division. Under these guide lines, the Atomic Data and Analysis Structure began and evolved into a professionally coded interactive computational support system linking to virtually all spectroscopic diagnostic and plasma modelling activities at JET. In the early nineties, there was a request from a number of European fusion laboratories and solar astrophysics laboratories that ADAS should be converted into a UNIX based system with IDL as its graphical interface. With JET's support the ADAS Project was set up, funded by subscription of participant laboratories and managed by the University of Strathclyde, to oversee the conversion over a two year period from JET-ADAS to IDL-ADAS. The ADAS Project is now in a maintenance and on-going development phase under the guidance of a steering committee on which all ADAS members are represented. Membership of the ADAS Project has now increased from the original five to more than seventeen distributed throughout the world.

2 ADAS organisation

The Atomic Data and Analysis Structure (ADAS) is an interconnected set of computer codes and data collections comprising three main components, namely, an interactive system operated through a graphical user interface, a library of key subroutines, and a very large database of fundamental and derived atomic data. The interactive part provides immediate display of important fundamental and derived quantities used in analysis together with a substantial capability for preparation of derived data. It also allows exploration of parameter dependencies and diagnostic prediction of atomic population and plasma models. The second part is non-interactive but provides a set of subroutines which can be accessed from the user's own codes to draw in necessary data from the

derived ADAS database. The database spans most types of data required for fusion and astrophysical application. The ADAS codes are organised into the seven series shown in table 1. ADAS1 is concerned with examining fundamental, that is essentially individual

Table 1: ADAS code series

Series	Content
ADAS1	Entry and validation of fundamental atomic data
ADAS2	Excited state populations of ions in a plasma
ADAS3	Charge exchange related emission
ADAS4	Recombination, ionisation and radiated power
ADAS5	General interrogation programs
ADAS6	Data analysis programs
ADAS7	Creating and Using Dielectronic Data

Table 2: Some ADAS data formats. The size of the database is ~500Mbytes.

Format	Content
adf01	bundle-n and bundle-nl charge exchange cross-sections
adf04	resolved specific ion data collections
adf09	direct resolved dielectronic recombination coefficients
adf11	iso-nuclear master files
adf12	charge exchange effective emission coefficients
adf13	ionisation per photon coefficients
adf15	photon emissivity coefficients
adf20	G(Te) functions
adf21	effective beam stopping coefficients
adf22	effective beam emission coefficients
adf31	feature archives

reaction, data. This is to be distinguished from the composite effects of many processes which are the subject of most of the rest of ADAS. ADAS2 is concerned with evaluating, within a generalised collisional-radiative framework, excited populations of specific ions in a plasma environment and then their radiation emission. It relies on availability of a reaction rate data collection for the ion in the ADAS database although ADAS2 has some provision for generating an approximate collection of such data when this is not so. ADAS3 is concerned with those situations in a plasma when charge transfer from neutral hydrogen (or its isotopes) or neutral helium in beams is a primary mechanism. ADAS4 is concerned with the ground and metastable populations of ions in a plasma and particularly their preparation and calculation for dynamical plasma models. It therefore operates with generalised collisional dielectronic recombination and ionisation coefficients, associated power loss coefficients and metastable fractions. ADAS5 provides a set of programs for interrogating data collections in the fundamental and derived database. The data classes addressed are those which have been found of particular importance for reduction of calibrated observed data. ADAS6 series is concerned with analysis of spectral data.

It includes implementation of the method of differential emission measure analysis, maximum likelihood spectral line fitting with full statistical analysis of errors and advanced fitting codes for analysing special features in terms of plasma parameters. ADAS7 series is dedicated to the fundamental calculation of dielectronic recombination, ionisation and excitation/auto-ionisation data including their organisation for applications. Altogether there are ~70 primary codes, IDL libraries of ~1000 subroutines and FORTRAN libraries of ~1500 subroutines arranged in a hierarchical structure and maintained under SCCS control. ADAS atomic modelling codes generally create data sets as well as normal graphical and printed output. These files are structured according to the requirements of the ADAS data base or for further ADAS programs.

There are 31 distinct data types in the ADAS databases. Each data set type has its layout and content precisely described. The prescriptions are called ADAS data formats or *adfs* and must be rigidly adhered to in preparation of personal data for use by the ADAS package. These formats apply both to fundamental and derived data. A subset is shown in table 2. It has been helpful to plan the structure of the adfs in discussion with fundamental producers in advance of substantive calculations.

All primary documentation, including manuals, tutorials, bulletins and datastatus, is provided on the world-wide-web at *http://patiala.phys.strath.ac.uk/adas* with a mirror site in the USA. Documentation is subject to periodic updating. The latest release of the main idl-adas user manual (version 2.1) was distributed in April.

3 ADAS special projects

Following planning discussions at ADAS annual workshops, teams are established for special projects. These small teams of three or four persons draw together special interests and best expertise from the ADAS consortium and beyond. The projects are designed to keep ADAS at the leading scientific edge of atomic physics and spectroscopy of plasmas and to ensure that useful codes and fundamental and derived data for experiment modelling and analysis enter the ADAS system for the benefit of all ADAS members. Current projects are shown in table 3

Table 3: Some current ADAS special projects

Project	Participants	Objective
DR Project	Badnell,Verner, O'Mullane, Pindzola Griffin, Gorcyzca	Intermed. coupling state select. DR coeffts. for ions of elements up to zinc aimed at astrophysics and heavy species in fusion.
GCR Project	Brooks, Dux, Jentschke, Lang, Mullane, Summers	Complete generalised collisional-radiative coeffts. for all light element to the highest precision aimed at fusion and astrophysics.
xPaschen Project	Korten, Hey, Mertens, Martin	Extended spectral fitting including Zeeman/ Paschen-Back multiplet feature primitives.
He-beam Project	Hoekstra, Anderson Brix, Menhart	Metastable resolved beam stopping & emission coeffts. for slow and fast helium beams as unrelaxed edge and quasi-relaxed deep probes.

4 ADAS at work

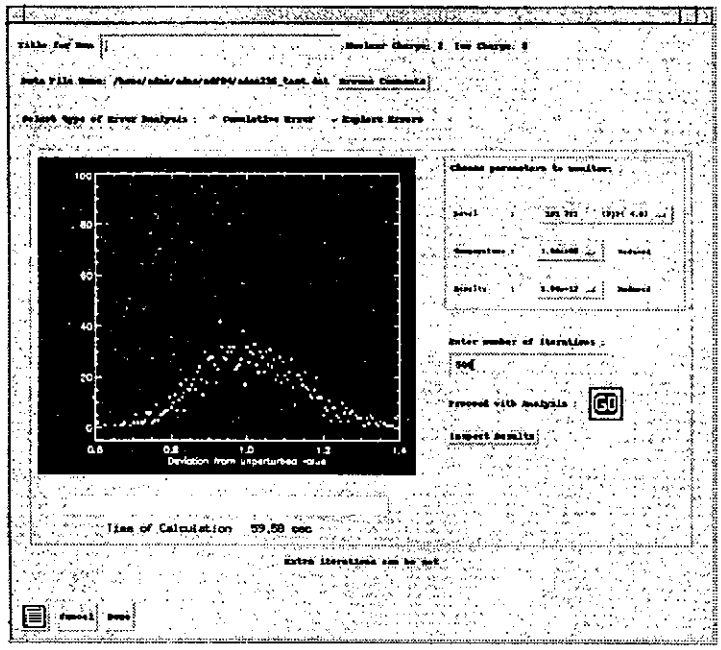

Figure 1: adas216 processing screen showing the $He^0(1s3p^3P)$ population error.

The detailed explanation of the scientific basis of the various ADAS codes is beyond the scope of this article. The extended formulation is given in the IDL-ADAS manual and in published works. Specialized codes often have their origin in the work and programs of a particular participant in the ADAS Project who advises on improvements and updates to the codes and on their scientific content and best use (for example, basic spectral fitting [*adas601*], Brooks et al. (1999); opacity and escape factors [*adas214*], Behringer (1997); sensitivity analysis [*adas216*], O'Mullane, 1999; dielectronic recombination and postprocessing [*adas701, adas702*], Badnell (1997). Precision and sensitivity are key issues for ADAS as a guide to realistic use of derived data in experiment analysis and in the targetting of expensive fundamental reaction calculations wisely. It is appropriate to illustrate the appearance of interactive ADAS with the processing screen of *adas216* as it builds a cumulative statistical error half-width estimate for an excited population in a plasma in the collisional-radiative regime from accuracy information contained in the source *adf04* data set of fundamental reaction rates. The mode of operation is Monte Carlo sampling within (assumed) Gaussian error distributions for the fundamental reactions and then repeated population calculations. Other modes for this code include creation or modification of the fundamental data 'error block' and the isolation of the error contributed by each fundamental process to the total error.

References

[1] Badnell N R 1997 *J. Phys.B.* **30** 1

[2] Behringer K H 1997 *Max-Planck-Institut-fuer-Plasmaphysik report* **IPP 10** /5

[3] Brooks D.H., Fischbacher G.A., Fludra A., et al. 1999 *Astron. & Astrophys.* **347** 277

[4] O'Mullane M G 1999 - to be submitted

SCROLL, A Superconfiguration Collisional Radiative Model With External Radiation.

A. Bar-Shalom[1], M. Klapisch[2#] and J. Oreg[1]

[1]*Nuclear Research Center Negev, Be'er Sheva, Israel.*
[2]*ARTEP, Columbia, MD 20415 USA.*

Abstract. A collisional radiative model for calculating non-local thermodynamical - equilibrium (non-LTE) spectra of heavy atoms in hot plasmas has been developed. It takes into account the numerous excited an autoionizing states by using superconfigurations. These are split systematically until the populations converge. The influence of an impinging radiation field has recently been added to the model. The effect can be very important.

Introduction

Radiation hydrodynamical simulations of laser produced plasmas require knowledge of the level populations of ions for their average charge Z*, their ionization energy, and their radiative properties. This knowledge is also necessary to interpret the emission spectra from hot laboratory and astrophysical plasmas. A common approximation in these problems has been to assume local thermodynamical equilibrium (LTE) –i.e. Saha-Boltzmann populations. The LTE approximation was used, for example, to develop the STA theory[1, 2]. However, non LTE effects are of dramatic importance to laser produced plasmas [3] – because of unavoidable gradients and radiative losses. To reach beyond LTE, one needs a collisional radiative model (CRM)[4] which requires transition rates between all levels.

For heavy ions of interest in laser fusion and x-ray lasers there are multiple charge states and extremely numerous excited and autoionizing manifolds. Although some highly efficient computational methods have been developed in the last decade[5, 6], there still needs to be some type of averaging procedure to treat the numerous excited configurations. Recently, we presented a model that is based upon the same method as the Super Transition Array (STA) theory, using superconfigurations (SCs) [1, 2] as effective levels with a rapidly convergent procedure that provides the detailed configuration non-LTE spectrum in the limit. This model, called "SCROLL" (Super Configuration Radiative cOLLisional) [7, 8] - calculates for the first time the effect of the numerous excited and autoionizing states on ionization balance and spectra of heavy elements. Furthermore, SCROLL provides accurate and detailed non-LTE opacities and emissivities which can serve as reliable benchmarks in the development of simpler and faster on-line models that can be used in numerical simulations of radiation-hydrodynamics. With the progress in computer hardware, we are considering using SCROLL for building atomic databases for hydrodynamical simulations. Since SCROLL has been already described in previous publications[7, 8], we will give here only a short overview and report on a the introduction of external radiation field in the model, and we will give examples.

Mailing address: c/o Naval Research Laboratory, Code 6730, Washington, DC 20375 USA.

Overview of SCROLL

SCROLL is an *iterative* collisional radiative model where the units of populations are superconfigurations. Because superconfigurations (SC) are loosely defined groups of numerous configurations of similar energies[1, 2], they can be refined in a stepwise manner until some convergence is reached. SCs are constructed from supershells σ, which are unions of energetically adjacent ordinary atomic subshells $s \in \sigma$, $s \equiv \mathbf{j}_s \equiv n_s l_s j_s$. A SC is defined by a set of supershell occupation numbers Q_σ . The Q_σ electrons are distributed among the subshells $s \in \sigma$ in all possible ways subject to $\sum_{s \in \sigma} q_s = Q_\sigma$. When the superconfiguration structure is fixed, the populations of the SC are obtained by solving the CRM rate equations:

$$\frac{dN_\Xi}{dt} = -N_\Xi \sum_{\Xi'} R_{\Xi\Xi'} + \sum_{\Xi'} N_{\Xi'} R_{\Xi'\Xi} \qquad (1)$$

where N_Ξ are the SC populations and $R_{\Xi\Xi'}$ are the SC transition rates, averaged over the initial configurations $C \in \Xi$ and summed over all final $C' \in \Xi'$. A basic initial assumption (relaxed in the course of the computation, as explained below) in this model is that *within* a superconfiguration Ξ, the configuration populations N_C are distributed according to the Saha - Boltzmann statistics: The SC average rates can thus be written as

$$R_{\Xi\Xi'} \equiv \frac{1}{U_\Xi(g)} \sum_{\substack{C \in \Xi \\ C' \in \Xi'}} U_C R_{CC'} \qquad (2)$$

where $R_{CC'}$ are the configuration average rates, and U_C are partition functions. In the case of one-electron jumps, we have $R_{cc'} \propto \frac{q_\alpha (g_\beta - q_\beta)}{g_\alpha g_\beta} R_0(\alpha, \beta)$. $R_0(\alpha, \beta)$ is the radial integral associated with the transition and is computed with the HULLAC code. The problem is estimating the average value of the shell occupation numbers q_α in a superconfiguration. It was shown in ref[9] that these average values can be computed with the help of a partition function algebra.

The assumption of LTE within SCs is relaxed by a convergence procedure where at each step, supershells are split, giving rise to a new set of SCs in Eq.(1). This splitting is done in a systematic manner following a "binary tree" algorithm. The initial population of these new SCs is taken as proportional to their partition functions. All the necessary new rates are then computed. Actually, only the occupation number factor needs to be re-evaluated, since the $R_0(\alpha, \beta)$ are taken from a pre-computed database. Then the steady state CRM matrix is rebuilt and solved. A sparse matrix algorithm is used, since the SCs belonging to charge states differing by more than one unit are not connected. The resulting populations are then compared to the initial ones. The SCs are split in this way repeatedly, until all N_Ξ converge. This convergence process eliminates gradually the explicit dependence of the rates – eq. (2) -

on the LTE Boltzmann factors in U_C. In the configuration limit it disappears completely. Note that in order to accelerate the convergence of this process, the temperature assumed for the LTE populations within the SC is not the electron temperature T_e, but an effective ionization temperature T_z defined by Busquet[10].

Introduction of external radiation

Photo-ionization is treated in SCROLL as other radiative transitions, except that the final state is a SC with one free electron. The free electron wavefunctions are computed consistently with the other wavefunctions, like for dielectronic recombination. Bound-bound transitions use the B Einstein coefficient. The plasma under consideration is supposed to be homogeneous and optically thin. This scheme is the most flexible for building databases connected to hydrodynamic simulations. In that case SCROLL will be applied to elementary plasma cells, and radiation transfer would be computed separately. SCROLL can handle any distribution of photons specified numerically. Obviously, if the plasma were subjected to a Planckian radiation field at $T_r = T_e$, LTE would be recovered, even at low electron density. Consequently, it is very desirable to include radiation effects in databases for hydrodynamical simulations. The problem is how to describe the radiation field in a database. For direct drive ICF, the radiation field is far from being Planckian. Figure 1 shows a typical intensity distribution extracted from a radiation hydrodynamic simulation. It is compared with a Planckian approximation (T_r=200eV) and with a diluted Planckian distribution (T_r=1000eV, D=0.001). The effect on the plasma of these two distributions is very different: The average charge Z* is 41.67 with no external radiation, 43.16 with T_r=200eV, and 50.09 with T_r=1000eV, D=0.01.

Figure 2 shows the influence of external radiation fields on the emission spectrum of a W plasma, with the two above mentioned distributions. The effect is very important, even with a rather small dilution factor. We are exploring the possibility of describing the radiation field by a superposition of Planckian distributions.

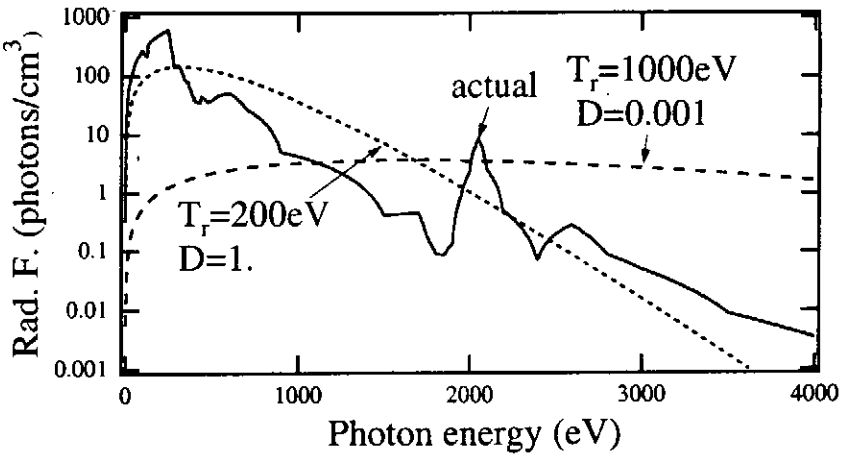

Figure 1. A typical radiation field in a simulation of laser produced W plasma, compared with Planckians at T_r =200eV and T_r =1000eV, with a dilution factor D=0.001.

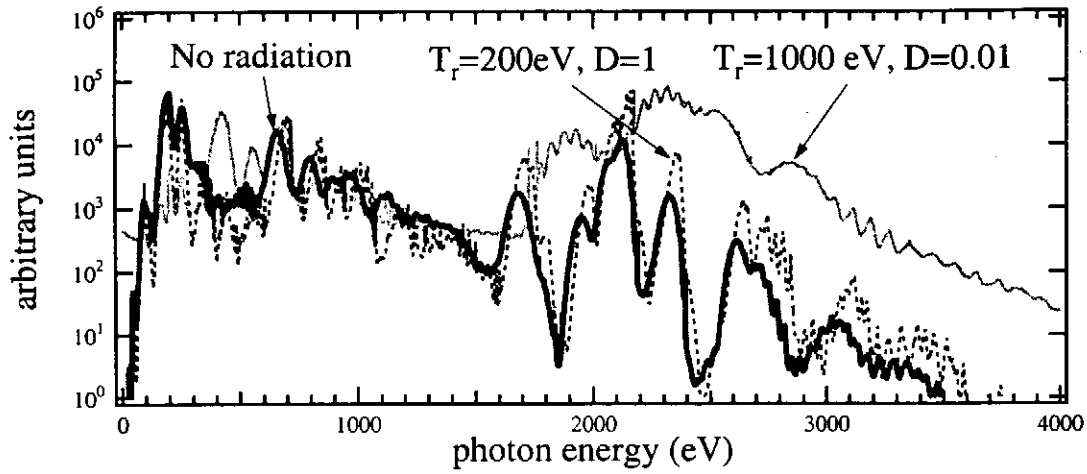

Figure 2. Theoretical emission spectrum of a tungsten plasma, at T_e=550eV and N_e=9x10^{20} cm^{-3} with no external radiation (plain thick line), with a Planckian at T_r=200eV (dotted line), and with a diluted Planckian at T_r= 1000eV ,D= 0.01 (gray line)

Conclusion

It has been shown that in a non-LTE computation, SCROLL is able to compute populations of highly ionized heavy elements with external radiation fields. The effect of these fields can be very important, since a Planckian radiation field at T_r= T_e would retrieve LTE at any density. SCROLL can compute the effect of a numerically specified photon distribution, but a compact description for interfacing with hydrodynamical simulations is needed. Work on that subject is in progress.

References

[1] A. Bar-Shalom, J. Oreg, W. H. Goldstein, D. Shvarts and A. Zigler, *Phys. Rev. A,* **40**, 3183 (1989).

[2] A. Bar-Shalom and J. Oreg, *Phys. Rev. E,* **54**, 1850 (1996).

[3] M. Klapisch, A. Bar-Shalom, J. Oreg and D. Colombant, *Phys. Plasmas,* **5**, 1919 (1998).

[4] R. W. P. McWhirter, *Phys. Reports,* **37**, 165 (1978).

[5] A. Bar-Shalom, M. Klapisch and J. Oreg, *Phys. Rev. A,* **38**, 1773(1988).

[6] A. Bar-Shalom, M. Klapisch and J. Oreg, *Comput. Phys. Comm.,* **93**, 21 (1996).

[7] A. Bar-Shalom, J. Oreg and M. Klapisch, *Phys. Rev. E,* **56**, R70 (1997).

[8] A. Bar-Shalom, J. Oreg and M. Klapisch, *J. Quant. Spectrosc. Radiat. Transfer,* **58**, 427 (1997).

[9] J. Oreg, A. Bar-Shalom and M. Klapisch, *Phys. Rev. E,* **55**, 5874 (1997).

[10] M. Busquet, *Phys. Fluids B,* **5**, 4191 (1993).

Atomic Processes in Near-Equilibrium Dense Plasmas

R. More and T. Kato
National Institute for Fusion Science
Toki, Gifu, Japan 509-52

Dense plasmas having a significant radiation environment are closer to thermal equilibrium (LTE) than usual "Collisional-Radiative" plasmas. Thermal equilibrium Saha-Boltzmann populations do not involve atomic cross-sections or A-values. Here we consider plasma conditions in which the populations are non-LTE and must be calculated from rate equations, but still are near LTE, so a perturbation method can be used to obtain a simplified description of atomic dynamics. The results are relevant to near-LTE plasmas in the surfaces of stars, to laboratory laser hohlraum experiments or other dense plasmas made from solid targets. Plasmas with significant radiation environment are discussed by Rose et al., Busquet et al., Klapisch et al., and Libby et al. References to these works and some near-LTE Collisional-Radiative calculations are given by More and Kato (1).

Atomic rate equations are linear first-order differential equations for a vector of atomic populations N_j. The general properties of the equations depend on the fact that the rates conserve ions, i.e., for each transition from state j to state k, the number density N_k increases and N_j decreases by the same amount. The equations describe ions in a specified environment, and neglect flow or other sources of ions and also neglect changes of the environment (electron density/temperature conditions, or radiation spectrum) produced by the atomic kinetics.

In the matrix form of the atomic kinetic equations,

$$\frac{dN_j}{dt} = \sum_k T_{jk} N_k$$

the diagonal term $T_{kk} = -\Sigma' T_{jk}$ guarantees conservation of ions. With this property, one can prove (it is also assumed that T_{jk} is not negative):

(1) A steady-state solution N_j^{SS} exists.

(2) For the steady state, the populations N_j^{SS} are positive.

(3) Other eigenfunctions of the transition matrix T_{jk} correspond to transient normal modes which have negative eigenvalues, so their time evolution is (stable) exponential decay (Gershgoren theorem). The transient modes have positive and

negative populations which describe the transfer of population as the system relaxes to the steady state. For each transient mode, the population sum $\Sigma N_j^{(m)}$ is zero.

(4) Since the transient modes have (some) negative populations it is worth comment that if a solution begins with a positive initial population $N_j(0)$, the population $N_j(t)$ remains positive for later times.

These properties can be proven with no additional assumptions. However, an approximate numerical solution may fail one of these requirements, for example if the numerical time-step is too large.

Next, we consider a plasma near LTE. In this case the transition matrix T_{jk} linking two levels j and k exactly obeys the condition of detailed balance:

$$T_{jk}\, N_k^o \;=\; T_{kj}\, N_j^o$$

(In this notation, T_{jk} is the transition from k to j). T_{jk} is a singular matrix and has no inverse. However we can consider a slightly smaller matrix T_E involving only excited states and in general this smaller matrix has an inverse. The inverse matrix also obeys a condition of detailed balance:

$$(T_E^{-1})_{jk}\, N_k^o \;=\; (T_E^{-1})_{kj}\, N_j^o$$

Corresponding to the equation $\Sigma_j T_{jk} = 0$, for each k the inverse matrix obeys

$$\sum_{j(\neq 0)} T_{0j}\;\; (T_E^{-1})_{jk} \;=\; -1$$

Now we consider a three-level near-LTE response function,

$$\Gamma^i_{jk} \;=\; dN_i / dT_{jk}$$

Here we have an atom(ion) in LTE and change one rate T_{jk} . For particle conservation we make the corresponding change in T_{kk}. The change moves the atom(ion) slightly out of LTE. The induced change in the population N_i is given by Γ^i_{jk} which can be explicitly written in terms of the inverse of the transition rate matrix:

$$\Gamma^i_{jk} \;= [(T_E^{-1})_{ik} \;-\; (T_E^{-1})_{ij}\,]\, N_k^o \qquad \text{(plus groundstate part)}$$

This equation requires a small correction for the change of the ground-state population (the correction does not change the results given below).

Γ^i_{jk} has three interesting properties (these are simple theorems):

A.) $\Sigma_s \ \Gamma^s_{jk} = 0$ (sum runs over all s including the groundstate)

B.) $N_j^o \ \Gamma^i_{jk} = - N_k^o \ \Gamma^i_{kj}$

C.) $N_j^o \ \Gamma^i_{jk} + N_i^o \ \Gamma^k_{ij} + N_k^o \ \Gamma^j_{ki} = 0$

Equation (A) says that populations are conserved, Eq. (B) is an expression of detailed balance, while the interpretation of Eq. (C) is not clear. Using Eq. (B) we can see that if the rates are changed consistent with detailed balance, the steady-state populations do not change: this is characteristic of LTE.

A certain combination of Γ-matrices involving <u>four</u> levels has an interesting symmetry. The combination is

$$Q_{ij,kl} = \Gamma^j_{kl} + (N_j^o / N_i^o) \Gamma^i_{kl}$$

The symmetry is the equation $Q_{ij,kl} = Q_{kl,ij}$. Like the other properties of Γ, this symmetry holds near LTE and is a consequence of detailed balance.

We apply these equations to a near-LTE plasma. The black-body photon population $n_{\nu'}$ for a line ν' (k → l) is altered by changing the photon temperature $T_{\nu'}$. Because of this change, the transition k → l is perturbed; four rate coefficients T_{kl}, T_{lk}, T_{kk} and T_{ll} are altered. We examine the <u>net</u> emission for another transition ν(j → i). This net emission is zero in LTE but in general is

$$E_\nu = h\nu \, A_{j \rightarrow i} \, N_j \, (n_\nu + 1) - h\nu \, A_{i \rightarrow j} \, N_i \, n_\nu$$

The near-LTE response matrix $R_{\nu,\nu'}$ is defined as the net emission E_ν divided by the temperature change which caused the nonequilibrium. The response matrix is then obtained by expressing E_ν in terms of Γ^i_{jk}, or rather, in terms of Qij,kl:

$$R_{\nu,\nu'} = \frac{E_\nu}{\delta T_{\nu'}} = \frac{h\nu \ h\nu'}{kT^2} A_{j \rightarrow i} A_{\ell \rightarrow k} (n_\nu^o + 1)(n_{\nu'}^o + 1) Q^{ij}_{k\ell}$$

This formula gives a general theoretical expression for the linear-response matrix and explicitly shows that $R_{\nu,\nu'}$ obeys the Onsager symmetry relation

$$R_{\nu,\nu'} = R_{\nu',\nu}$$

The matrix $R_{\nu,\nu'}$ gives the non-LTE linear response to non-equilibrium radiation at one frequency, but also describes the (quasi-steady) response to any radiation field sufficiently near a black-body function. One must integrate the frequency spectrum of the perturbations.

While the previous equations involved the atomic eigenstates, the response function $R_{\nu,\nu'}$ only explicitly refers to the radiation spectrum. If a detailed spectrum is summed over photon frequency groups, as in a practical plasma simulation, the response function $R_{\nu,\nu'}$ reports the result of the atomic calculation without mention of the coupling scheme and level structure. Using $R_{\nu,\nu'}$ we can compare NLTE calculations based on different atomic models and different coupling schemes. The comparison is much more informative than a mere comparison of ionization states.

Reference (1) compares a CR model for He-like aluminum with an average-atom calculation by comparing the linear-response matrix made by each method. The average-atom model does not include the singlet-triplet splitting which is a major feature of Helium-like ions. The CR model has a detailed treatment of the Helium-like ion but omits much of the coupling to adjacent charge states. Surprisingly the two response functions show the same pattern of emission and absorption features and are even in rough quantitative agreement, for example for the 3 to 2 emission induced by absorption from the K-shell. The similarity of emission/absorption is remarkable given the very different descriptions of atomic structure and atomic processes.

Both CR and average-atom calculations yield a symmetric response matrix and this confirms both the computational implementation of detailed balance and the suitability of the definition used for $R_{\nu,\nu'}$

Acknowledgement: We acknowledge useful discussions with Dr. Gerald Faussurier, who independently derived certain formulas given above.

Reference:

(1) More, R., and Kato, T., Physical Review Letters **81**, 814 (1998).

Atomic Database Systems

Izumi Murakami

[1] *National Institute for Fusion Science, Toki 509-5292, Japan*

Abstract. Brief introduction on atomic and molecular databases through WWW and the expected functions are presented. The NIFS database system which is opened through WWW is also introduced.

1 Atomic Databases in WWW

The computer network around the world has developed rapidly and widely and the World Wide Web (WWW) makes it very convenient for getting any kind of information from all over the world. With the WWW development, many atomic and molecular (AM) databases are now accessible via WWW. Many data centers have WWW home pages and have made their databases available through WWW. We can conveniently search data which we want from our computers.

Now we need a list of the databases which are available through the web in order to find easily what we want. Such a list of AM databases is maintained by Weizmann Institute at `http://plasma-gate.weizmann.ac.il/`. This is very useful for finding database addresses.

AM databases can be classified as in Table 1. The data center or database names the the Weizmann Institute list are given. Bibliographic databases are useful to search by atomic processes or element names as well as by author name. Numerical databases contain AM numerical data such as cross sections, rate coefficients, wavelengths, and oscillator strengths, sometimes with bibliographic information. As listed in Table 1, three kinds of data exist, i.e., raw data, compiled data, and evaluated data. Raw data here means calculated or experimental data produced by each author. Different kinds of data are required, according to users needs. That is, atomic physicists want to see raw data, but plasma physicists need evaluated data. Catalogues as a list of data sets or data collections of raw data and evaluated data are useful to get specific data. Not all modeling packages and atomic codes are open to the public, but some are available through WWW.

From the user's viewpoint, databases should be searchable and retrievable by various

Table 1: Category of databases and the data centers

Bibliography	e.g. Gaphyor, ORNL, RTAM, NIFS
Numerical databases	
Calculated (raw) data	e.g. TOPbase, Univ. of Kentuckey, CDS, SAM, Lund Univ.
Compiled data	e.g. CfA, NIST, CDS, NIFS, KAERI
Evaluated Data	e.g. IAEA, NIST, ORNL, JAERI,
Onsite calculation	e.g. NIST
Modeling package	e.g. ADAS, SCROLL, CHIANTI
Code library	e.g. Weismann, ADAS, Masaryuk Univ., CCC
Catalogues	e.g. CDS, NIST

conditions, such as elements, wavelength region, atomic processes, author name, journal name, year of publication, and so on. The retrieval procedure should be easy to understand. Good information on how to use, like a 'help pages', should be provided. Many database homepages have such information, but are not friendly enough to users. Feedback from users is quite important to improve database systems.

As outputs from databases, bibliographic information and/or numerical data as lists, data tables, or graphs are obtained. Graphs are very helpful for certain kinds of data, such as cross sections and rate coefficients, to see dependences on physical parameters or to compare data from different data sources. Numerical data lists and tables are useful when we want to use them, for example, in our own analysis or calculations.

2 Atomic Database at NIFS

The NIFS database is retrievable and display system of bibliographic data and numerical AM and PMI data [1]. Users can search and retrieve data through the web page at `http://dbshino.nifs.ac.jp/`. It is open for registered users for research purpose (no charge!). Registration can be done from the web page and an ID and password will be sent later by email.

As for bibliographic databases, 'FUSION' and 'AM' are databases of extensive bibliography extracted from INSPEC database on fusion science, and atomic and molecular physics, respectively. We also have the 'ORNL' database of bibliography on atomic collisions, collected at ORNL.

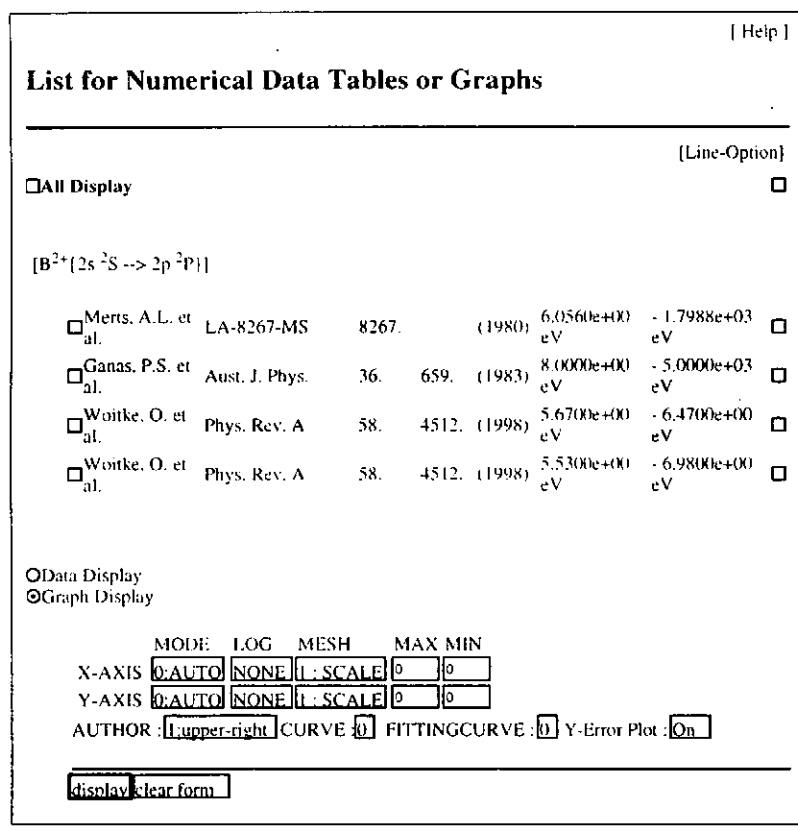

Figure 1: A page for selecting numerical data set for tables or a graph, or to specify parameters for drawing a graph after retrieving data on B^{2+} for AMDIS-EXCITATION.

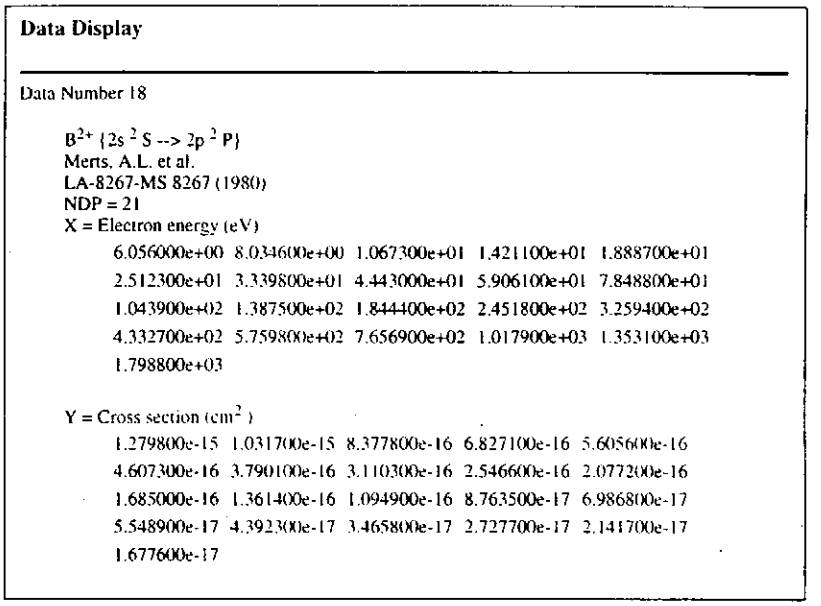

Data Display

Data Number 18

B^{2+} {$2s^2S$ --> $2p^2P$}
Mertz, A.L. et al.
LA-8267-MS 8267 (1980)
NDP = 21
X = Electron energy (eV)

6.056000e+00 8.034600e+00 1.067300e+01 1.421100e+01 1.888700e+01
2.512300e+01 3.339800e+01 4.443000e+01 5.906100e+01 7.848800e+01
1.043900e+02 1.387500e+02 1.844400e+02 2.451800e+02 3.259400e+02
4.332700e+02 5.759800e+02 7.656900e+02 1.017900e+03 1.353100e+03
1.798800e+03

Y = Cross section (cm^2)

1.279800e-15 1.031700e-15 8.377800e-16 6.827100e-16 5.605600e-16
4.607300e-16 3.790100e-16 3.110300e-16 2.546600e-16 2.077200e-16
1.685000e-16 1.361400e-16 1.094900e-16 8.763500e-17 6.986800e-17
5.548900e-17 4.392300e-17 3.465800e-17 2.727700e-17 2.141700e-17
1.677600e-17

Figure 2: An example of numerical data table on B^{2+} for AMDIS-EXCITATION.

As for numerical databases, we have 'AMDIS' for cross sections of ionization and excitation by electron impact; 'CHART' for cross sections of ionization and charge transfer by ion-atom collisions, 'SPUTY' for sputtering yield on monatomic solids, and 'BACKS' for energy and particle backscattering coefficients of light ions projected onto surface. Recently we have prepared a new database on recombination cross sections and rate coefficients in 'AMDIS' and have started to collect data.

These databases contain numerical data with bibliographic information. Numerical data are shown as tables or graphs which can be downloaded as PostScript files to your computers. For making a table or a graph, you can select the data set on the page like Fig.1. Figures 2 and 3 are examples of output table and graph. In the page of Fig.1 users can change a range of X-axis to make a graph like Fig.4. As an option, empirical formulae for ionization cross section, sputtering yields, and backscattering coefficients can be drawn with data points.

Any collaborations will be greatly appreciated for collecting data, submitting data, or requesting data, to advance the database and make it more comprehensive. Feedback from users is quite important for us. Please send any comments, requests, or questions on the database to dbmaster@dbshino.nifs.ac.jp.

References

[1] Murakami I, et al. 1998 *Proceedings of International Conference on Atomic and Molecular Data and their Applications (POSTER PAPER)*, eds. Wiese W. L. and Mohr P. J. (Gaithersburg, USA; NIST Special Publication 926), p57.

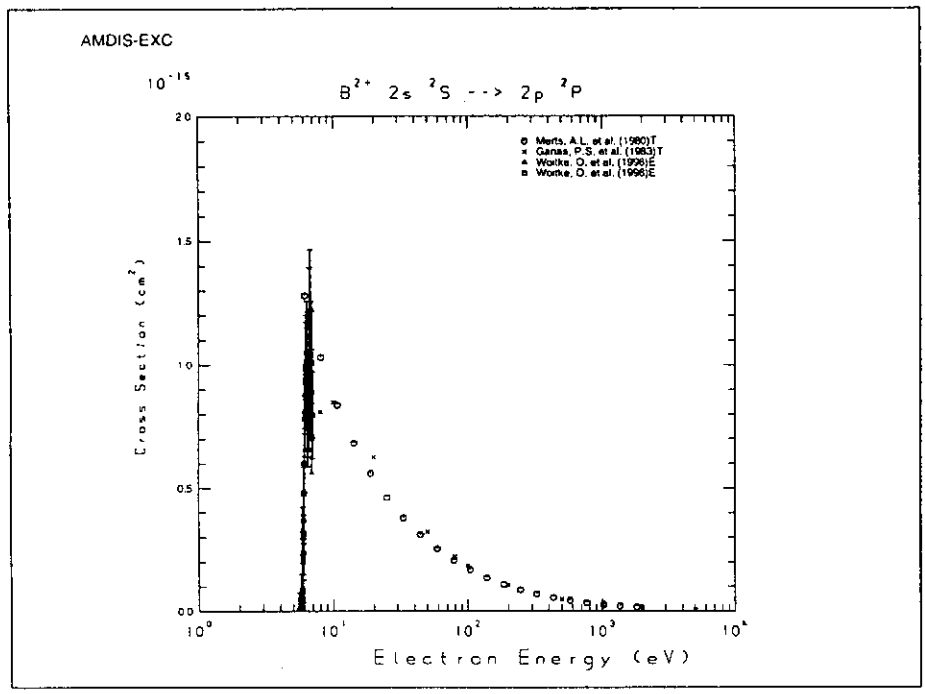

Figure 3: Output graph for excitation cross section of $B^{2+}(2s^2S \rightarrow 2p^2P)$ from AMDIS-EXCITATION (the same data as Fig.1).

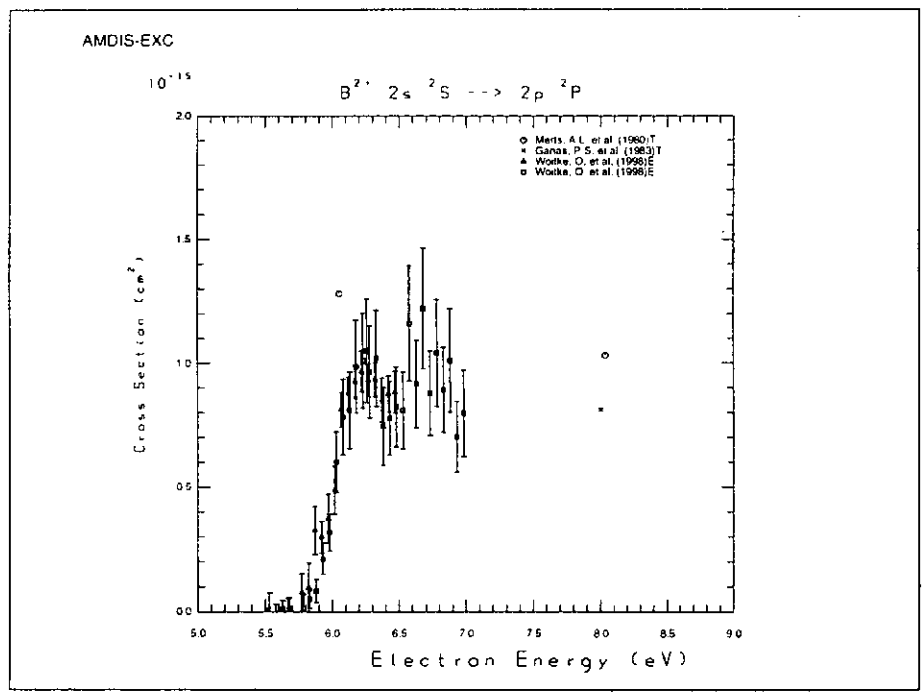

Figure 4: Excitation cross section of the same data as Fig.3, but for electron energy of 5eV-9eV as the X-axis range.

Recent Theoretical Studies On Excitation and Recombination

Anil K. Pradhan
Department of Astronomy, The Ohio State University
Columbus, Ohio, U.S.A. 43210.

July 11, 1999

Abstract

New advances in the theoretical treatment of atomic processes in plasmas are described. These enable not only an integrated, unified, and self-consistent treatment of important radiative and collisional processes, but also large-scale computation of atomic data with high accuracy. An extension of the R-matrix work, from excitation and photoionization to electron-ion recombination, includes a unified method that subsumes both the radiative and the di-electronic recombination processes in an ab initio manner. The extensive collisional calculations for iron and iron-peak elements under the Iron Project are also discussed.

1 Introduction

The modeling and spectral diagnostics of laboratory and astrophysical sources requires a comprehensive and precise set of atomic parameters for processes related to electron and photon interactions with atoms. Fig. 1 schematically illustrates some of the most important radiative and collisional processes: electron impact excitation (EIE), photoionization (PI), radiative and dielectronic recombination (RR and DR). Autoionization (AI) through resonant, doubly excited states plays an important role. Including AI we have: (a) photoionization and recombination as *inverse* processes, (b) electron excitation and recombination as *complementary* processes with respect to the electron+photon (hν) flux, and (c) RR and DR as a *unified* process of electron-ion recombination.

The coupled channel, or the close-coupling, approximation represents the electron-ion wavefunction in terms of channels corresponding to the levels of the ion (called "target"), and the spin and orbital angular momenta of the free electron.

$$\Psi_E(e+ion) = \sum_{i=1} \psi_i \theta_i + \sum_{j=1} C_j \Phi_J, \qquad (1)$$

where ψ_i is a target ion wave function in a specific state $S_i\ L_i$ and θ_i is the wave function for the free electron in a channel labeled as $S_i L_i k_i^2 \ell_i (SL\pi)$, k_i^2 being its incident kinetic energy relative to $E(S_i L_i)$ and ℓ_i its orbital angular momentum. The free channels are "open" or

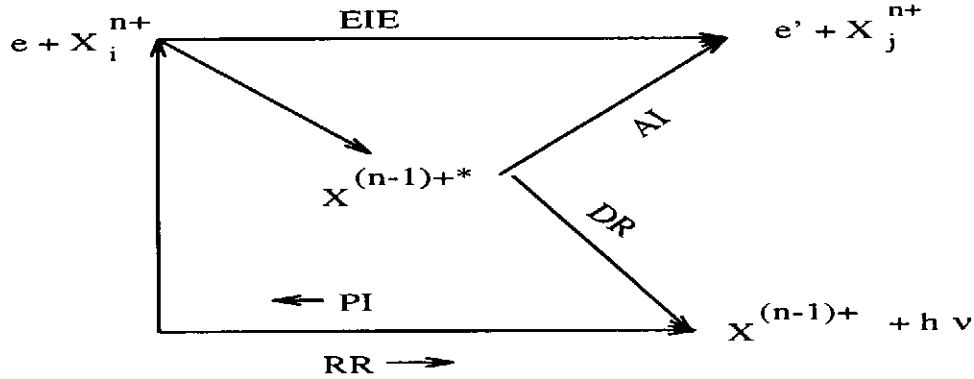

Figure 1: Electron-ion atomic processes

"closed" according to whether $k_i^2 <$ or $> E(S_iL_i$. A is the antisymmetrization operator for all $N+1$ electron bound states, with C_j as variational coefficients. The second sum in Eq. (1) represents short-range correlation effects and orthogonality constraints between the continuum electron and the one-electron orbitals in the target ion. For $E < 0$ (all channels closed) one obtains the (e+ion) bound state wavefunctions $\Psi_B(E)$, and for $E > 0$ the continuum or free state wavefunctions $\Psi_F(E)$. These yield the radiative transition probabilities for bound-bound transitions $< \Psi_B(E)\|\mathcal{D}\|\Psi_B(E') >$, the bound-free transitions or photoionization/recombination cross sections from $< \Psi_B\|\mathcal{D}\|\Psi_F(E') >$, where $\mathcal{D}$ may be the dipole operator. These parameters and collisional cross sections are obtained using the R-matrix method (Burke and Berrington 1993).

2 Electron Impact Excitation

The Iron Project

Employing the relativistic Breit-Pauli R-matrix (BPRM) codes the Iron Project aims at a comprehensive computation of collisional and radiative data for iron and iron-peak elements (Hummer *et al.* 1993). The primary emphasis is on electron excitation collision strengths and rate coefficients for iron ions Fe I - I VI. Results are reported in a continuing series of approximately 40 publications (details on www.astronomy.ohio-state.edu/~pradhan, and www.am.qub.ac.uk/projects/iron).

Review and Compilation of Data Sources

A recent review and evaluated compilation of data (Pradhan and Zhang 1999) will be available in a Landolt-Börnstein volume on Atomic Collisions (Springer-Verlag, Ed: Y. Itikawa). The article includes a table of evaluated data sources listing the method of calculation, atomic effects included, and an approximate accuracy rating. In addition, a table of collisional and transition probabilities data is included for ions in low ionization stages of a number of astrophysically abundant elements (the current version of this data table was compiled by Pradhan and Peng 1995, available from the author's Web site above).

TOPbase/TIPbase

The energy level, transition probabilities, and photoionization data from the Opacity Project (Seaton *et al.* 1994), and the collisional and radiative data from the Iron Project (Hummer *et al.* 1993) data will also be available from a Web site in preparation by C. Mendoza in collaboration

with members of these two projects (hyperlink from the author's Web site). At the present time TOPbase may be accessed via Internet. Login information may be obtained from the Author's homepage or directly as follows – European site at Centre de Donnes Strasbourg (telnet: cdsarc.u-strasbg.fr = 130.79.128.5), US site at HEASARC, NASA, GSFC (telnet: topbase.gsfc.nasa.gov = 128.183.126.111). At both sites enter username: topbase and password: Seaton+

3 Electron-ion recombination

Electron-ion recombination cross sections and rates may be calculated using the R-matrix method subsuming both the RR and DR processes in an *ab initio* and unified manner (Nahar and Pradhan 1992,1995; Zhang *et al.* 1999). The approach entails: (a) computation of photo-recombination cross sections from photoionization cross sections for low-lying bound states with $n \leq n_0 \approx 10$, via the Milne detailed-balance relation, and (b) DR cross sections from high-n resonances, $n_0 < n \leq \infty$, using analytic expressions for both the detailed and the resonance averaged cross sections using the DR theory by Bell and Seaton (1985). The computations in (a) include several hundred bound states of the (e+ion) system with low-n autoionizing resonances (up to $n \approx n_0$) delineated at several thousand photon energies. Employing the Breit-Pauli R-matrix method the calculations have been extended to highly charged ions including relativistic effects and associated couplings (Zhang and Pradhan 1997). For highly charged ions, such as the H-like and the He-like ions, the resonances in (a) could decay radiatively (Pradhan and Zhang 1997, Zhang *et al.* 1999) and radiation damping of the otherwise extremely narrow resonances, but with autoionization rates comparable to radiative rates, could be significant.

Fig. 2 shows the recombination cross sections for electrons with He-like C V, i.e $e + CV \rightarrow CIV$. Three independent sets of calculations are shown: photo-recombination (PR) cross sections (with radiatively damped resonances), the DR cross sections using the Bell and Seaton theory, and the electron impact excitation cross section at the threshold energy E = 0 for the dipole transition $1^1S_0 - -2^1P_0^o$. The unification and correspondence between the PR cross section, including resonant and background contributions, and the and DR cross section neglecting the background, is seen in the precise match at $n \approx 10$ (dashed line). The DR cross section rises to match the excitation cross section exactly at threshold, as expected, since the photon flux produced via DR as $n \rightarrow \infty$ must equal the electron scattering flux at E = 0 ($n = \infty$). Owing to interaction with the radiation field, the autoionizing resonances are broadened, smeared, and wiped out as $n \rightarrow \infty$. All three parts of the cross section in Fig.2 may be verified experimentally through recent ion storage ring and merged beam experiments (Zhang *et al.* 1999).

Unified recombination rates for all C and N ions (Nahar and Pradhan 1997), for all O ions (Nahar 1999), and for Fe I - V (references in Bautista and Pradhan 1998), and several other ions, have been obtained. The new rates, unlike previous works, also satisfy the photoionization equilibrium condition between photoionization/ recombination in a fundamentally consistent manner: the photoionization and recombination calculations are carried out *using the same set of atomic eigenfunctions* (Eq. 1). The new unified recombinations rates for Fe I –V differ considerably, by several factors, from the sum of RR and DR rates computed separately in previous works (Bautista and Pradhan 1998).

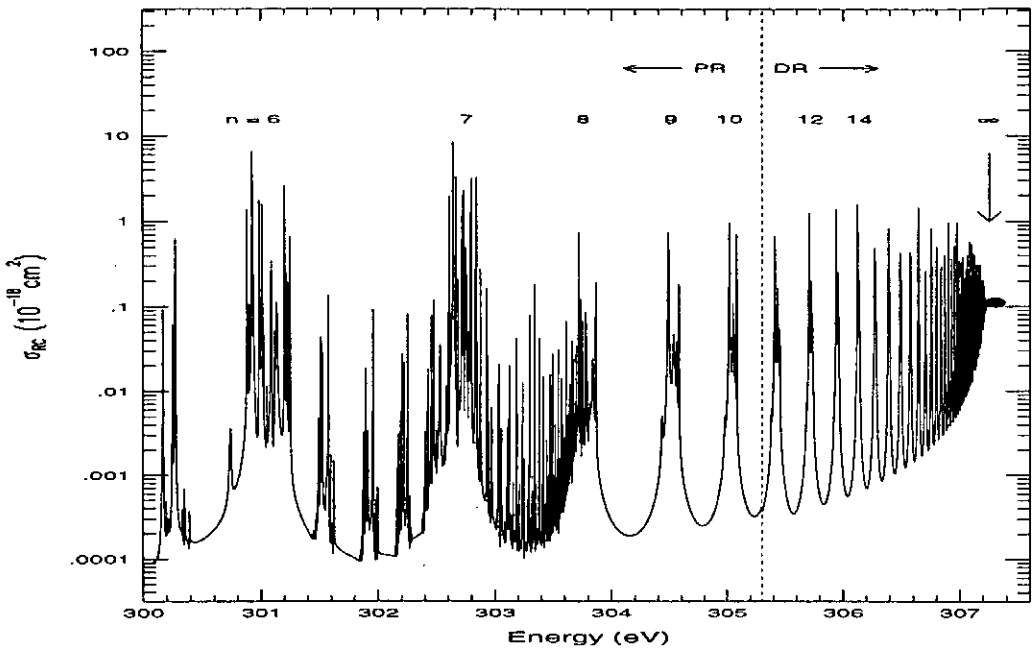

Figure 2: Correspondence between photo-recombination(PR), di-electronic recombination(DR), and electron impact excitation (filled circle and arrow at $n \rightarrow \infty$) cross sections for $e + C\ V \rightarrow C\ IV$ (Zhang *et al.* 1999).

4 References

Burke P G and Berrington K A 1993 *Atomic and Molecular Processes, an R-matrix Approach* (Intitute of Physics Publ. Bristol)

Bell R H and Seaton M J 1985 *Journal Of Physics B* **18** 1589

Hummer D G, Berrington K A, Eissner W, Pradhan A K, Saraph H E and Tully J A 1993 *Astron. Astrophys.* **279** 298

Nahar S N 1999 *Astrophys. J. Supp. Ser.* (submitted)

Nahar S N and Pradhan A K 1992 *Physical Review Letters* **68** 1488

Nahar S N and Pradhan A K 1995 *Astrophys. J.* **447** 966

Nahar S N and Pradhan A K 1997 *Astrophys. J. Supp. Ser.* **111** 339

Pradhan A K and H L Zhang 1997 *Journal Of Physics B* **30** L571

Seaton M J, Yu Y, Mihalas D and Pradhan A K 1994 *Mon. Not. R. astr. Soc.* **266** 805

Zhang H L and Pradhan A K 1997 *Physical Review Letters* **78** 195

Zhang H L, Nahar S N and Pradhan A K 1999 *Journal Of Physics B* **32** 1459

Acknowledgments

This work was supported partially by the U.S. National Science and Foundation and NASA. I am grateful to my colleagues Sultana Nahar and Hong Lin Zhang for contributions.

Recent Livermore Excitation and Dielectronic Recombination Measurements for Laboratory and Astrophysical Spectral Modeling

P. Beiersdorfer[1], G. V. Brown[1], M.-F. Gu[2], C. L. Harris[3], S. M. Kahn[2], S.-H. Kim[4], P. A. Neill[3], D. W. Savin[2], A. J. Smith[5], S. B. Utter[1], and K. L. Wong[1]

[1] *High-Temperature and Astrophysics Division, Lawrence Livermore National Laboratory, Livermore, CA 94550, USA*

[2] *Department of Physics, Columbia University, New York, NY 10027, USA*

[3] *Department of Physics, University of Nevada, Reno, NV 89557, USA*

[4] *Department of Physics, Pohang University of Science and Technology, Pohang, 790784, Korea*

[5] *Department of Physics, Morehouse College, Atlanta GA 30314, USA*

Abstract. Using the EBIT facility in Livermore we produce definitive atomic data for input into spectral synthesis codes. Recent measurements of line excitation and dielectronic recombination of highly charged K-shell and L-shell ions are presented to illustrate this point.

Introduction

X-ray spectroscopic measurements using the Livermore Electron Beam Ion Trap (EBIT) have been optimized over the past decade to provide definitive values of electron-impact excitation, ionization, and resonance excitation cross sections, as well as dielectronic resonance strengths. These measurements have covered a great number of excitation and recombination processes. Recent results have demonstrated several shortcomings of theoretical data. For example, the dielectronic recombination satellite emission involving spectator electrons with $n \geq 4$ contributing to the Kβ ($3 \rightarrow 1$) emission in heliumlike Ar^{16+} was shown to be considerably larger than expected from standard scaling procedures [1]. This EBIT result has now lead to a reassessment of line profile calculations of the heliumlike Ar^{16+} Kβ resonance line used for density diagnostics in laser fusion. Moreover, 30 years of calculations were shown to be unable to predict a reliable ratio for the singlet to triplet ratio of the $3d \rightarrow 2p$ line emission in neonlike Fe^{16+} [2]. The EBIT value for this ratio is in better agreement with theoretical data from 1967 [3] than with any calculation published since, despite the introduction of improved calculational techniques. The laboratory value markedly changed the amount of resonant scattering of the strong Fe^{16+} lines infered from solar corona observations. A third example is provided by measurements of the radiative power loss from highly charged krypton ions (Kr^{30+} through Kr^{34+}) performed at the EBIT facility in Berlin [4]. The measured radiative power loss exceeds that calculated with the average-ion model used in fusion [5] by a factor of two and also exceeds that of more refined model calculations using a fully collisonal-radiative model [6]. The higher rate impacts the design of radiative divertors and the power balance in tokamaks.

As the examples above illustrate, EBIT measurements are needed not only to assess the accuracy of theoretical data, but are now urgently needed to provide definitive data in areas in which calculations fail to produce atomic data with the accuracy required for spectral modeling. In the following, we present recent work at the Livermore EBIT facility relevant to laboratory and astrophysical plasma modeling that further illustrate this need.

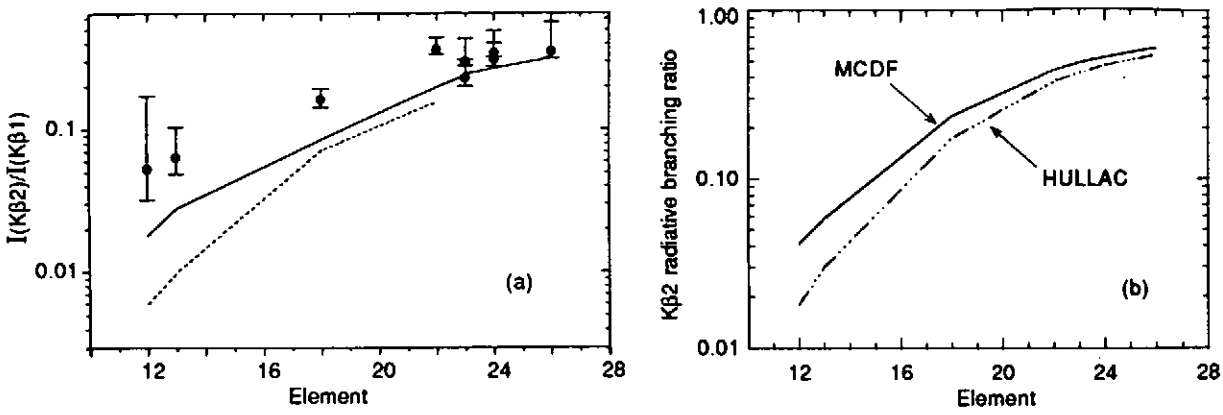

Figure 1: (a) Ratio of intercombination to resonance line in heliumlike Kβ spectra. The solid line (dashed line) represents calculations with the distorted-wave code of Sampson and Zhang (HULLAC); (b) Radiative branching ratio of the heliumlike Kβ line calculated with MCDF and HULLAC codes. (From [7].)

Intensity Ratio of $3 \rightarrow 1$ Lines in Heliumlike Ions

Using high-resolution crystal spectrometers, we have carried out systematic measurements of the $3 \rightarrow 1$ line emission from heliumlike ions. We have found significant disagrement between the measured and calculated ratios of the $1s3p\ ^3P_1 \rightarrow 1s^2\ ^1S_0$ intercombination and the $1s3p\ ^1P_1 \rightarrow 1s^2\ ^1S_0$ resonance line in low and medium Z ions [7]. This disagreement is illustrated in Fig. 1(a). The figure plots the ratios measured just above threshold for electron-impact excitation where direct electron-impact excitation is the only line formation mechanism. Also shown are the results from two theoretical calculations. The first uses the distorted wave code from Zhang *et al.* [8], the second the HULLAC package [9]. While the cross sections calculated with each code agree with each other, the final results differ significantly from the measured ratios. The reason is that the $1s3p$ levels have radiative decay channels besides deexcitation to ground. Consequently, the calculated excitation cross sections must be multiplied by the appropriate radiative branching fractions. In the first case, the branching fractions calculated with the MCDF method were used; in the second case, fractions calculated by the HULLAC package were used. These two methods produce significantly different branching ratios, as illustrated in Fig. 1(b). These differences are largest for the lower-Z heliumlike ions.

Uncertainties in the radiative rates alone, however, cannot explain all of the discrepancy between the calculated and observed line ratios. Calculations based on the relativistic configuration interaction method, which are deemed reliable to within about 1 %, have indicated that the actual branching fraction lies somewhere inbetween the two calculations shown in Fig. 1(b). Therefore, no further improvement of theory relative to experiment can be expected, even if very accurate branching fractions become available. Instead, part of the disagreement is likely to be due to inaccuracies in the distorted wave calculations.

Intensity Ratio of $3 \rightarrow 2$ Lines in Neonlike Ions

A detailed study of the line emission of neonlike Fe^{16+} has found significant disagrement between the measured and calculated ratios of the $2p^5 3d\ ^3D_1 \rightarrow 2p^6\ ^1S_0$ intercombination

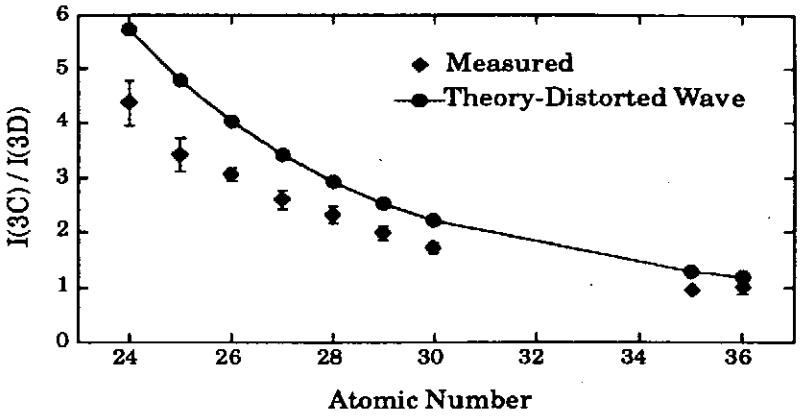

Figure 2: Ratio of intercombination and resonance line in neonlike ions. The solid line repesents results calculated in the distorted-wave approximation. (From [10].)

and the $2p^5 3d\ ^1P_1 \rightarrow 2p^6\ ^1S_0$ resonance line [2]. We have now completed a measurement of this line ratio as a function of Z and have uncovered a systematic disagreement for all ions studied [10]. The results are shown in Fig. 2.

Unlike the heliumlike $1s3p\ ^3P_1 \rightarrow 1s^2\ ^1S_0$ lines the neonlike lines decay essentially 100% to ground. Errors in radiative rates should, therefore, not be the reason for the disagreement. The disagreement must instead be caused by inaccuracies in the distorted-wave calculations of the excitation cross sections. These measurements confirm the problems uncovered with the Fe^{16+} ratio [2] mentioned in the introduction and show that they extend along the isoelectronic sequence.

Dielectronic Recombination Contributions to L-shell Lines

An area that has received essentially no theoretical or experimental attention is the contributions to L-shell emission lines from resonance excitation and high-n dielectronic satellites. We have made a systematic effort to measure all L-shell transitions in neonlike through lithiumlike iron, Fe^{16+} – Fe^{23+}. An inventory of these lines is given by Brown *et al.* [11]. An example of our measurements of the line formation processes producing a $3d \rightarrow 2p$ line in lithiumlike Fe^{23+} is shown in Fig. 3. Our measurements clearly show the different contributions to the line: direct electron-impact excitation and resonance excitation above 1.2 keV, high-n satellites below. Resonance excitation has been calculated in the iron project [12]; agreement with our measurements is marginal. The energy grid of these calculations is coarse, so that resonances are easily missed. Those that are not missed are given additional weight, so that agreement with our measurements is in part fortuitous (cf. Gu *et al.* [13]). The status of calculations is worse for high-n satellites. As illustrated in Fig. 3, the high-n satellites contribute a considerable fraction of the total line emission. These satellites blend with the resonance lines and spectroscopically cannot be resolved, and thus must be included to properly model astrophysical or laboratory spectra. At present, calculations of the satellites below threshold have not been carried out for most L-shell lines. We will soon have completed our measurement of all of the relevant satellite and resonance contributions for strong Fe^{16+} – Fe^{23+} lines making the need for calculations disappear.

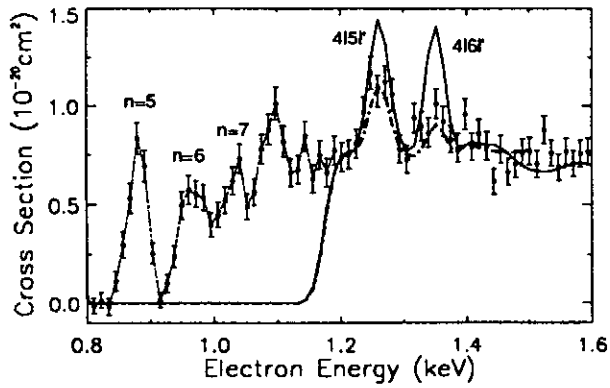

Figure 3: Excitation of the $3d_{5/2} \rightarrow 2p_{3/2}$ transition in lithiumlike Fe^{23+}. The solid line represents Iron Project calculations using the R-matrix method; the dashed line represents subsequent R-matrix calculations employing a much finer energy grid. (From [13].)

Conclusion

We have presented several recent results of our ongoing spectroscopic effort to provide atomic data for spectral modeling. We have illustrated several cases where measurements are more reliable and complete than calculations. Our measurements provide the atomic data needed for synthesizing accurate spectral models that cannot be provided with the same confidence using theoretical methods. In this sense, our EBIT facility and its spectroscopic equipment have become an analog computer where Nature computes the correct result for inclusion in spectral codes.

This work was performed under the auspices of the Department of Energy by Lawrence Livermore National Laboratory under contract W-7405-ENG-48. It was supported in part by the Office of Basic Energy Sciences, Division of Chemical Physics, (LLNL, Morehouse College), the Nevada DOE Office (UNR), as well as the National Aeronautic and Space Agency, Office of Space Science (LLNL, Columbia University). We also gratefully acknowledge support from the Livermore Collaborations Program for Historically Black Colleges and Universities and the Korea Science and Engineering Foundation (KOSEF).

References

[1] A. J. Smith et al., Phys. Rev. A **54**, 462 (1996).
[2] G. Brown et al., Astrophys. J. **502**, 1015 (1998).
[3] O. Bely and F. Bely, Sol. Phys. **2**, 285 (1967).
[4] R. Radtke, C. Biedermann, T. Fuchs, G. Fußmann, and P. Beiersdorfer, in prep., 1999.
[5] D. E. Post et al., At. Data Nucl. Data Tables **20**, 397 (1977).
[6] K. Fournier et al., in *AIP Conf. Proc. 443*, p.73, Woodbury, NY, 1998, AIP.
[7] A. Smith et al., in preparation, 1999.
[8] H. L. Zhang, D. H. Sampson, and R. E. H. Clark, Phys. Rev. A **41**, 198 (1990).
[9] A. Bar-Shalom, M. Klapisch, and J. Oreg, Phys. Rev. A **38**, 1773 (1988).
[10] G. Brown, P. Beiersdorfer, K. Reed, D. Liedahl, and K. Widmann, in preparation, 1999.
[11] G.V. Brown et al., in preparation, 1999.
[12] K. Berrington and J. Tully, Astron. Astrophys. Suppl. **126**, 105 (1997).
[13] M. Gu et al., Astrophys. J. **518**, 1002 (1999).

Experimental Recombination Rates for Highly Charged Ions

Reinhold Schuch[1]

[1] *Department of Atomic Physics, Stockholm University, Frescativ. 24, S-104 05 Stockholm, Sweden*

Abstract. Recent studies of recombination between free electrons and highly charged ions using electron coolers of heavy-ion storage rings have produced accurate rate coefficients of interest for plasma modeling and diagnostics. Some surprises were discovered which can lead to revisions of recombination models. With bare ions one finds at low energy a strong and puzzling deviation from radiative recombination theory. Dielectronic recombination with C3+, N4+) show that jj coupling gives essential contributions to the cross section also for light ions.

A revolutionary development in the experimental techniques for studying electron-ion collisions came end of the 80's with the advent of heavy-ion cooler storage rings[1, 2] and electron beam ion traps[3]. These devices allow investigations of reactions between electrons and ions in almost any charge state (q) with high resolution, signal-to-background ratio, and luminosity. Primarily recombination processes are studied, but work on electron impact excitation and ionization is done as well. Due to the permanently improving resolution and accuracy obtained at these devices recombination studies e.g. at storage rings made seminal contributions to fundamental atomic spectroscopy [4, 5, 6, 7, 8, 9]. A recent development of expanded electron beams has reduced the electron temperature distributions[10] to temperatures of e.g. $kT_\perp = 10^{-3}$eV transverse and $kT_{||} = 10^{-4}$eV longitudinal at the newly upgraded electron cooler in the storage ring CRYRING at Manne Siegbahn Laboratory in Stockholm. The measurements of recombination rate coefficients at such devices have also obtained increasing importance in plasma physics[11]. When comparing the experimental rate coefficients with calculations, one has to fold the theoretical cross section σ with the electron velocity distribution $f(\vec{v}_e)$ to get a theoretical rate coefficient $\alpha =< \sigma \cdot v >$.

Quite substantial deviations from the standard theories of recombination were found with the improved resolution and accuracy at the electron coolers [12, 13, 14, 11, 15, 16]. For astrophysical and plasma applications it is thus desirable to get recombination rate coefficients as function of temperature T directly from the measured rate coefficient $\alpha_{\rm exp}(E_{\rm rel})$: $\alpha(T) = 8\pi m_e/(2\pi m_e kT)^{3/2} \int \alpha_{\rm exp}(E_{\rm rel}) exp(-E_{\rm rel}/kT) dE_{\rm rel}$ Folding $\alpha_{\rm exp}(E_{\rm rel})$ with a Maxwellian temperature distribution is an approximation for low temperatures, where kT becomes comparable with $kT_\perp$. The error in the approximation is less then the experimental error of 5 % if kT $\geq 10 kT_\perp$. This condition satisfies also the approximation of replacing the center-of-mass energy scale $E_{\rm cm}$ by the mean longitudinal energy detuning of the two beams, called relative energy $E_{\rm rel}$. It is clear that the recombination coefficient needs to be measured over an appropriate wide energy range in order to make this folding valid.

The experimental rate coefficient is obtained from: $\alpha_{exp}(E_{\rm rel}) = \gamma^2 \frac{N_t^{corr}/\delta t}{n_e N^i (\ell/L)}$, where γ is the Lorentz factor and N^i for the number of stored ions. The detected recombined ion rate per time unit δt at $E_{\rm rel}$ of the scan $(N_t^{corr}/\delta t)$ is correcting for the electron capture background (at most a few percent at low $\alpha(E_{\rm rel})$). The number of circulating ions is

[1] E-mail : schuch@msi.se

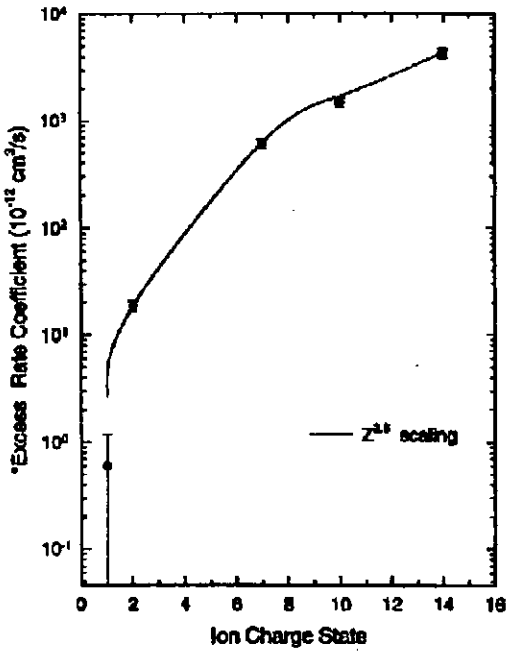

Figure 1: The "excess" recombination rate coefficients for different bare ions. A fit to the data points by a $Z^{2.8}$ dependence is shown (full line).

derived from $N^i = \mathcal{I}/(e\, f_s)$, with f_s the Schottky frequency and $\mathcal{I}$ the ion beam current, measured with the current transformer. L stands for the ring circumference, ℓ for the effective length of the interaction for recombination. In CRYRING e.g. is L=51.68 m and $\ell = 0.83 + -0.03m$. The values of α_{exp} have systematic errors of around 10%, originating mainly from the uncertainty in the ion current.

The recombined atoms or ions are separated from the stored ion beam in the ring by the first bending magnet after the electron cooler and detected by surface-barrier detectors, channel plates, or scintillators. Field ionization of loosely bound electrons in the motional electric field in this magnet limits the number of detected ions to those that recombined into states with values of the principal quantum number n smaller than some critical n_{max}. $E_{\rm rel}$ can be derived from the cooler cathode voltage U_{cath} and the Schottky frequency. Ways to get $E_{\rm rel}$ with high accuracy, which were developed at CRYRING, are described in ref.[17, 9]

The following basic processes of recombination are distinguished:

$$A^{q+} + ke^- \longrightarrow A^{(q-1)+} + ze^- + h\nu \ .$$

The cross section of radiative recombination (RR) ($z = k - 1, Z \geq$q, Z is the nuclear charge) diverges with $1/E_{\rm cm}$ and goes with $1/n$ predominantly in low n of ion $A^{(q-1)}$ [18]. In dielectronic recombination ($z = k - 1$, $Z >$q), a free electron is captured via a doubly excited state (n,n') which can emit a photon to complete recombination. The cross section reflects the atomic structure and radiative decay rates of the doubly excited state. In three-body recombination (TBR)(z=k-1>0, $Z \geq$q), one electron recombines in the vicinity of another electron by transferring energy and momentum to it[19]. Its rate coefficient should have a characteristic dependence on the electron temperature ($1/T^{4.5}$), density (ρ_e^2), ion charge (q^3), and favours very high n (n^7)[20].

The recombination rate coefficient measured for bare ions (where only RR and TBR

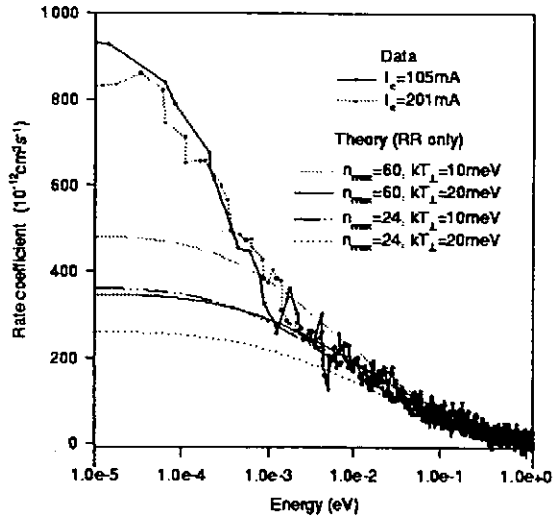

Figure 2: The rate coefficients for Ne^{7+} [24]) measured with electron beams of two different densities. The lines are calculated radiative recombination rate coefficients folded with $kT_\perp$ = 20meV and 10 meV.

can occur), e.g. for D^+, He^{2+}, N^{7+} Ne^{10+}, and Si^{14+} was found to be enhanced with increasing q (e.g. N^{7+} around factor of 2, Si^{14+} around factor of 4) compared to the RR rate coefficient. These enhancement factors were found for an electron temperature of $kT_\perp = 10^{-2}$eV and density $4{\cdot}10^7 cm^{-3}$. It appears at $E_{\rm rel}$ below 10^{-3} eV. Under the static conditions of cooling, the rate coefficients are found to correspond to those at $E_{\rm rel} \leq 10^{-4}$ eV. The RR rate coefficient $\alpha_{\rm rr}$ were subtracted from the measured rates[22] and the 'excess rates' are plotted in Figure 1. A best fit to these points is obtained by a $Z^{2.8}$ dependence, which is very close to that predicted for TBR[19]. An estimate of the TBR rate coefficient ($\alpha_{\rm TBR}$) for a flattened electron velocity distribution[20] gave to small a value to account for the measured enhancement. This is due to ionization of the very high n states, populated by TBR, by motional electric fields in the magnets. TBR could still contribute if these stabilize collisionally or radiatively to lower n. An estimate including radiative de-excitation and $\alpha_{\rm TBR}$ from Mansbach and Keck[21] showed an order-of-magnitude agreement with the measured "excess" rates[22]. TBR should be characterized by a quadratic dependence of the rate on the electron density. Such a dependence has been searched for with Ne^{10+}, where the measured rate coefficient is enhanced by a factor of 3 at zero relative energy. Still $\alpha_{\rm exp}$ is constant when changing ρ_e over a factor of 5 [23]. In more recent studies a dependence of the recombination rates on the guiding solenoidal field in the cooler was found. This longitudinal magnetic field forces the electrons onto cyclotron orbits which could result in the observed characteristics of the enhanced rates at small E_{rel}. A complete description can, however, not be given by any currently available theoretical model.

The transverse electron beam temperature $kT_\perp$, which dominates the calculated rates for a flattened electron beam, is known within about 25% from electron cooling force measurements[10], from fitting dielectronic recombination (DR) resonances near threshold[6, 24, 25, 26] and the observed fall-off of the laser induced recombination gain [27]. The val-

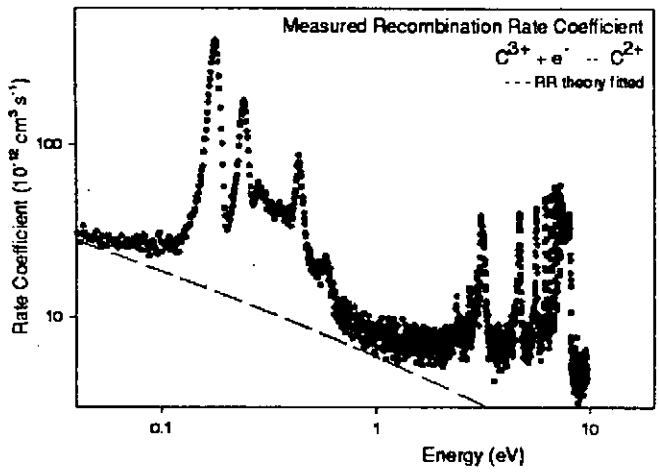

Figure 3: The experimental rate coefficients for recombination of C^{3+}. The dashed line shows the calculated radiative recombination rate.

ues derived from these different methods are quite consistent with each other and are in most of the cases above (about a factor two) the nominal transverse temperature. This discrepancy could probably be explained by influences of the merging and de-merging regions of the beams and by possible miss-alignments of electron and ion beam. A higher transverse temperature will in any case reduce the theoretical recombination rate at low energies. In Figure 2 an example for a measured recombination rate close to zero relative energy with Ne^{7+} is compared to convolutions of the RR cross section with different electron temperatures $T_\perp$, summed to different n_{max}[24]. The validity of the RR cross section is confirmed by the good agreement at $E_{\rm rel} \geq 1\ meV$. There are no dielectronic recombination resonances expected below 1 eV. In the same spectrum resonances at around 1 eV are used to obtain an estimate of $kT_\perp$ = 20meV. The experimental rate coefficient still rises at around 10^{-3} eV, *i.e.* below the transverse temperature, and gets about a factor of 2 higher than $\alpha_{\rm rr}$. It should be noted that reasonable agreement could be obtained if the transverse temperature of the electrons is as low as $\sim 2\ meV$. This low temperature contradicts, however, the temperature which fits the resonances in the same spectrum. In this experiment, data was taken with different electron densities (I_e = 105 mA and I_e = 201 mA), showing the same amount of enhancement. No indication of an electron density dependence was thus found here as well.

Recombination of carbon ions has many applications in astrophysical and fusion plasmas. We have reported high resolution measurements for recombination of C^{3+} to CIII [16]. The recombination spectrum in the region where 1s22pnl 1,3L resonances are expected between 0-8 eV is plotted in Fig.3. Most intensity is in the first group of resonances, between 0.2-0.6 eV above threshold which contains the 1s22p4l 1,3L doubly-excited states. The spectrum was assigned in detail by the aid of very accurate relativistic many-body perturbation calculations [28] by E. Lindroth. It was found that the strongest peaks in the spectrum must be explained by dielectronic recombination mediated by relativistic interaction, a process forbidden in pure LS-coupling. In particular for collisions at low energies,

it is not sufficient to perform calculations of DR only in the LS-coupling approximation, even if the atomic system is described with a very high accuracy in (non-relativistic) LS-coupling.

The dashed line in Fig. 3 shows the calculated radiative recombination rate using the Kramers formula with Gaunt correction. It is fitted to the data points by choosing an appropriate effective charge. At the Rydberg series limit, the fact that the ions pass through magnets and can be field ionized must be taken into account. DR intensity is missing at the high energy side of the series limit above n_{max}. This can, however, be corrected for quite well with extrapolation in n. The presence of an electric field in the interaction region enhances the dielectronic recombination rates in the high-n region[29]. It is due to mixing of ℓ in high n-states which increases strongly the autoionization rates of those with high ℓ values.

References

[1] R. Schuch in "Review of Fundamental Processes and Applications of Atoms and Ions" ed. by C.D. Lin, World Scientific Publ., Singapore (1993).

[2] F. Bosch in Physics of Electronic and Atomic Collisions ed. T. Andersen et al., Adam Hilger IOP Publishing Ltd (1993).

[3] R.E. Marrs, P. Beiersdorfer, D. Schneider , Phys. Today, Oct. 94, p.27.

[4] W. Spies et al., Phys. Rev. Lett. **69** (1992) 2768.

[5] G. Kilgus et al. Phys. Rev. **A47**, 4859 (1993)

[6] D.R. DeWitt et al. Phys. Rev. A50, 1257 (1994) and Journ. Phys. B28, L147, (1995)

[7] H. T. Schmidt, et al. Phys. Rev. Lett. **72**, p.1616 (1994).

[8] S. Mannervik et al. Phys. Rev. A55, 1810 (1997)

[9] W. Zong et al. Phys. Rev. **A56**, 386, (1997).

[10] H. Danared, et al. Phys. Rev. Lett.**72**, 3775 (1994).

[11] D. Savin, ApJ., 489, L115

[12] A. Wolf et al., Z.Phys.D **21**, S69 (1991).

[13] A. Müller et al., Phys.Scr., **T37**, 62 (1991).

[14] Gao Hui et al. Phys. Rev. Lett. **75**, 4381 (1995)

[15] D.R. DeWitt et al., Phys. Rev. **A53**, 2327, (1996).

[16] S. Mannervik *et al.*, Phys. Rev. Lett **81**, 313 (1998).

[17] R. Schuch et al. Hyperfine Interactions 99, 317, (1996).

[18] H.A. Bethe and E. Salpeter, Handbuch der Physik, Vol. 35 (1957) 88.

[19] D.R. Bates, et al. Proc. Roy. Soc. A **267**, 297 (1962).

[20] M. Pajek and R. Schuch, Hyperfine Interactions **108** 185 (1997)

[21] Mansbach P and Keck J **PR181** 275 (1969)

[22] Gao Hui et al. Journ. Phys. B Lett. 30, L1, (1997).

[23] Gao Hui et al., Hyperfine Interactions 99, 301-308, (1996).

[24] W. Zong et al., Journ. Phys. **B31**, 3729, 1998

[25] R. Schuch et al. Hyperfine Interaction **115**, 123, (1998).

[26] P. Glans et al., Nucl. Instr. Meth. B**154**, 97 (1999).

[27] S. Asp et al., Nucl. Ins. Meth. B117, 31 (1996)

[28] E. Lindroth, Hyperfine Interactions **114**, 219 (1998) and this volume.

[29] T. Bartsch et al., Phys. Rev. Lett. **79**, 2233 (1997)

Theory of dielectronic recombination and plasma effects

Yukap Hahn

Department of Physics, Univ. of Connecticut, Storrs, CT 06269
TRG, 49 Timber Drive, Storrs, CT 06268

Abstract: Current status of the various theoretical approaches to calculation of dielectronic recombination rates is summarized, with emphasis on the available data base and on the plasma effects of both the plasma ion (and external) fields andplasma electron collisional effects which seriously affect the rates and complicate compilation of data.

1. Introduction. Dielectronic recombination (DR) is one of the three known ways by which plasma electrons recombine with ions. The other two are the radiative recombination (RR) and three-body recombination (TBR). In all cases, the excess energy is released by the recombining electrons, and carried away by emitted photons in RR, by increased kinetic energy of the participating electrons in TBR, and in DR by one of the bound electrons as it is excited to form a multiply excited states of ions. The DR process was first suggested in the 1940's by Bates and Massey in connection with the astrophysical problems, and later its importance was recognized by Burgess. The realization in the 1970's, that the DR by impurity ions in tokamak was the dominant cooling mechanism, was probably the main incentive for much of the research activities since then, both experimentally and theoretically. For highly charged impurity ions in high temperature plasmas, heavy-ion accelerators with storate rings and EBIT have played a specially important role in generating experimental data, while for low-charged ions large effects of electric fields on DR rates were observed. There have been several reviews on the subject recently [1,2], so only a couple of pertinent points will be made; the 1992 reviews by the experts in the field, both experimental and theoretical, provides an excellent basis of reference.

a) Modelling of high T plasmas requires a complete set of DR rates, in addition to many other rates for the processes that are taking place. Most of the reactions involved are the topics of this workshop. But, inspite of much efforts of the past 30 years, the available data are far from complete. Besides, almost all data are for the initial ground states of ions.

b) At relatively low temperature, the plasma field and collisional effects can be important. Only a handful of cases have been analyzed, and no systematic compilation of data is currently possible. (See section 3 for further discussion).

In the simplified independent electron picture, the DR is a two-step process of excitation/capture, followed by a radiative decay to Auger stable final states. It is schematically described by

$$e_1^- + (e_2^- + A^{Z+1})_g \rightarrow [e_{1b}^{\prime} + (e_2^- + A^{Z+1})_a]_{d=a+b} \rightarrow (A^{Z-1+})_f^{\times} + x$$

where g = ground state $(n_g \ell_g)$ of the target ion with charge Z, a = excited intermediate state of the target with $n_a \ell_a$, d = compound doubly excited states of the recombined ion of charge Z-1 and $(n_a n_b)$, and f = final state of the recombined ion in a singly excited state with $(n_f = n_b)$. x = emitted radiation. The excitation energy $\Delta_{ag} = E_a - E_g$ is supplied

by the recombining electron, as $\Delta_{cb} = E_c - E_b = \Delta_{ag}$. This makes the DR a resonant process with sharp dependence on the continuum electron energy E_c.

It has been found convenient to categorize the DR process into three groups based on the different modes of excitation, although this separation becomes less clearcut as the number of open-shell electrons increases. We have, with $\Delta n \equiv n_a - n_g$ and $\Delta \ell \equiv \ell_a - \ell_g$,

(i) $\Delta n \neq 0$ involving inter-shell transitions with Δ_{ag} large and n_b small.

(ii) $\Delta n = 0$, $\Delta \ell \neq 0$ involving intra-shell transitions with Δ_{ag} and n_b of mederate size.

(iii) $\Delta n = 0$, $\Delta \ell = 0$, involving inter-multiplet transitions, with small Δ_{ag}, large n_b.

The doubly excited states (d) formed by the initial step of excitation-capture in the DR process are affected by the plasma effects, due to the plasma microfield of the plasma ions as well as any externally imposed electric and magnetic fields, and also the collisional effects of plasma electrons. We denote them as plasma field distortions (PFD) and plasma collisional transitions (PCT), respectively. These two effects are not additive, however, and must be included in modelling of the plasma in a consistent way, without double counting. The outer-shell electrons in state (d) with the principal quantum number n_b are in HRS for the excitation modes (ii) and (iii), and thus are most affected by the plasma effects.

2. The DR theories. Most of the data on the DR rates available thus far have been generated by a variety of theoretical methods, with varying degrees of accuracy. Since the work involved in the calculation of the rates is often complex and time consuming, much efforts have been expended to developing procedures that are suited for each specific purpose, and many extensive computer codes are available.

The DR rates and cross sections involve basically two building blocks, the autoionization and radiative decay probabilities, defined as $A_a(d_1 d_2 \rightarrow c, g) = 2\pi |< d_1 d_2 | V_{12} | c, g >|^2$, and $A_r(a \rightarrow f) = 2\pi |< f | \varepsilon \cdot \vec{r} | a >|^2$, respectively. Then, for example in the isolated resonance approximation, where overlapping resonances term are neglected, the DR rates are given by

$$\sum_d \alpha^{DR}(i \rightarrow d \rightarrow f) = (4\pi Ryd/k_B T_e)^{3/2} \sum_d (g_d/2g_i) \exp(-\varepsilon_c(d)/k_B T_e) A_a \Gamma_r / (\Gamma_a + \Gamma_r)$$

where $\Gamma_r(d) = \sum A_r(d \rightarrow f)$ and $\Gamma_a(d) = \sum A_a(d \rightarrow j)$. Thus, accurate α can be constructed once reliable A_a^f and A_r are available, which in turn depend critically on the various electronic wave functions involved in the A's. Theoretical methods employed may be summarized, in the order of increasing complexity and accuracy:

1) Scaled coulomb approximation with effective Z and quantum defects. The calculation can be analytic, and the approach is especially suited in treating high Rydberg state electrons and high Z ions. The overall behavior in Z, n, and T can then readily be inferred. But, the method is less accurate when high precision is sought.

2) Non-relativisitc distorted wave method for the continuum orbitals and model potential (or Hartree-Fock) bound state orbitals in the evaluation of A_r and A_a. Various angular momentum coupling schemes are available, such as LSJ, jjJ, and jK, etc. Some relativistic effects may be included perhaps for $Z < 30$, and cofiguration mixing can be incorporated.

3) Close coupling/ R-marix method for the continuum orbitals, and a set of model wave functions for the bound orbitals. For light ions, this is probably the most accurate approach, but involves many complex steps and often can be very time-consuming [3 – 5].

4) Relativistic distorted wave method, which is suited for treating highly stripped ions, especially for Z > 20, where the coulomb field is strong. Configuration mixing can improve the data.

3. Plasma effects - rate equations and rates. By the plasma effects, we mean a) the collisional effect of the central ion with the plasma electrons (PCT) and b) distortions of the electron orbitals (both bound and continuum) around the central ion by both the plasma microfield due to the plasma ions and externally imposed electric and magnetic fields (PFD). Generally, these effects can be incorporated either in the rates themselves or in the rate equations. But the rate equations are convenient in handling the collision effect, while the rates can readily handle the field effects.

3a. PFD. The static ion microfield is represented for example by the Holtzmark field, and its refinements can be made. Given the field, its effect on DR may be estimated by a simple 'full mixing' picture, where the spherical states are transformed to the stark states, via Clebsch-Gordan coefficients. However, this procedure does not depend on the field strength. A refined procedure is possible, in which a field-dependent phase factor is introduced. A more ambitious treatment involves diagonalization of the energy matrix that contains field shifts. For the excitation modes (ii) and (iii), experiments with light ions indicated that the change in the DR rates due to external electric fieldperturbation can be very large, increasing the rates by as much as a factor of ten. Theoretical analyses showed that such an enhancement is due to strong ℓ mixing with consequent redistribution of the Auger probability A_a relative to the dominant radiative probability A_r. In the simplest picture, this reduces purely to a state counting, in the spherical basis vs the stark (parabolic) bases.

In addition to the electric field effect, a magnetic field plus electric field can further modify the above result [6]; this case may be viewed as producing extra electric field in the Lorentz transformed drift frame with velocity $\vec{u} = c\vec{E}x\vec{B}/E^2$, with the change in the electric field of $\Delta\vec{E} = B^2\vec{E}/2E^2$.

3b. PCT. As noted, the PCT effect can be naturally included by employing the rate equations, which are usually truncated. On the other hand, it is possible to include the correction to this truncation in the rates a part of the collision effect in the rates by using a specially taylored Fokker-Planck operator, as $\tilde{\alpha}$ may be obtained by $\tilde{\alpha}^{DR}(m) \equiv [1 + \Omega]\,\alpha^{DR}(m)$, where Ω depends on the structure of the rate equations and rates. We have made some systematic study of the plasma collisional and field effects, for a simplified hydrogen plasma with carbon impurities [2].

4. DR rates - available data. In the study of high temperature astrophysical and laboratory plasmas, the DR rates are needed (A) for analyses of spectral lines emitted by impurity ions and (B) for modelling of plasmas to determine the ionization balance. Object (A) requires a small set of data of high accuracy, while (B) needs a large set of rates, which are presumably of less accuracy for practical reasons of difficulty in generating them. In 1989, a summary of the available DR data was given [7] for the Fe ions with the degree of ionization Z = 1 to 25. Except for a couple of regions of Z values where data existed, often with poor accuracy, much was not known. In 1993, the overall DR rates were summarized [7], in the form of empirical fitted formula, and poor status of the situation was pointed out. Since then some more high quality data became available, and Very little improvements have been seen since, but where there are new data, the fitted values have been improved, in some cases as much as an order of magnitude. As have been done previously, the rates were summarized in the form of empirical fitted formulas, but separately for each excitation modes discussed above. Only

the contribution from the excitation modes (i) and (ii) were considered. Mode (iii) is important only at low temperature, but the problem of field mixing can be serious.)
We emphasize several important points:
1. Almost all the data are for the target ions initially in their ground states. When these rates are used in the rate equation for modelling purposes, the DR from some of the long-lived excited states may be needed.
2. The rates are calculated routinely with the final (singly excite) states summed, so long as they are Auger stable; otherwise, the cascade effect must be included, that reduces the rates. This is in principle inconsistent with the rate equations to which they are applied.
3. As noted earlier, the contribution from excitation mode iii is usually not included in the empirical formulas. This must be rectified, with careful consideration of possible external field perturbations.

5. Summary. We have made three points of some importance in dealing with the DR processes in high temperature plasmas:

1. A more careful and consistent treatment is needed in defining the rates as they are used in a particular set of rate equations. This is especially relevant as to the way residual plasma collisional effect is to be included.

2. The DR data are much to be generated, with proper accuracy assessment, and adjusted to specific usage. The DR from the initial excited states are desirable, and the total rates, summed over all the singly excited final states, must be used with caution.

3. The DR rates associated with the excitation modes (ii) and (iii) are especially sensitive to external field perturbations, but nothing has been done. In view of large numerical efforts required in generating these rates, it is desirable to determine how the production and compilation can be systematized.

1. 'Recombination of atomic ions', eds. W. Graham et al (NATO ASI Series B: Physics 296)
2. Y. Hahn, Rep. Prog. Phys. 60, 691-759 (1997)
3. S. N. Nahar, M. A. Bautista and A. K. Pradhan, Phys. Rev. A58, 4593 (1998); S. N. Nahar and M. A. Bautista, Astro. J. Suppl. 120, 327 (1999); E. Behar et al, Phys. Rev. A54, 3070 (1996)
4. H. L. Zhang, S. N. Nahar and A. K. Pradhan, J. Phys. B32, 1459 (1999)
5. D. W. Savin et al, Astrophys. J. (1999), Columbia Univ. preprint
6. F. Robicheaux and M S. Pindzola, Phys. Rev. Lett. 79, 2237 (1997); T. Bartsch et al, Phys. Rev. Lett. 82, 3779 (1999)
7. Y. Hahn, JQSRT 49, 81 (1993) and Erratum 51, 663 (1994), and JQSRT Y. Hahn, JQSRT 41, 315 (1989); Y. Hahn, in 'Landolt-Bornstein Series, vol. I/17, Y. Itikawa ed. (1999)

Theory for Ionization of Atoms and Molecules by Electron-Impact*

Yong-Ki Kim
National Inst. of Standards & Technology, Gaithersburg, MD 20899-8423, U.S.A.

* Work supported in part by the United States Department of Energy.

The Binary-Encounter-Dipole (BED) model [1] is a theory for the differential ionization cross section, $d\sigma/dW$, where W is the kinetic energy of the ejected electron. The model requires the continuum dipole oscillator strength, df/dW. The BED model combines a modified Mott cross section and the asymptotic part of the Bethe cross section.

Many tried to combine the two theories by introducing empirical parameters to join them. The BED model uses asymptotic forms of σ_{ion} and $\sigma_{stop} = \int W(d\sigma/dW)dW$ to join the two theories without introducing any empirical parameters.

The BED cross section per orbital is given by

$$\frac{d\sigma(W,T)}{dW} = \frac{S}{B(t+u+1)}\left\{\frac{(N_i/N)-2}{t+1}\left(\frac{1}{w+1}+\frac{1}{t-w}\right)\right.$$
$$\left.+[2-(N_i/N)]\left[\frac{1}{(w+1)^2}+\frac{1}{(t-w)^2}\right]+\frac{\ln t}{N(w+1)}\frac{df(w)}{dw}\right\},$$

$$\sigma_{ion}(t) = \frac{S}{t+u+1}\left[D(t)\ln t+\left(2-\frac{N_i}{N}\right)\left(1-\frac{1}{t}-\frac{\ln t}{t+1}\right)\right],$$

with

$$D(t) = \frac{1}{N}\int_0^{(t-1)/2}\frac{1}{w+1}\frac{df(w)}{dw}dw,$$

$$N_i = \int_0^{\infty}\frac{df(w)}{dw}dw.$$

where T=incident energy, B=binding energy, U=kinetic energy, N=occupation number, t=T/B, u=U/B, w=W/B, $S=4\pi a_0^2 N(R/B)^2$, $a_0=0.529$ Å, and R=13.61 eV.

When reliable df/dW for each orbital is unknown, then we approximate it with hydrogen-like $df/dW = N/[B(w+1)^2]$. This simplification facilitates the integration of df/dW, and leads to the Binary-Encounter-Bethe (BEB) model [1] for the total ionization cross section, σ_{BEB}. The BEB model offers a simple analytic formula for σ_{BEB}. The BEB model can be used for both atoms and molecules.

$$\sigma_Q = \frac{S}{t+u+1}\left[\frac{Q\ln t}{2}\left(1-\frac{1}{t^2}\right)+(2-Q)\left(1-\frac{1}{t}-\frac{\ln t}{t+1}\right)\right],$$

$$Q = \frac{2}{N}\int\frac{B}{E}\frac{df}{dE}dE.$$

If Q is unknown, then we put Q=1 to get

$$\sigma_{BEB} = \frac{S}{t+u+1}\left[\frac{\ln t}{2}\left(1-\frac{1}{t^2}\right)+1-\frac{1}{t}-\frac{\ln t}{t+1}\right].$$

All terms in σ_{BED} have a sound physical basis, except for the u+1 in the denominator.

This term was introduced with the qualitative argument that the effective kinetic energy seen by the bound electron is the incident electron energy, T, plus the potential energy of the bound target electron, i.e., $T \Rightarrow T+U+B$ and $(T+U+B)/B=t+u+1$. The $u+1$ in the denominator acts as a t-dependent scaling of the cross section. This factor should disappear in the limit of $B \to 0$ as in the Mott, Rutherford, Bethe, and other theories. One can alter this factor slightly to adapt the BEB model to different class of targets, such as heavy atoms and ions.

For instance, for a heavy atom/ion we set $u'=(u+1)/[n(q+1)]$ for valence shells, $n>2$ (or use u from the effective core potential) with a net charge q of the target. Many examples and comparisons to available experiments on atoms and molecules are posted on a NIST web site [3].

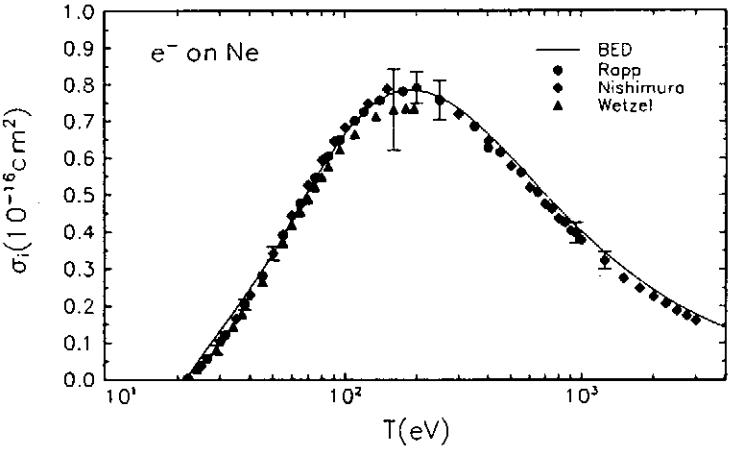

Fig. 1. Total ionization cross section of Ne. Solid line, BED theory; circles, experimental data by Rapp and Englander-Golden [4]; diamonds, data by Nishimura [5]; triangles, data by Wetzel et al. [6].

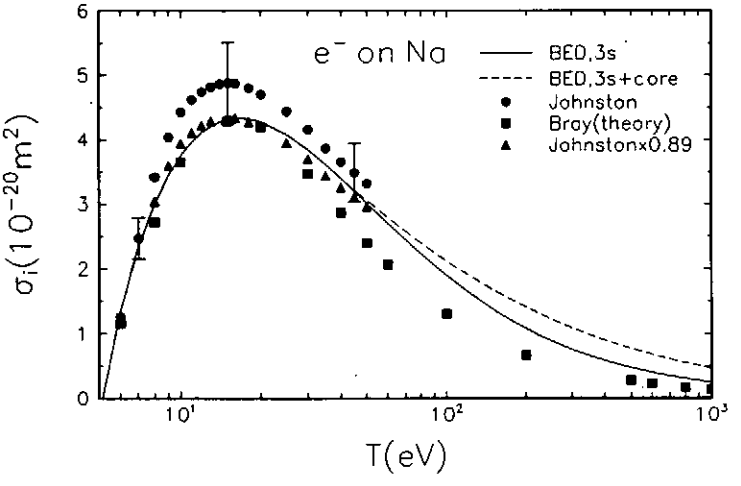

Fig. 2. Total ionization cross section of Na. Solid line, BED theory for the 3s electron; dashed line, BED theory for 3s and the core electrons; circles, experimental data by Johnston and Burrow [7]; squares, convergent close-coupling theory by Bray [8]; triangles, the data by Johnston and Burrow reduced by 11%.

Conclusions

1. The BEB model replaces the Lotz formula, based on much better physics.
2. The BEB model provides an analytic formula from threshold to $T \sim 5$ keV.
3. The BEB model is applicable to neutral atoms, ions, molecules, and radicals with minor modifications requiring only the ground-state wave function of the target.
4. For the energy distribution of ejected electrons, $d\sigma/dW$, reliable continuum oscillator strength for each orbital is required.
5. For He, a combination of the BED model with df/dW from the relativistic random

phase approximation provides the total ionization cross section accurate to ±5% from the threshold to T=1 keV [2]. Matching dσ/dW is also expected to be sufficiently accurate to serve as the normalization standard for other theories and experiments.

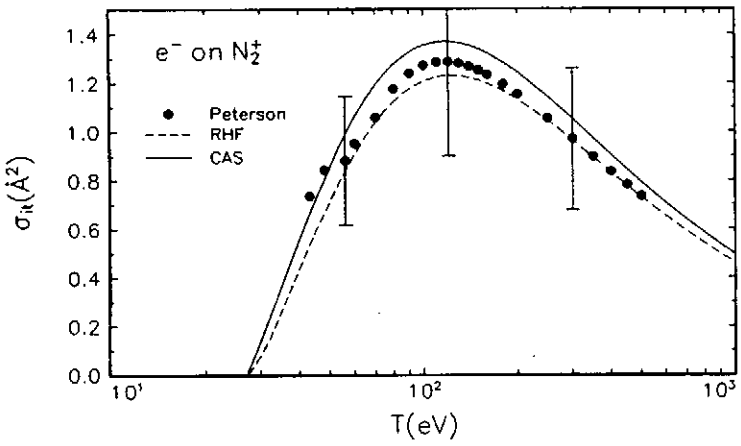

Fig. 3. Total ionization cross section of N_2^+. Solid curve, BEB theory with complete active space (= correlated) wave functions; dashed curve, BEB theory with restricted Hartree-Fock wave function; circles, experiment by Peterson et al. [9].

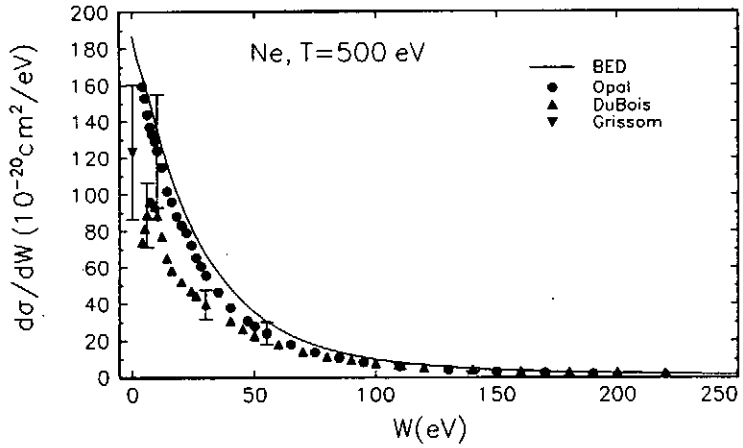

Fig. 4. Differential ionization cross section of Ne at T=500 eV. Solid curve, BED theory with RRPA continuum oscillator strength; circles, experimental data by Opal et al. [10]; upright triangles, data by DuBois and Rudd [11]; and inverted triangle, data by Grissom et al. [12].

References

[1] Y.-K. Kim and M.E. Rudd, Phys. Rev. A **59**, 3954 (1994).

[2] See poster at this conference by Y.-K. Kim, W. R. Johnson, and M. E. Rudd.

[3] http://physics.nist.gov/ionxsec.

[4] D. Rapp and P. Englander-Golden, J. Chem. Phys. **43**, 1464 (1965).

[5] H. Nishimura, private communication (1999).

[6] R. C. Wetzel, F. A. Baiocchi, T. R. Hayes, and R. S. Freund, Phys. Rev. A **35**, 559 (1987).

[7] A. R. Johnston and P. D. Burrow, Phys. Rev. A **51**, R1735 (1995).

[8] I. Bray, Phys. Rev. Lett. **73**, 1088 (1994).

[9]. J. R. Peterson, A. Le Padellc, H. Danared, G. H. Dunn, M. Larsson, R. Peverall, C. Strömholm, S. Rosén, M. af Ugglas, and W. J. van der Zande, J. Chem. Phys. **108**, 1978 (1998).

[10] C. B. Opal, E. C. Beaty, and W. K. Peterson, At. Data, **4**, 209 (1972).

[11] R. D. DuBois and M. E. Rudd, Phys. Rev. **17**, 843 (1977).

[12] J. T. Grissom, R. N. Compton, and W. R. Garret, Phys. Rev. **6**, 977 (1972).

Measurement of Electron Impact Ionisation Cross Sections in Highly Charged Ions

F J Currell, S. Ohtani, E. J. Sokell and H. Watanabe
The University of Electro-Communications, Chofu, Tokyo 182-8585, Japan
Cold Trapped Ions Project, ICORP, JST, Axis Chofu 3F, 1-40-2 Fuda, Chofu,
Tokyo 182-0024, Japan

Abstract

After a brief discussion relating to measurement in systems of lower charge, techniques to measure electron impact ionisation cross sections are reviewed with particular reference to few-electron highly charged ions. The advantages of Electron Beam Ion Traps for such measurements are outlined and the dynamics of creation of highly charged ions in such devices is discussed.

§1 Introduction

Knowledge of electron impact ionisation (EI) cross sections is important for plasma physics since electron impact ionisation is the dominant "plasma creation" reaction in a wide range of systems. This process gives rise to most laboratory plasmas and plays an important role in astrophysical plasmas. Whist there are good measurements available for ions of low charge state ($z<10$), there is far less experimental data available for highly charged ions. This makes confirmation of theoretical cross section calculations and the formulation of reliable scaling laws difficult. What is required is a body of consistent experimental data for a range of systems with different numbers of electrons and different charges. In this article, we will briefly review some measurements of EI cross sections for ions, concentrating mainly on few-electron highly charged ions. We will first however look at measurements involving ions of lower charge state, since this leads into the discussion of some of the difficulties involved in making measurements for higher charge states.

§2 Low charge states and scaling laws

There are good crossed beam measurements available for EI cross sections of few electron ions. The studies of ionisation of Hydrogen-like B, C, N and O by Aichelle et al [1] are especially noteworthy. Not only were quality cross sections given in this paper but also a simple scaling law was presented which accounts for all the low charged results. In the high energy limit, this scaling law tends to the Bethe-Born approximation. What is new and interesting is that it takes into account the low energy limit where Wanier theory must apply. The cross section is given from a universal shape function

$$\sigma(x)=\sigma_M\left[\cosh(\beta \ln x)\right]^{-1/\beta} \qquad (1)$$

where $x=(E-I)/E_M$, E is the electron impact energy, I the ionisation potential of the target and the following relationships have been determined for a nuclear charge Z by comparison to the experimental results

$$\sigma_M=\pi a_0^2\left(\frac{1.0975}{1.0278+Z-1}\right)^4 \qquad (2) \qquad E_M(Z)=I_H\left(3.31+5.07(Z-1)+1.65(Z-1)^2\right) \qquad (3)$$

with a_0 representing the Bohr radius, I_H being the binding energy of atomic hydrogen and $\beta=0.4$, an empirically determined parameter. A more established, frequently used scaling law is that of Lotz [2] which can be applied to systems with any number of electrons although it lacks the low energy asymptotic behaviour built into the above description.

§3 Basic description of a Electron Beam Ion Trap

From the form of the cross sections for lower charged ions, we can see that the measurement of cross sections for more highly charged ions is formidable since the expected signals are

small. Trapping ions so that they can be exposed to an electron beam for a long time is one way round these difficulties. An Electron Beam Ion Trap (EBIT) offers the required environment. A pair of super-conducting solenoids compress a high current, high energy, quasi-monoenergetic electron beam. This electron beam then both creates (by EI) and traps the highly charged ions. Axial trapping is achieved using a series of drift tubes. The physics and operation of these versatile devices has been described elsewhere [3,4,5] so we will only review the machine physics which is directly relevant to the measurement of EI cross sections.

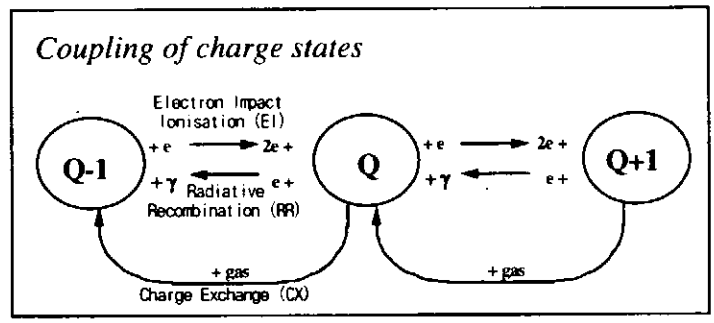

The dominant atomic physics processes related to the dynamics of ion creation in an EBIT are shown in the diagram opposite. Notice that all the reactions involve the charge of an ion changing by only one unit. This is because multiple ionisation and multiple charge transfer cross sections are usually negligible compared to the single ionisation and charge transfer counterparts. There is also loss of ions from the trap due to their kinetic energy. We can ascribe a 'normalised rate' to each process represented in the diagram and also one for the escape of ions from the trap. Doing this, we can then write an equation for the time dependence of the number density of ions of charge state q that reads

$$\frac{dN_q}{dt} = N_{q-1}R_{q-1}^{EI} - N_q\left(R_q^{EI} + R_q^{RR} + R_q^{ESC} + R_q^{CX}\right) + N_{q+1}\left(R_{q+1}^{RR} + R_{q+1}^{CX}\right) \tag{4}$$

Each normalised rate can be related to the cross section for the appropriate process via the density of the second collision partner (neutrals or electrons) and a factor describing the overlap between the two collision partners. For example, denoting the current density as J and the overlap factor between the ions of charge state q and the electron beam as f_q, the normalised rate for EI from charge state q reads

$$R_q^{EI} = \sigma_q^{EI}\left(\frac{J}{e}\right)f_q \tag{5}$$

It is possible to associate a characteristic temperature to each charge state at any instant in time. Collisional processes and ion-escape determine the energy dynamics, which are described within the framework of plasma physics [4,5,6,7]. The spatial distribution of ions of charge state q is a Maxwellian distribution of the form

$$n_q(\rho,z)d\rho dz \propto \rho \exp\left(-\frac{qV(\rho,z)}{kT_q}\right)d\rho dz \tag{6}$$

where T_q is the characteristic temperature of the ions and $V(\rho,z)$ is the electrostatic potential they experience. The overlap factor is the fraction of this distribution lying inside the electron beam. The task at hand is to determine the EI cross section from the overall dynamics. There are two regimes where the system simplifies, the onset period and once equilibrium is established.

§4 Equilibrium based measurements

The equilibrium condition of an EBIT for a constant source flux is given by

$$N_q\left(R_q^{EI} + R_q^{RR} + R_q^{ESC} + R_q^{CX}\right) = N_{q-1}R_{q-1}^{EI} + N_{q+1}\left(R_{q+1}^{RR} + R_{q+1}^{CX}\right) \tag{7}$$

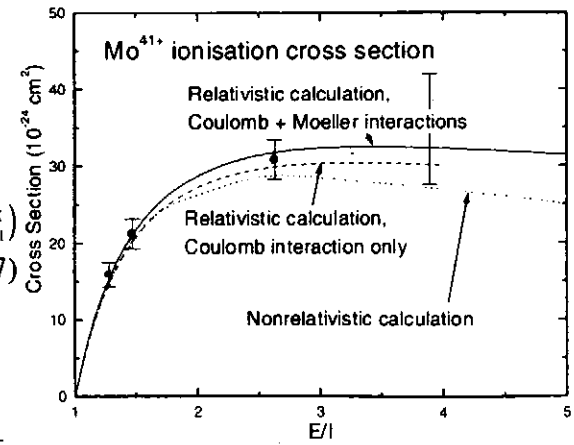

For bare ions, neglecting escape, and assuming the overlap factors of the bare and hydrogen-like ions to be the same, the EI cross section can then be written

$$\sigma^{EI}_{h\text{-}like} = \frac{N_{bare}}{N_{h\text{-}like}}\left(\sigma_i^{RR} + N_n\left\langle\sigma_i^{CX}\right\rangle\right) \qquad (8)$$

The conversion from rates to cross sections performed above is possible if the two species have similar overlap factors. The ratio of bare to hydrogen-like ions is determined from the RR rates detected with an SSD. The average charge exchange cross section is extrapolated away by measuring these rates at different neutral gas pressures. The EI cross section for the H-like ion can then be derived from the theoretical RR cross section for the bare ion.

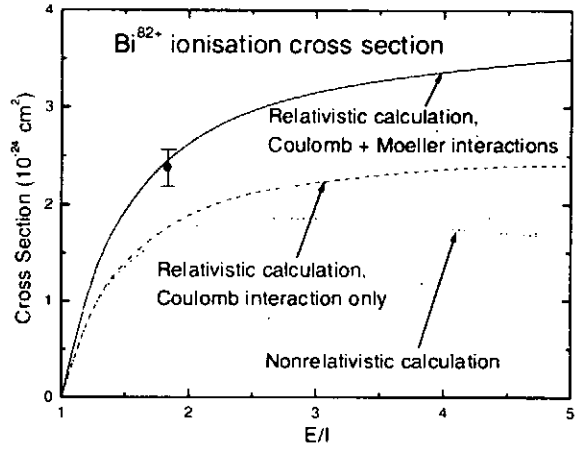

Some of the measurements presented by Marrs et al [8] are shown above. The highest energy point for the Bi measurements is particularly noteworthy since it distinguishes between inclusion and exclusion of the Moeller interaction. Extension of this technique to few-electron ions is less straightforward since L-shell capture features are not usually clearly resolved with an SSD. These difficulties have been overcome however by Stölker et al [9] who fit the energy distribution of detected photons produced by radiative recombination into the L-shell of Uranium highly charged ions.

§5 Onset measurements

Donnets and Ovsyannikov [10] made a series of measurements determining the ionisation cross sections from the rate of production of ions of various charge states. Encouraging agreement has been found between those measurements and crossed-beam measurements [1], suggesting that a similar technique might be applied for higher charge states. A program of such measurements is currently underway using the Tokyo EBIT. The essential instrumental difference between our aproach and that of Donnets and Ovsyannikov is that we use a 90^0 sector magnet rather than time of flight to charge analyse ions. Hence we unambiguously separate dumped and escaping ions as shown in the figure opposite. In this way we gain information about the temperature and population distributions. These measurements were made during a cycle chosen to expel the ions after a range of successively longer cooking times, allowing us to observe the onset behaviour. For each species, from each consecutive pair of dumps, we then define an 'observed production rate'

Time dependence of detection of Ar 16 to 18+ ions

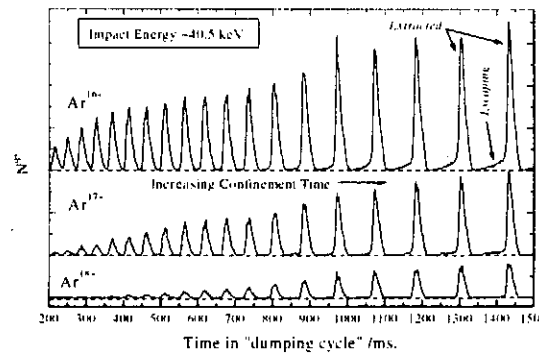

$$\tilde{R}_q(t) = \frac{J}{e}\sigma_q^{EI} f_q = \frac{1}{N_{q-1}}\frac{dN_q}{dt} \qquad (9)$$

Since $\tilde{R}_q(t)$ involves ratios of detected ions, the detector sensitivity cancels. A plot of $\tilde{R}_q(t)$ as a function of time is initially constant and then decreases. This decrease can occur because the terms we neglected in the time evolution equation are no longer negligible or the ion cloud

is expanding to be larger than the electron beam radius. Provided we use the observed production rate from the region where it is constant, we can be confident that the overlap factor is 1 (i.e. the ion cloud is inside the electron beam) and the onset condition holds.

As is shown opposite, we have determined relative cross sections in this manner, assuming the beam radius is constant as suggested by Herrmann theory [11]. The solid lines show comparisons between the measured data and known scaling laws. Our measured cross section could be placed on an absolute scale if we knew the current density or normalised to other cross sections. This is the present focus of our work.

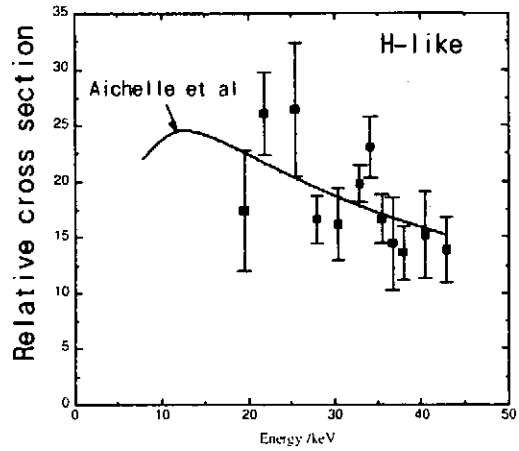

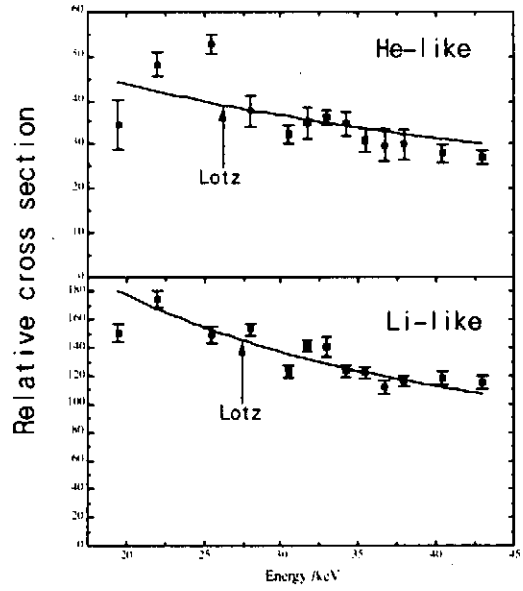

Conclusion

The environment provided by an EBIT is well suited to the measurement of electron impact ionisation cross sections of few electron highly charged ions although the measurements still remain challenging. Two distinct methods have been described by which these cross sections can be determined.

Acknowledgements

We thank all our colleagues involved with the Tokyo EBIT cold trapped highly charged ion program and Ross Marrs for fruitful discussions about cross-section measurement and for sending us his data reproduced above.

References

1. Aichele K *et al* 1998 J.Phys.B: At.Mol.Opt.Phys. **31**, 2369.
2. Lotz W 1967 Z. Phys. **206**, 205., Lotz W 1968 Z. Phys. **216**, 241
3. Levine M A, Marrs R E, Henderson J R, Knapp D A and Schneider M B 1988 Phys. Scr. **T22**, 157.
4. Fussmann G, Biedermann C and Radke R 1998 NATO ASI Series (Proceedings Summer School, Sozopol)
5. F. J Currell 1999 "The physics of electron beam ions traps" in "Trapping highly charged ions: fundamentals and applications", Ed. John Gillaspy, Nova Science Publishers, *in press*
6. Spitzer L Jr. 1956 "Physics of fully ionized gases" Interscience publishers, inc. New York. (Library of Congress Catalog Card no. 55-11452)
7. Rose D J and Clarke M Jr. 1961 "Plasmas and controlled fusion" MIT Press
8. Marrs R E, Elliot S R and Schofield J H 1997 Phys.Rev.A. **56**, 1338
9. Stöhlker Th, Kramer A, Elliot S R, Marrs R E and Schofield J H 1997 Phys.Rev.A. **56**, 2819
10. Donets E D and Ovsyannikov V P 1981 Sov. Phys. JETP **53**, 466
11. Herrmann G J 1958 Appl. Phys. **29**, 127

Overview of LHD Diagnostics

SUDO Shigeru and LHD Experiment Group

National Institute for Fusion Science, 322-6 Oroshi-cho, Toki, 509-5292 JAPAN

sudo@nifs.ac.jp

ABSTRACT The overview on the recent status and future plan of plasma diagnostics and data acquisition for LHD is briefly described. According to the successful starting of LHD experiments on March 31, 1998, the diagnostics have also launched in the adequate pace with providing the necessary basic data for plasma performance analysis. For this, the LHD data acquisition system, handling large amounts of data, is playing an important role in the experiment and data analysis.

I. INTRODUCTION

The Large Helical Device (LHD) [1] of the National Institute for Fusion Science (NIFS), Toki, Japan is a superconducting helical device, which is completed in December 1997 after 8 years construction phase [2].

The magnetic configuration of LHD, an optimized heliotron with double helix coils, is an extension of the medium-sized devices such as Heliotron-E, ATF and CHS. Target plasma parameters for LHD are a fusion triple product, $n_i \tau_E T_i \sim 10^{20}$ m^{-3} s keV, $\bar{\beta} \sim 5$ %, and steady-state operations with a plasma major radius, R_p= 3.9 m, a plasma minor radius, a_p= 50 - 65 cm, and magnetic field strength, B_t= 3 - 4 T. LHD features continuous helical coils and a clean helical divertor focusing on the edge configuration optimization. This activity is expected to promote helical fusion research and also to extend the understanding of toroidal plasmas through comparisons with large tokamaks.

The main mission elements of the LHD project are: (a) investigating current-less plasma characteristics such as transport under reactor relevant plasma conditions in a helical system, (b) demonstrating an average beta value of the level of 5% in a helical system, (c) studying divertor operation, and obtaining the basic data for steady-state operation, (d) studying the behavior of high energy particles, and conducting simulation experiments of alpha particles in reactor plasmas, and (e) understanding the general physics issues of toroidal plasmas with a complementary study to tokamak plasmas.

There were two experimental campaigns in the 1998 fiscal year. The transition to the super-conducting state was achieved after the initial 4-week cooling process at the first campaign. Special care was made to keep a homogeneous temperature distribution in the device. After that, the coil current was excited, and a magnetic field strength of 1.5 T in the axis of poloidal cross section was achieved, and it was increased to 2.75 T successfully at the end of second experimental campaign.

The first plasma experiments started on March 31, 1998 with 2 nd harmonic 84 GHz electron cyclotron resonance heating (ECH) with a few hundred kW at B = 1.5 T. The ohmic heating is not necessary for plasma production in contrast to tokamaks. In the second experimental campaign, the neutral beam injection (NBI) with 100 keV acceleration voltage and up to the power of 3.7 MW was applied. The highest electron temperature and the maximum line average density are 2.3 keV and 7 × 10^{19} m^{-3}, respectively. The energy confinement time is better by a factor of 1.5 than that predicted by the International Stellarator Scaling 95 [3]. The long pulse discharge with duration of 22 s was

successfully carried out by NBI with the power of 0.7 MW.

Through the experiments, LHD diagnostics were playing a significant role in the achievements, and the data acquisition system for the LHD diagnostics worked successfully from the first shot, and the performance was improved drastically during the two experiment campaigns. There are three categories for the LHD data acquisition: (a) object-oriented distributed database, (b) separate data acquisition systems, (c) real time data acquisition system. This strategy contributed very much to the flexibility and the reliability of the whole LHD data acquisition system. Owing to this system, the reliability of the LHD data acquisition is satisfactory. We will describe the overview of LHD diagnostics and the LHD data acquisition system.

II. OVERVIEW OF LHD DIAGNOSTICS

The key issues of Diagnostics for LHD are: (a) capability of multi-dimensional (2-D or 3-D) measurements because of a non-axisymmetric toroidal plasma, (b) advanced measurements with heat removal adequate for high heat flux and steady-state operation, and (c) an adequate data acquisition system handling large amounts of data for steady-state operation.

Taking the above issues into consideration, the design and R&D of plasma diagnostics have been progressed. The list of plasma diagnostics for LHD is given in Table I. We are still planning to increase the numbers to understand the 3-D feature of LHD plasma in future. It has been planned to obtain the fundamental plasma parameters from the beginning of the experiments. The heat removal in case of high heat flux and/or steady-state operation is partly investigated, but the level is still primitive because of relatively low heating power and short pulse duration in the initial stage of the experiments. During the 1st cycle experimental period (April – May 1998, Shot No. 1 - 1888), the following diagnostics were operated: Bolometer, Microwave Interferometer, Pulse Height Analyzer (PHA), Electron Cyclotron Emission (ECE), Visible Spectrometer, Vacuum Ultra Violet (VUV) Spectrometer, Balmer alpha line monitor, Diamagnetic Coil, Rogowski Coil. The interferometer supplied the line density information of the plasma already from the first shot successfully. The electron temperature of the ECH plasma was found to be more than 1 keV with X-ray PHA.

Major diagnostics were added for the 2nd cycle experimental period (September – December 1998, Shot No. 1889 - 7232). A YAG Thomson scattering system for measuring electron temperature and electron density has been constructed, and the measurement has been successfully made. It is working as a routine operation. The system can measure the scattered lights at 200 points along a major radius every 20 ms, giving full profiles of electron temperatures and densities. The spatial resolution ranges about 20 mm. Due to the high repetition rate of the YAG laser, the temperature distribution of the YAG rod becomes inhomogeneous, and it results in the change of the laser beam direction. Such a problem could be resolved by a feed-back mirror control system with piezo elements. The amount of the beam shift was reduced by a factor of 10.

ECE has three features of detection: Heterodyne radiometer, Michelson inteferometer, and Grating polychrometer (GPC). The heterodyne radiometer system with 24 channels has a good time resolution of 2 μs, but it should be calibrated with the Michelson inteferometer system. The time resolution of the Michelson inteferometer system has lower time resolution of 25 ms in turn. The grating polychrometer system with 12 channels has a time resolution of 5 μs.

A FIR interferometer system for measuring electron density using 13 laser beams with a Michelson geometry has been constructed. For this purpose, a 119 micron-m CH_3OH laser is adopted. The laser beam must be transferred about 40 m from the laser room to the interferometer located at LHD.

Primary charge exchange recombination lines for measuring ion temperature are: CVI

Table I Diagnostics for LHD.

DIAGNOSTICS	PURPOSE	BRIEF DESCRIPTION
Magnetic Probes	I_p, P_{pl}, Plasma Position & Shape	Rogowski, Mirnov, Flux Loops
μW Interferometer	$n_e L$	2mm/1mm wave, single channel
FIR Laser Interferometer	$n_e L(r)$	119μm-CH_3OH laser, 13 chords
μW Reflectometer	n_e for NBI Interlock, Fluctuation	
Thomson Scattering	$T_e(r)$, $n_e(r)$	200 spatial points, 20 ms interval
Electron Cyclotron Emission	$T_e(r, z)$	2-D Imaging
X-ray PHA	T_e, Impurities	20 ch Si(Li) , 4 ch Ge detector
Neutral Particle Analyzer	T_i, Energy Spectra f(E)	Time-of-flight method
CXRS	$T_i(r)$, Plasma Rotation $V_p(r)$	Radial profile
X-ray Crystal Spectroscopy	Ti(r)	0.1- 4nm, $\lambda/\Delta\lambda$: 10^4
Neutron Diagnostics	Neutron flux, T_i	NE-213 detectors, ^{3}He counters
Bolometers	$P_{rad}(r)$	metal film
VUV Spectroscopy	Impurities, T_i	1- 200 nm, $\lambda/\Delta\lambda$: 10^4
Visible Spectroscopy	$n_0(H)$, Z_{eff}	200- 700 nm, $\lambda/\Delta\lambda$: 5×10^4
Langmuir Probes	T_e, n_e	Fast scanning and fixed probes
Visible/Infrared TV	Plasma-Wall-Interaction	TV system
Soft X-ray Diode Array	MHD Oscillations	silicon surface-barrier diodes
μW/FIR Laser Scattering	Micro-instabilities	1mm/195μm multi-channel
Heavy Ion Beam Probe	Φp, Φp Fluctuation	Au^- or Tl^+, 6MeV, 100μA
Diagnostic Pellet	Particle Transport	TECPEL/TESPEL, C, Li
High-energy Particles	Particle Behavior & Loss	He beam probe, particle probes
Divertor Spectroscopy	Recycling, Particle Flux	
Li Beam Probe	Density Fluctuation	Li Beam
IR Bolometer Camera	$P_{rad}(r)$	IR 2-D Imaging

and NeX. The 22ch for the charge exchange recombination spectroscopy (CXRS) signal plus background light are observed at the NBI beam path. The CCD camera with 576 x 384 pixels is used for photo detection. The spatial resolution is 2 cm, and the time resolution is typically from 0.2 s to 1.0 s due to necessity of enough photon numbers. To increase the accuracy, a proof-of-principle of a new method "dig-dag" CCD processing with beam modulation was successfully shown in the satellite machine.

For measuring the radiating loss power including light and particles coming out the plasma, a multi-channel bolometer system is equipped. The sensor of this bolometer is metal film of which resistance is measured to interpret the temperature change due to heat flux. This aims to view both the core plasma and the divertor plasma, and also it is planned to work for long pulse operation. A new bolometry system is being also developed with an infrared (IR) imaging camera. The one IR imaging camera is already tested at CHS, and the basic function is proved. The IR imaging camera has been already installed on LHD for the coming experimental campaign.

A heavy ion beam probe is being constructed for measuring plasma potential, which is one of key parameters for helical plasmas. The maximum beam energy is set at 6 MeV. A positive ion beam is obtained after accelerating the negative gold ion beam with a tandem type accelerator. The primary beam enters through a bottom port and the secondary beam comes out from the side port in the toroidal direction. The beam energy of singly charged gold ions is 5.6 MeV for the 3 T standard operation. A method to control the 3-D beam trajectory in the helical magnetic field is developed.

According to the successful starting of LHD experiments, the diagnostics have also launched in the adequate pace with providing the necessary basic data for plasma performance analysis. The amount of the acquired data size was about 120 MB/shot in the last experiment campaign, and the total size in 1998 was 420 GB.

III. SUMMARY

The diagnostics and the data acquisition system for LHD are overviewed. The basic parameters such as temperature, density and impurities are well measured during the first and second experimental campaigns in 1998. The temporal developments of spatial profiles of these parameters contributed significantly to the physics analysis of plasma behavior. Our strategy is to assure the flexibility and the reliability for the whole LHD data acquisition, and in fact it was successful. The data amount of approximately 250 MB / shot has been already achieved in the last experiment campaign, and these data are contributing much to the physics analysis.

References

[1] A. Iiyoshi, M. Fujiwara, O. Motojima, N. Ohyabu, and K. Yamazaki, Fusion Technol. **17** 169 (1990).

[2] A. Iiyoshi, et al., Proc. of 17th IAEA Fusion Energy Conference (Yokohama, Japan. 1998) IAEA-CN-69/OV1/4.

[3] U. Stroth, et al., Nuclear Fusion **36**(1996)1063.

Elastic collisions and related transport processes in cold hydrogen plasmas

Predrag S. Krstić[1], and David R. Schultz[1]

[1] *Oak Ridge National Laboratory, Physics Division, Oak Ridge, TN 37831, USA*

Abstract. Owing to the critical role played by elastic processes in thermal power exhaust in the divertor region of fusion plasmas as well as in other gas/plasma environments and to its fundamental nature, we have performed extensive, highly accurate, fully quantal calculations of differential and integral cross sections for elastic, charge transfer, spin exchange, and vibrational excitation in slow collisions (0.1-100 eV) among isotopic variants of H^+, H, H_2 and He.

1 Introduction

The currently favored concept for power exhaust from a fusion reactor relies heavily on intense impurity radiation cooling at the plasma edge and on dissipation of plasma momentum through elastic and charge-exchange collisions of plasma ions with the neutrals in the divertor chamber. The low plasma temperatures prevailing in the divertor region (as low as 1 eV near the divertor plates) support existence of non-dissociated molecular species, neutral atoms and low charge states of impurity ions, defining a medium with very rich and complex atomic physics. The hydrogen atoms and molecules constitute the main portion of the neutral gas, though helium atoms are also present. The momentum transfer (diffusion) and charge exchange processes of the plasma ions (H^+) colliding with the neutrals (H, H_2, He) in the divertor are responsible for the dissipation of plasma momentum. Following charge transfer, the neutrals carry the energy, but not being controlled by the magnetic field, their diffusion becomes crucial for the power exhaust.

We studied five groups of collision systems, H^++H [2,3,4], H+H [2,3,4], H^++H_2 [1,2,4], H+H_2 [1,2,4] and H^++He [2,3,4]. When all isotopic variants of H are varied over all projectiles and targets, these constitute 51 collision systems. For each of the systems *ab initio*, fully quantal calculations are done with the best available interaction potentials at 31 center of mass (CM) collision energies E, between 0.1 and 100 eV, where $E=10^{0.1J-1}$ eV, with J=0,1,2,...,30. Differential cross sections were calculated for 768 CM scattering angles θ, constituting a set of abscissas for the 768th order Gauss-Legendre integration. The elastic, charge transfer (H^++H), spin exchange (H+H, H^++H) and vibrational excitation (H^++H_2, H+H_2) amplitudes were calculated by solving coupled channel equations for various partial waves by the method of logarithmic derivatives, where the number of partial waves taken guaranteed convergence of elastic amplitudes to five digits. The number of inelastic channels taken into account was also determined by similar convergence criteria of the elastic amplitudes in the energy range considered: Thus, for the H^++H systems the ground molecular state $1s\sigma_g$ as well as $2p\sigma_u$ and $2p\pi_u$ were taken into account; for H+H these were the ground singlet $X^1\Sigma_g^+$ and triplet $b^3\Sigma_u^+$ states; for H^++He only the ground state surface was needed; finally, for the H^++H_2 and H+H_2 elastic scattering on the ground vibrational state, nine excited vibrational states were needed for the convergence. In this way, the accuracy reached for the differential cross sections is in the range

[1] E-mail : krstic@mail.phy.ornl.gov, or schultz@mail.phy.ornl.gov

of 0.001-1% (the worst being for systems with molecular targets). Our calculation sets new benchmarks for the ion-atom and atom-atom cases in the energy range considered.

Besides the integral cross sections for elastic, σ_{el}, charge transfer, σ_{ct}, and spin exchange, σ_{se}, processes we also calculate momentum transfer (diffusion), σ_{mt}, and viscosity, σ_{vi}, integral cross sections, which are defined as integrals over the weighted [1-4] differential cross sections. The dominant contribution to σ_{mt} is from the backward CM scattering angles, while σ_{vi} is dominated by the differential cross sections for intermediate angles, $\theta \approx \frac{\pi}{2}$. Thus, to calculate σ_{el} as well as σ_{mt} and σ_{vi} accurately, one must maintain accuracy of the differential cross section $d\sigma_{el}/d\Omega$ over the full range of scattering angles (0-180°). But, $d\sigma_{el}/d\Omega$ for forward and backward angles could differ by a factor of 10^5, and this is one of the serious numerical difficulties of the calculation.

More than 3000 differential and more the 250 integral cross sections resulted from this calculation. These are all available on the web site of the Controlled Fusion Atomic Data Center (CFADC) of Oak Ridge National Laboratory, at *www-cfadc.phy.ornl.gov*. In addition, all cross sections are fitted to analytical forms [2].

No scaling of the differential cross sections when varying the isotope constitution of the same scattering species was found for the whole range of scattering angles. Still, for small angles near the forward direction the mass-dependent scaling exists for the limit value ($\theta \to 0$) as well as for the forward peak value and for its position (of $\sin\theta d\sigma/d\Omega$). On the other hand, all integral cross sections do scale with the isotope mass, except for the momentum transfer and viscosity which in most cases are independent of mass.

The center of mass system and atomic system of units are used throughout the text, except where noted.

2 H^++H, H^++H, H^++He

When the collision energy is high enough, the elastically scattered projectiles strongly peak in the forward direction while the recoiled targets, on the other hand, peak in a backward direction. As the energy decreases this feature is lost since the wave packets of both scattered projectiles and targets spread over all directions, and this has an important consequence to the ability to distinguish between the two type of particles in symmetric cases. Thus at low energies, one cannot tell for H^++H (and D^++D, T^++T) whether the protons (deuterons, tritons) detected are elastically scattered or produced by charge transfer in the target. Similarly, in symmetric cases, H+H (D+D, T+T) the detector counts both elastically scattered and recoiled atoms, without the ability to distinguish between the two: the two wave functions overlap and superimpose coherently (producing interference patterns, even in the integral cross sections). Still, in the absence of spin coupling, one can use a change of spin of the particles reaching the detector to clearly recognize recoiled targets. This does not solve the problem of unique recognition of elastically scattered particles, since recoiled particles do not neccessarily change spin. In typical experimental situations, averaging over nuclear spins of the nonpolarized projectile beam and of the nonpolarized target (in H+H cases, aditional averaging over electron spins is needed, too) the cross section for spin exchange $\sigma_{sym,se}$ and symmetric "elastic" scattering, $\sigma_{sym,el}$, emerge. For mass-asymmetric cases, like H^++D or H+T, the projectile and recoiled particles can be easily recognized by measuring their mass; in other words, the two wave functions are added incoherently, resulting in the cross sections being compatible with the classical definitions (each particle is labelled and traced throughout the process of scattering). For symmetric scattering, when the energy is high enough to minimize the

overlap, $\sigma_{sym,el} = \sigma_{el} + \sigma_{ct}$ which is the total scattering cross section for H^++H, rather than the elastic one. On the other hand, in the same energy limit $\sigma_{sym,se} = \sigma_{ct}$, which can be used to redefine the elastic cross section for mass-symmetric scattering in a unique way (including momentum transfer and viscosity) as $\sigma_{el} = \sigma_{sym,el} - \sigma_{sym,se}$. Such a definition is acceptable for integral cross sections, and results in an error not larger than 10% at E=0.1 eV, which drops to below 1% at E=1 eV. For symmetric neutral-neutral scattering, like the case of H+H, the integral cross section $\sigma_{sym,el} = 2\sigma_{el}$, owing to the symmetry of the problem. This relation is used to obtain an unique definition for σ_{el} irrespective of the isotopic constitution.

The effect of quantum indistinguishability of particles (QIP) is even more pronounced for the transport cross sections, like momentum transfer and viscosity (Figure 1). When the projectile and target masses are different (and, thus can be treated as distinguishable particles, DP), the differential elastic cross sections are strongly fowardly peaked, and their weighted integrals are governed by small contributions from the intermediate and backward angles. On the other hand, $\sigma_{sym,el}$ is peaked in both forward and backward directions, which significantly increases the transport cross sections. An extreme example is momentum transfer, which equals the elastic cross section in this case. As discussed above, the problem can be resolved (with allowance of some error at lower energies) by weighted integration of the difference of the elastic and spin-exchange differential cross sections, thus reaching isotopically invariant definitions. But, in the case of H+H, simple division by two would not work for the transport cross sections. As a recommendation to plasma modelers, the most accurate approach would be to consider transport of all protons, whether elastic or from charge transfer, simultaneously (for H^++H), and all hydrogen atoms, whether elastic or recoiled (for H+H) simultaneously. This would, for mass-asymmetric nuclei, mean an addition of the charge transfer (recoil) and elastic scattering cross sections. Inclusion in plasma model of $\sigma_{sym,el,mt,vi}$ and the corresponding cross sections for the charge tranfer (recoil) particles would mean a multiple counting.

The problems discussed are visible in Figure 1, where the integral cross sections for QIP versus DP are compared. None of these problems are present in the cases of H^++He, H^++H_2 and H+H_2 scattering, due to the obvious distinguishability of colliding particles.

3 H^++H_2, H+H_2

Since a typical rotational time for H_2 is smaller than the collision time for the energy range considered (0.1-100 eV) we assume the orientations of the diatom are frozen during the collision and perform the angular averaging of the cross sections. Concerning the vibrational degrees of freedom, nine excited states sufficed for the convergence of the elastic differential cross sections over the full range of angles. Particularly sensitive was calculation of the momentum transfer, since the vibrational excitations dominate toward the backward directions.

In the range of energies above a few eV, when the vibrational excitations become strong, our momentum transfer cross section for the ground vibrational state shows a large dip. This is not present in the classical calculations [5] or the fitting estimates [6], which do not take into account vibrational degrees of freedom.

Studying the cross sections for various orientations of H_2, an interesting conclusion may be drawn regarding mechanisms for scattering: H^+ projectiles interact with H_2 as a molecule at large distances, deforming the electron distribution of the covalent bond, while H projectiles scatter mainly on the closest atom of the molecule. As a consequence,

the elastic cross section with the H projectile do not change much between H and H_2 targets.

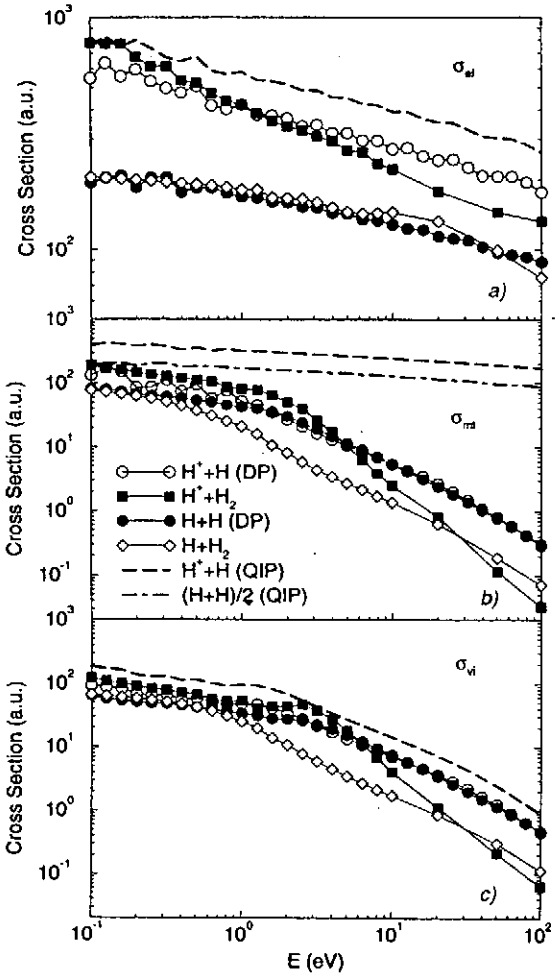

Figure 1: Integral *a)* elastic *b)* momentum transfer and *c)* viscosity cross sections for various systems studied.

Acknowledgements. This work has been supported by the US DoE, Office of Fusion Energy Sciences, at Oak Ridge National Laboratory, which is managed by the Lockheed Martin Enrgy Research Corporation under Contract No. DE-AC05-96OR22464.

References

[1] Krstić P.S.and Schultz D.R. 1999 *J. Phys. B* **32** 2415

[2] Krstić P.S. and Schultz D.R. 1998 *Atomic and plasma-material interaction data for fusion* **8** 1 (IAEA)

[3] Krstić P.S. and Schultz D.R. 1999 *J. Phys. B* **32** 3485

[4] Krstić P.S. and Schultz D.R. 1999 Phys. Rev. A **60** No. 3

[5] Bachmann P and Reiter D 1995 *Control Plasma Physics* **35** 45

[6] Phelps A V 1990 *J. Phys. Chem. Ref. Data* **19** 653

Ion–Ion Collisions

Erhard Salzborn[1] and Frank Melchert[2]

[1] *Institut für Kernphysik, Justus-Liebig Universität, 35392 Giessen, Germany*
[2] *Physikalisch-Technische Bundesanstalt, 38116 Braunschweig, Germany*

Abstract. Collisions between ions belong to the elementary processes occurring in all types of plasmas. In this article we give a short overview about collisions involving one–electron systems. For collisions involving multiply–charged ions we limit the discussion to one specific quasi–one–electron system.

1 Introduction

In recent years, the impetus for accurate cross section data for ion–ion collisions at energies in the keV–range has become great due to the research in thermonuclear fusion using either magnetic or inertial confinement. In magnetically-confined fusion plasmas, ion-ion reactions may provide effective tools for plasma diagnostics. Furthermore, the fusion plasma needs auxiliary heating by injection of powerful neutral hydrogen beams. Negative hydrogen ions H^- accelerated to energies of several $10^5 eV$ can be neutralized most effectively in so-called plasma-neutralizers [1] where the interaction between H^- and multiply-charged plasma ions X^{q+} dominates the neutralization process.

2 Experimental Method

The *crossed–beams* experiment used for the investigation of charge–changing ion–ion collisions was described in full detail earlier [5]. The experimental arrangement consists of an ultra-high vacuum chamber (typically $5{\cdot}10^{-11}$ mbar), a 'slow' (up to 20 kV) and a 'fast' (up to 200 kV) beam line. Both ion beams are produced in Electron Cyclotron Resonance ion sources. After momentum analysis they are collimated and made to intersect at an interaction angle of $\theta = 17.5^o$. Because of the low momentum transfer involved in the collision the reaction products remain within the parent ion beam after the interaction. They are separated from the incident ions by a two–step electrostatic deflector for each beamline and counted in single particle detectors. A time conincidence technique is employed to distinguish between background events from charge–changing reactions with the residual gas and true ion–ion signals.

3 One–Electron Systems

The investigation of collisions between protons and singly-charged helium ions is of considerable interest in plasma physics. Not only do these encounters occur inevitably in fusion plasmas but they also represent the simplest ion-ion collision system involving only one electron. Description of electron capture σ_C

$$H^+ + He^+ \longrightarrow H^0 + He^{2+} \qquad (1)$$

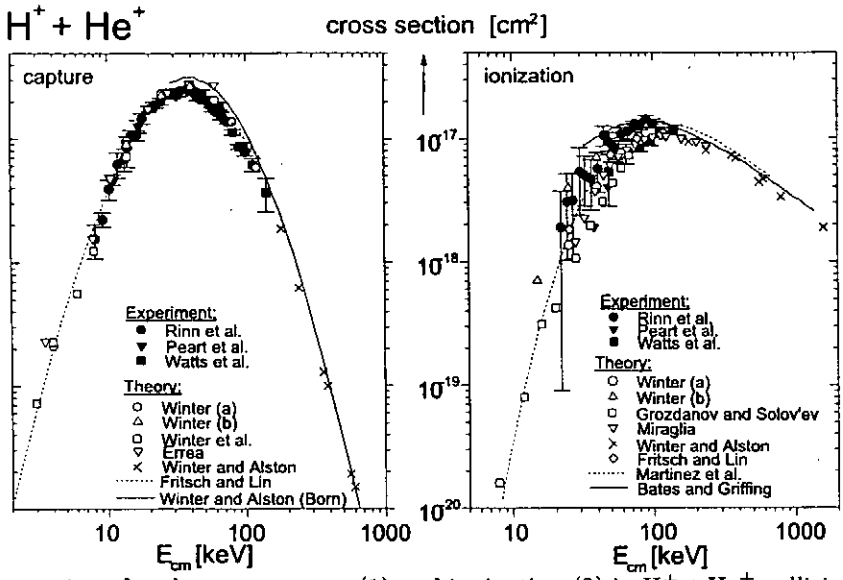

Figure 1: Cross sections for electron capture (1) and ionization (2) in $H^+ + He^+$ collisions, as a function of the cm-collision energy E_{cm}. Experimental *crossed-beams* results by Rinn et al. [2, 3], Peart et al. [6] and Watts et al. [7]. Most theoretical results are obtained by close-coupling (CC) calculations: Winter (a) [8]: Sturmian basis and pseudostates; Winter (b) [9]: 3-center atomic orbital (AO) basis; Winter et al. [10]: MO basis; Errea [11]: molecular orbital (MO) basis; Winter and Alston [17]: high energy CC; Fritsch and Lin [13, 14]: AO^+ basis; Grozdanov and Solov'ev [15]: MO basis; Miraglia [12]: CDW; Martinez et al. [16]: CDW-EIS; Winter and Alston [17] and Bates and Griffing [18]: Born approximation.

and ionization σ_I

$$H^+ + He^+ \longrightarrow H^+ + He^{2+} + e^- \tag{2}$$

is therefore an ideal testing ground for different theoretical models.

Three experimental groups [6, 7, 2] have studied these collisions independently and their experimental cross sections are compared with theory in Fig.1. In the high energy limit, the Born approximation is valid while for lower energies the continuum distorted wave calculation CDW-EIS with eikonal initial states by Martinez et al. [16] agrees as perfect with the ionization data as the atomic orbital AO^+ calculation by Fritsch and Lin [13] with the capture results. Since various authors confirm these findings, total cross sections for the reactions (1) and (2) are well described by theory.

For about two decades, theory was tested by comparing calculated and measured total cross sections. The first angular differential cross section has been measured by Kruedener et al. [4] for the electron capture of α-particles from He^+ ions:

$$He^{2+} + He^+ \longrightarrow He^+ + He^{2+} \tag{3}$$

This one-electron, charge-symmetric collision is resonant for $1s \rightarrow 1s$ electron capture and provides a unique testing ground for the study of the long-range Coulomb interaction in the quantum three-body problem. Kruedener et al. found an oscillatory structure the differential cross section $d\sigma/d\Omega$, plotted in Fig.2 as a function of the cm-scattering angle ϑ_{cm}.

In addition to the minimum in forward direction, another four minima of $d\sigma/d\Omega$ are resolved experimentally. The oscillation period increases with scattering angles. Forster et al. [19] used a semiclassical eikonal calculation which describes well the experimental data for low scattering angles ϑ_{cm}, but "runs out of phase" for larger ϑ_{cm}. The observed oscillatory structures in the differential electron capture cross section can be interpreted

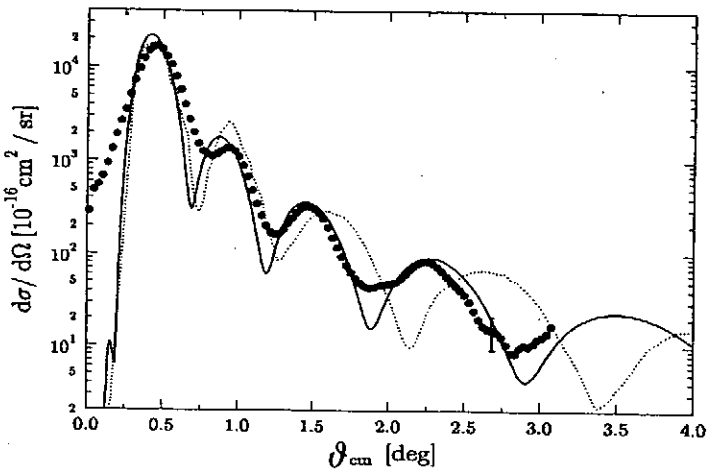

Figure 2: Angular differential cross sections for the electron capture (3) in $He^{2+} + He^{+}$ collisions at $E_{cm} = 2.5keV$. •: experiment, Kruedener et al. [4]; dotted line: semiclassical calculation, Forster et al. [19]; solid line: quantal calculation, Uskov and Presnyakov [4].

as interference between *gerade* and *ungerade* electronic states of the ionic molecule. Uskov and Presnyakov [4] presented a quantum approach based on a partial wave analysis using a molecular basis and delivered a very good description of the experimental data. We note that theory and experiment are compared on an absolute scale.

4 Collisions between Multiply-Charged Ions

Ion-ion collision data required for various applications are sparse; for collisions between multiply-charged ions they are practically absent. It is due to the recent development of powerful Electron Cyclotron Resonance (ECR) ion sources that *crossed-beams* experiments can be carried out with intense beams of multiply-charged ions. Up to now, however, only a few experiments, in which at least one ion carries a charge higher than one, have been performed.

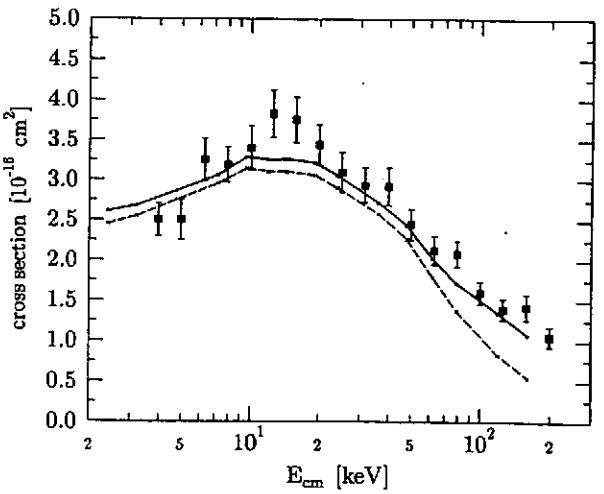

Figure 3: Cross sections for electron capture (4) in $^{3}He^{2+} + ^{13}C^{3+}$ collisions. Experimental data points by Melchert et al. [20] include 90% of statistical error. Close coupling calculation by Sidky and Lin [20] for capture to all He^{+} states (solid curve) and to the $He^{+}(1s)$ state only (dashed curve).

Here, we limit the discussion to electron capture in the quasi-one-electron collision system

$$^3He^{2+} + ^{13}C^{3+} \longrightarrow {}^3He^{+} + ^{13}C^{4+} \tag{4}$$

which was experimentally studied by Melchert at al. [20] and calculated by Sidky and Lin [20]. In their close-coupling calculation Sidky and Lin expand the active electron wave function as a sum of atomic states on both charge centers. The two inner electrons of the lithium-like C^{3+} ion are inert and enter as a model screening potential for the outer active electron. In Fig.3 measured and calculated cross sections are compared. Up to a collision energy of 50 keV the capture goes primarily to the $He^+(1s)$ channel, since the $He^+(1s)$ level is closest to the initial C^{3+} binding energy. As soon as one reaches the matching velocity, where the incoming He^{2+} ion is traveling at about the average speed of the C^{3+} valence electron, the capture spreads to other states of He^+, and the $1s$ state represents only half of the total capture probability (at $E_{cm} = 150\ keV$).

References

[1] A.S. Schlachter, K.N. Leung, J.W. Stearns, R.E. Olson: In *Production and neutralization of Negative Hydrogen Ions and Beams*, ed. by J.G. Alesi, AIP Conference Proceedings No. 158 (Brookhaven 1986) 631

[2] K. Rinn, F. Melchert, E. Salzborn: J. Phys. B **18**, 3783 (1985)

[3] K. Rinn, F. Melchert, K. Rink, E. Salzborn: J. Phys. B **19**, 3717 (1986)

[4] S. Kruedener, F. Melchert, K. v.Diemar, A. Pfeiffer, K. Huber, E. Salzborn, D.B. Uskov, L.P. Presnyakov: Phys. Rev. Lett **79**, 1002 (1997)

[5] S. Meuser, F. Melchert, S. Kruedener, A. Pfeiffer, K. v.Diemar, E. Salzborn: Rev.Sci.Instrum. **67**, 2752 (1996)

[6] B. Peart, K. Rinn, K. Dolder: J. Phys. B **16**, 1461 (1983)

[7] M.F. Watts, K.F. Dunn, H.B. Gilbody: J. Phys. B **19**, L355 (1986)

[8] T.G. Winter: Phys. Rev. A **35**, 3799 (1987)

[9] T.G. Winter: Phys. Rev. A **37**, 4656 (1988)

[10] T.G. Winter, G.J. Hatton, N.F. Lane: Phys. Rev. A **22**, 930 (1980)

[11] L.F. Errea, J.M. Gomez-Llorente, L. Mendez, A. Riera: J. Phys. B **20**, 6089 (1987)

[12] J.E. Miraglia: Phys. B **16**, 1029 (1983)

[13] W. Fritsch, C.D. Lin: J. Phys. B **15**, 1255 (1982)

[14] W. Fritsch, C.D. Lin: In *Thirteenth International Conference on the Physics of Electronic and Atomic Collisions* (Berlin 1983), Abstract of Contributed Papers, p 502

[15] T.P. Grozdanov, E.A. Solov'ev: Phys. Rev. A **38**, 4333 (1988)

[16] A.E. Martinez, R. Deco, D. Rivarola, P.D. Fainstein: Nucl. Instr. Meth. in Phys. Res. B **43**, 24 (1989)

[17] T.G. Winter, S.G. Alston: Phys. Rev. A **45**, 1562 (1992)

[18] D.R. Bates, G.W. Griffing: Proc. Phys. Soc. London **A 66**, 961 (1953)

[19] C. Forster, R. Shingal, D.R. Flower, B.H. Bransden, A.S. Dickinson: Phys. B **21**, 3941 (1988)

[20] F. Melchert, S. Meuser, S. Kruedener, A. Pfeiffer, K. v.Diemar, E. Salzborn, E.Y. Sidky, C.D. Lin : J.Phys.B: At.Mol.Opt.Phys.**30**, L697 (1997)

Molecular Processes in Divertor Plasmas

R.K. Janev

Macedonian Academy of Sciences and Arts, Skopje, Macedonia
International Atomic Energy Agency, Vienna, Austria*

1. Introduction

The main physics issues in development of controlled thermonuclear fusion on the basis of D-T plasma confinement are (i) to achieve the plasma burning conditions in the reactor ($T_{e,i} \simeq 10^{14}$ - 10^{15} cm^{-3}, $\tau_E > 1$ sec and $n_i T_i \tau_E > 5\times10^{15}$ cm^{-3} keV sec, where $T_e \simeq T_i=T$ and $n_e=n_i=n$ are the plasma electron/ion temperature and density, respectively, τ_E is plasma energy confinement time) and (ii) to control the sustained plasma burn. The achievement of these overall goals requires understanding and solving of many more specific problems, such as: additional plasma heating to reactor level temperatures, control of plasma stability and energy confinement, control of energy and particle losses from the plasma (particularly the radiative power losses due to impurities), continuous exhaust of thermal plasma power from the reactor (to avoid plasma overheating and thermal/radiation burn collapse) and of the fusion-born alpha particles (to avoid fuel dilution and degradation of plasma reactivity) etc. The present approach to resolving the impurity control and thermal power and particle exhaust issues is the use of a poloidal magnetic divertor to divert the peripheral plasma of the reactor into a special chamber, located outside the main torus, from where the thermal plasma power is exhausted. The parameters (T,n) of the divertor plasma are such that neutral and molecular species can co-exist with the plasma particles, which creates a medium of exceptionally rich atomic/ molecular collision physics [1]. In what follows, we shall briefly describe the physical conditions in divertor plasmas and the most important molecular processes that take place in these plasmas. Particular attention will be given to those molecular processes which take part in the divertor plasma cooling and volume recombination, i.e. play a role in resolving the thermal power exhaust problem. The atomic processes in divertor plasmas are described in detail elsewhere [2,3].

2. Physical conditions and composition of divertor plasmas

The concept of poloidal magnetic divertor in toroidal fusion devices is based on configuring the magnetic field at the plasma periphery in such a way that the magnetic field lines in that region become "open" and are allowed to strike certain material boundaries (divertor plates) at the bottom of the divertor chamber, located outside the torus. The large temperature gradients existing between the divertor plates and the last closed magnetic surface (separatrix) in the main torus create a strong convective flow of all charged plasma particles traversing the separatrix and the ionized wall impurities penetrating into the plasma periphery. This strong convective flow, directed toward divertor plates, shields the main plasma from the ingress of wall impurities and, at the same time, the vessel walls from the plasma particle impact (which creates such impurities). This divertor function helps resolving the impurity control problem. However, the diverted plasma heat and particle fluxes which are deposited on

* Until June 30, 1999

the divertor plates (on a rather limited area) impose severe requirements on plate materials regarding their erosion and thermo-mechanical properties. (For instance, in a D-T reactor of 1GW thermal power, the heat load on divertor plates amounts 30-40 MW/m^2, which no existing material can withstand.) In order to reduce the unacceptably high heat loads on divertor plates, the plasma energy and momentum have to be exhaused before they reach the divertor plates. This can be achieved only by inelastic atomic/molecular collisions (which transform the plasma energy into isotropic radiation) and momentum transfer collisions between divertor plasma ions and neutrals. For enhancing the plasma energy and momentum losses in the divertor region, controlled injection of strongly radiating and recycling impurities (such as N, Ne, Ar) and of cold molecular hydrogen is currently used in the large tokamak experiments. The inelastic energy losses reduce the divertor plasma temperature from levels of about 100 eV at the divertor entrance to about 1 eV in front of divertor plates and side walls. The cold molecular hydrogen injection raises the density of divertor neutrals to levels higher than the plasma density (~ 10^{14} cm^{-3}). Generic atomic plasma impurities in the divertor region are oxygen and those of the divertor wall materials (Be, C, W). Molecular impurities (such as CO, O_2, CO_2, C_mH_n) also exist in the cold divertor region.

We shall now briefly describe the molecular processes contributing to the divertor plasma cooling and recombination.

3. Plasma cooling by molecular processes

The most abundant molecular species in a divertor plasma is H_2. There is a recent evidence from TEXTOR tokamak experiments that H_2 can be vibrationally excited in the plasma periphery [4]. The most effective divertor plasma cooling molecular processes are those involving electron impact:

$$e + H_2(v) \rightarrow e + H_2(v') \quad , \quad v' > v \geq 0 \tag{1}$$

$$e + H_2(v) \rightarrow e + H_2^*(a,b,c^3\Lambda) \rightarrow e + H(1s) + H(1s) \tag{2}$$

$$e + H_2(v) \rightarrow e + H_2^+(v') + e \tag{3}$$

$$e + H_2^+(v) \rightarrow e + H_2^+(2p\sigma_u) \rightarrow e + H^+ + H(1s) \tag{4}$$

$$e + H_2(v) \rightarrow e + H_2^*(B,C,F^1\Lambda) \rightarrow e + H_2(v') + h\upsilon \tag{5}$$

Although the energy loss in the process (1) is small (~ 0.5 eV), this process is important for producing vibrationally excited H_2 at low temperatures ($T \lesssim 5$ eV). For plasma temperatures $T < 8$ eV, the most effective is the dissociative excitation (2), while for $T > 8$ eV the processes (3)-(4) are the main molecular plasma energy loss mechanisms. The process (5) is important both as a plasma loss mechanism and for producing vibrationally excited H_2. Important features of the reactions involving vibrationally excited states are the decrease of energy threshold and (generally) significant increase of the cross section with increasing v.

4. Molecular volume plasma recombination mechanisms

The recently discovered divertor "plasma detachment" regime, in which plasma detachment from divertor plates was observed [5,6] (accompanied by strong hydrogen line radiation), has stimulated search for potential atomic/molecular volume plasma recombination mechanisms. Two such mechanisms have been identified: the negative ion recombination channel [7] and the ion conversion recombination channel [8]. The chain of reactions involved in these recombination mechanisms at T ≤ 10 eV involve:

– negative ion scheme:

$$e + H_2(v \geq 4) \rightarrow (H_2^-)^* \rightarrow H(1s) + H^- \quad , \tag{6}$$

$$H^+ + H^- \rightarrow H(1s) + H^*(n=3) \quad . \tag{7}$$

The limiting process for this recombination channel is

$$e + H^- \rightarrow e + H + e \tag{8}$$

which for T > 1 eV is faster than reaction (7). Therefore, this recombination mechanism is effective only in the regions with T ≤ 1 eV.

– ion conversion scheme:

$$H^+ + H_2(v \geq 4) \rightarrow H + H_2^+(v)\,, \tag{9}$$

$$e + H_2^+(v) \rightarrow H + H(n \geq 2), n_m = 3\,, \tag{10}$$

The limiting process for this recombination channel is reaction (4). Only for T ≤ 1.5 eV the ion conversion scheme is operative. The Langevin limit for the rate coefficient of this reaction is 2×10^{-9} cm^3/s. It should be noted that reaction (9) is exothermic, but its rate coefficient is still not accurately known. It should be also noted that both recombination mechanisms rely on the existence of sizeable fractions of H_2 ($v \geq 4$) in the plasma.

Other possible volume plasma recombination schemes include

– H_3^+ assisted recombination

$$H_2 + H_2(v) \rightarrow H_3^+(v) + H^- \tag{11}$$

$$e + H_3^+(v) \rightarrow H_2(v' \geq 5) + H^*(n=2), (E > 4\,eV) \tag{12}$$

$$H^+ + H^- \rightarrow H + H^*(n=3) \quad . \tag{7}$$

– C_mH_n assisted recombination

$$H^+ + C_mH_n \rightarrow H + C_mH_n^+ \tag{13}$$

$$e + C_mH_n^+ \rightarrow C_mH_k + (n-k)H \tag{14}$$

The rate coefficients of reactions (11) and (13) are not known and it is, therefore, not possible to estimate the effectiveness of these recombination schemes. For m>n, the reaction (13) has quasi-resonant character and its rate coefficient should be large (10^{-8}-10^{-7} cm^3/s). The rate coefficients of reactions (12),(7) and (14) are all large.

– O assisted recombination

$$H^+ + O \rightarrow H + O^+ \tag{15}$$

$$O^+ + H_2(v) \rightarrow O + H_2^+ \tag{16}$$

$$e + H_2^+ + \rightarrow H + H \tag{17}$$

The reaction (15) is "accidentally" resonant and is, therefore, very fast. For v=3-4, the reaction (16) should also proceed rapidly. Therefore, presence of oxygen in the cold divertor regions is beneficial to the volume plasma recombination.

References

1. R.K. Janev, in: *Atomic and Molecular Processes in Fusion Edge Plasmas*, ed. by R.K. Janev (Plenum, New York, 1995), p.1.
2. R.K. Janev, Comments At. Mol. Phys. **26**, 83 (1991).
3. R.K. Janev, in: *Review of Fundamental Processes and Applications of Atoms and Ions*, ed. by C.D. Lin (World Scientific, Singapore, 1993), p.1.
4. A. Pospieszczyk, private communication (1998).
5. T.W. Petrie et al. J. Nucl. Mater. **196-198**, 848 (1992).
6. I.H. Hutchinson et al. Phys. Plasmas **1**, 1511 (1994).
7. R.K. Janev, D.E. Post et al. J. Nucl. Mater. **121**, 10 (1984).
8. S.I. Krasheninnikov et al. Phys. Lett. A **214**, 285 (1996).

Plasma Detachment with Molecular Processes in Divertor Plasmas

N. Ohno[1], N. Ezumi[1], D. Nishijima[1], S. Takamura[1], S.I. Krasheninnikov[2], A. Yu. Pigarov[2]

[1] *Department of Energy Engineering and Science, Graduate School of Engineering, Nagoya University, Nagoya 464-8603, Japan*
[2] *MIT Plasma Science and Fusion Center, Cambridge, MA, USA*

Abstract. Molecular processes in detached recombining plasmas are briefly reviewed. Several reactions with vibrationally excited hydrogen molecule related to recombination processes are described. Experimental evidence of molecular activated recombination observed in a linear divertor plasma simulator is also shown.

1 Introduction

Divertor has important functions in magnetically confined fusion devices such as control of heat and particle, removal of helium ash and so on. In next generation fusion devices intended to have a long pulse or steady state operation, heat flux onto divertor plate is expected to be quite high. Reduction of huge heat flux to the divertor plate is one of the most urgent issues in fusion research.

Plasma detachment with volumetric plasma recombination is considered to be the most promising method to reduce the heat and particle flux onto the divertor plate. Collisional radiative recombination process including radiative and three-body recombination has been clearly observed in detached plasmas of diverted tokamaks and a linear divertor plasma simulator.

On the other hand, new recombination processes associated with vibrationally excited hydrogen molecule, so called molecular activated recombination (MAR) were theoretically predicted by several authors. In this paper, MAR processes are briefly reviewed and its experimental evidence obtained in the NAGDIS-II (NAGoya DIvertor Simulator) device is also reported.

2 Molecular Activated Recombination

Reaction chains in MAR can be described as follows[1];

(a): $H_2(v) + e \Rightarrow H^- + H$ followed by $H^- + A^+ \Rightarrow H + A$,

(b): $H_2(v) + A^+ \Rightarrow (AH)^+ + H$ followed by $(AH)^+ + e \Rightarrow A + H$,

where $H_2(v)$ represents vibrationally excited hydrogen molecule and A^+ is plasma ion. MAR is expected to lead to an enhancement of the reduction of ion particle flux to the target, and to modify the structure of detached recombining plasmas because the rate coefficient of MAR is much greater than that of radiative and three-body recombinations (EIR) at relatively high electron temperature T_e above 0.5eV as shown in Fig. 1.

3. Experimental Setup

Figure 2 shows the schematics of the NAGDIS-II, which consists of a DC plasma discharge region and a divertor test region equipped with solenoid magnetic coils to generate a magnetic field strength up to 0.25T.

In the case of an attached plasma, the plasma is terminated by the water-cooled target plate at $X = 2.05$ m, where X means the distance from the anode. Neutral pressure P can be varied from less than 1 mTorr to 30 mTorr by introducing the secondary gas to the vacuum vessel or controlling the pumping speed of two turbo molecular pumps.

Three fast scanning double-probes were located at $X \sim 0.25$, 1.06 and 1.72 m, which are referred to as 'entrance', 'upstream' and 'downstream', respectively. Spectra of the visible light emissions were also observed at the upstream and downstream positions.

4 Experimental Results and Discussion

4.1 Helium Plasma with Hydrogen or Helium Gas Puff[2]

Figure 3 shows the change in spectrum of visible light emission from 310nm to 370nm observed in the downstream with hydrogen or helium gas puff. For a pure helium plasma, continuum and a series of visible line emissions from highly excited levels due to the conventional EIR were observed as shown in Fig. 3(c) and (d). Detailed analysis of the population distribution among the highly excited levels shows that T_e is about 0.4 eV by using the Boltzmann relation, because the distribution follows the Saha-Boltzmann distribution, that is, those excited states above a critical quantum number are in local thermodynamic equilibrium (LTE) with free electrons in the plasma. Analysis of the photon energy dependence of the continuum emission intensities also provides the same T_e.

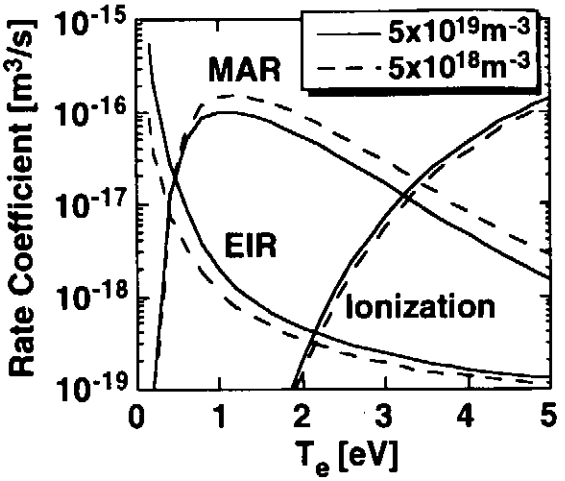

Figure 1: Rate coefficient of molecular activated recombination calculated with collisional-radiative code(CRAMD).

When a hydrogen gas was introduced into the helium plasma, the spectrum is found to be changed dramatically in Fig. 3(b) when the partial pressure of hydrogen gas exceeds a critical level ~ 1.4mtorr. There are neither continuum nor series of visible line emissions, that is, EIR does not occur at all in this plasma condition. Radial profiles of the ion flux measured both in the upstream and the downstream are illustrated in the insets of Fig. 3(a)-(d). The reduction of the ion flux along the magnetic field due to the EIR is found in the insets of Fig. 3(c) and (d). The reduction rates of the ion flux from the upstream to the downstream in Fig. 3(c) and (d) are almost the same, because of a very small helium pressure difference. On the other hand, in the inset of Fig. 3(b), we can see a strong reduction of the ion flux by the injection of a small amount of hydrogen gas. Moreover, the ion flux in the upstream has already decreased compared to that in the case of the pure helium detached plasma. This means that some plasma

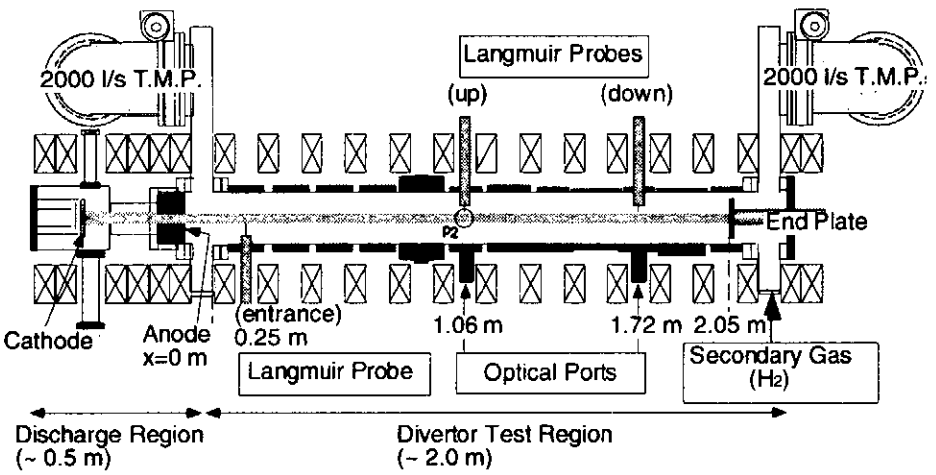

Figure 2: Schematics of the liner divertor plasma simulator NAGDIS-II

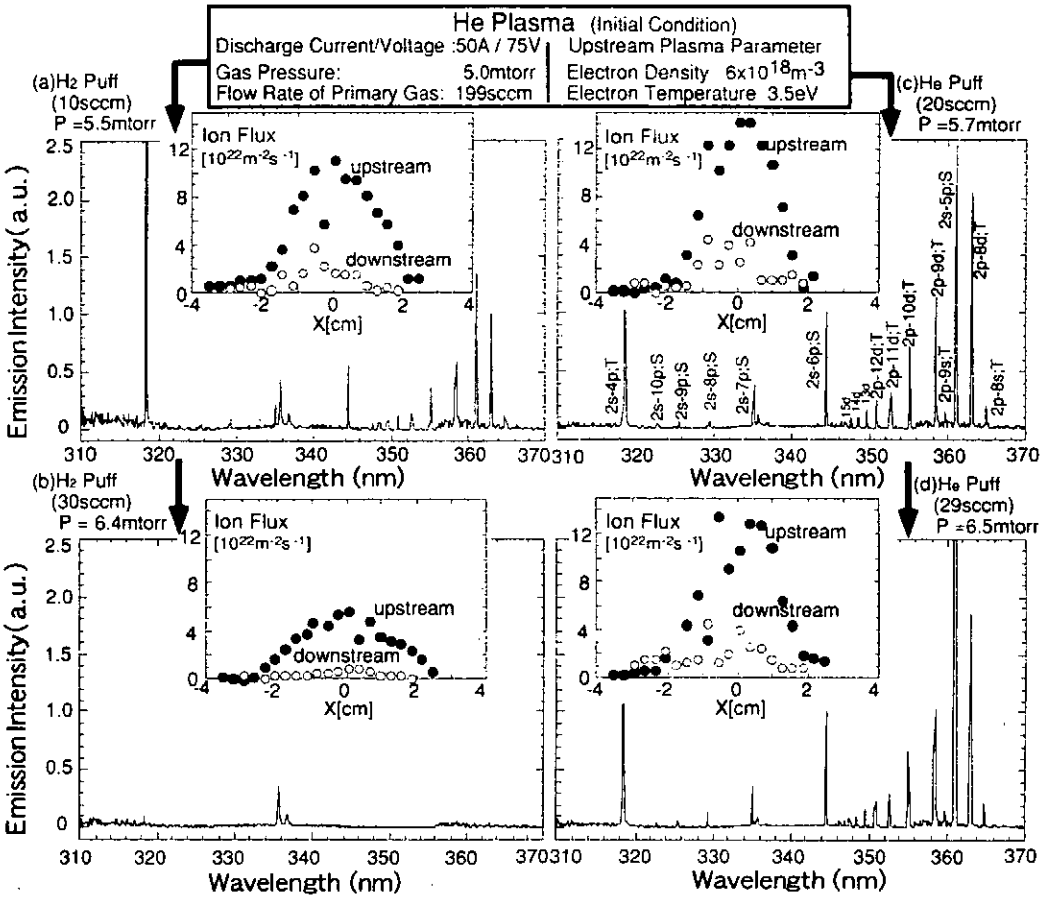

Figure 3: Visible emission spectra from helium plasmas with hydrogen gas puff: (a) and (b); and with helium gas puff: (c) and (d).

volumetric recombination process already starts to occur in the upstream, where T_e is relatively high. From these experimental results, we can conclude that there are the plasma volumetric recombination process coming from the effect of the molecular hydrogen (MAR) in our helium/ hydrogen mixture plasma.

The observed helium Balmer series spectra were analyzed with the CRAMD code[1] in detail. The population in excited states and corresponding line intensities are usually determined by the following three different mechanisms; i) EIR, ii) electron impact excitation from the ground state of atoms, and iii) MAR. Precise comparison between the experimental spectra and the relative line intensities obtained with the CRAMD code gives us MAR is the dominant populating mechanism among the above three candidates[2].

4.2 Hydrogen Plasmas with Hydrogen Gas Puff[3]

Radial profiles of the ion particle flux measured in the entrance , upstream and the downstream are shown in Fig. 4, when hydrogen gas was introduced into hydrogen plasmas. The plasma density at the center of the plasma column is about $1.0\text{x}10^{19}\text{m}^{-3}$ at the entrance. At $P \sim 4.0$mtorr, the ion particle flux along the magnetic field is found to reduce by an order of magnitude from the entrance to the downstream. When P is increased to be 10mtorr, there is little change of the ion particle flux in the entrance, however, the ion particle flux in the downstream becomes almost one-fiftieth as large as that in the entrance. We can see a strong reduction of the ion particle flux by the addition of a small amount of hydrogen gas. It is also found that no prominent continuum and series of visible line emissions from highly excited levels due to the conventional EIR were observed in both upstream and downstream at any gas pressure. It indicates

that the EIR dose not take responsibility for the reduction of the ion particle flux. These experimental results also suggest that there are the plasma volumetric recombination process coming from the effect of the molecular hydrogen (MAR) in hydrogen plasma with hydrogen gas puff.

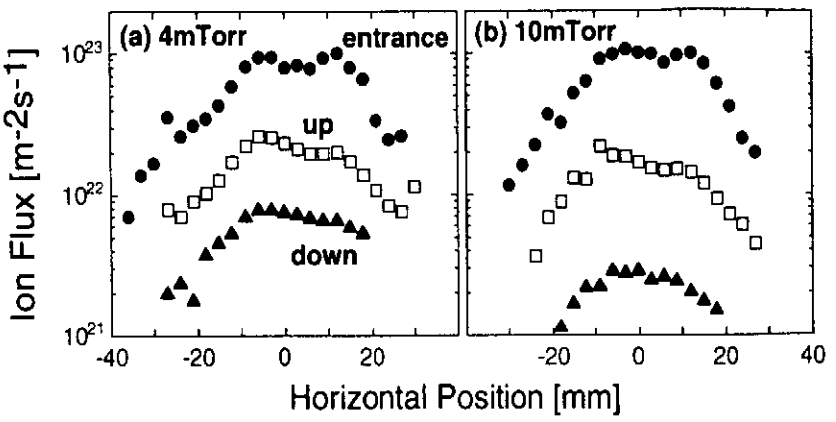

Figure 4: Radial profiles of ion flux of hydrogen plasmas with hydrogen gas puff.

We now consider the detached hydrogen plasma conditions where the EIR or MAR is dominating. The plasma particle loss rate per unit volume due the MAR and the EIR are described as $K_{MAR}n_e[H_2]$ and $K_{EIR}n_e^2$ respectively, where $[H_2]$ are hydrogen molecule density and K is rate coefficient. Figure 5 shows the electron temperature dependence of the ratio between the particle loss rate due to the MAR and EIR, that is, $R \sim K_{MAR}n_e[H_2]/ K_{EIR}n_e^2$, as parameters of the plasma density and the hydrogen gas pressure P. In the present experimental conditions ($P >$ 1 mTorr), the plasma particle loss due to the MAR is much greater than that due to the EIR. In order to realize the plasma condition where the EIR is dominating, the electron temperature should be cooled down to less than 0.3eV. Furthermore, to realize the detached hydrogen plasma due to the EIR at relatively high electron temperature about 1eV, much denser plasma ($> 5 \times 10^{19}$ m^{-3}) with the lower concentration of the hydrogen molecule are found to be required.

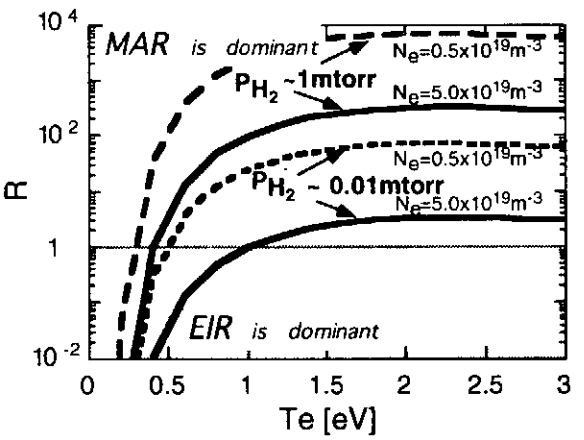

Figure 5: Electron temperature dependence of the ratio between the particle loss rate due to MAR and EIR.

5 Conclusion

Our conclusions are as follows;

1. Reduction of the ion particle flux and heat load to the target plate was clearly observed in hydrogen (helium) plasmas with the hydrogen gas puff due to the MAR.
2. Detailed analysis of Balmer and Balmar-like series spectra has been done by using the CRAMD code, which is in a good agreement with the experimental results.
3. In order to realize the detached hydrogen plasma where EIR is dominating in the present divertor simulator, much higher density plasma or effective cooling of the electrons should be required.

References

[1] Pigarov A Yu and Krasheninnikov I S 1996 Phys. Lett. A **222** 251

[2] Ohno N, Ezumi, N, Takamura S, Pigarov A Yu and Krasheninnikov I S 1998 Phys. Rev. Lett. **81** 818

[3] Ezumi N, Nishijima D and Kojima H *et al.* 1999 J. Nucl. Mater. **266-269** 337

Spectroscopic Study of JT-60U Divertor Plasma

H. Kubo, S. Higashijima, H. Takenaga, A. Kumagai+,
K. Shimizu, T. Sugie, S. Suzuki, A. Sakasai, and N. Asakura

Naka Fusion Research Establishment, Japan Atomic Energy Research Institute,
Naka-machi, Naka-gun, Ibaraki 311-0193, Japan
+Plasma Research Center, University of Tsukuba,
Tennohdai, Tsukuba-shi, Ibaraki 305-0006, Japan

Abstract

Particle behavior in the JT-60U divertor plasmas has been studied spectroscopically. Doppler profiles of the Dα line have been investigated for understanding of atomic and molecular processes in deuterium particle recycling and Dα line emission. Near the divertor plates, dissociative excitation from deuterium molecules and molecular ions plays an important role for the line emission. By investigation of spectral profiles of the He I line (667.8 nm), Doppler broadening due to elastic scattering by protons has been found. It is estimated that the penetration probability of the helium atoms from the divertor plates to the main plasma and the helium atom flux to the gap for pumping increase by 30% due to the elastic scattering. Intensity distribution of the CD band (around 430.5 nm) has been compared between the W-shaped divertor with a dome in the private flux region and the previous open one. The dome prevents the upstream transport of hydrocarbon impurity produced by chemical sputtering.

1. Introduction

One of the important requirements for steady state operation of a tokamak fusion reactor is particle control with a divertor. Understanding behavior of deuterium (hydrogen) atoms in the divertor region is necessary to control fueling and pumping. In order to design a divertor with high exhaust capability for fusion-produced helium particles, fundamental processes of helium atom behavior in the divertor plasma should be understood. Impurities are produced by plasma-material interaction in the divertor region, and their transport to the main plasma should be controlled to keep impurity concentration sufficiently low in the main plasma.

This paper presents spectroscopic study of deuterium, helium, and hydrocarbon particle behavior in the JT-60U divertor plasma. In order to understand the recycling and emission processes of the deuterium atoms, Doppler profiles of the Dα line have been observed with a high-resolution spectrometer and simulated with a neutral particle transport code [1,2]. For study of helium atom behavior, Doppler profiles of a He I line have been also investigated [3]. Hydrocarbon impurity is produced in the divertor region, because the material of the divertor plates and first walls is carbon. Spatial distribution of a CD band intensity has been investigated in order to study the hydrocarbon impurity transport [4].

2. Experimental setup and analysis procedure

A poloidal cross section of JT-60U is shown in Fig. 1. Confinement improvement and steady-state operation have been studied in divertor discharges with a W-shaped divertor at the bottom [5]. The W-shaped divertor is composed of divertor plates, dome and baffle plates. Neutral particles are exhausted through the gap between the inner divertor plates and the dome. Carbon-fiber composite tiles are used for the divertor plates and the top part of the dome, and isotropic graphite tiles are used for other inner surface of the vacuum vessel.

The diagnostics for the present divertor study are also shown in Fig. 1. Visible light from the divertor region is observed with a 60-ch fiber optic array. For observation of Doppler profiles of the Dα and He I (667.8 nm) lines, ten fibers are chosen and connected to a high-

resolution spectrometer [6]. Spatial distribution of the CD band (around 430.5 nm) intensity is observed with a spatial resolution of 1 cm using the 60 fibers and interference-filter optics [7]. Electron temperature and density are measured with the Langmuir probes at the divertor plates.

Emission of the Dα and He I lines is simulated with a neutral particle transport code (DEGAS) [8]. We modified DEGAS to simulate the Doppler profiles and to consider many atomic and molecular processes [1,3]. The CD band emission is simulated with an impurity transport code (IMPMC) [9]. The background divertor plasmas are determined using a simple divertor model from the Langmuir probe data.

In the present paper, L-mode plasmas with neutral beam heating power of 4 - 13 MW are discussed. In the discharges, the outer divertor plasmas are attached and the inner ones are detached. For investigation of the helium behavior, helium gas is puffed and the helium ion density is about 6 % of the electron density in the main plasma.

2. Doppler profiles of the Dα line

Spectra of the Dα line observed in the outer divertor plasma are shown in Fig. 2. The electron temperature and density are 90 eV and 0.5×10^{19} m^{-3} at the outer strike point, respectively. The spectra split into three components due to the Zeeman effect; the toroidal magnetic field at the outer strike point is 4.15 T. The spectral profile near the divertor plates is narrower than that in the upstream of the divertor plasma. The spectra simulated with the neutral transport code are also shown in the figure. The simulated line profiles agree reasonably with the observed ones. Composition of the simulated spectra is shown in the figure. The spectral profile can be explained to be composed of narrow and broad components; The narrow components are attributed to dissociative excitation and electron collisional excitation of the atoms produced by dissociation of deuterium molecules and molecular ions, and the broad components are attributed to electron collisional excitation of the atoms produced by reflection at the surface of the divertor plates and first walls and charge exchange between deuterium ions and atoms. Near the divertor plates, dissociative excitation plays an important role for the line emission. In the upstream, the contribution of the dissociative excitation decreases and that of the electron collisional excitation of atoms produced by the reflection and charge exchange increases. Because the kinetic energy of the atoms produced by the reflection and charge exchange is higher than that of the atoms produced by the dissociation, the spectral profile in the upstream is broader than that near the divertor plates.

3. Doppler profile of the He I line

Spectra of the π-component of the He I line observed in the outer divertor are shown in Fig. 3. The electron temperature and density are 40 eV and 0.6×10^{19} m^{-3} at the outer strike point, respectively. The spectrum in front of the divertor plates is narrow and similar to the instrumental function of the spectrometer, because the line is mainly emitted from low-energy helium atoms desorbed from the plates. The spectrum in the upper stream is broadened and asymmetric. In the figure, the simulated spectra are compared with the observed ones. The observed spectral line profiles are well reproduced by the simulation. The spectra obtained by the simulation neglecting the elastic scattering by proton collision are also shown in the figure. As shown in the figure, the broadening of the spectral profile in the upstream can be attributed to the elastic scattering. In the simulation, it is estimated that the penetration probability of helium atoms from the divertor plates to the main plasma and the helium atom flux to the gap for pumping increase by 30% due to the elastic scattering. The elastic scattering affects helium concentration in the main plasma and helium pumping efficiency.

4. Spatial distribution of CD-band intensity

From simulation using the impurity transport code, it was predicted that neutral hydrocarbon impurity produced at the first wall in the private flux region can readily access the upstream of the divertor plasma through the private flux region in the open divertor. A dome in the private flux region was expected to prevent the upstream transport. Spatial distributions of the CD-band intensity observed in the W-shaped and previous open divertor are shown in Fig. 4. The intensity around the null point in the W-shaped divertor is obviously lower than that in the open divertor. In the Fig. 4 (a), the simulated intensity distribution is also shown. The observed intensity distribution is reproduced by the simulation within a factor of two. The results suggest that the dome works to prevent the hydrocarbon impurity from invading the upstream as predicted.

5. Summary

In order to study the particle behavior in the divertor region, spectroscopic data were investigated considering many atomic and molecular processes. It was shown that atomic and molecular processes play important role in the particle behavior. As the divertor plasmas are expected to be denser and colder for tokamak fusion reactors, requirement of data and model of atomic and molecular processes is being enhanced to understand divertor plasmas.

References

[1] H. Kubo, et al., Plasma Phys. Control. Fusion, 40 (1998) 1115.
[2] A. Kumagai, et al., to be published in Plasma Phys. Control. Fusion.
[3] H. Kubo, et al., Plasma Phys. Control. Fusion, 41 (1999) 747.
[4] S. Higashijima, et al., J. Nucl. Mater. 266-260 (1999) 1078.
[5] Y. Kusama and the JT-60 Team, Phys. Plasmas, 6 (1999) 1935.
[6] H. Kubo, et al., Fusion Eng. Design, 34-35 (1997) 277.
[7] H. Kubo, et al., Plasma Phys. Control. Fusion, 37 (1995) 1133.
[8] D. B. Heifetz, *Physics of Plasma-Wall Interactions in Controlled Fusion*, ed D E Post and R Behrish (New York, Plenum) (1986) 695.
[9] K. Shimizu, et al., Proc. 15th Int. Conf. on Plasma Physics and Controlled Nuclear Fusion Research, Vol. 3, IAEA, Vienna (1996) 431.

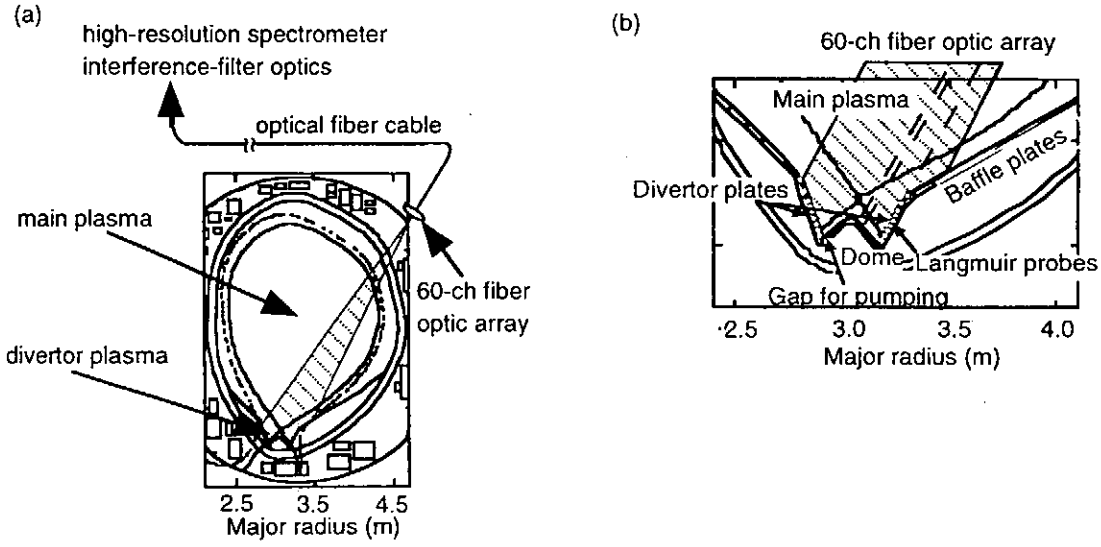

Fig. 1. Poloidal cross section of JT-60U and diagnostics. The divertor is enlarged in Fig. (b). The shaded area is observed with a 60-ch fiber optic array. The broken lines show the viewing chords that pass 0.5, 8, and 12 cm away from the outer divertor plates. They are referred to in Figs. 2 and 3.

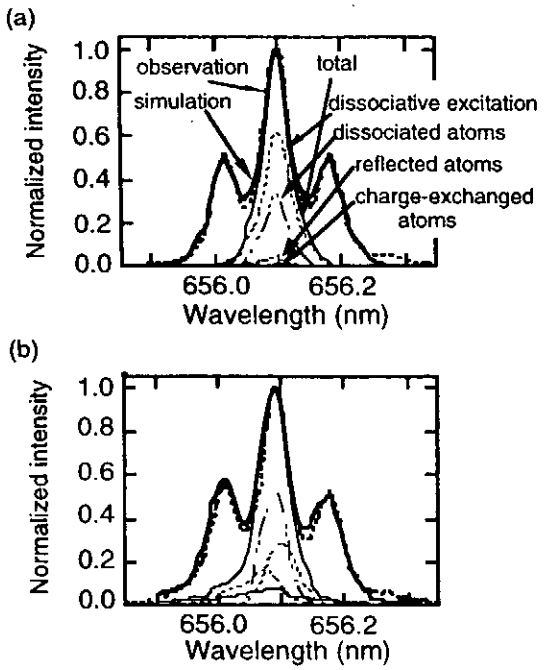

Fig. 2. Spectra of Dα line. (a) 0.5 cm and (b) 8 cm away from the outer divertor plates. The viewing chords are shown in Fig. 1. (b). The thick broken and solid lines indicate the observed and simulated spectra, respectively. The thin lines indicate the composition of the simulated spectra, for that the Zeeman effect is not considered.

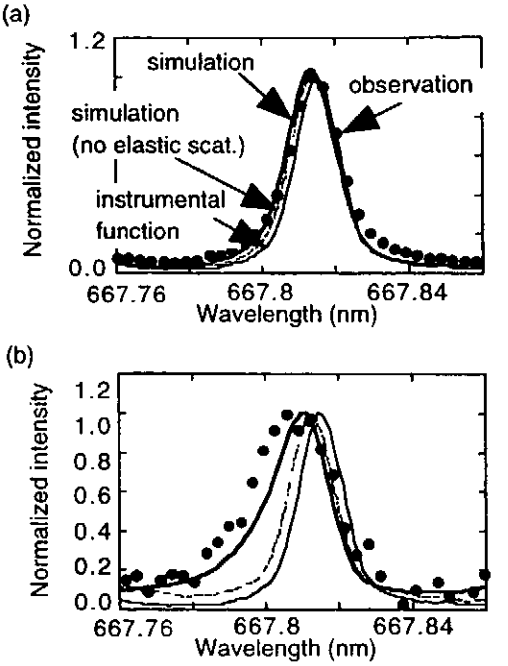

Fig. 3. Spectra of the π-component of the He I line. (a) 0.5 cm and (b) 12 cm away from the outer divertor plates. The viewing chords are shown in Fig. 1 (b). The points indicate the observation. The thick solid lines are the simulation, and the thick broken lines are the simulation neglecting the elastic scattering by proton collision. The thin lines show the instrumental function of the spectrometer.

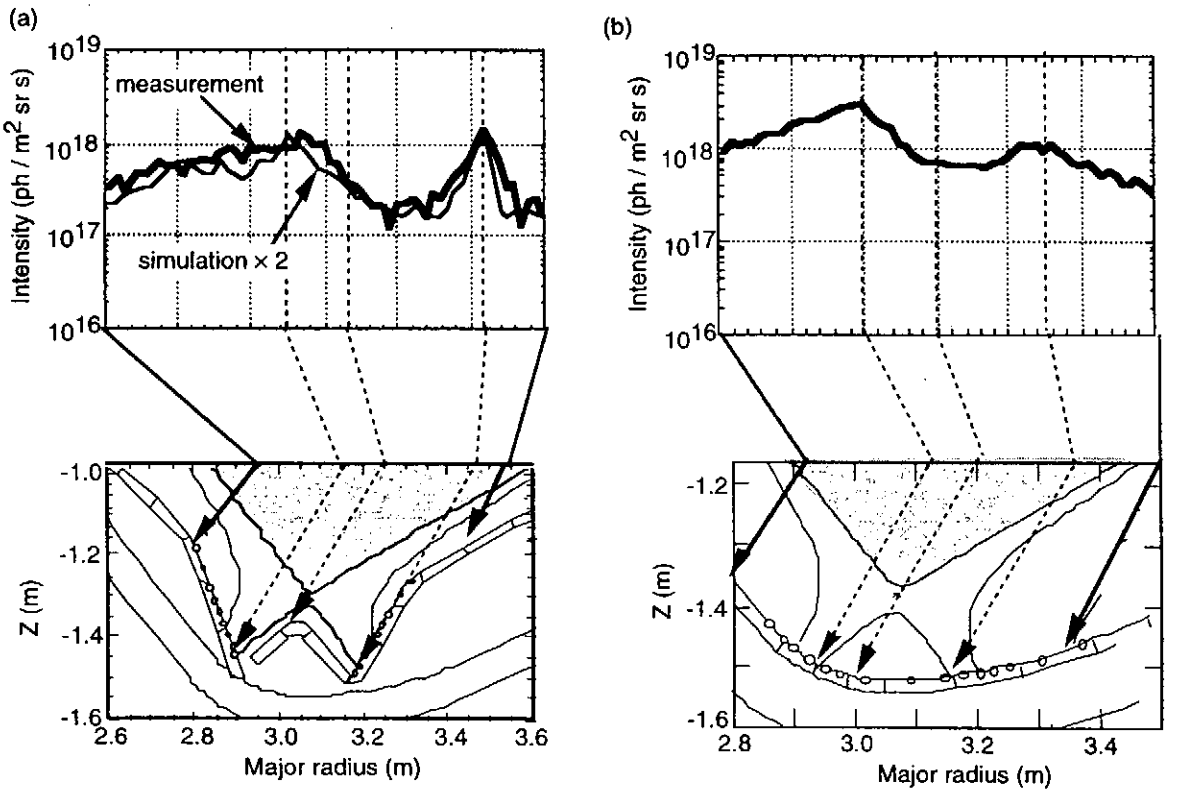

Fig. 4. Spatial distributions of the CD-band intensity in (a) the W-shaped and (b) open divertors. The thick lines indicate the measured intensity. The thin line shows the simulated intensity multiplied by two.

Atomic processes involving doubly excited levels in a low temperature dense plasma - recombination x-ray laser

Tetsuya Kawachi

Advanced Photon Research Center, JAERI-Kansai, Kizu, Kyoto, 619-0215, Japan

Abstract. Relative excited level populations of Li-like Al ions in a recombining plasma were measured using a spectrometer whose relative sensitivity was calibrated. A comparison of the experimental population distribution with a collisional-radiative (CR) model calculation indicates that atomic processes through doubly excited levels of the Be-like ions play an important role in the population kinetics of the Li-like ions.

1 Introduction

Recently, in a recombination x-ray laser research, a group of the present author proposed that atomic processes involving doubly excited levels, *i.e.*, dielectronic capture and ladderlike (DL) deexcitation and CR recombination from excited ions, played an important role in the population kinetics of the singly excited ions in a low temperature dense recombining plasma [1, 2]. A CR model calculation including these processes was performed on the Li-like Al recombining plasma, and the calculated population inversion density and gain coefficient of the $3d\ ^2D$-$4f\ ^2F$ and the $3d\ ^2D$- $5f\ ^2F$ lines was found consistent with the experiment [3, 4]. However, the population inversion density is a rather indirect quantity, and it is straightforward to compare the excited level populations with the CR-model. In this paper, we measure the excited level populations of the Li-like Al ions in a recombining plasma in which population inversion is generated. The experimental population distribution is comapred with our calculation.

2. Experiment and discussion

A 1 mm thick Al slab target was irradiated by Nd; glass laser light at a wavelength of 1.053 μm. The laser light consisted of 16 pulses, each 80 ps-long (FWHM), and separated by 100 ps. A combination of a spherical and a cylindrical lens made a line-focus on the target with 3 cm-long and 20 μm-wide. The irradiance was about 1.5×10^{12} W/cm^2. In this experiment the plasma was obesrved in its recombining phase at 600 μm from the target surface using a grazing incidence spectrometer with an x-ray CCD. The resolution in the wavelength was about 0.01 nm. The relative sensitivity of this spectrometer with the CCD was calibrated. With the use of this spectrometer, the $2s\ ^2S$ - $np\ ^2P$ series lines and the lines of the $2p\ ^2P$ - $ns\ ^2S$ and the $2p\ ^2P$ - $nd\ ^2D$ series of the Li-like Al were observed, where n is the principal

quantum number. In the following we call the former series the "resonance series", and the latter series altogether the "blending series".

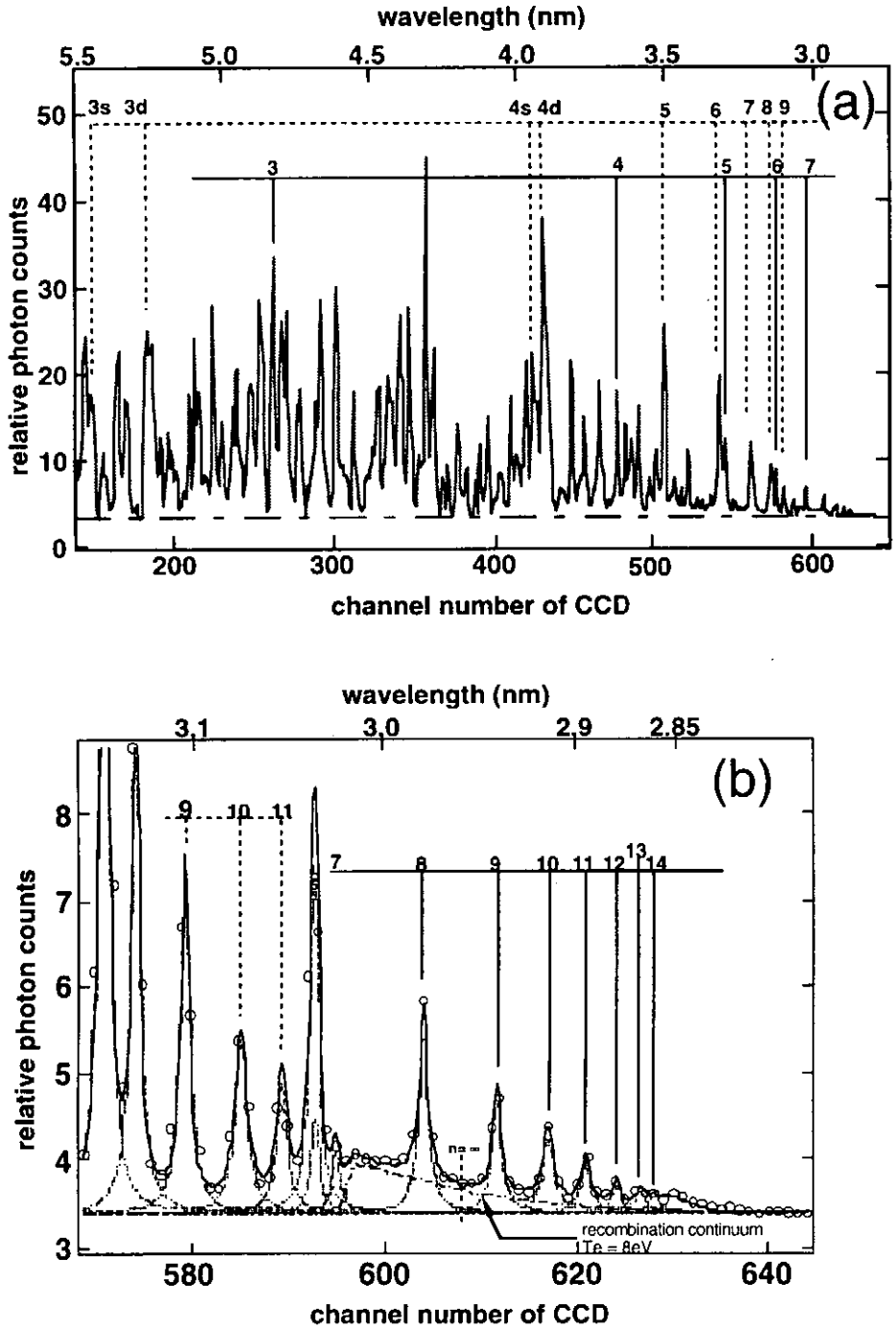

Figure 1. (a); A time-integrated spectrum of Li-like Al recombining plasma. The thick chain line represents the background level. The resonance and blending series lines are marked with the solid and dotted lines, respectively. The numbers put on these lines represent the upper level. (b); The spectrum around 570 ~ 645 channels. The open circles are the experimental points, the dotted curves are the spectral lines, the thin chain curve is the continuum radiation of the blending series, and the solid curve is the superposition of the spectral lines and the continuum radiation.

Figure 1 shows a typical time-integrated spectrum for the plasma length, l, of 0.5 cm.. The ordinate is the relative photon counts, and the abscissa is the channel number of the CCD or the wavelength. The open circles are the experimental points. The signal around 635 ~ 645 channels is assumed to be the background. The spectral lines of the resonance and the blending series of the Li-like Al are marked with the solid and the dotted line, respectively. The numbers put on these lines represent the upper level. The thin chain curve represents the continuum radiation of the blending series, whose slope indicates $T_e \sim 8$ eV. In view of the $2s\ ^2S$ - $np\ ^2P$ series lines the series limit is $n = 12 \sim 13$, which corresponds to the electron density of $n_e \sim 5.2 \sim 3.7 \times 10^{25}$ m^{-3}.[5] We fitted each spectral line by Lorentian and determined the relative intensity.. It should be noted that we measured the intensity of the several spectral lines for various target lengths and assured that the opacity effect was negligible for the plasma with $l = 0.5$ cm except the $n = 2$ - 3 lines.

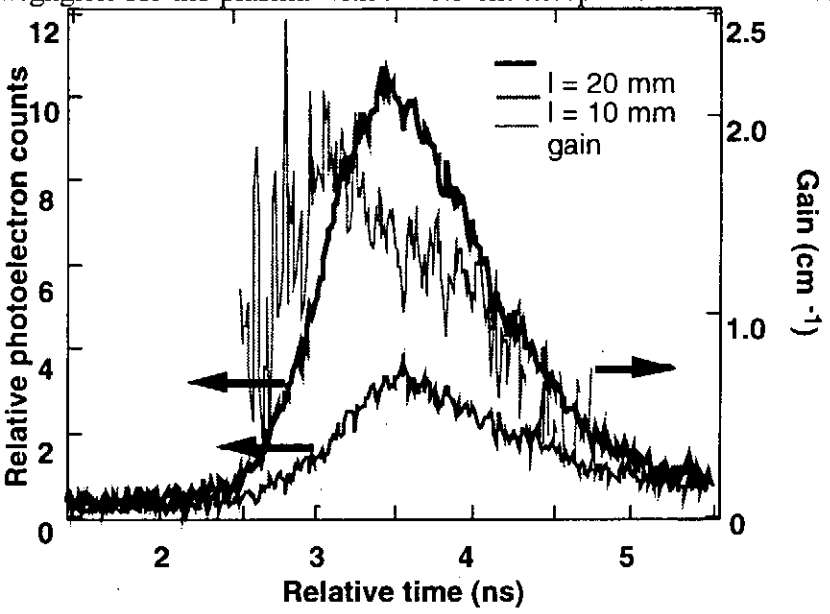

Figure 2. Time-resolved spectra of the $3d\ ^2D$ - $4f\ ^2F$ line intensity taken by the x-ray streak camera. The thick solid lines are the spectra for the cases of $l = 2$ cm and 1 cm, respectively, which are referred to the left hand side ordinate. The thin solid line is the amplification gain of the $3d\ ^2D$ - $4f\ ^2F$ line which is referred to the right-hand side ordinate.

We used another grazing incidence spectrometer with an x-ray streak camera, and observed temporal behavier of the $3d\ ^2D$- $4f\ ^2F$ line for various target lengths. The result is shown in Fig.2. In this figure, the abssissa is relative time, and the left-hand-side ordinate is relative photoelectron counts of the $3d\ ^2D$- $4f\ ^2F$ line for the plasma length of 2 cm and 1 cm. The amplification gain coefficient which is derived from these two lines is also shown. By this spectrum we assured that population inversion was generated in the present plasmas.

We derive the relative populations of the excited levels from Fig. 1 using the corresponding spontaneous transition probability. The derived experimental excited level populations are shown in Boltzmann plot (Fig. 3): The abscissa is the ionization potential of the excited levels in eV and the ordinate is the relative populations divided by their statistical weights. The closed triangles represent the np levels and the closed circles represent the combined ns and nd levels. The straight line in Fig. 3 corresponds to $T_e = 8$ eV.

We perform a CR model calculation for the present plasma under the quasi-steady state approximation. We include the atomic processes involving doubly excited levels, *i.e.*, DL deexcitation and CR recombination from excited ions. The details of these processes are described in the references [1, 2, 4 and 6]. Figure 3 shows the comparison of the CR-model calculation with the experimental result. We assume T_e = 8 eV, n_e = 4 × 10^{25} m^{-3}. Open triangles and Open circles represent the calculated results with the atomic processes involving doubly excited levels and without them, respectively. For the low-lying levels with $4 \leq n \leq 8$, the calculated result without the atomic processes involving doubly excited levels is 1 ~ 3 orders of magnitude larger than the experiment. Whereas with these processes, the calculated result is consistent with the experimental result within a factor of 3. This drastic decrease is mainly due to the CR-recombination from the excited ions through doubly excited Be-like ions. For the n = 3 levels, the calculated result with the atomic processes involving doubly excited levels is about 4 ~ 5 times smaller than the experiment, which may be due to the radiation trapping effect on the n = 2 - 3 transitions.

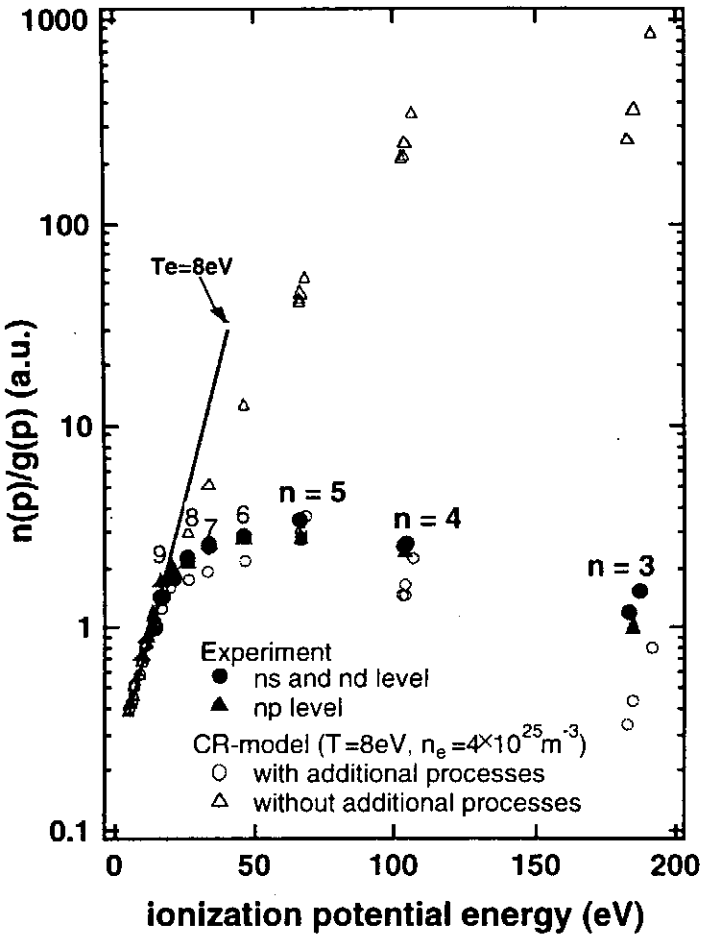

Figure 3. Experimental and calculated excited level populations in Boltzmann plot. The straight line corresponds to T_e = 8 eV. The closed triangles and circles are the populations of the *np* levels and the *ns* and *nd* levels combined, respectively. The open circles and triangles are the result of the CR-model with and without the additional atomic processes involving doubly excited levels, respectively.

References

[1] Kawachi T, *proc. 10th APS topical conference*, AIP-**381**, p 223. (1996).
[2] Kawachi T and Fujimoto T, 1997 *Phys. Rev. E* **55**, 1836 (1997).
[3] Moreno J C, *et al.*, *Phys. Rev. A* **39**, 6033 (1989).
[4] Kawachi T, *et al.*, J. Opt. Soc. Am. B7, 1863 (1997)
[5] Inglis D R and Teller E, *Astrophys. J.* **90**, 439 (1939).
[6] Fujimoto T and Kato T, *Phy. Rev. Lett.* **48**, 1022 (1982), *Phys. Rev. A* **32**, 1663 (1985).

X-Ray Spectroscopic Study of Astrophysical Plasma

Katsuji Koyama[1]

[1] *Dept. of Physics, Kyoto University, Kyoto, Japan*

Abstract. This paper discusses on extremely low-density space plasmas with the relation to laboratory plasmas. Extremely low density and large volume in the space provide us with a good laboratory to study elemental process, in particular those in non-equilibrium plasmas or very quick transient phendmena, which are difficult to access in ground laboratories. We demonstrate these aspects using the ASCA data, and discuss briefly on future prospects of space plasmas.

1 Space and Ground Laboratories

Astrophysical plasmas, like the other astrophysical objects, provide extreme physical conditions, which can be hardly obtained in ground laboratories. In this talk, I would like to invite you to a short tour to the astrophysical plasmas. Most of the data in this talk are taken from our X-ray satellite ASCA, the Advanced Satellite for Cosmology and Astrophysics. What is extreme in the space ? The plasma density, for example, ranges from more than 10^{18} kg/m^3 in a neutron star (nucleon plasmas or quark-gluon plasmas), to 10^{-27} kg/m^3 in an intergalactic space. This talk is concentrated on the low-density cases, on very low-density plasmas and their X-ray spectroscopies. In a low density plasma, elementary process would be purely appeared, hence is essentially important. If the density is very low, however, the chance for a particle to encounter to another is very rare, hence X-rays are rarely emitted. In an intergalactic plasma of a density of 1 atom /m^3, one X-ray photon from a unit volume of 1 m^3 is emitted every 10^{10} year. To study such a low-density plasma in a laboratory, we have to continue more than the age of the Universe. However, we did detect fairly strong X-rays from intergalactic space. This is due to the large volume of the plasma, which is nearly 10 million light years. Suppose that we are observing spherical plasmas with the same flux and angular size. Since the X-ray luminosity is proportional of n^2 times the volume, observed flux is given by;
$Fx \propto Lx/r^2 \propto n^2V/r^2 \propto n^2r^3/r^2 = n^2r.$
Therefore the plasma density is scaled with square root inverse of the distance r as $n \propto r^{0.5}$
If you want to observe extremely low-density plasmas, the more distant objects are the better. As I will demonstrate latter, time scale of many plasma processesm is inverse of density, a transient event of less than nano-sec in a laboratory plasma is frozen in a distant space plasma.

I will compare physical parameters between a large-scale space plasma and a small-scale laboratory plasma. As a large-scale plasma, I refer 1E0102-72.3, a bright supernova remnant in the Small Magellanic Cloud, because the physical parameters are well determined with the ASCA data. The SNR is a remnant of the plasma size of $D = 3 \times 10^{17}$m (diameter of the blast wave) after the supernova explosion of about 2000-year ago ($t = 6 \times 10^{10}$ sec), with the total explosion energy of $E = 10^{44}$ Joule in the interstellar number density $n = 3 \times 10^6$ /m ^{3}. As for a small-scale plasma, I show you a laser-induced explosion, by courtesy of Prof. Takabe. The physical parameters are: total induced energy $E = 10^3$ Joule, the size $D = 2 \times 10^{-2}$ m, the age $t = 10^{-8}$ sec and the number density $n = 10^{26}$

[1]E-mail : koyama@cr.scphys.kyoto-u.ac.jp

/m^3. We see that each parameters are largely different, for example total energy is 10^{41} times different. Still the non-dimensional parameter, $\alpha = D^{-1}(E/n)^{1/5}t^{2/5}$ is almost the same order of $0.1 \sim 1$. This means that astrophysical plasmas can be scaled by laboratory plasmas or inversely, we can predict laboratory plasmas by astrophysics.

2 Time Scales of Transient Plasmas

Quick transient phenomena in laboratory plasmas would be good objective in astrophysical plasmas, because the time scale should be largely expanded and even looks like to be almost frozen. Since the elemental process is two body collision, the transient phenomena are scaled by density (n) cross time (t).
The first is the ion and electron energy partition. If this process is due to a Coulomb collision, then the time scale of energy transfer from ion to electron is given:
$t_{i-e} = 10^{13}\langle A_i/Z_i^2\rangle kT^{1.5}/n_e \ln \Lambda$ [sec].
For typical parameters of space, namely plasma temperature of 1 keV and density of 1 particle /cc, energy equi-partition is taken 10^4 years.
The second is the ionization time scale. By collisions of high temperature electrons, ions are gradually highly ionized. The time scale to become ionization equilibrium is roughly given:
$t_{ion} = 10^{12}/n_e$ [sec].
Then typical time scale with electron temperature of 1 keV and density of 1 particle /cc, is more than 10^4 years. Accordingly, the transient plasma phenomena are almost unchanged in the time scale of a human life. Other words, if you want to trace an evolution of a space plasma, you should observe many samples with different evolution stage and re-construct the evolution history. However this paper only shows you a few snap-shots.

3 Equi-Partition of Ion and Electron

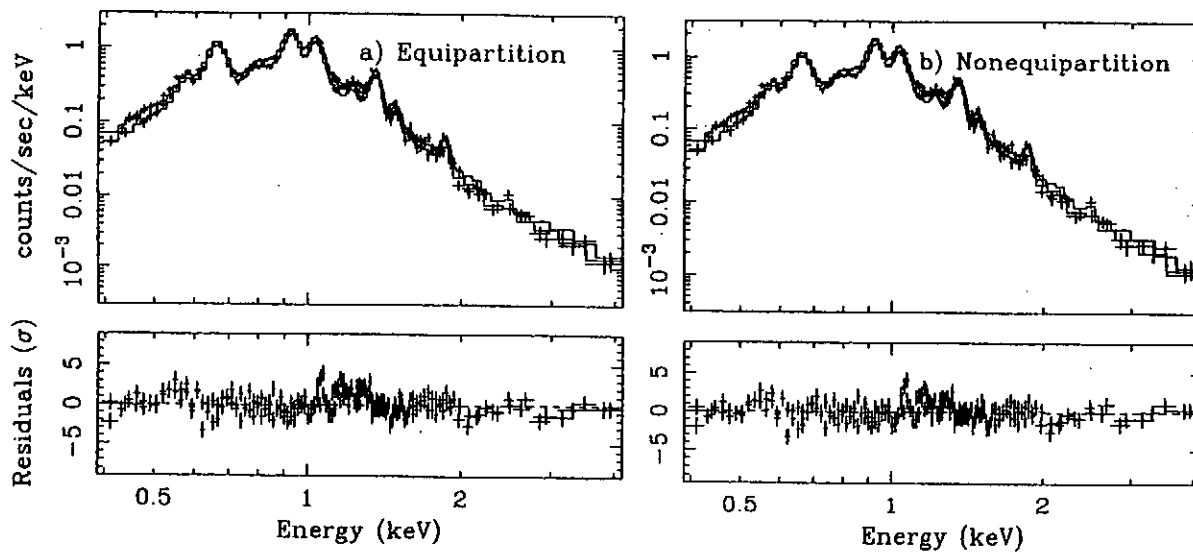

Fig 1: X-ray spectrum of 1E0102-72.3 and the best-fit model assuming equi-partition (a) and Coulomb interaction (b)

As we noted, the energy transfer time scale from atoms (ions) to electrons by a Coulomb interaction is very long. On the other hand, if some collective effects such as plasma instability are involved, the equi-partition time scale can be much shorter. Figure 1 is the X-ray spectrum of the young supernova remnant 1E0102-72 taken with ASCA. We assume two cases, equi-partition, and Coulomb interaction for the energy transfer. The best-fit model spectra are almost the same shapes. However underlining physical parameters are largely different. For example supernova explosion energy (E) for the Coulomb interaction is about 2 times larger than that of the equi-partition plasma. In other words, most of the thermal energy in the Coulomb interaction case is still containing in atoms (ions) due to the longtime scale. Since X-ray spectrum is sensitive to the electron temperature, the ASCA resolution is insufficient to judge whether the plasma is equi-partition or not. Direct observations of ion temperatures can be done with the next Japanese X-ray satellite ASTRO-E, which can measure thermal Doppler broadening of K-shell transition X-rays from heavy atoms.

4 Ionizing Plasma

The next issue is the ionization time scale. Suppose that a low temperature plasma is suddenly heated-up to produce high temperature electrons, then ionization states of atoms depends not only on the electron temperature but also on the electron density cross the elapsed time (nt). In the range of $\log(nt) < 11$, ionization degree is less than that expected from the equilibrium states to the electron temperature, which is achieved in the range of $\log nt > 12$. Since the ionization speed is a steep function of a electron temperature, while the recombination speed is not, the plasma in the range of $\log(nt) < 11$ is ionization dominant, hence is called as an ionizing plasma.

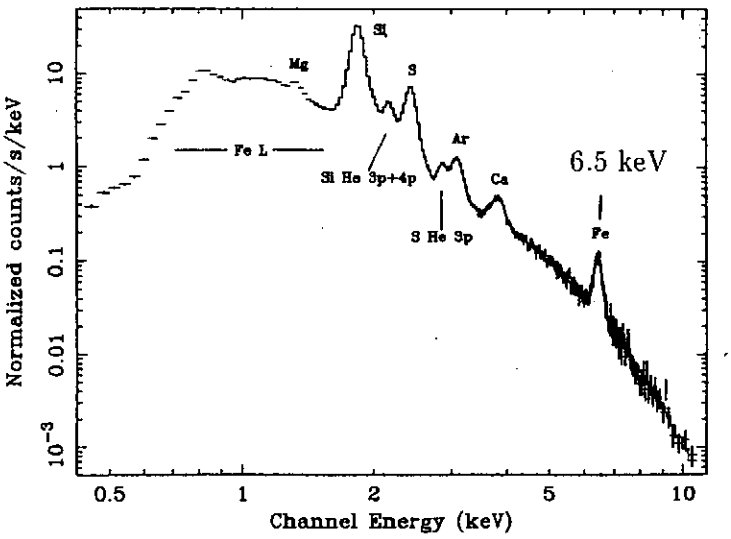

Fig 2: X-ray spectrum of the Tycho SNR. The K-shell transition line energy of iron is 6.5 keV

Supernova remnants, typical astrophysical plasma with the density of about 1/cc, age of about 1000 yr,are good examples of ionizing plasmas. Tycho, the famous astronomer in the 16-th century, observed a supernova explosion in AD 1572. An iron rich plasma in the Tycho supernova remnant is found by the iron K-shell transition lines. In this plasma, the electron temperature is estimated to be about 2 keV. Therefore iron atoms should be

ionized to He-like, with the K-shell line at 6.7 keV. But the X-ray spectrum given in figure 2 shows that the iron K-shell energy is 6.5 keV, which is still low ionization state (Hwang et al. 1998). The best-fit ionization parameters for iron and other light elements indicate that light elements are heated shortly after the SN explosion, but the iron plasma is very recently heated, by probably a reverse shock. I should note that, in a laboratory, these transient phenomena go very quickly, typically within less than 1 nano-second.

5 Photo Ionized Plasma

If the ionization rate balances to that of recombination, then we call this stage as ionization equilibrium. After reaching ionization equilibrium, electron temperatures cool via recombination processes, keeping the plasma to be ionization equilibrium. If the electron temperature is forced to be cooled-down rapidly, or alternatively a higher ionization sate is given by some methods, then the plasma should be recombination dominant. By X-ray photo ionization, a recombing plasma is made, because it produces highly ionized atoms with a rather low electron temperature. Figure 3 is a spectrum of photo-ionized plasma around the bright X-ray source Cyg X-3. Since the photo-ionizing X-ray source is in the line of sight, this spectrum also includes that of the original source. Still clear evidence for low temperature electrons and highly ionized atoms is found in the recombination edge structures of H-like silicon and sulfur atoms. The narrow widths of these structures tell you that the electron temperature is only about 20 eV, but there are fully ionized silicon and sulfur atoms (Kawashima and Kitamoto 1996).

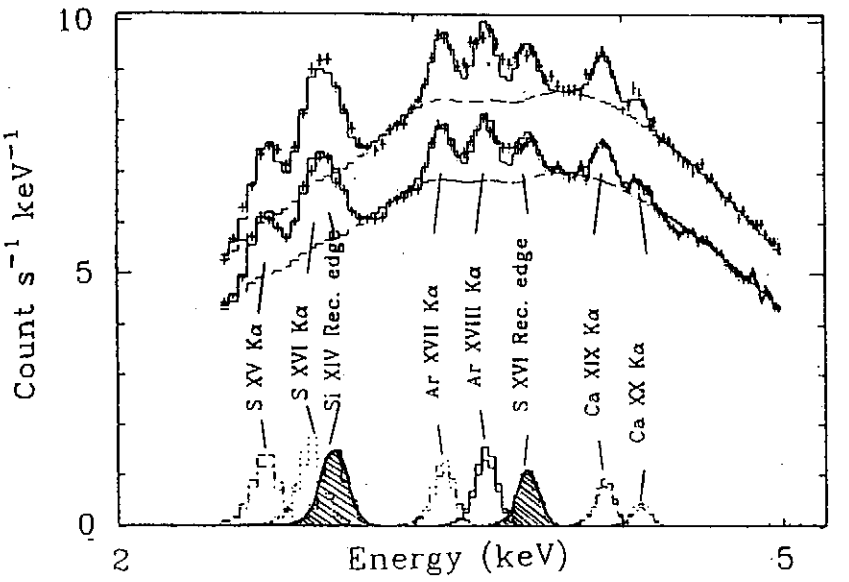

Fig 3: X-ray spectrum of Cyg X-3. The recombination edge structures of H-like silicon and sulfur atoms are shown in the hated areas.

References

[1] Kawashima K. and Kitamoto S. 1996 Publ. Astron. Soc. Japan **48** L113

[2] Hwang U., Hughes J. P. and Petre R. 1998 Astrophysical Journal **497** 833

Plasma Polarization Spectroscopy and Collision Cross Sections

Takashi Fujimoto and Manabu Nakai
Department of Engineering Physics and Mechanics,
Graduate School of Engineering, Kyoto University, Kyoto 606-8501, Japan

Abstract: In Plasma Polarization Spectroscopy (PPS), we observe the polarized spectral lines emitted from a plasma. For berylliumlike oxygen lines from a tokamak plasma the polarization feature is interpreted as due to the anisotropic velocity distribution of electrons which excite the ions. In this interpretation in terms of the population-alignment collisional-radiative (PACR) model various collision processes are involved concerning the population and the alignment; *e.g.*, transfer of the alignment (and the coherence) by collisional excitation and production of an alignment from a population by elastic collisions. These latter processes are little known so far.

1. Introduction

In atomic collision experiment, when an ensemble of atoms (or ions) is excited by a monoenergetic beam of electrons unequal 'populations' are created among the magnetic sublevels of an excited level, or alignment is created in this level besides its population, and the emitted radiation is polarized. In plasma, if the electron velocity distribution is anisotropic a similar situation is realized and the emitted radiation will be polarized, the polarization characteristics being dependent on the properties of this anisotropy. For instance, in addition to the isotropic Maxwellian distribution of electrons there may be a beam component,[1] or the effective temperature in the direction perpendicular to the magnetic field is different from that in the parallel direction.[2] Thus, from the observed polarization characteristics, we may investigate the anisotropic velocity distribution. This is the idea of Plasma Polarization Spectroscopy (PPS).[3]

Figure 1 shows an example of PPS observations; berylliumlike oxygen impurity lines emitted from a tokamak plasma are recorded with their polarized components resolved. The π-light is linearly polarized (We define the polarization direction as the direction of the oscillating electric field.) in the direction of the confining magnetic field of the plasma, or approximately in the toroidal direction, and the σ-light is approximately in the poloidal direction. The weakest line, $2s3s\,^3S_1 - 2s3p\,^3P_0$, is never polarized, while the stronger lines, $2s3s\,^3S_1 - 2s3p\,^3P_{1,2}$, have stronger σ-components (I_σ) than the π-components (I_π) in this example. We define *the intensity* of a line as $(2/3)(I_\pi+2I_\sigma)$. Instead of the polarization degree, we define *the longitudinal alignment* as $A_L = (I_\pi-I_\sigma)/(I_\pi+2I_\sigma)$. The latter two lines have A_L = -0.010 and -0.032, respectively.

2. Population-alignment collisional-radiative (PACR) model[3]

We assume axial symmetry along the quantization axis and the absence of coherence between the different levels (optical coherence) and among the magnetic sublevels in a level (Zeeman coherence). To each level, say level p, we assign two quantities, the population $n(p)$ and the alignment $a(p)$. See Fig. 2. A J=0 level does not have an alignment. The

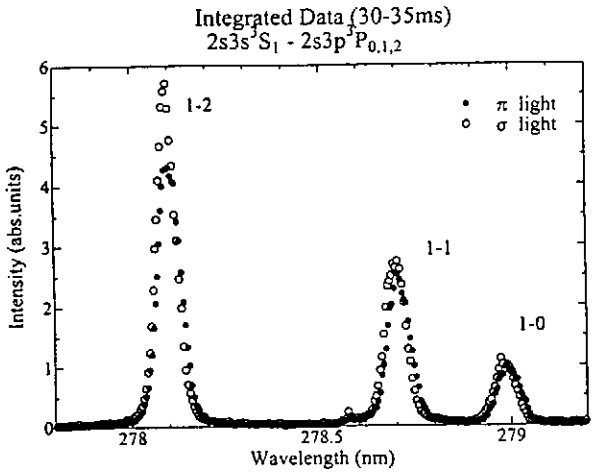

Fig. 1. An example of the polarization resolved spectra observed on the WT-3 tokamak at Kyoto University. Berylliumlike oxygen lines. The dominant constituent of the plasma is hydrogen and oxygen is an impurity. The (J=1←J=0) line is never polarized.

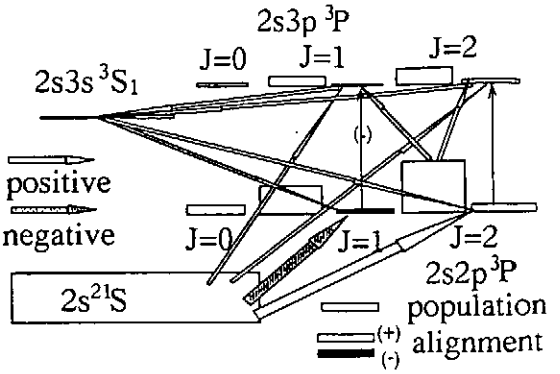

Fig. 2. Flow diagram showing the production and transfer of alignment among the low-lying triplet levels of berylliumlike oxygen. Each level has the population (blank box) and the alignment (shaded box). The J=0 levels do not have an alignment. The area of the boxes and the width of the arrows represent the magnitude of the population or of the alignment and that of the flow of alignment, respectively. Note that an alignment can be positive or negative. Not to scale for different configurations.

population is the zero-th moment of the expansion of the density matrix of atoms in this level in terms of the irreducible tensorial set, and the alignment is the second moment. Note that the density matrix is not normalized. The population $n(p)$ gives the intensity as defined above, and the ratio $a(p)/n(p)$ gives A_L.

We construct the rate equations for the population and for the alignment; Let $C(r,p)$ be the rate coefficient for production of population in level p from the population in r by electron collisions, or the conventional excitation or deexcitation rate coefficient, $A(r,p)$ be the radiative transition probability, $S(p)$ be the ionization rate coefficient, $C^{02}(r,p)$ be the rate coefficient for production of a population in level p from the alignment in level r, and $C^{02}(p,p)$ be that for conversion of the alignment into a population within level p.

$$\begin{aligned} dn(p)/dt = & \Sigma_{(r\neq p)}[C(r,p)\, n_e + A(r,p)]\, n(r) \\ & - [\ \{\Sigma_{(r\neq p)} C(p,r) + S(p)\}\ n_e + \Sigma_{(r\neq p)} A(p,r)]\, n(p) \\ & + \Sigma_{(r\neq p)} C^{02}(r,p)\, n_e\, a(r) \\ & - C^{02}(p,p)\, n_e\, a(p) \end{aligned} \qquad (1)$$

where n_e is the electron density in the plasma. The first two lines of the right-hand side are the conventional rate equation for the population, except that a Maxwellian distribution is assumed in the conventional case. The last two lines are correction due to the presence of unequal 'populations' among the magnetic sublevels, or of the alignment.

Let $C^{20}(r,p)$ be the rate coefficient for production of an alignment in level p from the

population in level r by electron collisions, $C^{20}(p,p)$ be that for production of an alignment from the population within level p, $C^{22}(r,p)$ be that for transfer of the alignment from level r to level p, $A^{22}(r,p)$ be the probability of transfer of the alignment from r to p by radiative transition and $C^{22}(p,p)$ be the rate coefficient for destruction of the alignment by electron collisions. The rate equation for the alignment is

$$\begin{aligned} da(p)/dt = & \Sigma_{(r\neq p)} C^{20}(r,p)\, n_e\, n(r) \\ & - C^{20}(p,p)\, n_e\, n(p) \\ & + \Sigma_{(r\neq p)} [C^{22}(r,p)\, n_e + A^{22}(r,p)]\, a(r) \\ & - [C^{22}(p,p)\, n_e + \Sigma_{(r\neq p)} A(p,r)]\, a(p). \end{aligned} \qquad (2)$$

Thus, the alignment is treated just like the population. It may be noted that the population is conserved among the levels, while the alignment can simply disappear. We assume stationary state. In solving the set of equations like eqs. (1) and (2) with $d/dt = 0$ we adjust the "shape" of the velocity distribution function (see below), so that the set of solutions of $n(p)$ and $a(p)$ gives good agreement with experiment. For the example of Fig. 1 the velocity distribution expressed by a toroidal temperature of 10 eV and a poloidal temperature of 100 eV gives rough agreement with experiment. n_e is 10^{19} m^{-3}. Figure 2 shows the 'flow diagram' concerning the alignments of the levels concerned.

3. Rate coefficients and cross sections

The rate equations (1) and (2) consist of various rate coefficients, and thus cross sections, some of which are rather exotic. We examine just one example: $C^{22}(r,p)$, transfer of alignment, for the purpose of illustration.

The velocity distribution of electrons is expanded in terms of Legendre polynomials,

$$f(v, \theta) = \Sigma_{(K)} f_K(v)\, P_K(\cos\theta). \qquad (3)$$

We define the transition cross section from the magnetic sublevel $\alpha' J' M'$ of level r to magnetic sublevel αJM of level p in the impact parameter (b) semiclassical expression

$$Q_{\alpha JM,\alpha' J' M'} = 2\pi \int | \langle \alpha JM | S_c | \alpha' J' M' \rangle |^2 \, b \, db \qquad (4)$$

where S_c is the collision matrix referred to the collision axis. The alignment transfer cross section due to the collisions in the direction of quantization axis is given as

$$Q^{22}_{\perp}(r,p) = \Sigma_{(MM')} (-1)^{J+J'+M+M'} \langle JJM\text{-}M | 20 \rangle \langle J'J'M'\text{-}M' | 20 \rangle \, Q_{\alpha JM,\alpha' J' M'} \qquad (5)$$

Where $\langle \cdots | \cdots \rangle$ is the Clebsch-Gordan coefficient. We also take into account the contributions from *oblique* collisions; These electrons regard the alignment as a coherence. We consider coherence transfer. For $q = 1$ or 2

$$Q^{22}{}_q(r,p) = \Sigma_{(MM'J')}(-1)^{J+J'+M+M'} \langle JJM(q-M)|2q\rangle \langle J'J'M'(q-M')|20\rangle \times 2\pi \int \langle \alpha JM|S_c|\alpha' J'M'\rangle \langle \alpha J(M-q)|S_c|\alpha' J'(M'-q)\rangle^* b\,db \quad (6)$$

The alignment transfer rate coefficient is given as[3]

$$C^{22}(r,p) = \int [Q^{22}{}_0(r,p) + Q^{22}{}_1(r,p) + Q^{22}{}_2(r,p)]\, 2f_0(v)/5\, v^3 dv + \int [2Q^{22}{}_0(r,p) + Q^{22}{}_1(r,p) - 2Q^{22}{}_2(r,p)]\, 2f_2(v)/35\, v^3 dv + \int [6Q^{22}{}_0(r,p) - 4Q^{22}{}_1(r,p) + Q^{22}{}_2(r,p)]\, 2f_4(v)/105\, v^3 dv. \quad (7)$$

Other rate coefficients except for $C^{22}(p,p)$, and thus the corresponding cross sections, are expressed in terms of the magnetic-sublevel-magnetic-sublevel cross sections like eq.(4).

Another process of interest is production of an alignment by directional elastic collisions. This gives the rate coefficient $C^{20}(p,p)$ in eq.(2). Recently, an experiment was performed which showed that an alignment is produced in low energy elastic collisions.[4]

4. Cross section data

In constructing the above PACR model, many kinds of cross sections are needed. Most of the existing data are for the excitation cross section $Q(p,r)$, or $Q^{00}{}_0(p,r)$. In terms of PPS this quantity is relevant in the situation where the velocity distribution is isotropic and the alignment is absent. In interpreting the experimental data as shown Fig. 1, we adopted the recommended cross section data for $Q(p,r)$ by Kato et al.[5] for many transitions and the magnetic-sublevel-magnetic-sublevel cross sections calculated by Csanak and Grabbe[6] by the distorted-wave method for the transitions shown in Fig. 2. We ignored other cross sections like eq.(6). Therefore, our above conclusion about the velocity distribution is tentative.

It is hoped that the cross section data necessary to construct the PACR model become available for important atomic and ionic species in plasma spectroscopy.

References

1. B. Coppi, F. Pegoraro, R. Pozzoli and G. Rewoldt , Nucl. Fusion **16**, 309 (1976).
   L. Pieroni and S.E. Segre, Phys. Rev. Letters **34**, 928 (1975).
2. M.D. Bowden, T. Okamoto, F. Kimura, H. Muta, K. Uchino, K. Muraoka, T. Sakoda, M. Maeda, Y. Manabe, M. Kitagawa and T. Kimura, J. Appl. Phys. **73**, 2732 (1993).
3. T. Fujimoto and S.A. Kazantsev, Plasma Phys. Control. Fusion **39**, 1269 (1997).
4. S. Trajmar, I. Kanik, M.A. Khakoo, L.R. LeClair, I. Bray, D. Fursa and G. Csanak, J. Phys. B **31**, L393 (1998).
5. T. Kato, J. Lang and K.E. Berrington, NIFS-DATA-2 (Institute for Fusion Science, Nagoya, 1990).
6. G. Csanak and S. Grabbe (private communication, 1997).

Working Groups on AM processes in Data and Planning Center in NIFS (April 1999 - March 2000)

Takako KATO

Data and Planning Center
National Institute for Fusion Science, Toki 509-5292, Japan

Since Dr. Murakami presented our database in this seminar (page 17), I would like to describe the activities of the Working Groups on Atomic and Molecular processes in the Data and Planning Center at NIFS. We have a joint research program in NIFS to promote the work in NIFS by collaboration with universities and institutes. In this fiscal year we have eight working groups listed below. Each group holds meetings in NIFS several times per year to compile/evaluate data or discuss problems related to their main topics. Travel expenses are supported by NIFS. We publish research reports for example in the NIFS - DATA series when we obtain results as a working group. These working groups help the communication between fusion plasma physicists and atomic physicists. We can find new problems and gradually develop new research fields. We list here the titles of our working groups and the name of a key person who takes responsibility for the group's activities:

1. Development of Plasma Polarization Spectroscopy
   FUJIMOTO, Takashi (Kyoto Univ.)
2. Development of atomic kinetic codes for hot dense plasmas
   SASAKI, Akira (JAERI)
3. Research on Opacity of medium Z and high Z plasmas
   TAKABE, Hideaki (ILE, Osaka Univ.)
4. Electron capture in collisions of C^{q+} and O^{q+} ions with H and He atoms below 1keV/u
   KIMURA, Mineo (Yamaguchi Univ.)
5. Evaluation of atomic data for Lithium ions
   MURAKAMI, Izumi (NIFS)
6. Working Group for Plasma Atomic and Molecular Processes
   KATO, Takako (NIFS)
7. Taskgroup for plasma-wall interaction issues in advanced fuel fusion reactors
   KAWAMURA, Takaichi (NIFS)
8. Taskgroup for plasma-wall interactions database and related simulation code library
   YAMAMURA, Yasumichi (Okayama Sci. Univ.)

Atomic and Molecular Data Activities at NDC/JAERI

Toshizo Shirai
Nuclear Data Center (NDC), Japan Atomic Energy Research Institute (JAERI)
Tokai-mura, Ibaraki 319-1195, Japan

See p-49 in this proceedings.

NIST Atomic Data Centers

Data Centers on Atomic Transition Probabilities and Line Shapes

Atomic Physics Division (842)
National Institute of Standards and Technology
100 Bureau Drive, Mailstop 8423
Building 221, Room A257
Gaithersburg, MD 20899 (USA)

Contact:
Jeffrey R. Fuhr
Phone: (301) 975-3204
E-mail: jeffrey.fuhr@nist.gov
Fax: (301) 990-1350
http://physics.nist.gov/asd

Atomic Energy Levels Data Center

Atomic Physics Division (842)
National Institute of Standards and Technology
100 Bureau Drive, Mailstop 8401
Building 225, Room B166
Gaithersburg, MD 20899 (USA)

Contact:
Arlene Robey
Phone: (301) 975-3221
e-mail: arlene.robey@nist.gov
Fax: (301) 975-4578
http://physics.nist.gov/asd

The ORNL Controlled Fusion Atomic Data Center

Predrag S. Krstić and David R. Schultz

Oak Ridge National Laboratory, Physics Division, P.O. Box 2008, Oak Ridge, TN 37831-6372, USA

1 Introduction

The Controlled Fusion Atomic Data Center (CFADC) was established in 1958 and its mission is to collect, evaluate, recommend, and disseminate atomic and molecular collision data of urgent need in fusion energy research and development. The CFADC is supported through the U.S. Department of Energy, Office of Fusion Energy Sciences, and is part of the Oak Ridge National Laboratory's Physics Division.

2 Brief History

In 1958 a data center was established informally at Oak Ridge National Laboratory by Dr. C. F. Barnett to collect, review, evaluate and compile numerical atomic collision data of interest to controlled thermonuclear fusion research. Its first cross section compilation was published in 1960. In 1963 this undertaking was formally established as the Atomic and Molecular Processes Information Center, with the primary task of producing extensive annotated bibliographic files of atomic data related to fusion processes and compiling evaluated atomic collision data pertinent to fusion research. In 1970 the Atomic and Molecular Processes Information Center (AMPIC) became the Controlled Fusion Atomic Data Center (CFADC).

Highlights of the CFADC activities include production of volumes of recommended atomic data for fusion, known as the "Redbooks" (ORNL Technical Reports published in 11 volumes, during the period of 1961-1990) as well as collection and publication of a categorized bibliography of atomic and molecular processes of interest in fusion research. The bibliography covers published articles during the period 1950 - present. Since the data center's inception in 1958, over 100 journals have been regularly searched and over 60,000 individual entries have been accumulated. Presently, the bibliography may be queried on-line, through the World Wide Web (WWW), regarding the entries since 1978 (approximately 30,000).

An important part of the CFADC activity has been coordination through the international network of data centers, under the auspices of International Atomic Energy Agency (IAEA).

3 Current Projects

Significant efforts are focused to make the CFADC-WWW site the front line interface of the CFADC activities. This Web site is intended to serve as an electronic interface between the Data Center's resources and the fusion energy community. The archival bibliographic entries dating from 1950 to 1977 will be added on-line in the near future, as well as approved portions of the database produced by the NIST-JILA data center before its recent closure. Present tokamak fusion research puts emphasis on processes

in the cool, dense plasma of the divertor and plasma edge, with increased significance of molecular and transport related atomic data. A large database of elastic and charge exchange processes for isotopic combinations of ions, atoms and molecules of hydrogen has been produced and made available on the Web. It is also published in volume 8 of the IAEA "Greenbooks", Atomic and Plasma-Material Interaction Data for Fusion.

ALADDIN is a database management system accepted by the International Atomic Energy Agency for the exchange of atomic and molecular data of interest in fusion energy research and development. The databases and codes are available at the CFADC web site. In addition, on-line versions of the most often requested "Redbooks" have been uploaded to this site. Finally, reference manuals for the Atomic Data and Analysis Structure (ADAS) codes, developed at JET/Strathclyde, is mirrored by the CFADC, and making certain Auburn/Rollins/Strathclyde ADAS atomic data sets broadly available on-line.

4 Initiatives

Members of the CFADC have been among the initial organizers of the new conference entitled International Conference on Atomic and Molecular Data and Their Applications (ICAMDATA). It is designed to re-establish awareness of the important role of atomic data and data center activities. In the current plan of CFADC is production of charge exchange data from excited vibrational states of hydrogen molecules at sub-electron volt energies, of importance for the divertor plasma energy balance and in astrophysical modeling. Other initiatives are oriented toward atomic and plasma physics data and modeling activities in astrophysics, and towards developing a coordinated program in atomic data collection and dissemination of interest for plasma processing.

5 Personnel

The staff of the Controlled Fusion Atomic Data Center at ORNL consists of D. R. Schultz, P. S. Krstić, and F. M. Ownby. In addition, the CFADC relies for its bibliographic search on ORNL consultants (F.W. Meyer, C.C. Havener, M.E. Bannister, and P.C. Stancil) and external consultants (H.B. Gilbody, T.J. Morgan, R.A. Phaneuf, M.S. Pindzola, and E.W. Thomas).

The CFADC may be contacted via telephone ((423)-574-4701), fax ((423)574-4745), email (krstic@mail.phy.ornl.gov) and by mail. On-linr resources are available through the WWW at (http://www-cfadc.phy.ornl.gov).

Acknowledgements. The CFADC at Oak Ridge National Laboratory is funded by the U.S. Department of Energy's Office of Fusion Energy Sciences under contract no. DE-AC05-96OR22464 with Lockheed Martin Energy Research Corporation.

IAEA Activities on Atomic and Molecular Data for Fusion

R.K. Janev

International Atomic Energy Agency, Vienna, Austria

On initiative of the International Fusion Research Council (IFRC), the International Atomic Energy Agency (IAEA) started in 1976 a broad range of activities on establishment of an international data bank for atomic and molecular data (A+M) of interest to controlled nuclear fusion research. The data bank consists of two parts, a bibliographic and a numerical one, the latter comprising spectroscopic, collisional and radiative data for fusion relevant species and collision systems. Later on (at the end of eighties), particle-surface interaction and material properties (PMI) data were added to the numerical database. The IAEA A+M/PMI data activity is regularly reviewed and supervised by the IFRC Subcommittee on A+M Data for Fusion.

In implementing the objectives of this activity, the IAEA, through its A+M Data Unit, organizes Coordinated Research Programmes of a duration of 3-5 years (3-4 of them running each year, with participation of 30-40 research laboratories and groups) to stimulate the generation of new A+M or PMI data for fusion. The compilation of bibliographic and numerical A+M/PMI data, as well as the critical assessment of compiled data, is conducted by a collaborative effort of the International A+M/PMI Data Centre Network, consisting of about 15 national data centres and coordinated by the IAEA. For coordination of their activity, the A+M/PMI Data Centre Network members meet biennially at the IAEA. Critical assessment of the data stored in the IAEA numerical databases is also performed by experts and advisory groups. The role of the IAEA A+M Data Unit is to maintain and periodically upgrade the A+M/PMI numerical databases and to disseminate the information to fusion researchers. The IAEA A+M/PMI numerical databases are stored in the ALADDIN system and are online accessible via WWW (http://www-amdis.iaea.org/aladdin.html). The IAEA bibliographic database (compiled mainly by ORNL and NIST A+M data centres) together with ALADDIN form the IAEA AMDIS system (http://www.iaea.org/programmes/amdis). At present, the access to the bibliographic database requires a telnet session.

The IAEA experience in the coordination of international efforts on establishing recommended databases of A+M/PMI data for fusion shows that such an approach is both cost effective and, through concentration of expertise, ensures high quality of the resulting product. The coordinated approach to database establishment also ensures timely response to urgent data needs in certain data application area (through focussing of joint efforts), as well as certain flexibility in the selection of the activity targets and optimal distribution of the available resources and expertise within the Network. Thematic networking and other forms of organized collaboration of the data centres (with possible inclusion of other research groups) is certainly an efficient way for establishing topical database. Collaboration with the data application communities is also beneficial for defining the scope of topical databases and for ensuring their usefulness.

Atomic data sources in the UK

Hugh P. Summers

[1] *Department of Physics and Applied Physics, Strathclyde University, Glasgow G4 0NG, UK*

Abstract. UK atomic databases and their objectives are summarised. These have mostly been generated by international collaborations and so are not to be exclusively identified with the UK. However, for the named databases, the UK is a major contributor to the source methodologies and codes.

There have been two fairly recent large-scale multi-participant, international atomic data generation projects. The first - the Opacity Project - (Seaton,1987) has a product of gf-values and photo-ionisation cross-sections archived in TOPBASE (*http://cdsweb.u-strasbg.fr*). Following the completion of the Opacity Project, the international team was reformed into the Iron Project (Hummer et al., 1993) for the generation of electron impact collision cross-section data, primarily for ions of iron. This was based on state-of-the-art R-matrix calculations originating at Queen's University, Belfast and University College, London. The cross-section product of the Iron Project is in process of being archived in TIPBASE (*http:// - n.a.*) and the project has been extended to nearby elements. A fresh development is the RmaX project for calculation of both electron and photon induced transitions of atoms and ions in the soft X-ray regime for astrophysics. The calculations are exploiting advances in the R-matrix method to achieve higher precision for K- and L-shell excitation and ionization. There is no substantive data output at this stage.

There is large systematic production of state selective dielectronic data by a UK/USA collaboration (Badnell et al., 1995) - the DR Project. The first substantial tranche of production of LS-coupled data was in 1992/93. It resolved metastable parents and tabulated coefficients to both lower LS-resolved levels and bundled higher nS-shells. The DR Project is continuing with very large intermediate coupling production aimed at medium weight elements. DR Project data is prepared for iso-electronic sequences and structured for population calculations in the ADAS Project (*http://patiala.phys.strath.ac.uk/adas/*). The database is also archived at Oak Ridge CFADC (*http://www.cfadc.ornl.gov*). An activity for state selective ionisation including excitation auto-ionisation - the Ionisation Project - has been constituted by the same team and again specified for the ADAS Project. Light element data has been generated so far but an intermediate coupling extension paralleling the DR Project is in development.

The older Belfast K-matrix fundamental database of R-matrix calculations is no longer maintained. However, there is substantial production of electron impact collision data in the R-matrix approximations by the Belfast School, carried out independently of the large named projects. This significant collision data resource is available in data journals and directly from the authors. There is similar production at University College London, University of Strathclyde and Sheffield Hallam University.

References

[1] Badnell N R, Griffin D C, Pindzola M S et al. 1995 *AIP Conf. Proc.* **322** 85.

[2] Hummer D G, Berrington K A, Eissner W et al. 1993 *Astr. & Astrophys.* **279** 298.

[3] Seaton M J 1987 *J. Phys. B* **20** 6363.

ATOMIC DATABASE ACTIVITIES IN RUSSIA

A.Ya. Faenov
Multicharged Ions Spectra Data Center of VNIIFTRI (MISDC), Mendeleevo, Moscow region, 141570 Russia

The database activities in Russia have been developed in connection with UV and soft X-ray spectroscopic studies of high-temperature plasmas. Two form of database production are used: i) a set of computer programs to calculate radiative and collisional data for any atom or ion, and ii) development of numeric database systems with the data stored in the computer. The advantages of the first approach is obvious, however, for accurate values of wavelengths and other atomic constants of complex atoms and ions only the second approach is possible.

The first approach is used in the Lebedev Physical Institute (Moscow) where theoretical methods and computer codes ATOM, IONCOL and GKU were developed for calculating different atomic processes. The ATOM code has been developed for calculating atomic (ionic) parameters, radiative and autoionization probabilities and cross sections for electron-atom (ion) collisions. The IONCOL code is applied for ion-atom and ion-ion processes. The GKU code is employed for calculation of the plasma ionization state, excited level populations and spectral line intensities. These three codes are interconnected.

The second approach is used in the Institute of Spectroscopy (Troitsk, Moscow region), TRINITI (Troitsk, Moscow region) and MISDC of VNIIFTRI (Mendeleevo, Moscow region).

An atomic data bank BIBL for plasma physics, atomic physics, astrophysics etc. is being developed at the Institute of Specroscopy.and could be reached by Internet (http://das101.isan.troitsk.ru)

The results of TRINITI activities are: i) HiBase software for hierarchical management af atomic data on PCs, ii) specialized databases on excitation and ionization of atoms and ions by electron impact, iii) compilation of experimental and theoretical data on the cross sections of Ne^{q+} ionization, iiii) files with energy levels, oscillator strength and other information to be used as input for plasma calculation (H- to Ne-like Ne, Al, Ar and Fe), iiiii) specialized bibliography database for two-electron transitions in ion-atom collisions.

The large numerical database SPECTR have been created in MISDC. The database "SPECTR" software is based on FoxPro Database Management System. The information is stored in well-known DBF-format and can be transferred easily into another formats. Now DB "SPECTR" is really database on characteristics of isolated atoms and ions, i.e. on spectral lines (wavelengths and radiative probabilities) and energy levels. The small number of collisional data were inputted practically only for to test software developed. Because of MISDC research team works in the field of X-ray spectroscopy, the main part of data (about 75%) refers to the multicharged ions. DB SPECTR contains: i) published experimental data. For X-ray region database contains practically all published experimental data, for UV and visible regions – only some data, ii) own experimental data for multicharged ions. For example only during last 5 years we have produced new accurate data on satellite lines caused by radiative transitions in He-, Li-, Be-, B-, C-, N-, O-, F-, Na-, Mg- like ions, on high-n transitions in He- and Ne-like ions, iii) theoretical data, both published (not all, of course) and calculated especially for DB "SPECTR" in some Russian (or Soviet) institutes. Now DB SPECTR contains more than 400000 numerical records on spectral lines, energy levels, ionization potentials, excitation cross sections and rates, ionization cross sections and rates, dielectronic recombination rates, and references.

I am pleased to thank L. Presnyakov, A. Ryabtsev and I. Skobelev for valuable discussions.

AMO Data Centre in KAERI

Yongjoo Rhee and Jongmin Lee

Laboratory for Quantum Optics
Korea Atomic Energy Research Institute
P.O.Box 105, Yusong, Taejon 305-600, Korea

AMODS (Atomic, Molecular, and Optical Database System) accessible through http://amods.kaeri.re.kr has been providing numerical information on the atomic and molecular spectroscopy and collisional cross-sections since its first appearance on the internet in March 1997, after about one year of internal preparation in KAERI. It is now in its second phase in that its web pages and data structures are evolved from its first version which contains a limited amount of data and naive arrangement of individual html documents. AMODS is first launched as a data source for the spectroscopy community of Korean scientists to support people who need AMO data and it is still growing to be copious.

AMODS is now comprised of 8 separate databases; i.e. atomic spectral lines (ASL), transition probabilities (TP), atomic energy levels (AEL), atomic transition lines (ATL), ALADDIN on-line execution (ALAD), fundamental constants (CONST), electron impact cross sections (IMPACT), and internal database (ID), among which the last one (ID) is for internal use only and can be seen on the home page menu by some specific IP addresses.

The original archived data of ASL, TP, AEL and ATL are obtained from the CDS database of Strasbourg University in France, followed by stratification and structural arrangement accoding to atomic elements or wavelengths. The initial pages of these 4 databases are organized in a periodic table manner so that searchable elements can be easily chosen by users. Fortran source codes and related data files of ALADDIN database are from A+M Data Unit of IAEA. Two of the fortran files of ALADDIN are slightly modified in the I/O routines so that they can be run on WWW basis and communicate with CGI programs of web server to obtain the calculating parameters of users. Numerical output data can be seen as an ascii format or graphic format generated by gnuplot. Some of fundamental constants recommended by CODATA86 are compiled in Acrobat pdf format for easy reference of contants with high degree of resolution. Electron impact excitation cross-sections of molecules are being compiled in IMPACT. Cross-sectional data based on cubic interpolation of the oxygen molecule obtained in the crossed-beam experiments has been compiled and still more data on other molecules are being worked on. The search results can be seen as a graphic format using gnuplot. The internal database is access-controlled both by perl script and by the access-control file of the web server since it contains some of our raw experimental results which have not been published yet and some copy-right sensitive information. By perl script the menu of the home page looks different according to the connecting web browser's IP address and the internal database is not seen by the users outside of our laboratory.

AMODS is continuously evolving toward the completion of a database of numerical data on atoms, molecules and quantum optics as well as toward the highest availability in the internet environment.

Atomic and Molecular Database in China

Yu-Bo Qiu[♯], Yu Zou[♯], Jun Yan[*]

[1♯] *Institute of applied and computational mathematics, Beijing 100088, China.*
[*] *Center of Atomic and Molecular Sciences, Department of Physics, Tsinghua University Beijing 100084, China*

With years of hard work, We have established and developed the Atomic and Molecular Database, which are based on Visual FoxPro and can be run on Windows 95 or Windows NT system. Our database is composed of four sub-system: 1) maintenance sub-system; 2)retrieve sub-system; 3)management sub-system for super-user; 4)user's guide sub-system. In the retrieve sub-system, the system can search out (or calculate out) data automatically according to the user's retrieve value, then output the results in forms of printing in tables (or figures), or saving as ASCII files according to the user's needs.

In our Database, we have collected a large mount of atomic Molecular data, which mainly include:

1) about 390,000 records of spectra data (both experimental and theoretical).

2) about 2,300 records of ionization potential data (both experimental and theoretical).

3) about of 75,000 records of atomic (ionic) energy level data (both experimental and theoretical).

4) Atomic collisional process data of Ne-like and Ni-like, which include interaction between radiation field and atoms(ions); collisions between electrons and ions, such as electron collision excitation, ionization, di-electronic recombination et. al.; and collisions between ions and atoms.

Although many work have been done, we need international communication and cooperation in many fields, such as communication of atomic and molecular data and their compiling methods; collaboration of the research work on the data which share the common interests; and the communication of the management system of the database.

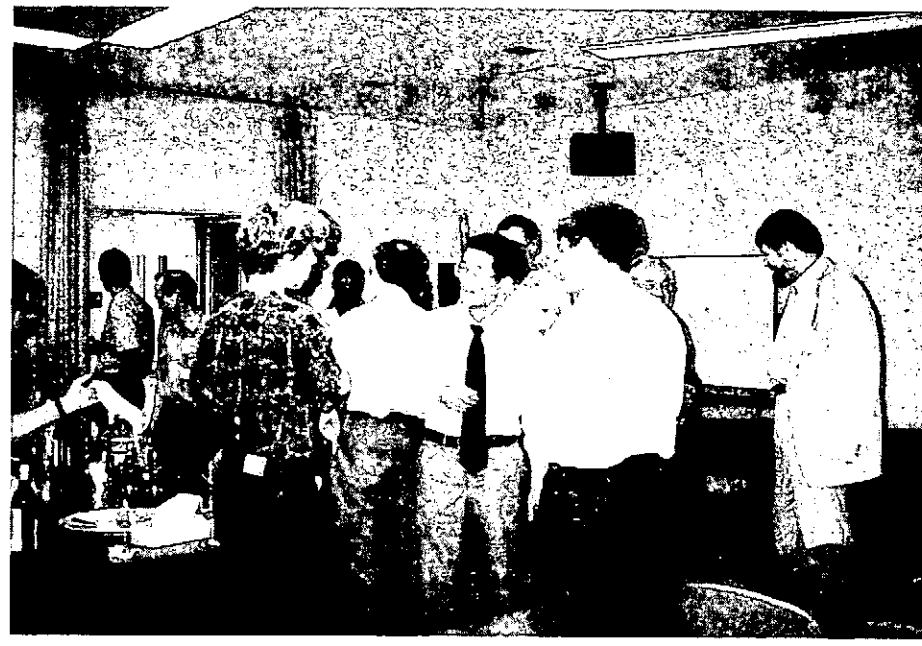

DATABASE FOR INELASTIC COLLISIONS OF LITHIUM ATOMS WITH ELECTRONS, PROTONS AND MULTIPLY CHARGED IONS

J. SCHWEINZER[1], R. BRANDENBURG[2], I. BRAY[3], R. HOEKSTRA[4], F. AUMAYR[2], R.K. JANEV[5], AND HP. WINTER[2]

[1]*Max-Planck-Institut für Plasmaphysik, Boltzmannstrasse 2, D-85748 Garching, Germany*
[2]*Institut für Allgemeine Physik, TU Wien,Wiedner Hauptstrasse 8-10, A-1040 Wien, Austria*
[3]*Dept. of Physics, Flinders University, GPO Box 2100, Adelaide 5001, Australia*
[4]*KVI Atomic Physics, Zernikelaan 25, 9747 AA Groningen, The Netherlands*
[5]*International Atomic Energy Agency, P.O. Box 100, A-1400 Vienna, Austria*

Extended Abstract

Cross section information on inelastic collisions of Li in its ground state as well as in excited states colliding with electrons, protons and multiply charged ions [1] is not only of fundamental interest, but also of considerable practical importance for diagnostics of magnetically confined fusion plasmas by means of Li beam spectroscopy [2,3,4,5]. Injection of a beam of fast (1-10 keV/amu) neutral lithium atoms into the edge of a magnetically confined plasma delivers diagnostic information such as radial electron density profiles and concentrations and temperatures of impurity ions in a non-perturbing manner. Analysis of the emission lines of injected lithium atoms, which provides information on the electron density in the plasma edge, requires knowledge of the populations of all excited atomic states as well as of the Li beam intensity attenuation. Evaluation of the diagnostic raw data relies on modelling the attenuation of the Li($n\ell$; n = 2 - 4) state beam fractions [2]. The success of this diagnostic method depends strongly on the availability of reliable data for cross sections of inelastic collisions of lithium atoms with plasma particles such as electrons, protons and multiply charged impurity ions.

Experimental and theoretical cross section data for collisional processes of Li atoms in the ground state and excited (up to n = 4) states with electrons, protons and multiply-charged ions have already been collected in [1] and [6]. Cross section scaling relations based on semi-empirical formulae which have to be regarded as rough cross section estimates for the processes of interest have been used to generate cross sections for processes for which no information was available in the literature. This approach has been extensively used particularly for collisional processes involving excited Li states, and especially for collisions with protons. The expected error for this procedure was in some cases more than 100 %.

Recently, detailed investigations of the composition of neutral states [7] along the penetration path of a lithium beam injected into a fusion plasma revealed considerable discrepancies between measurements and the population of specific excited states as derived from beam attenuation models using the atomic collision data of [1]. These differences triggered experimental and theoretical activities to improve the atomic database. In this work we use advanced theoretical methods to derive accurate cross sections for all inelastic processes involving collisions with Li atoms like single electron capture (SEC), ionization and excitation. These theoretical results are critically tested against the newest available experimental data. In all cases good or at least satisfactory agreement between measurements and theory is found. A similar confidence level of our theoretical results is also expected for cases where no experimental verification is feasible. However, there are still processes where neither calculated nor experimental data exist. The relevant cross sections, which mainly involve Li(4ℓ) states, are derived by using scaling relations as described in [1]. The latter are of minor importance from the point of view of fusion plasma diagnostics, thus deserving less attention with respect to accuracy. The "recommended" cross sections for the considered processes, generated either by (1) critical assessment of available experimental and theoretical data, or (2) by calculations alone, or (3) by application of scaling relations, have been fitted to analytic expressions which ensure correct asymptotic behaviour of the cross sections. These "recommended" cross sections are presented by giving their analytic-fit expressions and tabulating the values of all parameters entering these analytic fits. Furthermore, the recommended cross sections are presented in graphical form together with the new cross section data used for their generation.

References

[1] D. Wutte, R.K. Janev, F. Aumayr, M. Schneider, J. Schweinzer, J.J. Smith and HP. Winter, Atomic and Nucl. Data Tab. **65** 155 (1997).
[2] J. Schweinzer, E. Wolfrum, F. Aumayr, M. Pöckl, HP. Winter, R. P. Schorn, E. Hintz and A. Unterreiter, Plasma Physics and Controlled Fusion **34** 1173 (1992).
[3] R. P. Schorn, E. Wolfrum, F. Aumayr, E. Hintz, D. Rusbüldt and HP. Winter, Nucl. Fusion **32** 351 (1992).
[4] E. Wolfrum, F. Aumayr, D. Wutte, HP. Winter, E. Hintz, D. Rusbüldt and R. P. Schorn, Rev. Sci. Instrum. **64** 2285 (1993).
[5] J. Schweinzer, F. Aumayr, P. Platzer, M. Schneider, D. Wutte and HP. Winter, Comp. Phys. Comm. **88** 83 (1995).
[6] R.K. Janev, J.J. Smith, F. Aumayr, D. Wutte, M. Schneider, HP. Winter and J. Schweinzer, IAEA report INDC(NDS)-267 (1993)
[7] R. Brandenburg, J. Schweinzer, S. Fiedler, F. Aumayr and HP. Winter, Plasma Phys.Contr. Fusion **41** 471 (1999)

Relativistic many-body calculations of excitation energy and radiative transition probabilities for many-electron ions

U.I. Safronova and W.R. Johnson

[1] *Department of Physics, University of Notre Dame, IN 46556, USA*

Abstract. Energy levels, line strengths, oscillator strengths, and transition rates are calculated for electric dipole $nl_1nl_2[LSJ]$–$nl_3nl_4[L'S'J']$ transitions in Be- (n=2), Mg- (n=3), Zn- (n=4) and Sm- (n=5) like ions with nuclear charges ranging from $Z = N$ to 100 where N is number of electron in system.

1 Method and Discussion

This method is based on relativistic many-body perturbation theory (MBPT), agrees with MCDF calculations in lowest-order, includes all second-order correlation corrections, includes corrections from negative energy states, and is *gauge independent.*

Reduced matrix elements, oscillator strengths, and transition rates are calculated for electric dipole $nl_1nl_2[LSJ]$–$nl_3nl_4[L'S'J']$ transitions in Be- (n=2), Mg- (n=3), Zn- (n=4) and Sm- (n=5) like ions with nuclear charges ranging from $Z = N$ to 100 where N is number of electron in system. The MBPT including the Breit interaction, is used to evaluate retarded E1 matrix elements in length and velocity forms. The calculations start with a (N-2)- electron core Dirac-Fock potential and includes all possible two-electron configurations. We use first-order perturbation theory to obtain intermediate coupling coefficients and second-order MBPT to determine the matrix elements. Second-order MBPT energies are used to determine the transition energies used in the evaluation of transition probabilities.

Including negative energy contributions allowed us to obtain 0.1 - 1% agreement between results calculated in length and velocity forms. The negative-energy contributions are especially important for magnetic-dipole transitions as was demonstrated by investigation of transitions rates for all lines in $2l2l'$ configurations and some $2l3l'$ - $2l2l$ lines in Be-like ions with nuclear charges ranging from $Z = 4$ to 100. Comparison of our results is made with available theoretical and experimental data for the entire sequences.

Figure 1 compares rates for resonance and intercombination transitions in Be-, Mg-, and Zn-like ions. A comparison of fine-structure intervals for Be-like Kr^{32+}, Mg-like Kr^{20+}, and Zn-like Kr^{6+} is given in Table 1 and shows 1% agreement with recommended NIST data [1].

Acknowledgements. The work of WRJ was supported in part by National Science Foundation Grant No. PHY-95-13179. UIS acknowledges partial support by Grant No. B503968 from Lawrence Livermore National Laboratory.

References

[1] T. Shirai, K. Okazaki, and J. Sugar, J. Phys. Chem. Ref. Data **24**, 1577

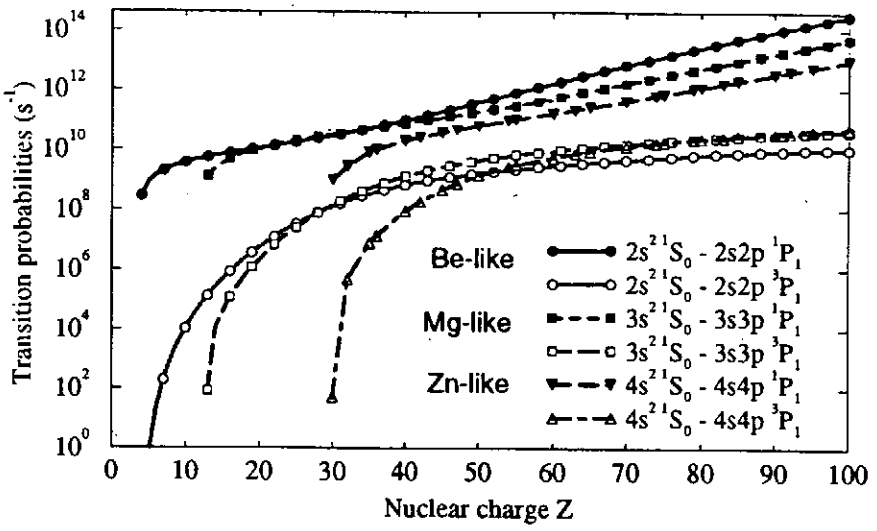

Figure 1: Transition probabilities $A(ns^2\ ^1S_0 - nsnp\ ^{1,3}P_1)$ as functions of Z.

Table 1: Fine-structure splitting of the $nlnl'\ ^3P$, ^3D, ^3F terms in cm^{-1} for Be-, Mg-, and Zn- like Kr (Kr^{32+}, Kr^{24+}, and Kr^{6+}), : MBPT and NIST data, Ref. [1].

		Be-like, n=2		Mg-like, n=3		Zn-like, n=4	
conf.	splitting	MBPT	NIST	MBPT	NIST	MBPT	NIST
$nsnp$	$^3P_1 - {}^3P_0$	83521	83270	22672	22702	2743	2705
$nsnp$	$^3P_2 - {}^3P_1$	424778	424670	78478	78432	6528	6458
np^2	$^3P_1 - {}^3P_0$	388916	389100	70983	71245	4535	4482
np^2	$^3P_2 - {}^3P_1$	81020	82600	90827	90940	8869	8776
$nsnd$	$^3D_2 - {}^3D_1$			7151	7280	428	444
$nsnd$	$^3D_3 - {}^3D_2$			11586	11648	493	699
$nsnd$	$^3F_3 - {}^3F_2$					187	170
$nsnd$	$^3F_4 - {}^3F_3$					257	270
$npnd$	$^3P_1 - {}^3P_0$			-79767	-80400		
$npnd$	$^3P_2 - {}^3P_1$			41393	42500		
$npnd$	$^3D_2 - {}^3D_1$			5531	5300		
$npnd$	$^3D_3 - {}^3D_2$			-11037	-11500		
$npnd$	$^3F_3 - {}^3F_2$			48719			
$npnd$	$^3F_4 - {}^3F_3$			69440	69300		
nd^2	$^3F_3 - {}^3F_2$					13361	13500
nd^2	$^3F_4 - {}^3F_3$					13653	14600

Magnetic-Dipole Transitions between Ground-State Fine-Structure Levels of Ti-like Highly Charged Ions

Daiji Kato[1], Tsunemitsu Fukami[2], Tohru Kinugawa[1], Shunsuke Ohtani[1,2], Hirofumi Watanabe[1], and Chikashi Yamada[1,2]

[1] *Cold Trapped Ions Project, JST, Axis-Chofu bldg. 3F 1-40-2, Tokyo 182-0024, Japan*
[2] *Institute for Laser Science, University of Electro-Communications, Tokyo 182-8585, Japan*

Abstract. Accurate wavelengths of magnetic-dipole (M1) transitions in ground-state fine-structure levels $(3d^4)_J$ of Titaniumlike highly charged ions were obtained with *ab-initio* calculations. The wavelengths of the transition between the lowest level in $(3d^4)_{J=3}$ and the lowest level in $(3d^4)_{J=2}$ are in excellent agreement with measurements for Sb^{29+}, I^{31+}, Xe^{32+}, Cs^{33+}, Ba^{34+}, Nd^{38+}, Gd^{42+} and Au^{57+} ions. Calculations of M1 transition probability with the same wavefunctions predicted a value to be about 10% smaller than a measurement for Xe^{32+} ion.

Visible lines emitted from Titaniumlike highly charged ions were observed with Tokyo Electron Beam Ion Trap (Tokyo-EBIT). These lines are due to forbidden transitions in ground-state fine-structure levels. The ground-state of the Titaniumlike ions has four 3d valence electrons, and consists of 34 fine-structure levels. The lowest five levels have J=0, 1, 2, 3, 4, and in the non-relativistic limit they form a LS coupled multiplet of ^{5}D state. At large atomic numbers, their energy levels separate into two groups; the lower one is essentially a j-j coupled state of $3d^4_{3/2}$ with J=0, and the upper four with J=1, 2, 3, 4 form a j-j coupled multiplet of $3d^3_{3/2}3d_{5/2}$. The visible lines observed with the Tokyo-EBIT are due to the forbidden transition from the J=3 level to the J=2 level. Calculations of wavelengths by Feldman *et al.* [1] with Multi-Configuration Dirac-Fock (MCDF) code of Desclaux have a discrepancy of about 5% from measurements for the same transition. Beck [2] improved calculations of the wavelengths, but the improved wavelengths are available only for some elements which were already measured. Present work complements available and accurate calculations of the wavelengths.

GRASP92 code [3] was used to implement the present calculations. A set of Dirac-Fock basis functions was optimized to both of the J=2 and the J=3 levels with the Extended-Optimal-Level (E/OL) mode of the MCDF method. Configuration space was divided to two parts: P and Q which are mutually orthogonal. The P space consists of a set of reference configurations, and the Q space represents the complementary part of the configuration space. The P space was represented by configurations of $3d^4$, $3s^{-1}3d^5$, $3s^{-2}3d^6$ and $3p^{-2}3d^6$, and the Q space was approximated by $3l^{-1}nl'(4 \le n \le 7; l' \le 6)$ and $3d^{-2}nln'l'(4 \le n, n' \le 6; l, l' \le 5)$. Numbers of the reference configurations with J=2 and 3 were 127 and 116, respectively, and those of the Q space configurations were 7529 and 8502, respectively. In a Hamiltonian matrix to be diagonalized, off-diagonal part of the Q space was set to be zero in the present calculations. By ignoring the off-diagonal part of the Q space matrix elements, a CPU-time required to calculate the Hamiltonian matrix elements showed a marked decrease while contributions from the Q space was correctly included in results as long as they could be treated as a perturbation. The lowest order QED corrections except for the self-energy correction were also included in total Hamiltonian matrix elements. The nuclear charge distribution was represented by the spherically symmetric Fermi model throughout the present calculations.

[1]E-mail : kato@hci.jst.go.jp

Table 1 shows some of the present calculations of the wavelengths with available measurements and other calculations. The present calculations are in excellent agreement with the measurements; discrepancies are within 1 % from all the available measurements. Table 2 shows the present calculation of the M1 transition probability for Xe^{32+} ion with an measurement by Serpa *et al.* [4]. About 10 % discrepancy remains in the M1 probability. Contribution of the electric-quadrupole (E2) transition is negligible; the E2 probability was calculated to be six orders of magnitude smaller than the M1 probability.

Z	Present calculation	Other calculations	Measurements
50 (Sn)	501.349103	483.53[1]	—
51 (Sb)	472.905701	—	470.24(3)[5]
53 (I)	430.705924	—	430.33(8)[5]
54 (Xe)	415.644516	395.25[1], 407.93[2]	413.88(7)[5], 413.94(20)[6]
55 (Cs)	402.846528	—	402.14(12)[5]
56 (Ba)	393.649494	386.63[2]	393.08(18)[5], 393.24(20)[6], 393.239(8)[7]
60 (Nd)	375.382776	355.68[1], 367.93[2]	375.3(2)[8]
64 (Gd)	371.202955	367.53[2]	371.3(2)[8]
70 (Yb)	367.670749	356.45[1]	—
74 (W)	362.568715	354.61[1]	—
79 (Au)	353.097066	—	353.2(2)[9]
82 (Pb)	346.272389	342.73[1]	—
92 (U)	320.898321	319.97[1]	—

Table 1: Wavelengths (nm) of transition between the lowest level in $(3d^4)_{J=3}$ and the lowest level in $(3d^4)_{J=2}$. Numbers in parentheses are experimental uncertainties, *e. g.* 393.08(18) represents 393.08 ± 0.18.

Present calculation	Other calculation	Measurement
419.56093	499[1]	465(30)[4]

Table 2: Magnetic-dipole transition probabilities (sec^{-1}) between the same levels as in Table 1 for Xe^{32+} ion. Number in a parenthesis is an experimental uncertainty, *e. g.* 465(30) represents 465 ± 30.

References

[1] U. Feldman, P. Indelicato and J. Sugar, *J. Opt. Soc. Am.* **B 8** (1991) 3

[2] D. R. Beck, *Phys. Rev.* **A 56** (1997) 2428

[3] F. A. Parpia, C. F. Fischer and I. P. Grant, *Comput. Phys. Commun.* **94** (1996) 249

[4] F. G. Serpa *et al.* , *Phys. Rev.* **A 55** (1997) 4196

[5] C. Yamada *et al.* in preparation

[6] C. A. Morgan *et al.* , *Phys. Rev. Lett.* **74** (1995) 1716

[7] D. J. Bieber *et al.* , *Phys. Scr.* **T73** (1997) 64

[8] F. G. Serpa *et al.* , *Phys. Rev.* **A 53** (1996) 2220

[9] E. Träbert *et al.* , *Phys. Scr.* **58** (1998) 599

Model electron density approximations for electron radiative transitions in the field of complex ions

Ludmila Bureyeva[1] and V.Lisitsa[2]

[1] *Scientific Council on Spectroscopy of the RAS, Leninski Pr., 53, Moscow, 117924, Russia*
[2] *RRC "Kurchatov Institute", Kurchatov Sq., 1, Moscow, 123182, Russia*

Abstract. Electron radiative transitions in the fields of complex ions with heavy cores are under consideration. Theoretical models based on model electron density approximations make it possible to express all types of radiative transitions in terms of atomic electron density distribution with a close connection between a radiated frequency and effective radius of radiation.

The present report is to combine together different kinds of approximations to construct universal theoretical models for free-free, free-bound and bound-bound electron transitions in the field of heavy ions with complex cores where the core polarization effects are of importance. The universal models are supposed to obtain scalings for radiation processes and corresponding results for plasma applications.

The models include equation for electron density normalization conditions, equation for imaginary part of atomic core polarization (or corresponding ionization cross section) in the frame of local plasma model approximation for many-electron atoms, dispersion (Kramers-Kroning) relationship for determination of the real part of atomic polarizability and the equation for the ratio of standard and polarization radiative transition probabilities. The set of these equations makes it possible to express intensities of polarization radiation processes in free-free [1], free-bound and bound-bound radiative transitions in terms of electron density distribution in a selfconsistent manner.

Alternative models for approximate determination of ionization cross sections are analyzed. They include in particular the large frequency (short time of atomic states evolution) approximation which makes it possible to express the atomic polarizabilities in terms of structure of wave function of atomic ground states.

The present approach is to combine together different kinds of approximations to construct universal theoretical models for all types of electron transitions in the field of heavy ions with complex cores where the core polarization effects are of importance. The universal models are supposed to obtain scalings for radiation processes and corresponding results for plasma applications.

The related problem of Lamb shift determination for multicharged ions with the help of precise measurements of Rydberg state energies in the limit of infinity values of principle quantum numbers n is also under consideration. The experiments on recombination of Li-like ions in ESR installation opens possibilities for determination of Rydberg state energies with high energy resolution [2].

The theoretical calculations are connected with estimations of polarization energy shifts of Rydberg atomic states due to their polarization interaction with Li-like ion core. The relativistic energy calculations for Li-like ions is well known in the limit of high nuclear charges with the help of Z^{-1} expansion method the corresponding polarization energy shift of Rydberg states can be expressed in terms of polarization quantum defect which is in its turn directly connected with energy difference of the core containing Lamb

[1]E-mail : bureyeva@sci.lebedev.ru

shifts. So the observations of polarization shifts open possibilities for direct determinations the Lamb shift.

Acknowledgements. This work was performed with the support of the Russian Ministry of Sciences and Technology (project "Theoretical spectroscopy of Rydberg states of atoms and ions") and the RFBR (project 98-02-16763).

References

[1] Tsytovich V N and Ojringel I M 1992 *Polarization Bremsstrahlung* New York Plenum
[2] Spies W et al. 1995 Nucl.Instr.Meth.B **98** 158

Atomic model based on semi-classical theory

Takeshi Nishikawa[1], Jun-ya Yano

Dep't of Electrical and Electronic Eng., Okayama University, Okayama 700-8530, Japan

Abstract. Parametric potential for semi-classical theory is discussed in detail. We found that a new set of scaling parameter for the theory is required if we want to use it for practical purposes.

Recently, semi-classical theory based on the Bohr-Sommerfeld quantum condition

$$\oint P(r)\, dr = \left(n - l - \frac{1}{2}\right)\pi$$

is interested simply because it can give fairly good numerical values with less computation time. In the inertial confinement fusion (ICF) research, the screened hydrogenic model (SHM) is still widely used. The SHM has been established for a long time and has been used for many problems. If we could use the semi-classical theory for the ICF research, we have to show that the theory can give energy levels as accurate as or more accurate than the SHM do.

Different from the SHM, the semi-classical theory requires the ionic potential. Since the potential would be the key issue for the energy level calculation, a lot of model potentials are proposed. Among them, parametrized potentials are convenient for practical purposes. But which of them are appropriate for the potential of the semi-classical theory? This is an important question and we need a prescription for that.

R. M. More suggests the parametric potential proposed by M. Klapisch is also useful for the semi-classical theory[1]. The charge distribution $\rho_n(r)$ is determined by the hydrogen-like wavefunction of quantum-mechanics.

$$\rho_n(r) = |\phi_n|^2 = \sum_n \frac{P_n}{4\pi r^2}\left({A_n}^2 r^{2n} e^{-2\alpha_n r}\right)$$

There is a scaling parameter α_n which determines the electronic charge distribution. P_n is a number of electron in the nth shell and A_n is a normalization constant of the charge distribution.

P. Pankratov proposed a parametric potential which uses the electronic charge distribution of the WKB wavefunction[2]. The distribution is determined by the semi-classical electron orbit.

$$\rho_n = \frac{{Q_n}^2}{4\pi^2 n^3 r^2 P_{nl}(r)}, \quad P_{nl}(r) = \sqrt{E_{nl} + V(r) - \frac{(l+1/2)^2}{2r^2}}$$

Therefore, resulting charge distribution has discontinuity at turning points. Although this effect is shielded on the resulting potential form since it is given as the solution of the Poisson equation. He reported that the potential gave fairly good numerical values for non-hydrogenic ions. For both charge distributions, the Poisson equation can be solved analytically.

[1]E-mail : nisikawa@elec.okayama-u.ac.jp

Though charge distribution is quite different between two models, we cannot see a clear difference on energy level calculation. But the semi-classical theory with the screened charge of the SHM cannot give better results than the SHM including l-splitting[3] do, especially for partially ionized high-z ions. A new set of screened charge (screening parameter) is required for practical purposes.

We found a difficulty on non-relativistic formulation of the semi-classical theory. To reproduce accurate energy level of He-like ground state by the non-relativistic framework of the semi-classical theory, $Q_n \sim 1.6255$ for He-like He ($Z = 2$), ~ 5.550 for He-like C ($Z = 6$), ~ 12.03 for He-like Al ($Z = 13$), ~ 18.3 for He-like Fe ($Z = 26$). Until for the case of He-like Al, Q_n's which reproduce exact values are reasonable, but for the case of He-like Fe, $Q_n = 18.3 \sim Z - 8$ is not. This is likely due to the spin-orbit interaction. Energy dependence on Q_n of semi-classical theory is much smaller than that of the SHM. In the semi-classical theory, $Q_n = 0$ is required to realize H-like energy levels. But in the SHM, $Q_n = Z$. A formulation based on the relativistic theory would be required.

We made a comparison study of dependence on the screened charge. Pankratov defined the screened charge

$$Q_n = Z - \sum_{n' \leq n} \sigma_{nn'} P_{n'}$$

in which the screening constants are those of More[4]. More's original definition for the screened charge is

$$Q_n = Z - \sum_{n' < n} \sigma_{nn'} P_{n'} - \frac{1}{2} \sigma_{nn} P_n$$

Instead, Pankratov introduced exchange potential

$$V(r) = \alpha \left(\frac{3}{\pi} \rho(r) \right)^{1/3}$$

His analysis shows that $\alpha = 0.5$ is the best. This term has a strange behavior because $V(r)$ is simply proportional to the charge density. In addition, we checked a definition by Lee, of which screening constant is given by Marchand *et al.*[5].

$$Q_n = Z - \sum_{n' < n} \sigma_{nn'} P_{n'} - \frac{1}{2} \sigma_{nn} \max(P_n, P_n - 1)$$

As a result, More's and Lee's definition have a similar tendency. For highly charged ions, More's definition of screened charge gives the best results. Only near neutral Pankratov's definition gives the best results.

Acknowledgements. One of the authors (T.N.) gives his thanks to Prof. R. M. More of the National Institute of Fusion Science for valuable discussions.

References

[1] R. M. More, Ann. Physics **207**, 282 (1991).
[2] P. Pankratov, Phys. Rev. A **46**, 5497 (1992).
[3] F. Perrot, Phys. Scripta **39**, 332 (1989).
[4] R. M. More, J. Quant. Spectrosc. Radiat. Transfer **27**, 345 (1982).
[5] R. Marchand and S. Caillé, Y. T. Lee, J. Quant. Spectrosc. Radiat. Transfer **43**, 149 (1990).

Detailed atomic model of short pulse laser pumped x-ray lasers

Akira Sasaki, Takayuki Utsumi, and Kengo Moribayashi

Advanced Photon Research Center, Kansai Research Establishment, Japan Atomic Energy Research Institute, Miiminami-cho Neyagawa-shi, Osaka 572-0019, Japan

Abstract. We have developed a detailed atomic model of electron collisional excited x-ray lasers. The set of levels should be considered in the calculation is investigated through comparison of results using different atomic models. Mixing of the population in the fine structure levels of $3d^9 4l$ configurations and the dielectronic recombination from the ground state of Ni-like ion to the Cu-like ion are found to cause significant reduction of the gain. The present model will constitute a useful tool to design and diagnose x-ray lasers.

1 Introduction

High gain and saturated output have been achieved in transient collisional x-ray lasers using Ni-like ions[1]. The gain is produced in non-LTE, short pulse laser produced plasmas, which is subject to rapid heating as well as expansion cooling. As the plasma is even difficult to diagnose, numerical simulation plays an importance role to realize efficient short wavelength lasers[2]. We have developed a new fast and accurate collisional radiative model. We combines the detailed atomic model for Ni-like ions[3], and super configuration model[4] for more than 10 ion stages below and above Ni-like to investigate the atomic kinetics of complex multiple charged ions of high-Z elements.

2 Development of the atomic model

The level diagram of the Ni-like collisional x-ray laser is shown in Fig.1. The most prevailing laser transition is from $3d^9 4d(3/2,3/2)J=0$ to $3d^9 4p(5/2,3/2)J=1$. The essential processes to obtain laser oscillation can be divided into two steps. Firstly, the target atom is ionized until the Ni-like ion becomes the most abundant in the plasma. Secondly, the Ni-like ion is excited to the upper laser level through strong collisional excitation. Both the ionization and excitation should be carried out efficiently to obtain high gain.

We designed the atomic model with which we can calculate the ion abundance of the plasma and soft x-ray gain in the short pulse laser irradiated plasmas. We included the fine

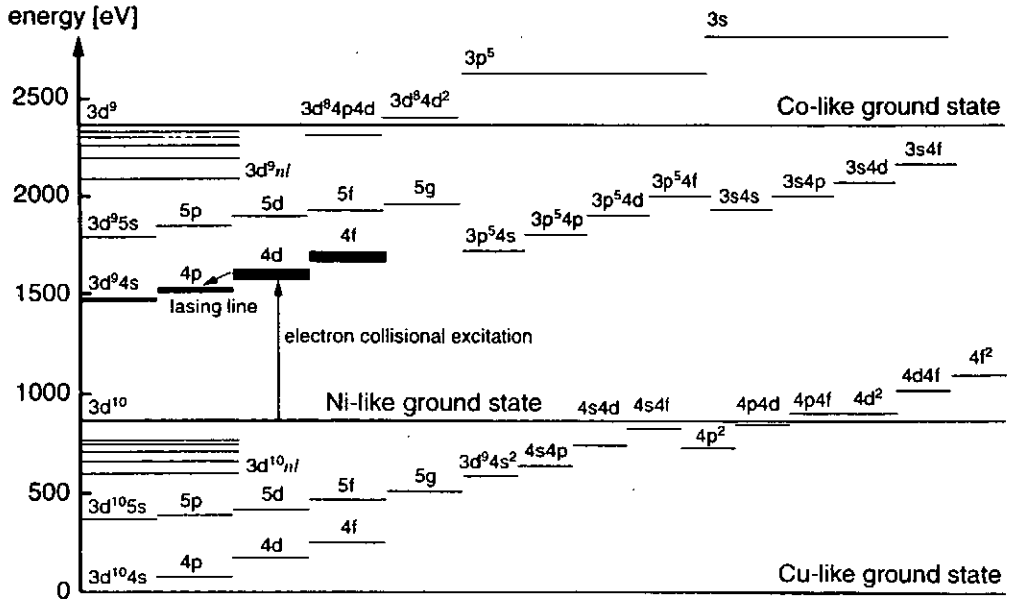

Figure 1: Level diagram of Ni-like Xe.

structure levels of $3d^9 4l$ configurations, because difference of the population between the levels in $3d^9 4p$ and $3d^9 4d$ produces the gain. On the other hand, number of M- and N-shell ions from Pd-like to Ar-like are included to calculate the ion abundance over a wide range of temperature and density. The energy levels and rate coefficients for the detailed levels are calculated by HULLAC. Configuration averaged levels are considered for highly excited states ($3d^9 5l$), multiple ($3d^8 4d4p$, $3d^8 4d^2$) and innershell ($3p^5 4l$, $3s4l$), as well as Cu-like highly excited states ($3d^9 4l4l'$). Higher excited states of Ni-like ions and levels belong to other ion stages are averaged over the shell for the principal(-*n*) or principal and orbital quantum number (-*nl*) of the electrons, where the level energy, collisional and radiative rates are calculated using an in-line atomic model based on the screened hydrogenic approximation.

3. Result and Discussion

Figure 2 shows (a) the steady-state soft x-ray gain in the $3d^9 4d(3/2,3/2)$ J=0 to $3d^9 4p(5/2,3/2)$ J=1 transition at λ=100Å and (b) abundance of the Ni-like Xe. Large gain coeffcient (>10/cm) is obtained only inside the limited parameter region where n_e=0.3-2 x10^{21}/cm^3, and T_e=250-300eV. At higher density and lower temperature, the gain decreases rapidly because the populations of levels within $3d^9 4p$ and $3d^9 4d$ configurations approaches thermal equilibrium through collisional mixing.

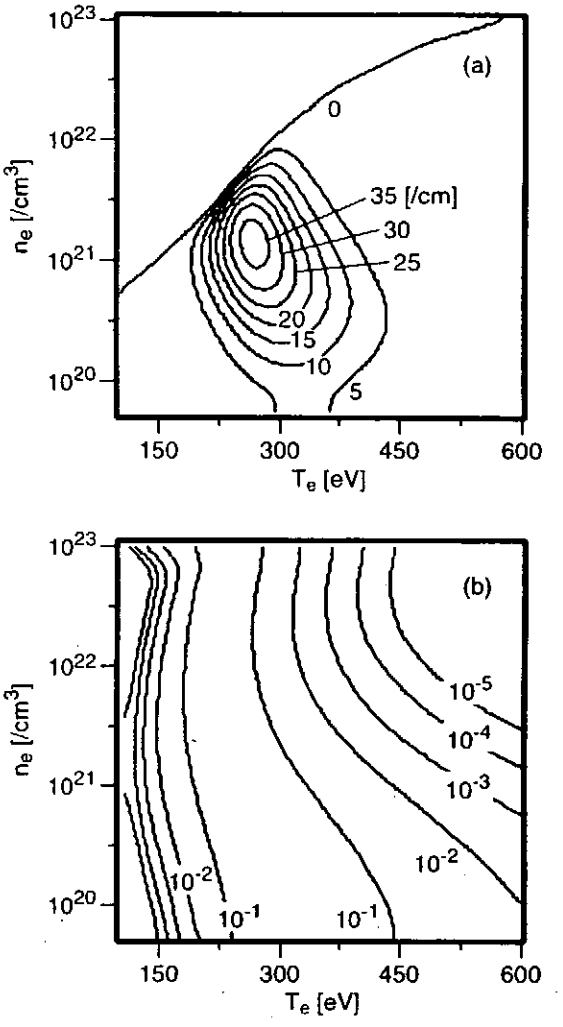

Figure 2: (a) Electron temperature and density dependence of the soft x-ray gain in 4d (3/2,3/2) J=0 - 4p (5/2,3/2) J=1 transition and (b) abundance of Ni-like ion of Xe.

Gain calculated with the fine structure levels in the $3d^9 4s$ and $3d^9 4f$ configurations is found to be almost half of that obtained without these levels. Furthermore, the dielectronic recombination through Cu-like $3d^9 4l4l'$ configurations causes similar decrease of gain due to reduced population of the Ni-like ground state[5]. The gain is found to be less sensitive to other highly excited states and multiple- and innershell excited states.

In conclusion, we have developed an atomic model of the collisional x-ray lasers. Influences of the major atomic processes to the gain have been investigated. This model will be applied to calculations of the gain of the Ni-like collisional x-ray lasers from Mo to W, and should be useful in analyzing atomic processes in other situations including high Z materials.

References

[1] J.Dunn, A.L.Osterheld, R.Shepherd, W.E.White, V.N.Shalyaptsev, and R.E.Stewart: Phys. Rev. Lett. **80**, 2825(1998).

[2] J.Nilsen: J. Opt. Soc. Am. **B14**, 1511 (1997).

[3] M.Klapisch, A.Bar-Shalom: J. Quant. Spectrosc. Radiat. Transf., **58**, 687 (1997).

[4] A.Bar-Shalom, J. Oreg, and M. Klapisch: Phys. Rev. **E56**, R70 (1997).

[5] J.Abdallah Jr., R.E.H.Clark, J.M.Peek, and C.J.Fontes, J. Quant. Spectrosc. Radiat. Transf.,**51**, 1(1994).

ELECTRON IMPACT EXCITATION OF Gd XXXVII

KM Aggarwal*, PH Norrington‖, KL Bell‖, FP Keenan*, GJ Pert† and SJ Rose‡
*Department of Pure & Applied Physics, Queen's University, Belfast BT7 1NN, UK
‖Dept. of Applied Maths. & Theoretical Physics, Queen's University, Belfast BT7 1NN, UK
†Department of Physics, York University, York YO10 5DD, UK
‡Plasma Physics Group, Rutherford Appleton Laboratory, Oxon OX11 0QX, UK

Abstract. Energy levels and radiative rates for transitions among the 107 fine-structure levels belonging to the $(1s^22s^22p^6)$ $3s^23p^63d^{10}$, $3s^23p^63d^94\ell$, $3s^23p^53d^{10}4\ell$, and $3s3p^63d^{10}4\ell$ configurations of Ni-like Gd XXXVII have been calculated using the GRASP code. The collision strengths have also been computed but among the lowest 59 levels only, at 4 representative energies of 200, 400, 600 and 800 Ryd, using the Dirac Atomic R-matrix code. Detailed calculations for collision strengths and rate coefficients are in progress.

Electron collisional excitation for nickel - like ions has been of interest for some time because of the large laser amplification in the EUV and X-ray regions. However, the only calculations available are those by Hagelstein[3] and Zhang et al[6]. The energy levels and radiative rates for such ions have been accurately determined by including the relativistic effects, which are highly important for the Ni-like ions, in the generation of the wavefunctions. Additionally, these workers have used the Distorted Wave (DW) code for the computations of collision strengths. However, the main deficiency of the available data is the exclusion of resonances in the computations of the rate coefficients, which are likely to significantly contribute, even at the high temperatures at which the data are required. Additionally, the data for collision strengths and rate coefficients available so far are for transitions from the ground state only, whereas for the reliable modelling of the plasmas results are also required for all transitions among the excited levels. Therefore, the aim of the present motivation is to explore the contribution of resonances to the collision strengths, and to report the collision data for all transitions.

We have used the fully relativistic GRASP code[2] to generate the wavefunctions, and the Dirac Atomic R-matrix Code[4] (DARC) to calculate the collision strengths Ω. While the radiative rates have been calculated among all the 107 levels, the corresponding calculations for Ω are restricted to lowest 59 levels because of computational limitations. Our energy levels and those of Zhang et al[6] differ by less than 2 eV, except for two levels, for which the present energies are higher by up to 5 eV. However, the orders of the levels is slightly different in a few instances. This is perhaps a direct consequence of the inclusion of larger CI by Zhang et al, as Hagelstein (who has used the same configurations as us) also obtains the same energy order. However, the level energies of Hagelstein are the highest among the three calculations, and differ up to 5 eV, corresponding to only $\sim 0.3\%$.

The length and velocity forms of our oscillator strengths for transitions from the ground level (see Table 1) agree to within 7%, which is highly satisfactory. Agreement between the present f- values and those of Zhang et al[6] ($n \leq 4$) is within 10% for all transitions, but the differences with their values obtained from GRASP are $\sim 20\%$ for one of the transitions ($3d^{10}\ {}^1S_0$ - $3s3p^63d^{10}4p_{1/2}\ {}^3P_1$). Incidentally, for this transition their f- value from the $n \leq 5$ calculations is the highest, whereas that of Hagelstein[3] is the lowest. Overall, the agreement among the various calculations is highly satisfactory.

The preliminary collision strengths obtained at 4 representative energies of 200, 400, 600 and 800 Ryd, are found to be in excellent agreement, for most of the transitions, with those available earlier. However, differences for some of the transitions, especially at energies above 400 Ryd, are of up to 25%, with the DW[6] Ω being invariably higher as seen in Figure 1. In particular, these differences are noticeable for the electric quadrupole (0^e - 2^e) transitions, which are forbidden in the jj coupling scheme. The Ω for these transitions are comparatively small, and the contribution (if any) of the higher neglected partial waves is negligible. Since a large range of partial waves ($J \leq 40.5$) has been included in order to obtain convergence, and relativistic (and CI, although limited) effects have also been included in both the target description and the scattering part, we do not see any apparent deficiency in our work and expect the results to be accurate to within 10%. It is expected that the rate coefficients will be different from those generated using previous data, due to the inclusion of resonances. To account for these, detailed calculations for collision strengths at a large number of electron energies are in progress. Further details about the calculations and numerical values of collision strengths can be found in our recent publication[1].

The work reported in this paper has been financed by the EPSRC of the UK.

Table 1. Transition probabilities (A) and oscillator strengths for transitions from the ground state of Ni-like Gd XXXVII. ($a \pm b \equiv a \times 10^b$). For level index see Reference 1. *a*: Present results [$n \leq 4$], *b*: Hagelstein[3] [$n \leq 4$], *c*: Sampson et al[5] [$n \leq 4$], *d*: Zhang et al[6] [$n \leq 4$], *e*: Zhang et al[6] [$n \leq 4$], *f*: Zhang et al[6] [$n \leq 5$].

I	J	$A^a(s^{-1})$	GRASP^a(L)	GRASP^a(V/L)	YODA^b	GRASP^c	DFS^d	GRASP^e	DFS^f
1	9	2.2692+12	0.1216	0.96	0.121	0.111	0.1137	0.1115	0.1148
1	12	5.8290+12	0.3043	0.96	0.305	0.273	0.2861	0.2754	0.2897
1	15	7.3293+11	0.0363	0.95	0.036	0.032	0.0338	0.0325	0.0343
1	37	1.0683+13	0.3895	0.97	0.384	0.362	0.3790	0.3696	0.3805
1	39	4.0189+11	0.0143	0.94	0.016	0.011	0.0138	0.0138	0.0141
1	49	3.0964+13	1.0728	0.93	1.090	1.059	1.0521	1.0284	1.0514
1	59	2.0337+14	6.6425	0.93	6.650	6.123	6.4721	6.3644	6.1322
1	65	1.4733+12	0.0437	0.98	0.047	0.043	0.0397	0.0401	0.0467
1	69	6.4126+11	0.0171	0.97	0.018	0.017	0.0166	0.0166	0.0161
1	74	4.2168+13	1.1042	0.97	1.110	1.060	1.1087	1.0640	1.0808
1	88	2.3947+13	0.5322	0.97	0.553	0.511	0.5282	0.5145	0.4276
1	93	1.7038+12	0.0367	1.00	0.020	0.035	0.0383	0.0307	0.0486
1	95	7.0288+12	0.1436	1.00	0.143	0.138	0.1446	0.1363	0.2618

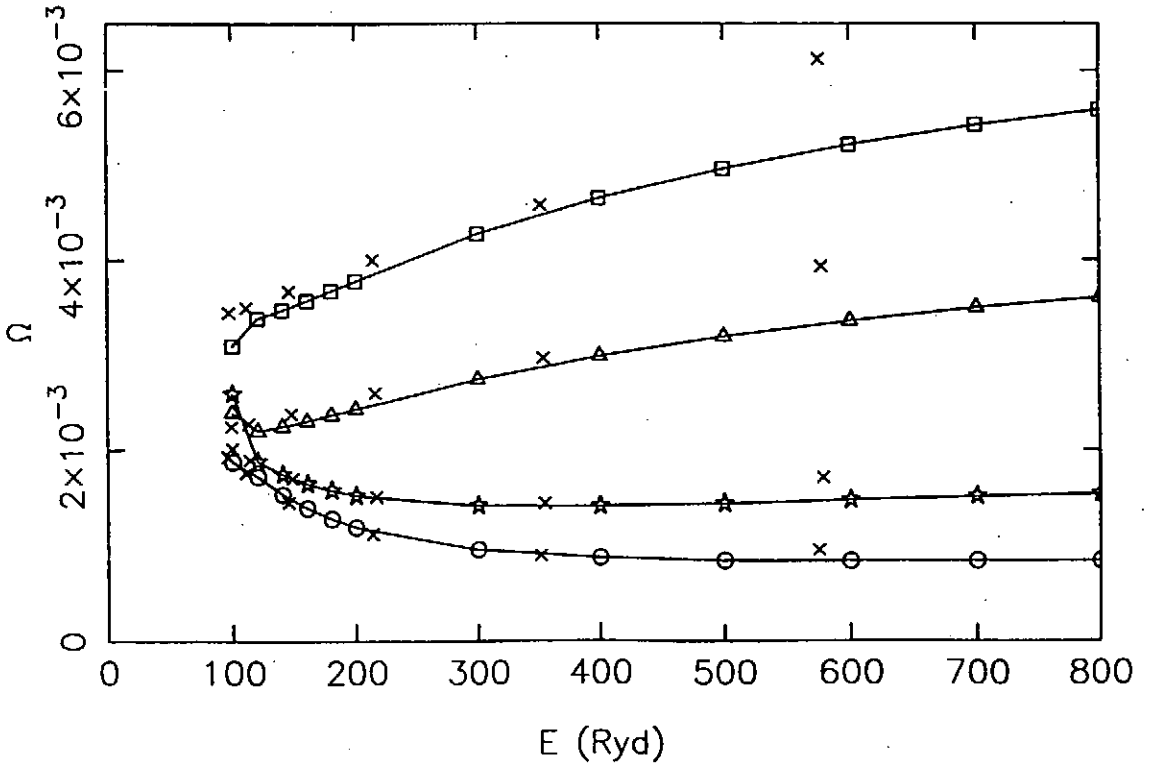

Figure 1: Comparison between present and Zhang et al (1991, crosses) total collision strengths for four transitions of Gd XXXVII at energies above thresholds (in Ryd). continuos line: present results, circles: 1-20, squares: 1-25, triangles: 1-30, and stars: 1-33 transition. For level index definition see Reference 1.

References

1. KM Aggarwal et al 1999 J.Phys. B32 - in press.
2. KG Dyall et al 1989 CPC 55 425
3. PL Hagelstein 1986 Phys. Rev. A34 874
4. PH Norrington and IP Grant 1999 CPC - in prep.
5. DH Sampson et al 1989 Phys. Rev. A40 604
6. HL Zhang et al 1991 ADNDT 48 91

ELECTRON IMPACT EXCITATION OF Fe XXI

K. M. Aggarwal and F. P. Keenan

Department of Pure and Applied Physics, The Queen's University of Belfast,
Belfast BT7 1NN, Northern Ireland, U. K.

Abstract. Collision strengths for transitions among the lowest 46 fine-structure levels belonging to the $(1s^2)$ $2s^22p^2$, $2s2p^3$, $2p^4$ and $2s^22p3\ell$ configurations of C-like Fe XXI have been calculated, at energies above thresholds in the range $80 \leq E \leq 480$ Ryd, using the Dirac Atomic R-matrix code. Configuration interaction as well as relativistic effects have been included while generating the wavefunctions from the GRASP code. Collision strengths for transitions among the lowest 5 levels are tabulated at 4 energies, and comparisons with other available values are shown for some of the transitions.

Iron is an abundant and important element in the solar corona and chromosphere, with an abundance of 7.51 on the scale log [H] = 12.0. Emission lines of Fe XXI have been observed in the X-ray and EUV regions of solar and astrophysical plasmas, and are also important in the studies of laser produced plasmas and magnetically confined controlled thermonuclear reactor research. Therefore, a number of workers in the past have studied its atomic parameters including oscillator strengths, collision strengths and rate coefficients. However, most of the calculations, especially for the last two parameters, have been confined to the transitions among the $(1s^2)$ $2s^22p^2$, $2s2p^3$ and $2p^4$ configurations. Bhatia et al[4] have calculated collision strengths Ω for transitions involving the levels of the $2s^22p3\ell$ configurations also. They have used the Distorted Wave (DW) code of University College London, and have reported their Ω at only one energy (90 Ryd). More recently, Zhang and Sampson[7,8] have performed more elaborate calculations for transitions among the $(1s^2)$ $2s^22p^2$, $2s2p^3$, $2p^4$, $2s^22p3\ell$, $2s2p^23\ell$ and $2p^33\ell$ configurations of C-like ions with $9 \leq Z \leq 54$ including Fe XXI. They have used the relativistic DW code but have calculated Ω at 6 energies above thresholds only. Clearly, they have neglected the resonances which dominate the threshold energy region, and whose contribution significantly enhances the values of excitation rate coefficients, especially for the forbidden transitions, as has already been demonstrated in our earlier work[1] on this ion, for transitions among the lowest 20 fine-structure levels among the $(1s^2)$ $2s^22p^2$, $2s2p^3$ and $2p^4$ configurations. In this paper we report similar data for Ω for transitions among the lowest 46 fine-structure levels belonging to the $(1s^2)$ $2s^22p^2$, $2s2p^3$, $2p^4$ and $2s^22p3\ell$ configurations of Fe XXI.

For generating the wavefunctions, we have used the fully relativistic GRASP code[5]. The energy levels and oscillator strengths have already been discussed in our earlier work[2]. For calculating Ω, we use the Dirac Atomic R-matrix Code[6] (DARC). The R-matrix boundary radius has been taken to be 2.0 au, and 20 continuum orbitals have been included for each channel angular momentum for the expansion of the wavefunction. This allows us to compute Ω up to an energy of 480 Ryd, more than sufficient for the calculations of excitation and deexcitation rate coefficients up to a temperature of 1.5×10^7 K. The maximum number of channels for a partial wave is 178, and the corresponding size of the Hamiltonian is 3574. It takes about 3 hours on the Cray (at Rutherford Appleton Laboratory) to diagonalise the matrix for one partial wave of one parity. In order to obtain the converged Ω at all energies and for all transitions, we have to include the contribution of all partial waves with $J \leq 36.5$. Clearly, this makes the calculations very time consuming, and in addition there is a problem of data handling from a large number of files, as the program (under the present limitations) cannot run for more than 10 partial waves at a time. Although Ω for most of the transitions have converged due to the inclusion of such a large range of partial waves, there are some allowed transitions for which even this large range is not sufficient for convergence. Therefore, to take account of this, we have included a "top-up", based on the sum rules.

At present Ω have been computed at energies above thresholds only, so that comparisons can be made with the available data. Detailed calculations in the threshold energy region, which is dominated by resonances, are in progress. Therefore, the excitation rate coefficients or equivalently the effective collision strengths, cannot yet be determined but will hopefully be available soon. In Table 1, we report Ω for transitions among the levels of the $1s^22s^22p^2$ configuration, at 4 energies of 100, 200, 300 and 400 Ryd. In Fig. 1 ($a-d$) we compare our Ω with those of Zhang & Sampson [7,8] for 4 transitions viz. (a) $2s^22p^2\ {}^3P_0$ - $2s2p^3\ {}^3D^o_1$, (b) $2s^22p^2\ {}^3P_0$ - $2s2p^3\ {}^3P^o_1$, (c) $2s^22p^2\ {}^3P_0$ - $2s^22p3d\ {}^3P^o_1$, and (d) $2s^22p^2\ {}^3P_0$ - $2s^22p3d\ {}^1P^o_1$. In general, the agreement between the present R-matrix and DW [4,7,8] collision strengths is satisfactory (within 20%) for transitions with $\Omega \geq 0.01$ (as seen in figures a and b). But for weaker transitions (as seen in figures c and d), the agreement between the two sets of Ω is within a factor of two only. Detailed discussion on these comparisons and Ω for other transitions can be found in our recent publication[3].

The work reported in this paper has been financed by the EPSRC of the UK.

Table 1. Collision strengths for transitions within the $1s^2 2s^2 2p^2$ configuration of Fe XXI.

Transition	E = 100	200	300	400 Ryd
$^3P_0$ - $^3P_1$	7.1013-3	3.6508-3	2.2101-3	1.4718-3
$^3P_0$ - $^3P_2$	1.1401-2	1.0554-2	1.0419-3	1.0459-2
$^3P_0$ - $^1D_2$	1.2312-3	6.1485-4	3.7961-4	2.6832-4
$^3P_0$ - $^1S_0$	1.5966-4	6.7908-5	3.6073-5	2.2063-5
$^3P_1$ - $^3P_2$	2.5676-2	1.9349-2	1.7004-2	1.5954-2
$^3P_1$ - $^1D_2$	1.2499-2	8.0616-3	6.3909-3	5.6173-3
$^3P_1$ - $^1S_0$	1.6812-3	7.7385-4	4.3214-4	2.7066-4
$^3P_2$ - $^1D_2$	3.5195-2	2.8188-2	2.5816-2	2.4844-2
$^3P_2$ - $^1S_0$	4.5389-3	3.7385-3	3.5403-3	3.4949-3
$^1D_2$ - $^1S_0$	2.1277-2	2.3324-2	2.4723-2	2.5687-2

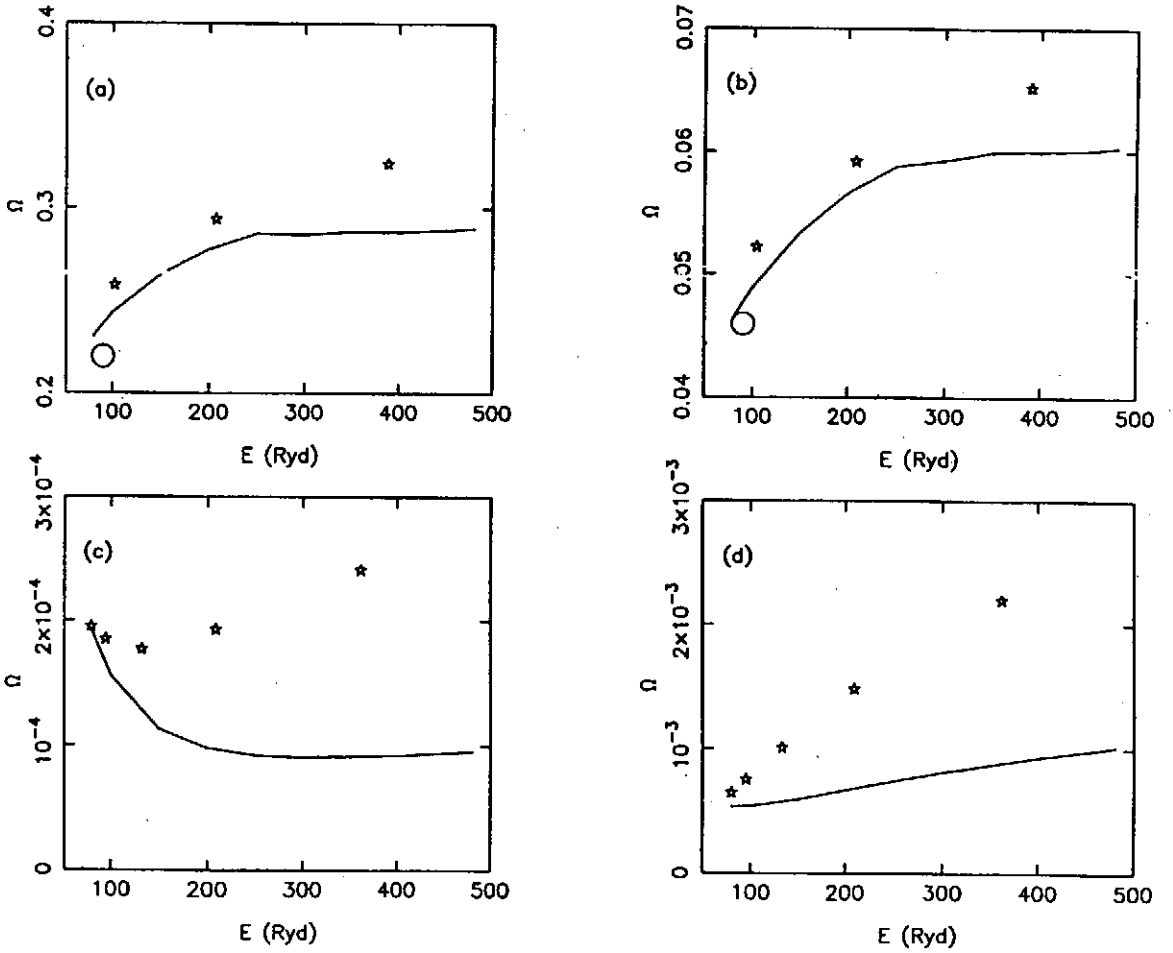

Figure 1. Comparison of present *R*-matrix (solid curve) and DW collision strengths of Zhang & Sampson (1996, 1997: stars) and Bhatia et al (1987: circle) for four transitions of Fe XXI: (*a*) $2s^2 2p^2\ ^3P_0$ - $2s2p^3\ ^3D^o_1$, (*b*) $2s^2 2p^2\ ^3P_0$ - $2s2p^3\ ^3P^o_1$, (*c*) $2s^2 2p^2\ ^3P_0$ - $2s^2 2p3d\ ^3P^o_1$, and (*d*) $2s^2 2p^2\ ^3P_0$ - $2s^2 2p3d\ ^1P^o_1$.

References

1. KM Aggarwal 1991 ApJS 77 677
2. KM Aggarwal et al 1997 ApJS 108 575
3. KM Aggarwal et al 1999 J.Phys. B32 3585
4. AK Bhatia et al 1987 ADNDT 36 453
5. KG Dyall et al 1989 CPC 55 425
6. PH Norrington PH & IP Grant 1999 CPC - in prep.
7. HL Zhang & DH Sampson 1996 ADNDT 63 275
8. HL Zhang & DH Sampson 1997 ADNDT 65 183

Doubly and triply excited states for different plasma sources

R. M. More[1] and U. I. Safronova [2]

[1] *National Institute for Fusion Science, Oroshi-cho, Toki, Gifu, 509-52, Japan*

[2] *Department of Physics, University of Notre Dame, IN 46556, USA*

Abstract. Autoionizing rates of doubly excited states as $nln'l'$ configurations with n=2-9 and n'=2-9 are calculated. Analytical expressions of decay amplitude for two-electron system are derived. Expressions for autoionizing rates with averaging over LS are obtained for many-electron systems. The n and l dependence of doubly excited states as $nln'l'$ configurations configurations are investigated.

1 Introduction

Knowledge of the basic characteristics of doubly and triply excited states is often required for solving modeling ionization phenomena in partially-ionized plasmas. These states are usually autoionizing and have a strong effect on the radiation spectrum and plasma ionization balance. Although they are sometimes omitted, autoionizing states should be included in evaluation of the equilibrium partition function for plasma LTE (local thermodynamic equilibrium). Their radiative decay is accompanied by formation of satellites to the resonance lines of ions of the next more highly charged ion and these satellites give information useful to the diagnostics of high-temperature plasma. Decay of autoionizing states can also affect population kinetics of excited levels and the radiation intensity of spectral lines.

In going from atoms to ions, a number of qualitatively new physical effects contribute to the formation of the autoionizing level spectrum. In highly charged ions as for the inner shells of heavy atoms, the role of relativistic inercombinations increases and the LS-coupling is a poor approximation. For ions of high Z the character of the spectrum changes significantly: the fine structure and hyperfine splitting increase and, in addition to dipole transitions, the higher multipoles become important. Because the autoionization decay rate is only weakly dependent on the nuclear charge Z, the rapid rise in the radiation width with Z can lead to qualitative changes in the behavior of cross-sections for various elementary processes in the vicinity of resonances.

2 Decay Amplitude

A decay amplitude [1]

$$\gamma(aLS, a_0klLS) = \sqrt{\frac{2\pi}{k}} \left\langle aLS \left| \sum_{i>j} 1/r_{ij} \right| a_0klLS \right\rangle \qquad (1)$$

for two-electron system could be described in the following form [2]

$$\gamma^{LS}(n_1l_1n_2l_2;n_4l_4kl_3)=(-1)^{L-(l_1-l_2+l_3-l_4)/2}\sqrt{(2l_1+1)(2l_2+1)(2l_3+1)(2l_4+1)}$$
$$\times\sqrt{\tfrac{2\pi}{k}}\eta(n_1l_1,n_2l_2)\sum_l(-1)^l\left[P_l(n_1l_1n_2l_2;n_4l_4kl_3)\begin{Bmatrix} l_1 & l_2 & L\\ l_4 & l_3 & l\end{Bmatrix}\right. \tag{2}$$
$$\left.+(-1)^S P_l(n_2l_2n_1l_1;n_4l_4kl_3)\begin{Bmatrix} l_2 & l_1 & L\\ l_4 & l_3 & l\end{Bmatrix}\right]$$

where

$$P_l(n_1l_1n_2l_2;n_4l_4kl_3)=R_l(n_1l_1n_2l_2;n_4l_4kl_3)(-1)^{l+(l_1+l_2+l_3+l_4)/2}\begin{pmatrix} l_1 & l_3 & l\\ 0 & 0 & 0\end{pmatrix}\begin{pmatrix} l_2 & l_4 & l\\ 0 & 0 & 0\end{pmatrix} \tag{3}$$

and $\eta(n_1l_1,n_2l_2)=1$ if $n_1l_1\neq n_2l_2$ and $\eta(n_1l_1,n_2l_2)=1/\sqrt{2}$ if $n_1l_1=n_2l_2$.
A radial integral for decay amplitude could be defined as

$$R_l(kl_1n_2l_2;n_4l_4n_3l_3)=\int_0^\infty r_1^2dr_1\int_0^\infty r_1^2dr_1\frac{r_<^l}{r_>^{l+1}}R_{kl_1}(r_1)R_{n_2l_2}(r_2)R_{n_4l_4}(r_2)R_{n_3l_3}(r_1) \tag{4}$$

where $R_{nl}(r)$ and $R_{kl}(r)$ are discrete and continuos hydrogenic functions. After simple, but cumbrous calculations, we can obtain for the radial integral [3]

$$R_l(kl_1n_2l_2;n_4l_4n_3l_3)=\sqrt{\tfrac{k}{1-e^{-2\pi/k}}}\frac{(2k)^{l_1}}{\sqrt{1(1+1/k^2)\cdots(l_1^2+1/k^2)}}$$
$$\times\prod_{i=2}^4\frac{1}{(2l_i+1)}\sqrt{\frac{(n_i+l_i)!}{(n_i-l_i-1)!}}\left(\frac{2}{n_i}\right)^{l_i}\frac{2}{(n_i)^2}$$
$$\times\sum_{m_i=0}^{n_i-l_i-1}\frac{(-1)^{m_i}}{m_i!}\frac{(2l_i+1)!(n_i-l_i-1)!}{(2l_i+1+m_i)!(n_i-l_i-1-m_i)!}\left(\frac{2}{n_i}\right)^{m_i} \tag{5}$$
$$\times\left(B_l^{(1)}(kl_1,n_il_im_i)+B_l^{(2)}(kl_1,n_il_im_i)\right)$$

where

$$B_l^{(1)}(kl_1,n_il_im_i)=\frac{(1-l+\bar{l})!(2+l+\bar{l}')!}{b^{3+l+\bar{l}'}(1/n_3-ik)^{1-l+\bar{l}}}\left(\frac{1/n_3^2+k^2}{4k^2}\right)^{l_1}e^{-\frac{2}{k}arctg(kn_3)}$$
$$\times\sum_{p=0}^{1-l+\bar{l}}\frac{1}{p!(1-l+\bar{l}-p)!}\frac{|\Gamma(l_1-n+1)|^2}{\Gamma(l_1-n+1-p)\Gamma(l_1+n+l-\bar{l}+p)}\left(\frac{1-in_3k}{1+in_3k}\right)^p \tag{6}$$

and

$$B_l^{(2)}(kl_1,n_il_im_i)=\left[\sum_{s=0}^{2+l+\bar{l}'}\frac{(2+l+\bar{l}')!}{(2+l+\bar{l}'-s)!}-\sum_{p=0}^{1-l+\bar{l}'}\frac{(1-l+\bar{l}')!}{(1-l+\bar{l}'-s)!}\right]$$
$$\times\frac{(3+\bar{l}+\bar{l}'-s)!(-1)^{l+\bar{l}'-s}}{b^{s+1}(L-ik)^{3+\bar{l}+\bar{l}'-s}}\left(\frac{L^2+k^2}{4k^2}\right)^{l_1}e^{-\frac{2}{k}arctg(\frac{k}{L})}$$
$$\times\sum_{p=0}^{3+\bar{l}+\bar{l}'-s}\frac{1}{p!(3+\bar{l}'+\bar{l}-s)!}\left(\frac{L-ik}{L+ik}\right)^p \tag{7}$$
$$\times\frac{|\Gamma(l_1-n+1)|^2}{\Gamma(l_1-n+1-p)\Gamma(l_1+n-2-\bar{l}'-\bar{l}+s+p)}$$

The following designations are used:

$$L=b+\frac{1}{n_3},\ b=\frac{1}{n_2}+\frac{1}{n_4},\ \bar{l}=l_1+l_3+m_3,\ \bar{l}'=l_2+l_4+m_2+m_4,\ n=\frac{1}{ik}$$

Let us demonstrate some examples.

$$R_0(ks1s;2s2s) = \frac{16}{3}\sqrt{\frac{k}{1-e^{-2\pi/k}}}\frac{3+2k^2}{(4+k^2)^4}e^{-\frac{2}{k}arctg\frac{k}{2}}$$

$$\begin{aligned} R_1(ks1s;2p2p) = \tfrac{16}{243}\sqrt{\tfrac{k}{1-e^{-2\pi/k}}}\Big\{\tfrac{32}{(1+4k^2)}e^{-\frac{2}{k}arctg2k} \\ -\tfrac{1013+432k^2+102k^4+8k^6}{(4+k^2)^4}e^{-\frac{2}{k}arctg\frac{k}{2}}\Big\} \end{aligned} \tag{8}$$

$$R_0(kp1s;2s2p) = -\frac{80}{3\sqrt{3}}\sqrt{\frac{k(1+k^2)}{1-e^{-2\pi/k}}}\frac{1}{(4+k^2)^4}e^{-\frac{2}{k}arctg\frac{k}{2}}$$

$$\begin{aligned} R_1(kp1s;2p2s) = -\tfrac{1024}{81\sqrt{3}}\sqrt{\tfrac{k(1+k^2)}{1-e^{-2\pi/k}}}\Big\{\tfrac{1}{(1+4k^2)}e^{-\frac{2}{k}arctg2k} \\ -\tfrac{811+864k^2+204k^4+16k^6}{(4+k^2)^4}e^{-\frac{2}{k}arctg\frac{k}{2}}\Big\} \end{aligned} \tag{9}$$

$$\begin{aligned} R_1(kd1s;2p2p) = -\tfrac{2048}{243}\sqrt{\tfrac{k(1+k^2)(4+k^2)}{1-e^{-2\pi/k}}}\Big\{\tfrac{1}{(1+4k^2)^2}e^{-\frac{2}{k}arctg2k} \\ -\tfrac{407+100k^2+8k^4}{128(4+k^2)^4}e^{-\frac{2}{k}arctg\frac{k}{2}}\Big\} \end{aligned} \tag{10}$$

3 Decay Amplitude for many-electron system

The matrix elements for autoionizing rate could be derived from the decay amplitude as

$$\Gamma^{LS}(n_1l_1n_2l_2;n_1'l_1'n_2'l_2' \,\|n_4l_4kl_3) = \gamma^{LS}(n_1l_1n_2l_2;n_4l_4kl_3)\gamma^{LS}(n_1'l_1'n_2'l_2';n_4l_4kl_3) \tag{11}$$

Sum over $n_4l_4kl_3[LS]$ gives us an autoionizing widths of LS term. We will not suppose to consider the mixing of configurations and $n_1l_1n_2l_2 = n_1'l_1'n_2'l_2'$ in this approximation. For this purpose the autoionizing rate could be calculated as

$$\Gamma^{LS}(n_1l_1n_2l_2\,\|n_4l_4kl_3) = \left[\gamma^{LS}(n_1l_1n_2l_2;n_4l_4kl_3)\right]^2 \tag{12}$$

For many applications, it is not important so detailed data with fixed LS. It is more convenient to use data averaging over LS. For this purpose, we have to consider the following expression:

$$A(n_1l_1n_2l_2\,\|n_4l_4kl_3) = \frac{\sum_{LS}(2L+1)(2S+1)\Gamma^{LS}(n_1l_1n_2l_2\,\|n_4l_4kl_3)}{\sum_{LS}(2L+1)(2S+1)} \tag{13}$$

The result of this averaging is [4, 5]

$$\begin{aligned} &A(n_1l_1n_2l_2;n_3l_3kl_4) \\ &= \tfrac{2\pi}{k}(2l_3+1)(2l_4+1)\sum_l\Big[\tfrac{1}{(2l+1)}P_l^2(n_1l_1n_2l_2;n_3l_3kl_4) + \tfrac{1}{(2l+1)}P_l^2(n_1l_1n_2l_2;kl_4n_3l_3) \\ &\quad -\sum_{l'}\begin{Bmatrix} l_1 & l_4 & l' \\ l_2 & l_3 & l \end{Bmatrix}P_l(n_1l_1n_2l_2;n_3l_3kl_4)P_{l'}(n_1l_1n_2l_2;kl_4n_3l_3)\Big] \end{aligned} \tag{14}$$

In the case of equivalent electrons, we obtain the following formula

$$A(n_1l_1n_1l_1;n_3l_3kl_4) = \frac{2\pi}{k}\frac{(4l_1+1)}{(2l_1+1)}(2l_3+1)(2l_4+1)\sum_l\left[\frac{2}{(2l+1)}P_l^2(n_1l_1n_2l_2;n_3l_3kl_4)\right.$$
$$\left.-\sum_{l'}\left\{\begin{array}{ccc} l_1 & l_4 & l' \\ l_1 & l_3 & l \end{array}\right\}P_l(n_1l_1n_1l_1;n_3l_3kl_4)P_{l'}(n_1l_1n_1l_1;kl_4n_3l_3)\right] \quad (15)$$

We investigate n and l dependence of doubly excited states as $nln'l'$ configurations and triply excited states as $2snlnl'$ configurations. Even after averaging over LSJ, we obtain 8116 kinds of $A(n_1l_1n_2l_2;n_3l_3kl_4)$ and $A(n_1l_1n_1l_2;n_3l_3kl_4)$ decay amplitudes with n=2-7 and n'=2-7. Including configurations with n, n' equal to 8 and 9 give additional decay amplitudes (10,340 and 20,799 respectively) for doubly excited states. We discuss systematic features which can help to compress enormous data-set.

The probability of an autoionizing decay in a general multi-electron ion could be derived from results for two-electron system:
$(n_1l_1)^{p_1}(n_2l_2)^{p_2}(n_3l_3)^{p_3}$ and $(n_1l_1)^{p_1}(n_2l_2)^{p_2}$.
We must study two types of transitions:

$$\begin{array}{c}(n_1l_1)^{p_1}(n_2l_2)^{p_2}(n_3l_3)^{p_3} \Rightarrow (n_1l_1)^{p_1-1}(n_2l_2)^{p_2-1}(n_3l_3)^{p_3+1}k\ell \\ (n_1l_1)^{p_1}(n_2l_2)^{p_2} \Rightarrow (n_1l_1)^{p_1-2}(n_2l_2)^{p_2+1}k\ell\end{array} \quad (16)$$

For LS averaged autoionization decay probabilities, one obtains in the two cases:

$$\begin{array}{c}\Gamma^N\left[(n_1l_1)^{p_1}(n_2l_2)^{p_2}(n_3l_3)^{p_3} \Rightarrow (n_1l_1)^{p_1-1}(n_2l_2)^{p_2-1}(n_3l_3)^{p_3+1}k\ell\right] \\ = p_1p_2\left(1-\frac{p_3}{N_3}\right)A(n_1l_1n_2l_2;n_3l_3k\ell)\,,\end{array} \quad (17)$$

and

$$\begin{array}{c}\Gamma^N\left[(n_1l_1)^{p_1}(n_2l_2)^{p_2} \Rightarrow (n_1l_1)^{p_1-2}(n_2l_2)^{p_2+1}k\ell\right] \\ = \frac{1}{2}p_1p_2\left(1-\frac{p_3}{N_3}\right)A(n_1l_1n_1l_1;n_2l_2k\ell)\end{array} \quad (18)$$

where $N_i = 2(2l_i+1)$ and where $A(n_1l_1n_2l_2;n_3l_3k\ell)$ is the two-electron decay probability.

Acknowledgements. The work of U.I.S. was supported by Grant No. B503968 from Lawrence Livermore National Laboratory.

References

[1] Safronova U I and Johnson W R 1998 *Physica Scripta* **58** 116
[2] Matulis A Yu and Safronova U I 1970 Optika and Spectroscopiya **28** 1077
[3] Matulis A Yu, Safronova U I and Tolmachev V V 1964 Litovskii Physic Sbornik **4** 331
[4] Aglitskii E V and Safronova U I 1985 *Spectroscopy of Autoionizing States of Multicharged Ions* (Energoatomlizdat, Moscow)
[5] Safronova U I 1989 Physica Scripta **T26** 59

Dielectronic recombination rate coefficients to the excited states of Be-like ions

I. Murakami[1], T. Kato[1] and U. I. Safronova[2]

[1] *National Institute for Fusion Science, Oroshi-cho, Toki, Gifu, 509-52, Japan*

[2] *Department of Physics, University of Notre Dame, IN 46556, USA*

Abstract.
Energy levels, radiative transition probabilities and auto-ionization rates for Be-like Ne (Ne^{6+}) including $1s^2 2pnl$ ($n = 2-9$, $l \leq 9$) and $1s^2 3l'nl$ ($n = 3-6$, $l \leq (n-1)$) states are calculated by using multi-configurational Hartree-Fock (Cowan code) method. Autoionizing levels above the $1s^2 2s$ and $1s^2 2p$ thresholds were considered and their contributions were computed.
The dielectronic recombination rate coefficients from Li-like Ne (Ne^{7+}) ions to Be-like Ne (Ne^{6+}) ions for excited states of Ne^{6+} ions are calculated. The values for the excited states with higher principal quantum number n are extrapolated and the total dielectronic recombination rate coefficients are derived.

1 Introduction

In order to solve the rate equation of the populations of ions, it is necessary to include many numbers of levels of the highly excited states for the case of dense plasma. The population of the excited states is determined mainly by the excitation from the ground state and the recombination from the ions at low densities. When the electron density increases, the excitation processes from the excited states become important. In the case of recombining plasma, the recombination to each excited state is necessary to estimate the populations of ions. These data are also necessary to obtain the effective recombination rate coefficients at high electron densities.

2 Results and Discussion

Dielectronic recombination (DR) is a process, which plays an important role in plasma dynamics, and also is a subject of interest in studies of atomic structure. An increase in ionic charge involves variation in the ratio between probabilities for radiative and radiationless decay of autoionization levels and between the amplitudes of direct and resonant transitions [1, 2]. The contribution of resonance processes, giving rise to autoionizing states of ions, to the total charged-particle inelastic scattering cross section also increases. A rapid increase in radiation width, ($\Gamma \sim Z^4$), with the autoionization probability being very weakly dependent on nuclear charge Z, may lead to qualitative changes in the behavior of the cross section for various elementary processes. In the theoretical descriptions of multiple charged ions a coherent treatment of the configuration mixing effects corresponding to quasi-degenerate states or states with almost coinciding energy becomes especially important [3, 4, 5].

This large interaction between 2s5g and 2p4f configurations for Be-like neon leads to the increasing of the DR rate coefficient for excited lines with n=5 comparison with the DR rate coefficient for excited lines with n=4 (see Table 1). As a result, we found the

Table 1: Mixing coefficients for even complex states with J=4 for Be-like Ne

		$(2s5g + 2p4f)$ mixing			
	$2s5g\ ^3G_4$	$2s5g\ ^1G_4$	$2p4f\ ^3F_4$	$2p4f\ ^3G_4$	$2p4f\ ^1G_4$
$2s5g\ ^3G_4$	0.77263	0.41272	-0.08765	-0.45275	-0.14060
$2s5g\ ^1G_4$	-0.40220	0.79768	0.06781	0.15665	-0.41536
$2p4f\ ^3G_4$	0.43466	0.20415	0.08621	0.81912	0.29415
$2p4f\ ^3F_4$	0.04346	-0.01046	0.98791	-0.14090	0.04597
$2p4f\ ^1G_4$	-0.22237	0.38820	-0.06479	-0.27562	0.84538
		$(2s6g + 2p5f)$ mixing			
	$2s6g\ ^3G_4$	$2s6g\ ^1G_4$	$2p5f\ ^3F_4$	$2p5f\ ^3G_4$	$2p5f\ ^1G_4$
$2s6g\ ^3G_4$	0.99719	0.03650	-0.01727	0.01731	-0.00845
$2s6g\ ^1G_4$	-0.03655	0.99695	0.01139	-0.00301	-0.02276
$2p5f\ ^3G_4$	0.02833	0.00074	0.59892	-0.61598	0.30438
$2p5f\ ^3F_4$	0.00026	-0.00023	0.66490	0.71704	0.19656
$2p5f\ ^1G_4$	-0.00138	0.03036	-0.36976	0.10021	0.76872

Table 2: Mixing coefficients for even complex states with J=3, 4 in Be-like O

		$(2s6g + 2p4f)$ mixing			
	$2s6g\ ^3G_3$	$2p4f\ ^1F_3$	$2s6d\ ^3D_3$	$2p4f\ ^3F_3$	$2p4f\ ^3G_3$
$2p4f\ ^3G$	0.69115	-0.03309	-0.01511	-0.05538	0.70575
$2p4f\ ^3F$	0.08354	-0.39332	-0.05070	0.91044	-0.02988
$2p4f\ ^3D$	-0.00082	-0.11131	0.06117	0.03844	0.00014
$2p4f\ ^1F$	0.11273	0.86023	0.30920	0.38268	-0.03337
$2s6g\ ^3G$	0.70204	-0.05830	-0.02813	-0.11411	-0.69953
		$(2s6g + 2p4f)$ mixing			
	$2s6g\ ^3G_4$	$2s6g\ ^1G_4$	$2p4f\ ^3F_4$	$2p4f\ ^3G_4$	$2p4f\ ^1G_4$
$2p4f\ ^3G$	0.65198	0.19352	-0.04232	0.69958	0.16240
$2p4f\ ^3F$	0.12172	-0.06901	0.98908	-0.03944	0.02135
$2p4f\ ^1G$	-0.20207	0.59252	0.04410	-0.14724	0.75046
$2s6g\ ^3G$	0.68069	0.23588	-0.09142	-0.67469	-0.12992
$2s6g\ ^1G$	-0.21535	0.73677	0.09703	0.14579	-0.61602
		$(2s7g + 2s8g + 2p5f)$ mixing			
	$2s7g\ ^3G_3$	$2s8g\ ^3G_3$	$2p5f\ ^1F_3$	$2p5f\ ^3F_3$	$2p5f\ ^3G_3$
$2p5f\ ^3G$	0.02574	0.03168	0.16178	0.32840	0.92867
$2p5f\ ^3F$	0.00010	0.00017	-0.33667	0.89119	-0.25599
$2p5f\ ^1F$	0.00012	0.00020	0.91029	0.29225	-0.26237
$2s7g\ ^3G$	0.99573	0.00256	-0.00423	-0.00857	-0.02385
$2s8g\ ^3G$	-0.00715	0.99856	-0.00522	-0.01056	-0.02920

rather complicated DR(n) distribution: DR(n=3) and DR(n=5) is large than DR(n=4) and DR(n=6). Increasing DR(n) for $n \geq 7$ should be explained by transitions from autoionizing states $2pnl$. The similar behavior, it was observed for Be-like oxygen, but the large interaction is happened between 2s6g and 2p4f configurations (see Table 2).

Acknowledgements. The work of U.I.S. was supported by Grant No. B503968 from Lawrence Livermore National Laboratory.

References

[1] Fujimoto T 1979 J. Phys. Soc. Japan, **47** 265.
[2] Hahn Y 1985 Advances in Atomic and Molecular Physics, **21** 123.
[3] Kato T, Safronova U I and Ohira M 1997 Phys. Scr. **55** 185.
[4] Moribayashi K and Kato T 1997 *NIFS-DATA* 41
[5] Murakami I, Kato T, and Safronova U I 1999 *NIFS-DATA* 50

Electron-impact single ionization of Kr^{10+} and Kr^{11+} ions

Huaguo Teng[1], Pierre Defrance[2], Chunyang Chen[3] and Yanseng Wang[3]

[1] *Institut für Kernphysik, Justus-Liebig-Universität Giessen, D-35392 Giessen, Germany*
[2] *Université catholique de Louvain, Institut de Physique, B-1348 Louvain-La-Neuve, Belgium*
[3] *Institute of Modern Physics, Fudan University, Shanghai 200433, P. R. China*

Abstract. Detailed distorted wave calculations are presented for electron-impact ionization of Kr^{10+} and Kr^{11+} ions and very good agreement with the experimental measurement are obtained.

1 Introduction

Electron-impact ionization of atomic ions is one of important fundamental process both in astrophysical and in fusion plasmas. Collisional data such as cross sections or rate coefficients is needed for understanding and diagnostics of these plasmas (Janev 1991; Müller 1991).

In fusion research, krypton has been recognised as a good candidate for spectrocopic diagnostics of the ion temperature in the plasma edge as well as in the central plsma. In addition, It will also contribute to the control of the radiative cooling of the plasma. However, for krypton ions of charge q higher than 8, both theoretical and experimental data are very scarce. The ionization cross sections of Kr^{10+} and Kr^{11+} ions have been measured by Oualim *et al.* (1995). Besides the direct ionization, they also observed the obvious structure which is attributed to excitation-autoionization process. Detailed theoretical calculation including both direct and excitation -autoionization processes has not been carried out because of the complicated open d-shell structures of these ions. The semi-empirical Lotz formula (Lotz 1968) that includes the direct ionization underestimates the total cross section by 40−50%. Thus, a detailed theoretical calculation including both direct ionization and excitation-autoionization processes is expected.

2 Computation

Calculations are carried out in the single configuration, distorted wave approximation for electron-impact ionization of Kr^{10+} and Kr^{11+} ions for incident electron energies ranging from above the threshold to 3000 eV. The direct ionization cross sections are calculated for the ejection of 3s, 3p and 3d subshell electrons from the ground configurations of both Kr^{10+} and Kr^{11+} ions; the excitation-autoionization cross section are calculated for the inner-shell excitations of the type 3p$\rightarrow$ nl ($n = 4, 5, 6; l = 0, 1, 2, 3$) and 3s$\rightarrow$ n$'l'$($n' = 4, 5; l' = 0, 1, 2, 3$). In addition, for Kr^{11+} ion, the inner-shell excitation of the type 2p$\rightarrow$ 3d, 4 l($l = 0, 1, 2, 3$) are also included. The radiative decay effect has been investigated by carrying out explicit calculations of the radiative rates and autoionizing rates and the effect has found to be negligible. The present results show that the direct process dominates the total ionization cross section for the two ions and contributions of excitation-autoionization are about 15% and 13% of the total cross sections for Kr^{10+}

[1]E-mail :huaguo.teng@strz.uni-giessen.de

and Kr^{11+} ions, respectively. The present results are in very good agreement with the experimental measurement of Oualim *et al.* (1995).

Acknowledgements. Support from the Giessen DFG-Graduiertenkolleg *Theoretische und experimentelle Schwerionenphysik* is gratefully acknowledged.

References

[1] Janev R K 1991 *Physica Scripta* **T37**, 5
[2] Müller A 1991 *Physica Scripta* **T37**, 14
[3] Oualim E M, Duponchelle M, and Defrance P 1995 *Nucl. Ins. Methods in Phys. Res.* **B98** 150
[4] Lotz W 1968 *Z. Phys.* **216** 205

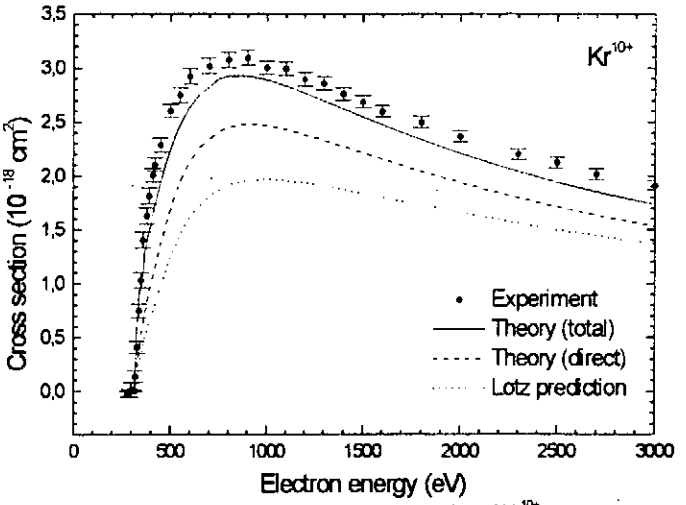

Figure 1. Electron-impact ionization of Kr^{10+}

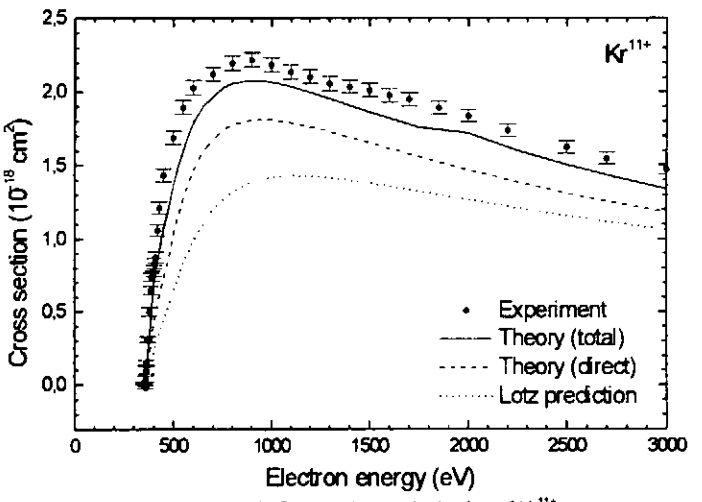

Figure 2. Electron-impact ionization of Kr^{11+}

Differential Ionization Cross Sections for Rare Gases*

Yong-Ki Kim,[1] Walter R. Johnson,[2] and M. Eugene Rudd[3]

[1] National Inst. of Standards & Technology, Gaithersburg, MD 20899-8423, U.S.A.
[2] Dept. of Physics, Univ. of Notre Dame, Notre Dame, IN 46556, U.S.A.
[3] Dept. of Physics & Astronomy, Univ. of Nebraska, Lincoln, NE 68588-0111, U.S.A.
* Work supported in part by US DOE and NSF.

The Binary-Encounter-Dipole (BED) model [1] is a theory for the differential ionization cross section, $d\sigma/dW$, W being the secondary electron energy. The model requires realistic continuum dipole oscillator strength, df/dW, to obtain reliable $d\sigma/dW$, though hydrogenic df/dW can be used to obtain accurate total ionization cross section, $\sigma_{ion} = \int (d\sigma/dW)dW$, for some atoms and many molecules and radicals.

The differential cross section $d\sigma/dW$ and the integrated cross section σ_{ion} per orbital based on the BED model [1] are given by

$$\frac{d\sigma(W,T)}{dW} = \frac{S}{B(t+u+1)}\left\{\frac{(N_i/N)-2}{t+1}\left(\frac{1}{w+1}+\frac{1}{t-w}\right)\right.$$

$$\left.+[2-(N_i/N)]\left[\frac{1}{(w+1)^2}+\frac{1}{(t-w)^2}\right]+\frac{\ln t}{N(w+1)}\frac{df(w)}{dw}\right\},$$

$$\sigma_{ion}(t) = \frac{S}{t+u+1}\left[D(t)\ln t+\left(2-\frac{N_i}{N}\right)\left(1-\frac{1}{t}-\frac{\ln t}{t+1}\right)\right],$$

with

$$D(t) = \frac{1}{N}\int_0^{(t-1)/2}\frac{1}{w+1}\frac{df(w)}{dw}dw,$$

$$N_i = \int_0^{\infty}\frac{df(w)}{dw}dw.$$

where T is the incident electron energy, B is the orbital binding energy, U is the orbital kinetic energy, N is the orbital electron occupation number, t=T/B, u=U/B, w=W/B, $S=4\pi a_0^2 N(R/B)^2$, $a_0=0.529$ Å, R=13.61 eV.

We used the relativistic random phase approximation (RRPA) [2] to calculate df/dw for rare gases. To facilitate the integration in D(t) above, the RRPA df/dw for He was fitted to a power series $df/dw = ay^3+by^4+cy^5+dy^6$, where y=B/(W+B). For He, the fitting coefficients are: a=8.24012, b=-10.4769, c=3.96496, and d=-0.0445976.

The BED $d\sigma/dw$ for He with the RRPA df/dw leads to σ_{ion} for He within ±5% of reliable experiments from the threshold to T=1 keV (Fig. 1). The BED $d\sigma/dW$ for He at T=100 eV [3] is compared to available experiments in Fig. 2. Similar procedure for Ne leads to σ_{ion} within ±5% of experiments for T=50-500 eV [4].

Conclusion

1. When reliable df/dw is available, the BED model can provide accurate $d\sigma/dW$ for small atoms. The differential and integration ionization cross sections for He based on

the BED model and df/dw from the RRPA are accurate to $\pm 5\%$, and can serve as standard cross sections.

2. For multishell atoms, such as Ar, df/dw from RRPA may not be sufficient to get reliable $d\sigma/dW$ and σ_{ion} because of inter-orbital interference in the non-dipole part of the cross sections.

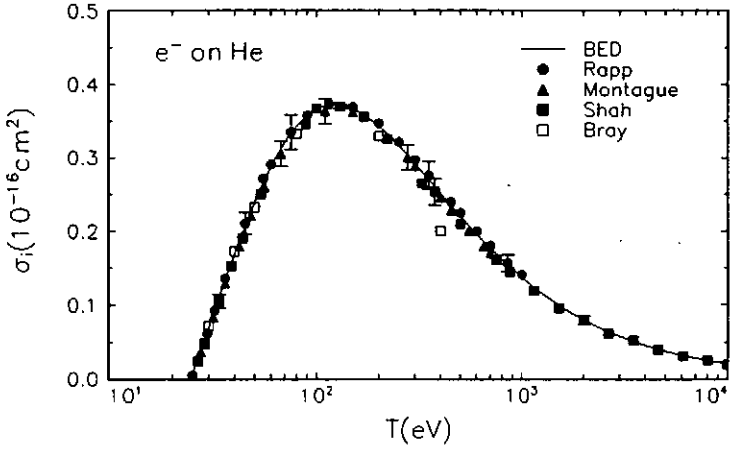

Fig. 1. σ_{ion} of He. Solid curve, BED theory; circles, experimental data by Rapp and Englander-Golden [5]; triangles, data by Montague et al. [6]; filled squares, data by Shah et al. [7]; open squares, convergent close-coupling theory by Bray and Fursa [8].

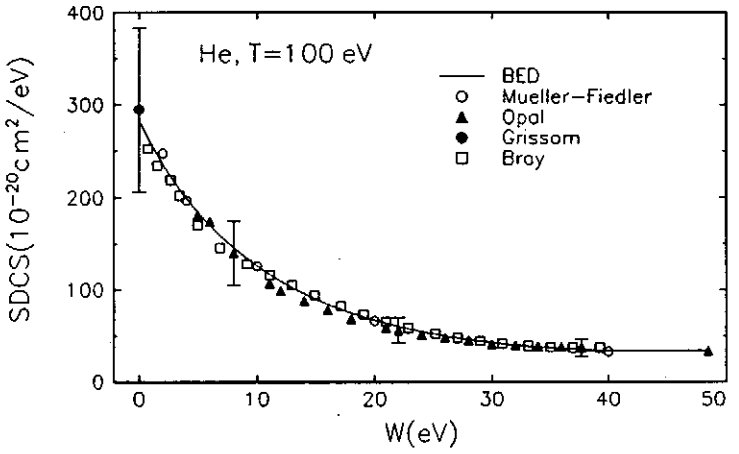

Fig. 2. $d\sigma/dW$ of He at T=100 eV. Solid curve, BED theory; open circles, experimental data by Müller-Fiedler et al. [9]; triangles, data by Opal. et al. [10]; filled circle, data by Grissom et al. [11]; squares, convergent close coupling theory by Fursa and Bray [12].

References

[1] Y.-K. Kim and M.E. Rudd, Phys. Rev. A **59**, 3954 (1994).

[2] K.-N. Huang, W.R. Johnson, and K.T. Cheng, At. Data Nucl. Data Tables **26**, 33 (1981), and references therein.

[3] Y.-K. Kim, W.R. Johnson, and M.E. Rudd, to be published (He).

[4] Y.-K. Kim, H. Nishimura, W.R. Johnson, and M.E. Rudd, to be published (Ne).

[5] D. Rapp and P. Englander-Golden, J. Chem. Phys. **43**, 1464 (1965).

[6] R. G. Montague, M. F. A. Harrison, and A. C. H. Smith, J. Phys. B **17**, 3295 (1984).

[7] M. B. Shah, D. S. Elliot, P. McCallion, and H. B. Gilbody, J. Phys. B **21**, 2751 (1988).

[8] I. Bray and D. V. Fursa, Phys. Rev. Lett. **76**, 2674 (1996).

[9] R. Müller-Fiedler, K. Jung, and H. Ehrhardt, J. Phys. B **19**, 1211 (1986).

[10] C. B. Opal, E. C. Beaty, and W. K. Peterson, At. Data, **4**, 209 (1972).

[11] J. T. Grissom, R. N. Compton, and W. R. Garret, Phys. Rev. **6**, 977 (1972).

[12] D. V. Fursa and I. Bray, Phys. Rev. A **52**, 1279 (1995).

Relativistic theory of electron-impact excitation of highly-charged ions

Takashi Kagawa and Takako Kawasaki
Department of Physics, Nara Women's University, Nara 630-8506, Japan

Recently there has been growing interest in the electron-impact excitation of ions to specific magnetic sublevels since the polarization of a radiation emitted from an excited ion has been observed in the electron-atom collision experiment with a spin polarized electron beam and in the spectroscopic study of emissions from laboratory plasmas. [1]

In the theoretical treatment of the excitation processes of HCI's, various relativistic effects on the energies and wavefunctions of a target ion, the interaction between a free electron and a target one, and continuum wavefunctions for a free electron must sufficiently be taken into account in the theory. However, it has been proved that rigorous fully-relativistic treatment of interaction between a free and a bound atomic electrons based on the quantum electrodynamics (QED) requires formidable tasks in the evaluation of a great many number of S matrices using the many-body perturbation theory. Therefore the Born approximation with use of a semi-relativistic two-electron interaction operator such as the Coulomb-Breit interaction one has been developed as one of useful and practical ways in relativistic treatment of electron-atom collision processes. In the Born procedure for the evaluation of electron-impact excitation cross sections of atomic systems one can easily extend various nonrelativistic approximation methods to relativistic cases. Along this line, Carse and Walker [2] and Walker [3] have given relativistic cross sections for electron-impact excitation of hydrogenic atoms with the relativistic Coulomb Born (RCB) and relativistic distorted-wave Born (RDWB) approximations. Zhang et.al. and his group [4, 5, 6] have developed a computer code to calculate the RDWB cross sections for the electron-impact excitation to a specific magnetic sublevels of HCI's.

However, few relativistic calculations of cross sections for electron-atom scattering processes such as the excitation between magnetic levels have so far been reported except that of Zhang et. al.. In this case accuracy of the calculated cross sections could also be sensitive to wavefunctions used for a target atomic system. So it is desiable to examine the reliability and limitation of the relativistic Born approximation which can be a starting point to improve the relativistic scattering theory for various inelastic processes in atomic systems with wide range of incident-electron energies.

In this work, we give a formula for the RDWB electron-impact excitation cross section of atomic systems developed based on the non-relativistic DWB theory and make a computer code to calculate RDWB cross sections, where the relativistic configuration interaction (RCI) method [7] is used to obtain wavefunctions for a target atomic system.

We carry out some test calculations for the electron-impact excitation cross sections and collision strengths of H-like and He-like systems to see an accuracy of our numerical method adopted in making a code. Calculated results of RCB cross sections for H-like atoms and integrated RDWB collision strengths for He-like iron are compared with other theoretical ones in Table 1-3, where only the Coulomb interaction between two electrons are taken into account in the T matrix. Our results are in good agreement with those of Zhang et. al. in all cases listed here. Improvement of our code to obtain accurate cross sections in various HCI's is now in progress.

[1] Proceedings of the Japan-US Workshop and the International Seminar on Plasma Polarization Spectroscopy, Jan. 1998, Kyoto, Eds. T. Fujimoto and P. Beiersdorfer, Research Report of National Institute for Fusion Science, NIFS-PROC Vol. **37**.

[2] G. D. Carse and D W Walker, J. Phys. B6,2529 (1973).
[3] D.W. Walker , J. Phys. B7,97 (1974).
[4] H. L. Zhang, D. H.Sampson and R. E. H. Clark, Phys. Rev. A42,198 (1990).
[5] M. K. Inal, H. L. Zhang and D. H.Sampson, Phys. Rev. A46,2449 (1992).
[6] C. J. Fontes, H. L. Zhang and D. H.Sampson, Phys. Rev. A59,295 (1999).
[7] T. Kagawa, Y. Honda and S. Kiyokawa, Phys. Rev A44, 7092 (1991).

Table 1. Comparison of RCB n=1-2 excitation cross sections of H-like atoms by electron impact with the impact energy of the ionization one, that is, $E_i = |E_{1s}|$.

	Z=50			Z=100		
Transition	This work	Walker	Zhang	This work	Walker	Zhang
$1s-2s$	0.4439	0.4445	0.4438	0.8273	0.8304	0.8269
$1s-2p_{1/2}$	0.5537	0.5536	0.5536	0.5222	0.5228	
$1s-2p_{3/2}$	1.0124	1.0133	1.0133	0.5968	0.5974	0.5940

Table 2. RDWB collision strengths for electron-impact excitation from the ground state of $(1s)^2(1^1S_0)$ to the $1s2l$ excited states in He-like iron (Z=26) with scattered electron energy $E_f = 70$eV.

	Collision strengths	
Transition	This work	Zhang et.al.
$(1s2s)_{J=0}[2^1S_0]$	7.295	7.687
$(1s2s)_{J=1}[2^3S_1]$	3.717	3.626
$(1s2p)_{J=0}[2^3P_0]$	2.512	2.267
$(1s2p)_{J=1}[2^3P_1]$	7.915	8.079
$(1s2p)_{J=2}[2^3P_2]$	11.420	10.650
$(1s2p)_{J=1}[2^1P_1]$	21.790	21.220

Table 3. Partial RDWB collision strengths for electron impact excitation from the ground state of $(1s)^2[1^1S_0]$ to magnetic sublevels of M_f in the $(1s2s)[2^3S_1]$ state in He-like iron with various incident electron energies in Rydberg. Upper and lower values of the collision strength for each M_f are obtained by us and Fontes et. al. [6], respectively and excitation energies are given as E_{ex} and those in the parentheses in reference [6].

	E_i(Ry)				
M_f	550	700	900	1200	2000
$(1s2s)_{J=0}[2^3S_1]$	$E_{ex} = 487.87(487.75)$(Ry)				
0	1.101	0.8420	0.6123	0.4060	0.1888
	1.078	0.8206	0.5995	0.4051	0.1880
1	1.110	0.8422	0.6126	0.4146	0.1889
	1.078	0.8206	0.5995	0.4051	0.1881

Relativistic calculation of electron impact excitation rate coefficients in helium-like ions

Eiji Kimura[1] , Shinobu Nakazaki [1], Keith A. Berrington [2], and Patrick H. Norrington [3]

[1] *Department of Materials Science, Faculty of Engineering, Miyazaki University, Miyazaki 889-2192, Japan*

[2] *School of Science and Mathematics, Sheffield Hallam University, Sheffield S1 1WB, UK*

[3] *Department of Applied Mathematics and Theoretical Physics, Queen's University, Belfast BT7 1NN, UK*

Abstract. Collision strengths for electron impact excitation of He-like ions (S^{14+}, Ca^{18+} and Fe^{24+}) are calculated using the Dirac Atomic R-matrix Code (DARC) which has been developed mainly by Norrington and Grant. The lowest 17 states and the lowest 31 states are included in the calculation. Rate coefficients are obtained for transitions from the ground $1s^2\ ^1S_0$ state to the fine-structure levels of all excited states of $1s2\ell$ ($\ell = 0, 1$) and $1s3\ell$ ($\ell = 0, 1, 2$) configurations. The resulting values are compared with the results of previous calculations.

1 Introduction

The intensities of emission lines arising from transitions in He-like ions are frequently used to determine the electron temperature and density of a plasma, such as solar corona and fusion plasmas. To interpret the observed data, the knowledge of the electron impact excitation of the He-like ions are required. For very highly charged ions, it is necessary to consider the relativistic effects.

Zhang and Sampson [1] obtained rate coefficients for excitation of He-like ions with nuclear charge number Z in the range $8 \leq Z \leq 74$ by electron impact in the Coulomb-Born approximation with including the electron exchange and resonance effects approximately. Pradhan [2] reported the rate coefficients for Ca^{18+} and Fe^{24+} using the collision strength calculated by the distorted wave and the close-coupling approximation. They included intermediate coupling and resonance effects. Keenan et al. [3] estimated the rate coefficients for He-like ions between F^{7+} and Mn^{23+} with an interpolation of the rate coefficients for other He-like ions (O^{6+}, Mg^{10+}, Ca^{18+} and Fe^{24+}). Kimura et al. [4] made the calculation with the R-matrix method and with term-coupling coefficients to include the intermediate coupling effects. They obtained the fine-structure collision strengths of S^{14+}.

The most accurate treatment of the relativistic effects for the electron-ion scattering problem is done by solving the Dirac equation (Norrington and Grant [5]). In the present paper, we report a theoretical systematic study of He-like ions (S^{14+}, Ca^{18+} and Fe^{24+}) with use of the R-matrix method based on the Dirac equation.

2 Theory

Two R-matrix calculations are carried out. The first includes only the $n = 1$, 2 and 3 orbitals with 17 corresponding target states. The other is a more complete calculation including the $n = 4$ orbitals with 31 corresponding target states. We use the computer

[1] E-mail : eiji@phys.miyazaki-u.ac.jp

code DARC (Dirac Atomic R-matrix Code) of Norrington and Grant to calculate the R-matrix on the boundary of a sphere. Integral cross sections are calculated with the partial cross sections summed up to $J = J_{max}$ ($J_{max} = \frac{39}{2}$ ($\frac{21}{2}$) for the 17 (31) states calculation), when necessary, contributions from the partial waves higher than $J = J_{max}$ are taken into account with an extrapolation.

3 Results and Discussions

Effective collision strengths are calculated for transitions from the ground $1s^2\ ^1S_0$ state to all fine-structure levels of the excited states of $1s2\ell$ ($\ell = 0, 1$) and $1s3\ell$ ($\ell = 0, 1, 2$) configurations. They are obtained for a temperature range $T_e = (1 \times 10^6 - 1 \times 10^8)$ K for S^{14+}, $(1 \times 10^{6.2} - 1 \times 10^{8.2})$ K for Ca^{18+} and $(1 \times 10^{6.8} - 1 \times 10^{8.8})$ K for Fe^{24+}. This is the range of the largest fractional abundances of S^{14+}, Ca^{18+} and Fe^{24+}, if they are in ionization equilibrium (Arnaud and Rothenflug [6]).

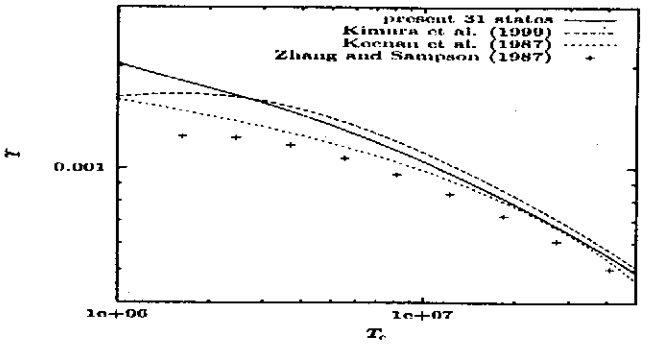

Figure 1: The effective collision strengths Υ for the $1s^2\ ^1S_0$ - $1s2s\ ^3S_1$ excitation of S^{14+}.

A comparison is made between the present result and the previous data. Figures 1 shows a typical comparison between the present results and the previous data for the excitation of the levels $1s2s\ ^3S_1$. The present result agrees with the previous data, except in the region of low temperature. The difference from data of Keenan et al. [3] and Zhang and Sampson [1] at low temperature is due to the resonance effects. The present calculation takes into account the states with $n \leq 4$. The discrepancy between the present results and those of Kimura et al. [4] may be ascribed to the difference in the resonance structure in the two sets of collision strength. Kimura et al. [4] carried out a semi-relativistic calculation by using the LS coupling R-matrix method with term-coupling coefficients. The present calculation is based on the fully relativistic theory. As for the resonance structure, therefore, the present calculation should be more accurate.

References

[1] Zhang H and Sampson D H 1987 Astrophys. J. Suppl. **63** 487

[2] Pradhan A K 1985 Astrophys. J. Suppl. **59** 183

[3] Keenan F P, McCann S M, and Kingston A E 1987 Physica Scripta. **35** 432

[4] Kimura E, Nakazaki S, Eissner W B, and Itikawa Y 1999 Astron. Astrophys. in press

[5] Norrington P H, and Grant I P 1987 J. Phys. B **20** 4869

[6] Arnaud M, and Rothenflug R 1985 Astron. Astrophys. Suppl. **60** 425

Dielectronic Recombination Rates for Iron L-shell Ions from Storage Ring Experiments

S. Schippers[1], N.R. Badnell[2], T. Bartsch[1], C. Brandau[1], M.H. Chen[3], M. Grieser[4], G. Gwinner[4], A. Hoffknecht[1], S.M. Kahn[5], J. Linkemann[4], A. Müller[1], R. Repnow[4], A.A. Saghiri[4], D.W. Savin[5], M. Schmitt[4], D. Schwalm[4], and A. Wolf[4]

[1] *Institut für Kernphysik, Justus-Liebig-Universität, 35392 Giessen, Germany*
[2] *Department of Physics, University of Strathclyde, Glasgow, G4 0NG, United Kingdom*
[3] *Lawrence Livermore Laboratory, Livermore, CA 94550, USA*
[4] *Max-Planck-Institut für Kernphysik, 69120 Heidelberg, Germany*
[5] *Columbia Astrophysics Laboratory, Columbia University, New York 10027, USA*

The measurement of electron-ion recombination rates at storage rings is an active field of modern research. With the proper choice of storage ring facility — the heavy ion storage rings TSR at the Max-Planck-Institut für Kernphysik in Heidelberg, CRYRING at the Manne-Siegbahn Institute in Stockholm, ESR at GSI in Darmstadt and ASTRID at the University of Aarhus currently devote large fractions of their beamtimes to electron ion recombination studies — nearly any combination of ion species and charge state can be investigated nowadays. The unique possibility of merging a cooled ion beam with electrons in storage ring electron coolers has facilitated the exploration of many novel phenomena in atomic collision physics such as the spectroscopy of doubly excited states in highest Z ions where the atomic structure is determined by relativistic and QED effects, recombination at lowest energies where an unexplained enhancement of the experimental recombination rate beyond theoretical expectations is observed, interference effects between dielectronic recombination (DR) and radiative recombination (RR), and the influence of external electromagnetic fields on DR rates. The current status of these activities has been reviewed recently[1].

The potential of storage ring based electron ion recombination experiments to provide accurate absolute recombination rate coefficients for applications in plasma and astrophysics has been realized already long ago and up to now a large body of recombination data has been accumulated[2]. Early studies concentrated mainly on the recombination of Li-like and Na-like ions, since these ions on the one hand are simple enough to be treated by theory with high accuracy and on the other hand provide strong $\Delta n = 0$ recombination channels via $2s \rightarrow 2p$ and $3s \rightarrow 3p$ core excitations, respectively. Today for Li-like ions the agreement between recombination theory and experiments is on the 20% level, i. e. on the level of the experimental accuracy. However, ions containing more electrons are still a challenge for theory and benchmarking experiments are vitally needed as has been demonstrated, e. g. by Schippers et al.[3] who for Ar-like Ti^{4+} ions found deviations of up to a factor 3 between experimental and available theoretical recombination rate coefficients.

A research programme aiming at providing accurate experimental recombination rates for the open-L-shell iron ions Fe^{17+} to Fe^{23+} is currently carried out[4,5] at the heavy ion storage ring TSR of the Max-Plank-Institut für Kernphysik in Heidelberg, Germany. These ions are of utmost astrophysical importance since their line emission will be a main diagnostic tool for astrophysical objects in future satellite based X-ray spectroscopic observations. Especially large theoretical uncertainties exist for low temperature DR rates of Fe L-shell ions which are a key ingredient in models describing photoionized plasmas such as interstellar media around cataclysmic variables, X-ray binaries or active galactic nuclei[4].

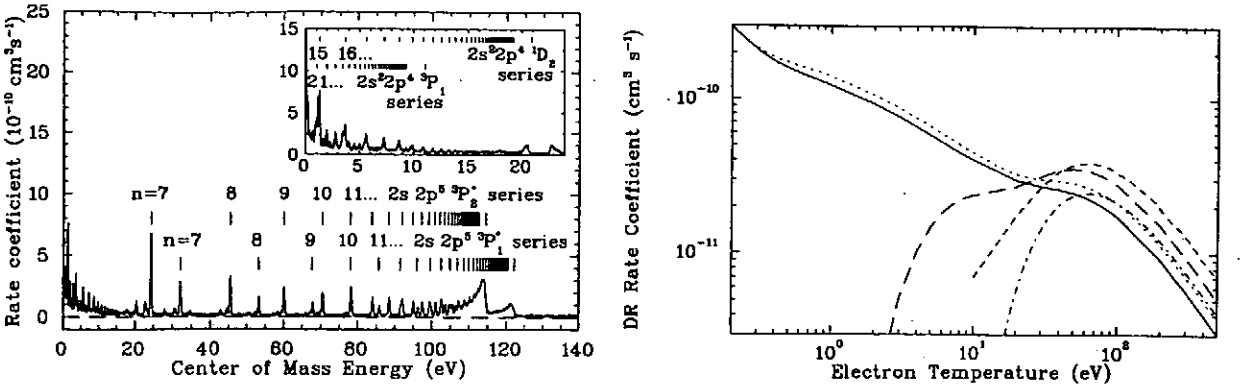

Figure 1: The left panel shows an experimental high resolution Fe^{18+} recombination spectrum exhibiting Rydberg series of DR resonances attached to several series limits. The right panel displays Maxwellian averaged Fe XIX to Fe XVIII $\Delta n = 0$ DR rate coefficients. The solid line is our experimental result with an uncertainty of less than 20% in the absolute rate. Also shown are existing theoretical calculations by Roszman (long-dashed curve), Dasgupta and Whitney (short-dashed curve) and the Burgess formula (short dash-dot curve). The dotted curve represents results of new multi-configuration Dirac-Fock calculations also published in Ref. 5 where references to the other theoretical work are given and where the figures are taken from.

Our collaboration has measured DR rates of Fe^{17+}, Fe^{18+} (Refs. 4 and 5), Fe^{19+}, Fe^{20+} and Fe^{21+} (in preparation). Measurements with Fe^{22+} and Fe^{23+} ions will follow in the near future. Already our Fe^{17+} experiment[4] gave access to data so far neglected in theoretical calculations yielding the contribution to the thermal rate coefficient from DR channels involving $2s^2 2p^5\,{}^2P_{3/2} \rightarrow 2s^2 2p^5\,{}^2P_{1/2}$ fine structure core transitions; they effectively dominate the DR rate at plasma temperatures below 2 eV.

Fine structure core transitions are also important for the recombination of Fe^{18+} ions as can be seen in the left panel of Fig. 1. At electron ion center-of-mass energies below 20 eV the experimental recombination spectrum exhibits two series of DR resonances due to ${}^3P_2 \rightarrow {}^3P_1$ and ${}^3P_2 \rightarrow {}^1D_2$ transitions within the $2p^4$ core. These dominate the DR rate coefficient at low electron temperatures as shown in the right panel of Fig. 1. Conventional theory employing only the *LS*-coupling does principally not account for fine structure transitions and consequently at low plasma temperatures yields results orders of magnitude lower than the experiment. A realistic theoretical description has to include relativistic effects. Indeed a fully relativistic multi-configuration Dirac-Fock calculation[5] is able to reproduce the experimental result within the experimental uncertainties (dotted curve in Fig. 1). At higher plasma temperatures the existing theories differ from each other by factors of up to 2. Our experimental result unambiguously clarifies this situation.

We gratefully acknowledge financial support by the German Federal Minister for Education, Science and Research (BMBF) under contract nos. 06 GI 475 and 06 HD 854. Travel and living expenses for DWS were supported by NATO Collaborative Research Grant CRG-950911.

References

1 S. Schippers, Physica Scripta **T80** (1999) in print.
2 A. Müller, in *Atomic and Plasma-Material Interaction Data for Fusion*, Suppl. to Nucl. Fusion, Vol. 6 (IAEA, Vienna, 1995), pp. 59–100.
3 S. Schippers et al., J. Phys. B **31**, 4873 (1998).
4 D. W. Savin et al., Astrophys. J. (Lett.) **489**, L115 (1997).
5 D. W. Savin et al., Astrophys. J. Suppl. Ser. (1999) in print.

Accurate calculations on dielectronic recombination resonances

Eva Lindroth[1] and Maria Tokman[1]

[1] *Department of Atomic Physics, Stockholm University, Frescativ. 24, S-104 05 Stockholm, Sweden*

Abstract. Relativistic many-body perturbation theory is used to calculate autoionizing, doubly excited, states in Li-like ions.

In electron-ion collisions, a free electron may be captured by an ion which is simultaneously excited. If the excited ion subsequently decays radiatively to a bound state Dielectronic Recombination (DR) is completed. DR is a fundamental recombination process which has applications in astrophysics and fusion plasmas and it is also important for studies of the structure and decay channels of atomic doubly excited states.

In recent years storage ring measurements of the DR process have resulted in high energy resolution data as well as absolute determination of the recombination rate. For selected systems a detailed comparison between theory and experiment can thus be done and the effect of common approximations tested. Lithium-like systems are well suited for such a comparison due to the relatively simple structure of both the Li-like initial ion and the Be-like recombined ion which makes them within reach of ab initio calculations. We have developed a method to calculate doubly excited states and DR resonances which combines relativistic (or non-relativistic) many-body perturbation theory in an all-order formulation with complex rotation(employed in order to deal with autoionizing states). The method has hitherto been applied to DR of He^+ [1] and to a series of lithium-like ions; Ar^{15+} [2], C^{3+} [3], N^{4+}, F^{6+} [4], Ne^{7+} [5] and and Kr^{33+}. The calculations are focused on the lowest lying resonances, where the experimental accuracy is highest.

In the DR process an electron recombines with an ion through

$$A^{q+} + e^- \rightarrow A^{(q-1)+**} \rightarrow A^{(q-1)+*} + h\nu. \tag{1}$$

and in the limit when Eq. 1 can be regarded as a two-step process the integrated cross section, or resonance strength S_d, can be written as

$$S_d = \int \sigma_d(\varepsilon_e)\, d\varepsilon_e = \frac{\hbar^3\pi^2}{2m_e E_d}\, \frac{g_d}{g_i}\, \frac{A^a_{i\rightarrow d} \sum_s A^{rad}_{d\rightarrow s}}{A^a + \sum_s A^{rad}_{d\rightarrow s}}. \tag{2}$$

where the multiplicity of the intermediate doubly excited state is given by g_d, that of the initial target state by g_i and E_d is the position of the resonance relative the ionization threshold. $A^a_{i\rightarrow d}$ is the transition rate into the doubly excited state d and $A^{rad}_{d\rightarrow s}$ is the radiative transition rate from state d to a state s, below the ionization threshold. If there is only one autoionization channel open then $A^a_{i\rightarrow d} = A^a$, where A^a is the autoionization rate of state d. For light systems it generally holds that $A^a \gg A^r$ and then $A^a A^{rad}/(A^a + A^{rad}) \approx A^r$, i.e. the resonance strength is proportional to the slowest decay rate of the doubly excited state. The strength is further inversely proportional to position of the resonance.

[1] E-mail : lindroth@atom.msi.se

In light ions the autoionization rate is usually the completely dominating decay channel; often as much as six orders of magnitude larger than the radiative channel. Since the slowest decay rate determines the recombination strength the autoionization rate can vary drastically without affecting the recombination strength. States which are forbidden to autoionize within LS-coupling may have three to four orders of magnitude slower decay rate then the LS-allowed transitions, but since the radiative decay rate is even slower this has no effect on the dielectronic recombination rate. Calculations within LS-coupling will thus in general miss recombination resonances. In all the studied light Li-like ions resonances appear which can only be formed due to spin-orbit induced LS-mixing. In C^{3+} and F^{6+} the effect of these resonances is dramatic since some of them are situated just above the ionization threshold of the recombined ion and the factor $1/E_d$ in Eq. 2 enhance the recombination strength, see Fig 1.

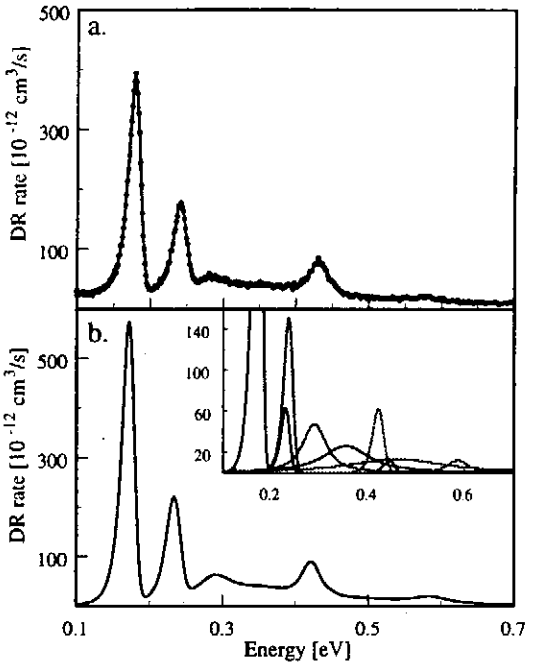

Figure 1: The calculated resonance strengths for DR of C^{3+}, folded with the electron temperature(b), can be compared with the experimental rate coefficients(a) (from Ref. [3]). The insert shows the contributions from the individual resonances. These are due to doubly excited states dominated by configurations $1s^2 2p4\ell$. Eleven of the twenty possible terms based on these configurations lie above the ionization threshold and contribute to the dielectronic recombination. The two lowest energy peaks, which are also the most prominent, are due to the LS-forbidden resonances $(2p4d)^3D^o$ and $(2p4f)^{1,3}F^e$.

References

[1] D. R. DeWitt *et al.*, J. Phys. B **28**, L147 (1995).

[2] W. Zong *et al.*, Phys. Rev. A **56**, 386 (1997).

[3] S. Mannervik *et al.*, Phys. Rev. Lett **81**, 313 (1998).

[4] P. Glans *et al.*, Nucl. Instr. Meth. B **154**, 97 (1999).

[5] E. Lindroth, Hyperfine Interactions **114**, 219 (1998).

SINGLY DIFFERENTIAL CROSS SECTION FOR $H(e,2e)H^+$ REACTION PROCESS

A. C. Roy

Department of Physics, University of Kalyani, Kalyani 741235, India

Recently, Shyn [1] has reported absolute measurements of doubly differential cross section (DDCS) for $H(e,2e)H^+$ reaction process at incident energies from 25 to 250 eV. He first integrated the DDCS over the angles of the detected electron to obtain singly differential cross section (SDCS) and then integrated again over the SDCS to get the total cross section (TCS). The TCS predicted by Shyn, however, overestimates other existing experimental data [2 –5] at 60 eV and higher, up to 250 eV.

In a previous communication [6] we applied the Glauber approximation (GA) to calculate DDCS for the primary electrons for $He(e,2e)He^+$ reaction at incident energies of 100, 300, and 500 eV. It has been pointed out that the DDCS predicted by the GA are in reasonably good agreement with experiment and with the distorted-wave Born calculation (DWBA) of McCarthy and Zhang [7] for the asymmetric geometry. The GA was subsequently applied to obtain DDCS for $H(e,2e)H^+$ reaction at incident energies of 100, 150, and 250 eV [8]. The cross sections predicted by this method were found to agree closely with those of the coupled pseudostate approximation (CPA) of Curran and Walters [9], especially at low ejection energies. In the absence of any experimental data, it was, however, not possible to assess the effectiveness of the GA in predicting SDCS for $H(e,2e)H^+$ process.

In the present work we evaluate SDCS for electron impact ionization of atomic hydrogen and compare our results with the measured data of Shyn[1] and the corresponding cross sections of other theoretical methods. We include in the present calculation the effect of exchange within the framework of eikonal approximation. Table 1 shows the present exchange-modified Glauber approximation (GA-EX) results for the incident energy of 60 eV. The present method predicts a less rapid decrease of the SDCS with increasing secondary electron energy than the experiment. A similar observation has also been made by Konovalov and McCarthy [10] who applied the DWBA method. Furthermore, we notice that the GA-EX cross sections are in better agreement with experiment for the asymmetric geometry than for the symmetric case. With the increase of incident energy, the present cross sections are also found to agree more closely with experiment.

TABLE 1. Singly differential cross section in units of 10^{-17} cm^2/eV for $H(e,2e)H^+$ process at the incident energy of 60 eV.

Ejection energy (eV)	GA-EX[a]	Experiment
1.0	1.01	1.35
3.0	0.75	0.94
5.0	0.59	0.55
8.0	0.45	0.36
10.0	0.39	0.32
15.0	0.33	0.19

[a]Present exchange-modified Glauber approximation results.

References

1. T. W. Shyn, Phys. Rev. A. **45**, 2951 (1992).
2. M. B. Shah, D. S. Elliott, and H. B. Gilbody, J. Phys. B. **20**, 3501 (1987).
3. G. O. Jones, M. Charlton, J. Slevin, G. Laricchia, A. Kover, M. R. Poulsen, and S. N. Chormaic, J. Phys. B. **26**, L483 (1993).
4. W. L. Fite and R. T. Brackmann, Phys. Rev. **112**, 1141 (1958).
5. E. W. Rothe, L. L. Marino, R. H. Neynaber and S. M. Trujillo, Phys. Rev. **125**, 582 (1962).
6. H. Ray, U. Werner, and A. C. Roy, Phys. Rev. A. **44**, 7834 (1991).
7. I. E. McCarthy and X. Zhang, J. Phys. B. **22**, 2189 (1989).
8. H. Ray, A. C. Roy, and U. Werner, Can. J. Phys. **70**, 1309 (1992).
9. E. P. Curran and H. R. J. Walters, J. Phys. B. **20**, 337 (1987).
10. D. A. Konovalov and I. E. McCarthy, J. Phys. B. **25**, L451 (1992).

Proton impact excitation of lithium–like ions

M. McKeown, R. H. G. Reid and F. P. Keenan

School of Mathematics and Physics, The Queen's University, Belfast BT7 1NN, UK

Abstract. A close-coupling semi-classical method has been used to calculate the cross section for proton-impact excitation of the allowed $1s^2 2s\,^2S \rightarrow 1s^2 2p\,^2P$ transition in Li-like ions. It is shown that a commonly-used low-energy first-order approximation is not valid. Results are presented for $C^{3+} + H^+$ collisions.

In a slow collision between two positively-charged ions, the Coulomb repulsion keeps the ions apart and so limits the coupling between the electronic states of the target ion caused by the electrostatic interaction with the perturbing ion. If the action of this coupling is sufficiently small, then the cross section for excitation of the target can be calculated using the first-order formulation of Alder *et al* [1].

For electric-quadrupole excitation, this first-order approach at low impact-energies has proved to be very useful, both as a basis for approximate formulations [2], and as a means of extrapolating close-coupling results to low energies [3].

However, for electric-dipole excitation, our close-coupling semi-classical calculations have shown that the action remains large even for very slow and distant collisions. Figure 1 shows semi-classical excitation probabilities for a component of the $1s^2 2s\,^2S \rightarrow 1s^2 2p\,^2P$ transition in $C^{3+} + H^+$ collisions. There is a significant difference between our close-coupling results and the results of the first-order theory [1], even when the latter is of the order of 10^{-2}.

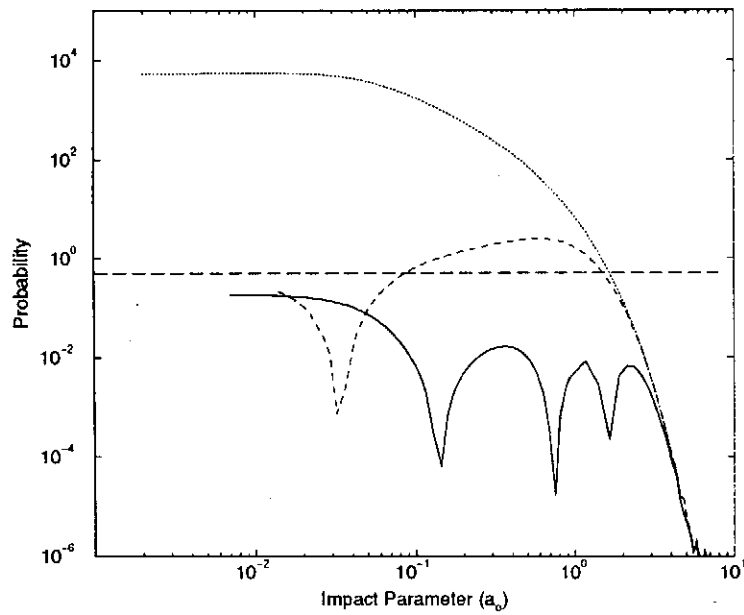

Figure 1. Probability of $2s\,^2S_{1/2,-1/2} \rightarrow 2p\,^2P_{1/2,1/2}$ excitation in $C^{3+} + H^+$ collisions at barycentric energy of 30 au. Solid curve, semi-classical close-coupling. Dotted (highest) curve, first-order semi-classical [1]. Dashed curve, first-order semi-classical using short-range-modified matrix elements. Long-dashed curve, probability = 1/2.

In our calculation, we use physically-reasonable short-range forms of the interaction matrix elements, based on the forms for hydrogenic ions. In contrast, in the formulation of Alder *et al* [1] the asymptotic forms of the matrix elements are used for all separations. The first-order probability resulting from these short-range-modified matrix elements is also shown in Figure 1. It is clear that our use of short-range-modified matrix elements is not the main source of the discrepancy between the close-coupling and the first-order results.

The failure of the low-energy first-order approximation has dramatic consequences for the cross section, as is illustrated in Figure 2. In the low-energy wing, our semi-classical close-coupling results are very significantly less than the results of Laming *et al* [4] who used a quantal, first-order approximation analogous to the semi-classical approximation for electric-quadrupole excitation given by Seaton [2]. We note, incidentally, that the discrepancy at high energies is due to our use of short-range-modified matrix elements.

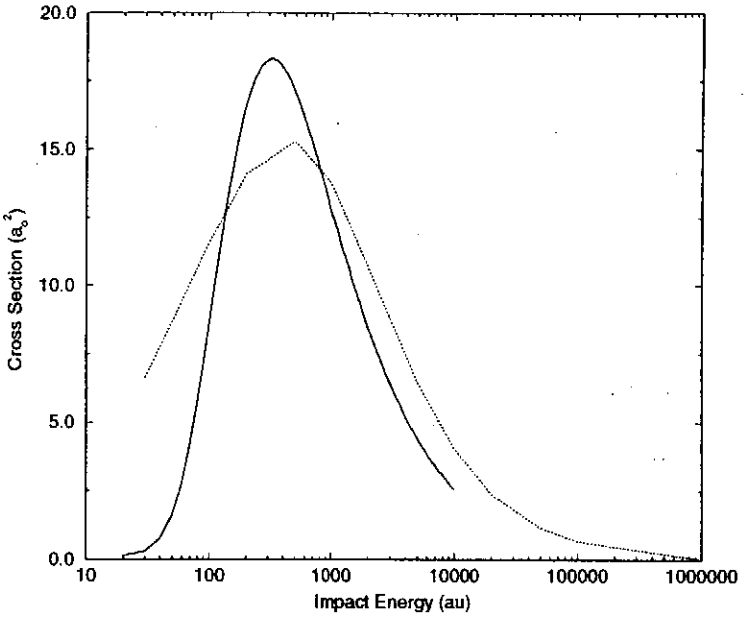

Figure 2. Cross section for 2s $\rightarrow$ 2p excitation of C^{3+} by proton impact. Solid curve, semi-classical close-coupling (present). Dotted curve, first-order-quantal based approximation [4].

References

[1] Alder K, Bohr A, Huus T, Mottelson B and Winther A 1956 *Rev. Mod. Phys.* **28** 432

[2] Seaton M J 1964 *Mon. Not. R. Astron. Soc.* **127** 191

[3] Foster V J, Keenan F P and Reid R H G 1994 *Phys. Rev. A* **49** 3092

[4] Laming J M, Raymond J C, McLaughlin B M and Blair W P 1996 *Astrophys. J.* **472** 267

Monte-Carlo Particle-In-Cell Simulation of the Charge Exchange Process Between Sm and Sm^+

[1]Sun Kook Kim, Yongjoo Rhee, and Jongmin Lee

Korea Atomic Energy Research Institute, P.O.Box 105, Yusung, Taejon, 305-600, Korea

Abstract. MC(Monte-Carlo)-PIC(Particle-In-Cell) simulation were carried out for the charge exchange process between Sm and Sm^+ in plasma. The electrostatic field was calculated using the PIC method. For the calculation of the electric field, quadratic interpolation of macro-particle is adapted. For the various background neutral atom number density, plasma decay phenomena are investigated.

The atomic processes in plasmas are those of the most important physical phenomena in many real plasma systems such as glow discharges, fusion reactor, laser plasma. In low energy plasma, which is usually encountered in an industrial situation, a lot of atomic collisions occur. These collisions induce ionization, excitation through electron collisions with ions. The charge exchange process, however, takes place between neutral atoms and ions. Especially the charge exchange between a neutral atom and its ion is called resonant. For the study of a various atomic processes in plasmas, we have developed a simulation code that can treat various kinds of atomic processes. In this report, the resonant charge exchange process between Sm and Sm^+ is reported.

The simulation of the charge exchange processes are usually carried out by MC(Monte-Carlo) method[1]. This method deals with physical probability by random process using the probability determination mechanism. When an atom and an ion collide with each other, there is a probability to exchange an electron. This probability or the resonant charge exchange cross-section is usually measured by experiments, but it is well known that the charge exchange cross-section is difficult to measure when the energy of the plasma is not so high. We adapt the model of the charge exchange process of reference [2]. From the reference [2], the resonant charge exchange cross-section is

$$\sigma_{ia}^{ch.ir}(E) = \sigma_0[1 + a\ln(\frac{E_0}{E})]^2,$$

where E is the impact energy of the ion with respect to the atom, $\sigma_0 = \sigma(E_0)$, E_0 = 1eV. Figure 1 shows the resonant charge exchange cross-section calculated from the above model equation as a function of the kinetic energy of the ion.

From the above equation, we see that as the energy of an ion is low, the charge exchange cross-section is large. We studied the density effect of the charge exchange process using MC-PIC method. PIC method is a widely used method in plasma physics, such as the low energy plasma processing, semiconductor simulations, and plasma display panel simulations. By this method we can include the macroscopic electrostatic force and we can find the exact motion of the macro-particles which consist of ions and electrons. In this study we adapt the quadratic interpolation of the macro-particle to the cell, which is a good way to stabilize the numerical calculation of the plasmas[3]. Calculated electric field by PIC method and SOR (Successive Over Relaxation) algorithm is shown in Figure 2. In the figure the particle distribution is also denoted. As the density of the background atoms are large, the charge exchange collision occurs more frequently. We studied the density effect of the background atom quantitatively.

[1] E-mail : skkim4@nanum.kaeri.re.kr

When an external electric field is applied to the plasma, the plasma exhibits some collective motion. Plasma is mobile matter that shields the external field. We studied the characteristics of the Sm-plasma in an external electric field. When an external electric field is applied, the plasma is decayed onto the wall, in addition to the diffusive behavior due to binary collision. The diffusion effect for the various background density is also investigated.

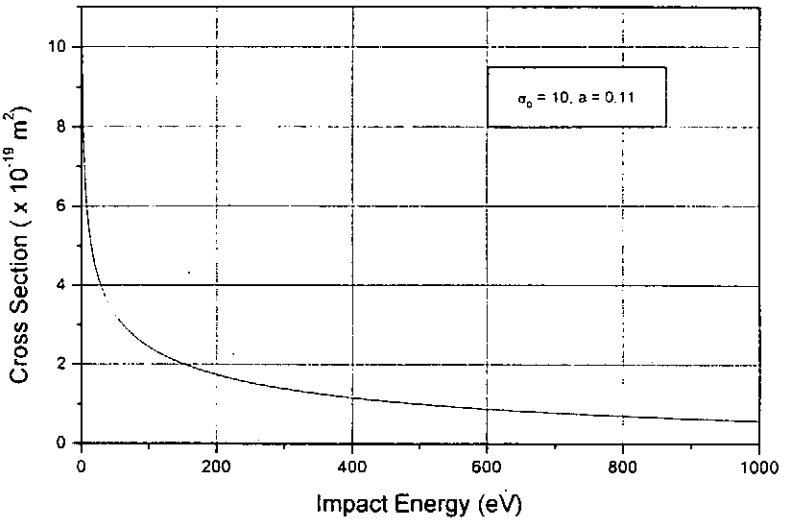

Figure 1. The resonant charge transfer cross-section according to the reference [2].

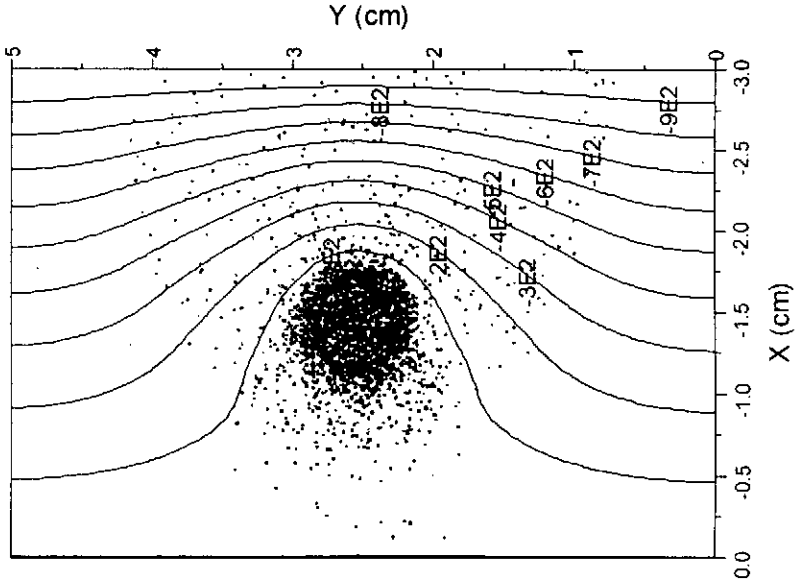

Figure 2. The calculated electric field and particle distribution.

References

[1] C. K. Birdsall 1991 IEEE Trans. Plasma Phys. **19** 65

[2] A. Anders 1990 *A Formulary for Plasma Physics* Akademie-Verlag, Berlin Chap. 3

[3] R. W. Hockney and James W. Eastwood 1981 *Computer Simulation Using Particles* McGraw-Hill, New York Chap. 5

Cross Section Measurement of Electron Impact Dissociation into Neutral Radicals from SF_6 and C_3HF_7O

Hirotaka Toyoda, Hironori Kanda and Hideo Sugai
Department of Electrical Engineering, Nagoya University

In microfabrication processes of semiconductor devices such as film deposition or etching, various kinds of molecular gases are used. To understand the plasma chemistry and to control the plasma process, various cross sections such as electron-impact dissociation, ionization are needed for each processing gas. Amongst the various elementary processes, dissociation cross sections from molecules into neutral radicals are believed to be one of the most important data for modelling and simulation of plasmas, because neutral radicals play very important roles in the plasma processes. However, only few data of neutral dissociation cross sections have been published so far. Recently, we have developed a method for the cross section measurement of electron-impact dissociation of molecules into neutral radicals, which is based on the radical detection by apparance mass spectrometry[1]. So far, this method has been successfully applied to the measurement of the neutral dissociation cross sections from various molecules such as methane (CH_4)[2,3], carbon tetrafluoride (CF_4)[4], silicon tetrafluoride (SiF_4)[5], trifluoromethane (CHF_3)[4], octafluoro-cyclobutane (c-C_4F_8)[6]. In this paper, we report the absolute cross section of electron dissociation into SF_3 neutral radicals from sulfur hexafluoride (SF_6). Cross section of hydrofluoroether-227 is also presented. Both SF_6 and HFE-227 are used in dry etching of semiconductor material: SF_6 is an etching gas for metals and HFE-227 attracts much attentions, from environmental problem point of view, as an alternative etching gas which has short lifetime in ozone layer.

Cross section measurements are made in a dual-electron-beam device combined with a quadrupole mass spectrometer (QMS). This system consists of three compartments which are differentially pumped with two turbomolecular pumps. The first compartment is a grounded dissociation cell where a primary electron beam incident on a sample gas at energies of E=5-200 eV and currents of I_e=0.1-40 μA dissociates molecules flowing at a pressure of 10^{-3}-10^{-2} Pa, and the electron is collected by a cylindrical cup (collector) of 1.2 cm in diameter and 1.6 cm in length. The second compartment is a detection cell (pressure 10^{-5}-10^{-4} Pa) where a probing electron beam emitted from a rhenium filament at energies of E_Q=10-25 eV selectively ionizes radicals effusing from the dissociation cell through a 4-mm-diameter orifice into an ionization chamber. The ionized radicals are mass-separated by the QMS, and output pulses from a secondary electron multiplier in the QMS system are counted and processed by a computer. The third compartment is an electron source cell at pressures of 10^{-4}-10^{-3} Pa where the primary electron beam is generated from a hot filament biased negatively to $-V_d$. The primary beam is injected through a 3-mm-diameter orifice along a magnetic field of ~0.06 T provided by a pair of permanent magnets, in order to minimize the beam energy spread and to define the beam trajectory. Pressure in the detection cell is measured by a spinning rotor gauge, from which pressure in the dissociation cell is evaluated.

In the dissociation cell, the primary electron beam collides with molecules and creates various neutral radicals and ionic species. First, ions are eliminated by the positive bias (~10 eV) of the ionization chamber and the QMS with respect to the dissociation cell. Neutral radicals are detected using threshold ionization techniques[1]. Prior to the cross section

measurement, radical signal is measured as a function of the primary electron beam current and the pressure in the dissociation cell. The result indicates that the radical signal is proportional to both the beam current and the pressure. This means that the radical is produced through single electron collision process and that the secondary process in the dissociation cell is negligible.

To determine the absolute cross section, the relataive cross section is calibrated using the ionization cross section of SF_3, and measuring the known dissociation cross section into neutral radicals from CF_4 or N_2. This calibration procedure includes the effect of the radical surface loss in the dissociation cell. The mass discrimination effect of QMS is carefully examined by measuring the ionization signal intensities of several atoms and molecules and comparing the intensities with the published ionization cross sections. The absolute cross section for SF_3 radical production is obtained to be $1.79\times10^{-19}m^2$ at an electron impact energy of 100 eV. The absolute values of partial cross section for the dissociation of SF_6 into SF_3 radicals is shown in Fig.1. We estimate that the absolute uncertainty of the cross section is $\pm$100% and the relative uncertainty is $\pm$20%, as discussed previously[3]. In the same way, the absolute cross sections for neutral dissociation from HFE-227 into CF_x radicals have been obtained for the first time.

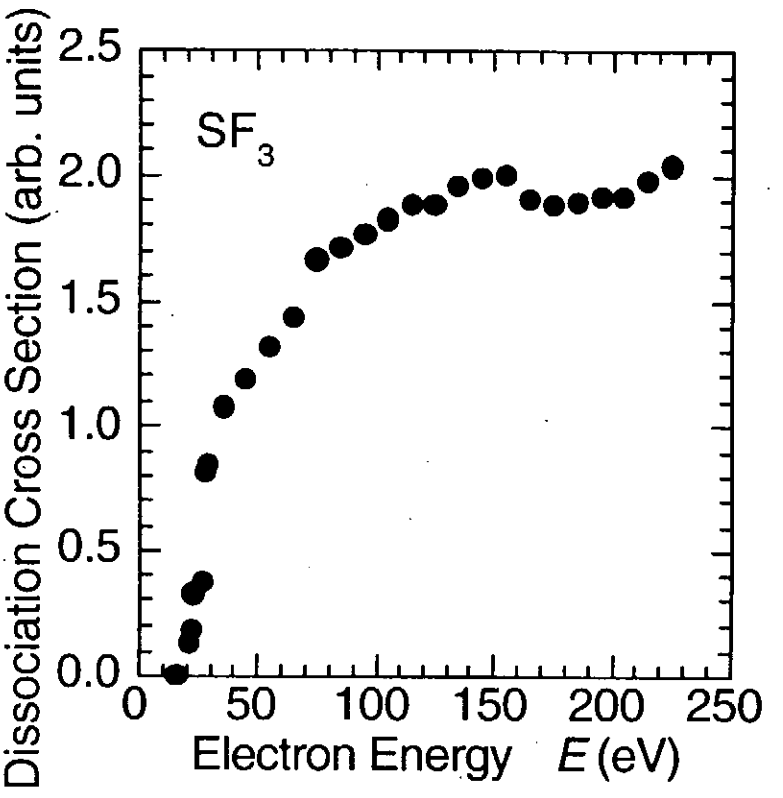

Fig. 1. Absolute cross section of electron impact dissociation from SF_6 into SF_3 neutral radical.

In summary, we have obtained the absolute cross section of electron impact dissociation of SF_6 into SF_3 neutral radicals and HFE-227 into CF_x neutral radicals based on the unique radical detection technique, i.e., appearance mass spectrometry.

References

1) H. Sugai and H. Toyoda: J. Vac. Sci. Technol. A**10** (1992) 1193.
2) T. Nakano, H. Toyoda and H. Sugai: Jpn. J. Appl. Phys. **30** (1991) 2908.
3) T. Nakano, H. Toyoda and H. Sugai: Jpn. J. Appl. Phys. **30** (1991) 2912.
4) H. Sugai, H. Toyoda, T. Nakano and M. Goto: Contrib. Plasma Phys.**35** (1995) 415.
5) T. Nakano and H. Sugai: J. Phys. D **26** (1993) 1909.
6) H. Toyoda, M. Iio and H. Sugai: Jpn. J. Appl. Phys. **36** (1997) 3730.

Dissociation in atom and diatom collisions

Kazuhiro Sakimoto[1]

[1] *Institute of Space and Astronautical Science, Yoshinodai, Sagamihara, Japan*

Abstract. Collision induced dissociation and vibrational/rotational transition in He + H_2 are studied by using a semiclassical method in which one degree of freedom (i.e., relative radial motion) is described by classical mechanics and the others by quantum mechanics. In the present semiclassical treatment, the quantum motions, i.e., the vibration, dissociation, orbital rotation, and molecular rotation, are solved accurately without introducing any decoupled approximations. The energy dependence of the cross sections and the momentum distributions of dissociative fragments are calculated at the total energies $E < 10$ eV. Also carried out is the calculations using a centrifugal-sudden (CS) and infinite-order-sudden (IOS) approximation, and the reliability of these approximations are examined.

1 Introduction

Recently, it has become possible to carry out three dimensional (3D) quantum mechanical calculations for rotational, vibrational, and also dissociative transitions in hyperthermal (> a few eV) molecular collisions.[1] However, the previous quantum mechanical 3D studies for hyperthermal collisions assumed an infinite order sudden (IOS) or vibrational sudden approximation. The use of the vibrational sudden approximation is limited to very high vibrational states for light molecules such as H_2.[1] The applicability of the IOS approximation for high energy collisions has not yet been examined sufficiently. To do that, we must consider the rotational degrees of freedom satisfactory. However, since even the IOS approximation requires time consuming calculations for high energy collisions, the consideration of rotational motion becomes extremely troublesome in a fully quantum mechanical manner.

Very recently, I have introduced a semiclassical theory to study hyperthermal molecular collisions. In the semiclassical method, the relative radial motion is treated in classical mechanics, and the other motions are in quantum mechanics. In previous studies,[2] I have applied the semiclassical theory to He + H_2 collisions in the case that restricted (collinear, T shaped, $\cdots$) configuration, coplanar geometry, or the IOS or centrifugal sudden (CS) approximation is assumed. It has been shown that the semiclassical method provides a good agreement with a full quantum mechanical one, and is very useful to gain the physical insight into the collision dynamics including some quantum mechanical natures. The present paper carries out the calculation of hyperthermal He + H_2 collisions by using a semiclassical theory, and takes the quantum motions (orbital rotation, molecular rotation, vibration, and dissociation) accurately.

2 Results

The upper figure shows the cross sections for vibrational excitation and dissociation in He + $H_2(v = j = 0)$. The lower figure shows the momentum distribution of dissociative fragments.

[1]E-mail : sakimoto@pub.isas.ac.jp

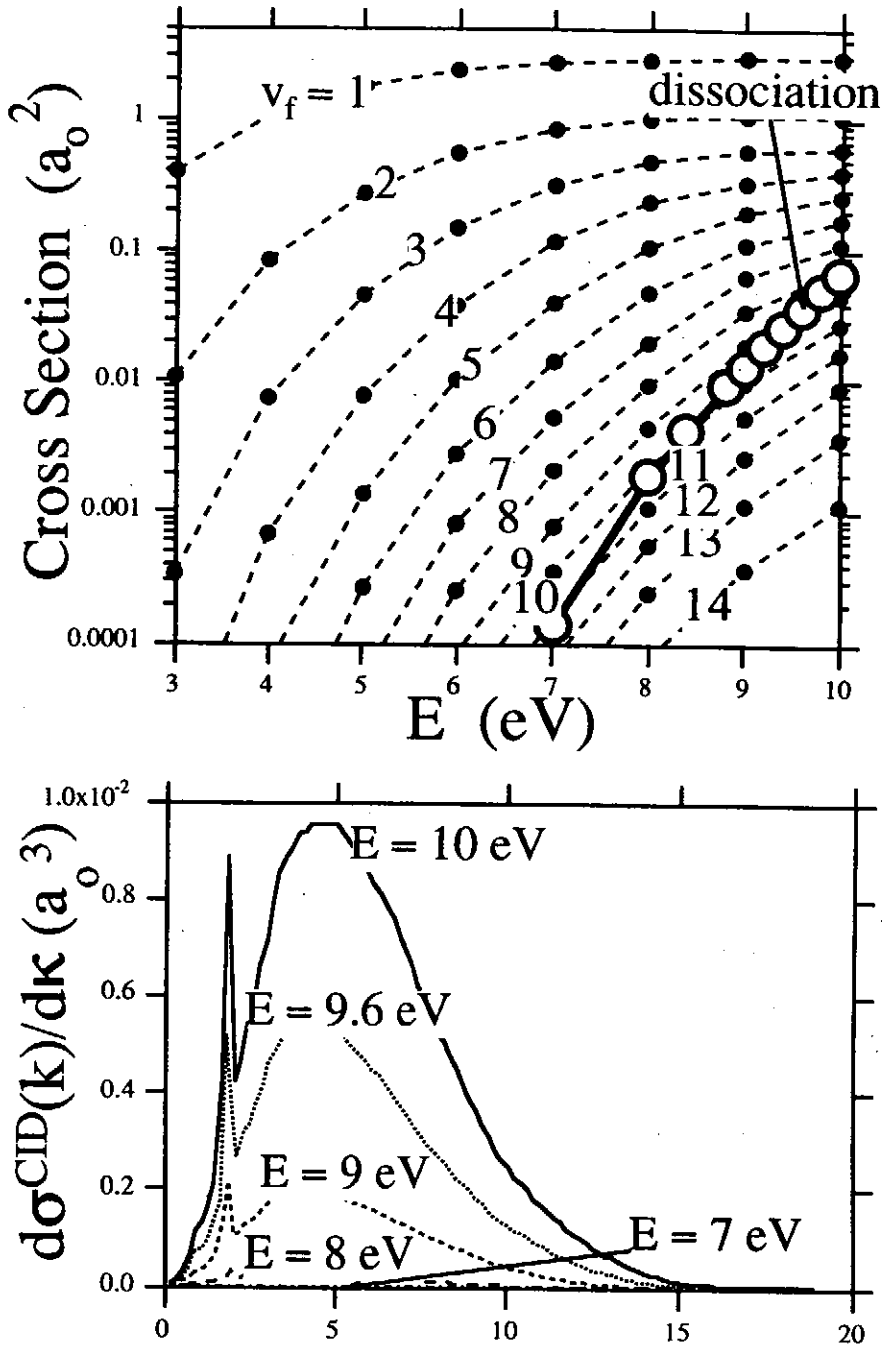

References

[1] B. P. Pan and J. M. Bowman, J. Chem. Phys. **103** (1995) 9661; **109** (1998) 1734; K. Nobusada and K. Sakimoto, J. Chem. Phys. **106** (1997) 9078; Chem. Phys. Letters **288** (1998) 311; K. Sakimoto, J. Phys. **B30**, 3881 (1997); Chem. Phys. **228**, 167 (1998).

[2] K. Sakimoto, Chem. Phys. **236**, 123 (1998); Phys. Chem. Chem. Phys. (J. Chem. Soc., Faraday Trans.) 1 (1999) 1273; J. Chem. Phys. **110** (1999) 11233; Chem. Phys. (1999) in press; J. Chem. Phys. (1999) to be submitted.

Dissociative recombination and dissocaitive excitation of H_2^+

Hidekazu Takagi[1]

[1] *Kitasato university, School of Medicine, Sagamihara, Kanagawa, 228-8555 Japan*

Abstract.
The dissociative processes in $H_2^+ + e$ collision are theoretically investigated at the collision energies between 1 eV and 12eV. The multichannel quantum defect theory is applied to the present calculation with extending it to include the dissociative channels. A higher order effect is taken into account by introducing 'closed dissociative channel'. For various initial vibrational states, the cross section of the dissociative recombination and dissociative excitation will be shown.

In the collision of $H_2^+ + e$ at the energies between 1 eV and 12 eV, the dissociative processes are derived from the electron capture to the infinite number of two-electron excited states, whose potential curves are dissociative. These states constitute some Rydberg manifolds converging to the first excited states of H_2^+ $(2p\sigma_u)$. Figure 1 shows potential energy curves of these states. By applying the multichannel quantum defect theory (MQDT) to those Rydberg manifolds, we can analytically cope with the infinite number of core excited Rydberg states. Using the discretized dissociative wave function together with the vibrational one, we have extended the MQDT to include the dissociative states[1].

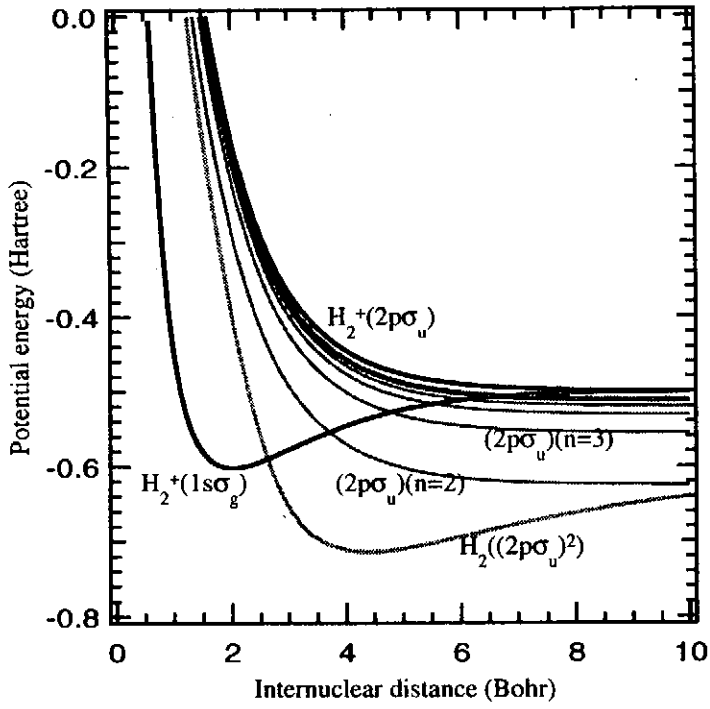

Figure 1. Potential energy curves of core excited Rydberg states in H_2. The ionic potentials are also shown for the ground and first excited states.

In the present MQDT calculation, we have taken into account the couplings among the dissociaitve channels by employing virtual dissociative states, which we call 'closed dissociative channels'[2, 3, 4]. For the lowest two-electron excited states $(2p\sigma_u)^2$, we calculated precise scattering matrix by solving the off-the-energy-shell Lippmann-Schwinger equation[5]. The dissociative two-electron excited states adopted in the present calculation are the lowest one and Rydberg manifolds of the symmetries $^1\Sigma_g$, $^1\Sigma_u$, $^1\Pi_g$, $^3\Pi_g$, and $^3\Pi_u$. The configuration interaction strength of those states with the initial electronic state were taken after the calculation by Tennyson[6]. The interaction induced by the adiabatic quantum defect was neglected because this was a minor contribution. The result on the dissociative recombination (DR) and dissociative excitation (DE) is respectively shown in Figure 2 and 3. Both these cross sections have structures depending on the initial

[1]E-mail : takagi@kitasato-u.ac.jp

vibrational state (v). As the vibrational state becomes higher, an outstanding peak of the DR cross section shifts to lower collision energy, its magnitude becomes larger, and the DE cross section tends to be larger.

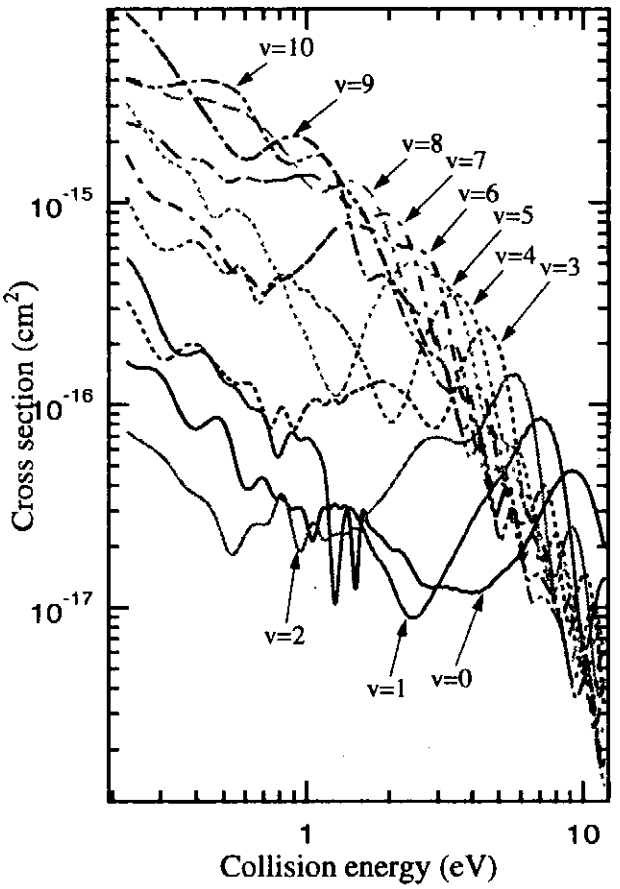

Figure 2. Dissociative recombination cross section of $H_2^+(v)$. The result is convoluted by the energy resolution of 0.1 eV.

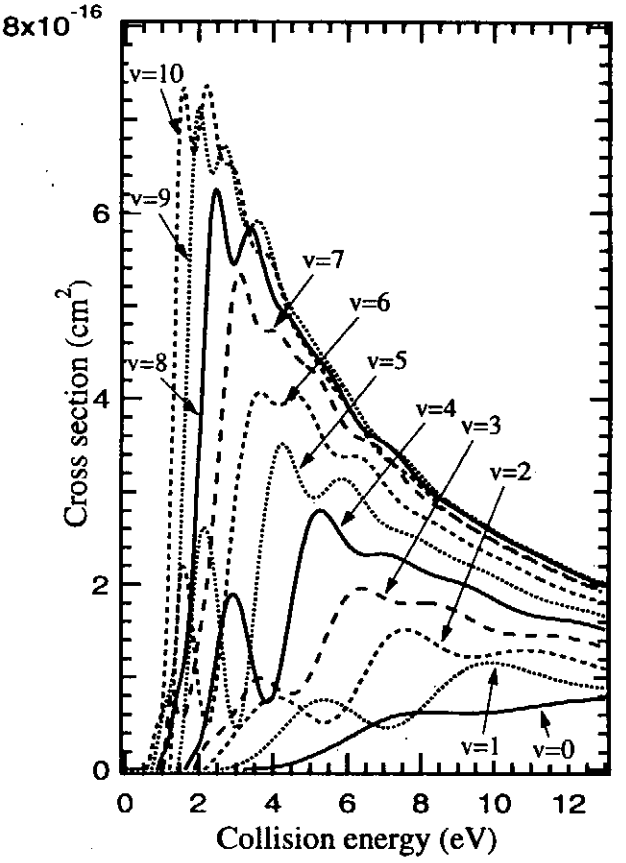

Figure 3. Dissociative excitation cross section of $H_2^+(v)$.

References

[1] Takagi H 1996 in *Dissociative recombination, Theory, Experiment, and Application III,* ed. Zajfman D *et al* (World Sientific, Singapore)

[2] Takagi H 1999 to be published in *Dissociative recombination, Theory, Experiment, and Application IV,* ed. Larsson M *et al* (World Sientific, Singapore)

[3] Takagi H 1999 *ICPEAC abstracts* **21** 407

[4] Tanabe T *et al* 1998 *J. Phys. B* **31** L297

[5] Takagi H 1999 *ICPEAC abstracts* **21** 406

[6] Tennyson J 1996 *At. Data Nucl. Data Tables* **64** 253

X-ray line polarization plasma spectroscopy: polarization database and plasma diagnostics

Alla Shlyaptseva[1], Alexander Petrashen [1], Victor Kantsyrev [1], Sergei Kazantsev [2], and Ulyana Safronova [3]

[1] *Department of Physics, University of Nevada, Reno NV 89557, USA*
[2] *DASOP-L.P.S.H. Section Meudon, Observatoire de Paris, 92195 Meudon Cedex, France*
[3] *Department of Physics, University of Notre Dame, IN 46556, USA*

Abstract. Polarization Plasma Spectroscopy provides important information about anisotropy of processes occuring in plasmas. In particular, electron beams represent an anisotropic excitation mechanism leading to the emission of partially polarized radiation. In this work, X-ray line polarization spectroscopy is proposed to study low- and moderate-density plasmas. For this purpose, we create a new atomic database of polarization characteristics which includes the amplitudes of the autoionization decay and degrees of polarization. We discuss the application of these results to diagnostics of high-energy, non-Maxwellian electron beams and magnetic field in plasmas. This work demonstrates the importance of X-ray Line Polarization in plasma diagnostics.

1 Introduction

Polarization Plasma Spectroscopy provides information about anisotropy of processes occurring in plasmas. The International meeting on Plasma Polarization Spectroscopy which was held in Kyoto in 1998 demonstrated the vitality of this new research field and its unique applications to the plasma diagnostics. In particular, X-ray line polarization plasma spectroscopy is a powerful new tool for the investigation of plasma anisotropy. It can be used for diagnostics of plasmas with very different density, from a low-density to a dense plasma. This is a multi-step problem which requires a creation of the new type of the atomic database, the ability of appropriate theoretical modeling and experimental monitoring of the polarization-dependent spectra.

2 Polarization radiation characteristics database for dielectronic satellite lines

Atomic and polarization characteristics of dielectronic satellite lines of Li-, Be-, B-, and C-like ions were calculated. MZ code (perturbation theory method) was employed to obtain energy levels, radiative transition probabilities, and autoionization rates for doubly-excited states for ions in the broad range of nuclear charge Z. Besides the total autoionization rates, the amplitudes and partial rates of autoionization decay via different channels were computed. Using the photon density matrix formalism, the degree of polarization of dielectronic satellites was expressed through the autoionization decay amplitudes. Atomic and polarization characteristics were used as input data to calculate polarization-dependent spectra of dielectronic satellites, i.e., the spectral intensity distribution of lines associated with a given polarization state, parallel or perpendicular to the electron beam.

[1]E-mail : alla@physics.unr.edu

Application to the EBIT and low-density plasma sources. The polarization properties of dielectronic satellite lines in Li-, Be-, and B-like Fe ions excited through resonant electron capture by an electron beam were studied. Theoretical polarization-dependent spectra agree well with experimental data collected at the Livermore Electron Beam Ion Trap where dielectronic satellite line emission from Fe ions produced at different energies of the electron beam was simultaneously recorded with two crystal spectrometers [1].

Application to moderate plasma density radiation sources. As the density of the electron beam increases, new channels of electron capture appear, and the atomic and polarization characteristics of the satellite lines change. Using the density matrix formalism, the polarization characteristics of dielectronic satellites of Be- and C-like Fe were calculated produced at different energies and densities of the electron beam [2].

3 Diagnostics of plasma anisotropy

X-ray line polarization is sensitive to the electron distribution function and magnetic field, important plasma characteristics, that, in general, have not been measured adequately. The difference in line intensities between two polarization states will yield information on these plasma characteristics. In particular, K-shell polarization-dependent spectra of dielectronic satellites can be used to diagnose the energy, density and directionality of the electron beams.

The influence of the magnetic field on the X-ray line polarization. A model incorporating anisotropy of the electron impact excitation and the internal magnetic field was analyzed by means of a solution of the equation for the density matrix [3]. In the present work, the particular case of multiply-charged Ti ions was considered when the alignment of the excited states was created in the axially symmetric plasma source. The diagnostic possibilities of the X-ray L-shell line polarization spectroscopy of Ti ions for estimation of the magnetic field were studied.

Measurements of the soft X-ray line polarization. The method is used which employed two identical x-ray spectrometers differing only in orientation with respect to the symmetry axis of a plasma source. Moreover, two new polarimeters/spectrometers are developed for precise measurements of polarization characteristics of separate spectral lines or groups of closely located lines [4].

Acknowledgements. This work was supported by DOE, SNL, UNR, and NSF.

References

[1] Shlyaptseva A S, Mancini R C, Neill P and Beiersdorfer P 1997 *Rev. Sci. Instrum.* **68** 1095; 1999 *J. Phys. B* **32** 1041

[2] Shlyaptseva A S and Safronova U I, "Theoretical atomic and polarization characteristics of X-ray dielectronic satellite lines of C-like ions", 1998 DAMOP 43 N 3 1298 HP 11

[3] Kazantsev S A, Petrashen A G, and Firstova N M 1999 *Impact Spectropolarimetric Sensing.* Plenum Publishing Corporation New York, London

[4] Kantsyrev V L, Bauer B S, Shlyaptseva A S, Bruch R F, Phaneuf R A, 1997 *New EUV and x-ray optical instrumentation for hot plasma imaging, polarimetry, and spectroscopy, using glass capillary converters and multilayer mirrors*, **CP409**, *Dense Z-Pinches*:Fourth International Conference, AIP Press, 499

Impurity Diagnostics in the GAMMA 10 Tandem Mirror

M. Yoshikawa[1], Y. Okamoto[1], E. Kawamori[1], T. Ito[1], C. Watabe[1], Y. Watanabe[1], K. Ikeda[2], N. Yamaguchi[3] and T. Tamano[1]

[1] *Plasma Research Center, University of Tsukuba, Tsukuba, Ibaraki 305-8577, JAPAN*
[2] *National Institute for Fusion Science, Toki, Gifu 509-5952, JAPAN*
[3] *Toyota Technological Institute, Tempaku, Nagoya 468-8511, JAPAN*

Abstract. We have constructed spectroscopic measurement systems in the wavelength range from soft X-ray to visible lights. We observed absolute impurity line intensities, Doppler line broadenings and Doppler shifts of impurity lines and time dependent radial profiles of the impurity lines in the GAMMA 10 tamdem mirror.

1 Introduction

Impurity lines and continuum radiations in the wavelength range from visible to soft X-ray (SX) are emitted from fusion plasmas. These emissions provide us with information of radiation power losses, a potential formation in the radial direction and ion density profiles which directly relate to the impurity transport in magnetically confined plasmas. In a GAMMA 10 tandem mirror plasma carbon (C) and oxygen (O) ions are mainly observed as impurity lines [1-5]. We prepared two 2-D UV-visible (UV/V) spectrograph systems (2000-6700 Å), time- and space-resolving vacuum ultraviolet (VUV) (150-1050 Å) and SX (20-350Å) spectrographs for impurity diagnostics. Details of these spectrographs are shown in the previous papers [1-5]. The two UV/V spectrograph systems are absolutely calibrated by using a tungsten ribbon filament lump. Absolute calibration experiments for the VUV and the SX spectrographs have been conducted by using synchrotron radiations at the Photon Factory in the High Energy Accelerator Research Organization. Thus, we are able to obtain the absolute intensities of emitted spectral lines of radial distribution. In order to obtain impurity ion temperatures, we use the UV/V spectrograph and measure Doppler broadenings of the impurity spectral lines. Impurity ion densities are obtained by using a collisional radiative model (CRM) calculation code which is provided by T. Kato [6]. Radial electrostatic potential profiles are obtained by measuring plasma rotations of variously charged impurity ions. In order to measure time dependent impurity ion profiles in the radial direction, the VUV and the SX spectrographs are used.

2 Experiments

The GAMMA 10 is a 27m long tandem mirror consisting of a 5.6 m long axisymmetric central cell, anchor cells for suppressing MHD instability and axisymmetric end mirrors for forming the plug/barrier potentials. A hydrogen plasma in the central cell is produced and heated by ICRH and plug potentials are produced by ECRH. A typical electron density in the central cell is 2×10^{12} cm^{-3}, an electron temperature is 80 eV and an ion temperature is 5 keV. The UV/V spectrographs are set on both the central cell and the anchor cell. The VUV and the SX spectrographs are set on the central cell and the barrier cell, respectively. A typical output spectra of these spectrographs are shown in Fig. 1. Figure 1 (a) and (b) show the spectrum of OV (2781, 2787, 2790 Å) lines in the central cell and the anchor cell, respectively, Fig. 1 (c) shows VUV spectrum in the central cell and

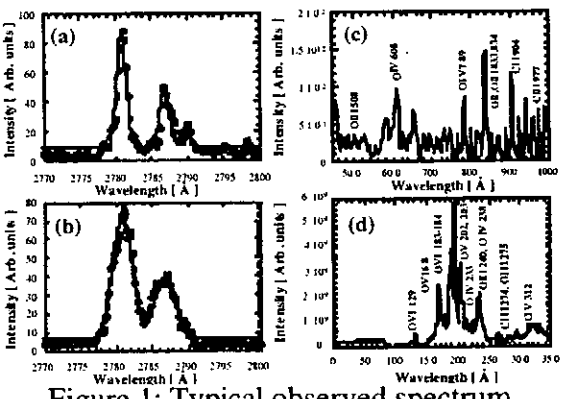

Figure 1: Typical observed spectrum.

Fig. 1 (d) shows the SX spectrum in the barrier cell. The OV ion temperature is about 0.4 keV in the central cell and 7 keV in the anchor cell. The cyclotron frequency of O^{4+} in the anchor cell is equal to $\omega_{ci}/4$, where ω_{ci} corresponds to the fundamental cyclotron frequency of hydrogen ions. The O^{4+} ion may be heated due to cyclotron higher harmonic damping. We compared the measured CII line intensity to that from CRM calculation (Fig. 2). This shows that the C^+ ion density is about 2×10^7 cm^{-3}. Time dependent C ion radial profiles are shown in Fig. 3. From the results of C ion behavior, we make a model of impurity transport. First, the impurities are emitted from the vacuum vessel wall by the electron impact and the charge exchange neutral particle impact and come into the plasma during the plasma formation phase, first 40 ms during plasma discharge. Next, the impurities are ionized by the electron impact, the ion impact and the charge exchange. As the plasma grows, the charge states of impurity ions are increases, and the peak region of each state impurity moves towards the outer region. When ECRH is on, a plug potential is made. Then, the ions, hydrogen ion and impurity ions, are axially confined by the plug potential. After ECRH off, the impurity ion peaks appear in the same region as that before ECRH is on. The impurity ions come into the plasma only during plasma formation phase. If the impurity come there another time sequence, the impurity ion intensity must increase at that time. From this measurement, we obtained the impurity ion confinement time, $\tau_{imp} < 20$ ms.

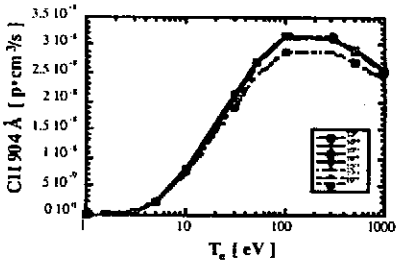

Figure 2: CRM calculation.

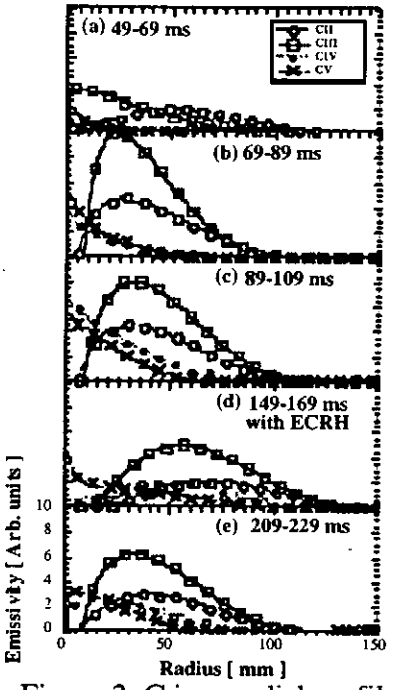

Figure 3: C ions radial profiles.

3 Conclusion

We conclude that we have constructed the spectroscopic measurement systems in the wavelength range from SX to visible lights. Moreover we have observed the impurity line intensities, Doppler line broadenings, Doppler shifts by UV/V spectrograph and time dependent radial profiles of the impurity lines by the VUV and the SX spectrographs. Then we constructed a model of impurity ion behavior.

Acknowledgements. The authors would like to thank the GAMMA 10 Group for their operational and diagnostic support. We would like to thank Dr. T. Kato for kindly providing us CRM calculation codes.

References

[1] K. Ikeda et al., Phys. Rev. Lett. **78**, 3872 (1997).
[2] K. Ikeda et al., Rev. Sci. Inst. **70**, 332 (1999).
[3] N. Yamaguchi et al., Rev. Sci. Instrum. **65**, 3408 (1994).
[4] M. Yoshikawa et al., J. Synchrotron Rad. **5**, 762 (1998).
[5] N. Yamaguchi et al., J. Plasma Fusion Res. **71**, 867 (1995).
[6] T. Kato et al., Fusion Engineering and Design **34-35**, 789 (1997).

Spectroscopic study of hydrogen transport in a low temperature plasma

Bingjia Xiao, Kobayashi Kazuki and Satoru Tanaka
Department of Quantum engineering and Systems Sciences
Faculty of Engineering, The University of Tokyo

Abstract: Hα spectra are modeled in a linear plasma, MAP[1]. In comparison to the experiments, better agreements were obtained if the energy of dissociated atom is assumed ~ 0.45 eV and the reflection yield is assumed lower than that predicted by current database. There may exist high population of vibrationally excited molecules. Calculation also shows large energy sinks which could not verified by our experiments. Probably it is overestimated for the energy loss of electron from molecular dissociation in the current database.

1. Experimental

The plasma column in the second chamber of MAP is with the size of 40 cm(length) and ~5 cm (diameter). The electron temperature is ~ 13 eV and density ~ 3. × $10^{17}/m^3$. The neutral pressure in the chamber is kept constant as 0.25 mTorr via a diffusion pump. Hα spectra at different positions to the target were observed via a telescope and a monochromator with resolution of 0.012 nm. All the spectra recorded show narrow broadening and the decomposed spectra shows a component with the neutral energy less than 1 eV. Experiment also showed strong decrease in near target region but little in the regions far from the target.

2. Numerical simulation via DEGAS 2[3,4,5].

In DEGAS 2, at given geometry and plasma parameters, neutrals are modeled in a Monte-Carlo fashion as they encounter collisions with the plasma and the interactions with material surfaces as well. The final results are indeed the neutral distribution solution of Boltzmann equation. Hα spectrum can be modeled by recording the wavelength and intensity within the observation volume (detector) according to the atomic and molecule processes.

In MAP, the diameter of the chamber is 50 cm which is much larger than that of the plasma column (5 cm). The background pressure is almost constant in experiment. Therefore we only perform the neutral transport calculation in the plasma column and we consider that the neutrals escape from the plasma when they reach the plasma circumference. The background neutrals are taken as a hydrogen molecular puff (molecular temperature was assumed in the order of room temperature ~0.05 eV) with flux of $4.\times10^{21}/m^2s$.

We take into account ionization, charge exchange and recombination of H , dissociation and ionization of H_2 and ion dissociation of H_2^+. Other reactions and elastic scattering have much small cross sections and are not considered. Hydrogen ions reflected with yield R_N and energies, $E_{refl} = R_E(E_i + \phi)$ where ϕ is the floating potential taken to be ~$3T_e$ and the plasma flux is $n_e C_s$ where C_s is the sound speed of ions which is taken to be $\sqrt{k(T_e + T_i)/m_i}$ [5,6]. We assume that part of the incident H (H^+) would be reflected as H, with the rest desorbed as H_2.

3. Results and Discussion

Modeled spectra underlying current database [8,9] are much broader than those by experiment. This can not be explained well by geometry and plasma parameter effects. When we assume the energy of dissociation products as 0.45 eV and reflection yield as 0.08 (20 % of the value predicted by refl.dat[2]), good match with the experiment can be obtained (Figs. 1-2). However, neutral atoms are mainly from the dissociated atoms which in the most cases have energies about 3 eV (Reaction A). The possible explanation of our observation is that there may exist high populations of vibrationally excited hydrogen molecules in the chamber. These molecules vibrationally excited can give rise to low energy atom dissociation via the repulsive state $^3b\Sigma$ of H_2 and the states $^2X\Sigma$ and $2p\sigma$ of H_2^+. In MAP plasma, the temperature is

~ 10 eV, which is in the turning point to provide higher probability for the electron induced molecular excitation. Moreover, the molecules can be desorbed from the walls with the states vibrationally excited. Also, because of the thin structure of MAP plasma, there is higher probabilities for H_2 (v=0) to be vibrationally excited and escape from the plasma column before being dissociated. This would bring about higher population of vibrationally excited H_2 around the plasma which can re-enter the plasma to be dissociated. The vibrationally excited H_2, especially v>=4, can also give rise to the dissociation, H_2 (v>0) + e → H + H$^-$ and then H$^-$ + H$^+$ → H which have larger cross sections (~ 2 orders) than the volumetric recombination of H$^+$ with electrons. Because of ion temperature of MAP plasma is relatively low (less than 1 eV), this could partly contribute to the population of low energy atoms. Low energy H atoms have shorter collision mean free path than those with high energy have. So Hα is mainly contributed by the low energy atoms in our observations and we conclude that there is high population of vibrationally excited H_2 in our case. Calculation also shows the electron energy loss rates due to the collision with neutral is ~0.1 MW/m^3 which could cause an electron temperature decrease of 20~ 30 eV and result in strong Hα intensity decrease along the plasma axis which can not be verified by experiment. Most probably the data [8,9] overestimate the electron energy loss in the dissociation processes.

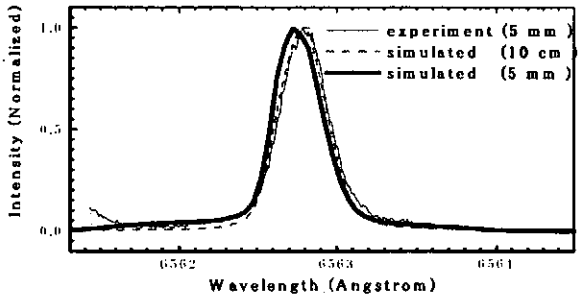

Fig. 1 Hα spectrum

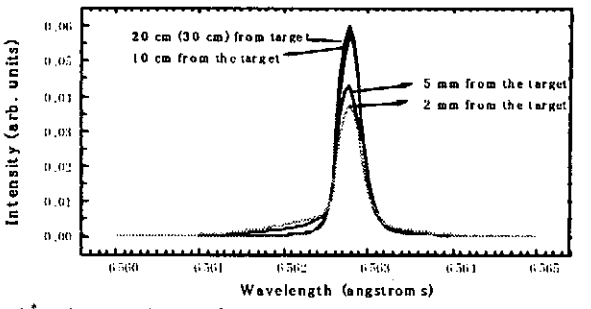

Fig. 2 Illustration of Hα intensity distribution.

4. Conclusions

From this study, in MAP plasma, there is high population of hydrogen neutral atoms with low energy (less than 1 eV) and they are most possibly the dissociated products of vibrationally excited hydrogen molecules. Reflection yield in the case of low energy ion incidence may be much less than that predicted by the current database at least to carbon targets. So we should pay enough attention when we perform the modeling of high recycling low temperature edge plasma and neutral transport based on the current databases.

5. Acknowledgement

We are very grateful for Dr. Daren Stotler to permit us to use DEGAS 2 code and also for his many instructions and help. This work is partly supported by JSPS grant-in-aid.

References:

[1] K. Kobayashi, S. Ohtsu and S. Tanaka, J. Nucl. Mat. 266-269 (1999) 850-855
[2] David N. Ruzic, Nuclear Instruments and Methods in Physics Research. Vol. B47 (1990) pp.118-125.
[3] Daren Stotler et al., 12th topical meeting on high-temperature plasma diagnostics, Princeton, NJ, 1998
[4] Daren Stotler and Charles Karney, Contrib. Plasma Physics, 34(1994) 2/3, 392-397
[5] P. C. Stangeby, in *Physics of Plasma-Wall Interactions in Controlled Fusion*, edited by D. E. Post and R. Behrisch (Plenum Press, New York, 1986), NATO ASI Series, p41
[6] D. Heifetz D. Post, M. Petravic, J. Weisheit and G. Bateman, J. Comp. Phys. 46(1982) 309
[7] A. Pospieszczyk et al., J. Nucl. Mat. 266-269 (1999) 138-145
[8] "Elementary Processes in Hydrogen-Helium Plasmas", by R.K. Janev, W.D. Langer, K. Evans & Jr. D.E. Post, Jr. Springer Series on Atoms and Plasmas, Springer-Verlag (Berlin, Heidelberg, New York), 1987.
[9] R. K. Janev et al., Atomic and Plasma-Material Interaction Data for Fusion (Supplement to the journal Nuclear Fusion) 4 (1993)

Experimental Characterization of laser-produced plasmas for intense soft x-ray lasers

Hiroyuki Daido, S. Sebban*, H. Tang, N. Sakaya, Y. Tohyama, T. Norimatsu, K. Mima and Y. Kato**
Institute of laser Engineering, Osaka University, Suita, Osaka 565-0871, Japan
S.Wang, Y.Gu and G.Huang
National Laboratory on high Power Lasers and Physics, P.O.Box 800-211 Shanghai, China
K. Murai
Osaka National Research Institute, AIST, MITI, Ikeda, Osaka 563-8577, Japan
R. Butzbach, I. Uschmann, M. Vollbrecht and E. Förster
Institute of Optics and Quantumelectronics, Friedrich-Schiller University Jena, Max-Wien-Platz 1, D-07743 Jena, Germany
F. Koike
School of Medicine, Kitasato University, 1-15 Kitasato, Sagamihara, 228 Japan
Present addresses: *Laboratoire d'Optique Appliquee, Ecole Nationale de Techniques Avancees Chemin de la Huniere 91761 Palaiseau Cedex, France
** Japan Atomic Energy Research Institute, Kansai Establishment, Kizu Kyoto 619-0215, Japan

Nickel (Ni)-like soft x-ray laser from various materials have been obtained successfully using a slab target pumping with multiple laser pulses[1-7]. Sophisticated plasma profile control by prepulse or multiple pulse pumping technique both in transverse and axial directions from the line focusing axis plays a significant role to produce intense x-ray laser beams. The laser beam of 1.053 μm wavelength was focused to a line of 1.1 cm length and 50 μm average width (FWHM) for each target as shown in Fig. 1. The slab target at the right hand side acts as an oscillator and the target at the left hand side acts as an amplifier. We have changed the length of the target at the left hand side. At the forward traveling wave side, we have measured higher intensity x-ray laser beam than that at the opposite side. The laser pulse train for pumping was composed of prepulse and a main pulse with an individual pulse width of 100 ps. The pulse to pulse separation has been changed from 600ps to 3 ns for optimization. The laser pulse energies were approximately 10 J for the prepulse and 240 J for the main pulse which corresponds to the irradiance at a line focus area of $\sim 1\times 10^{13}$ and $\sim 3\times 10^{14}$ W/cm^2, respectively.

We have performed experiments step by step in order to obtain the shorter wavelength lasing. The prepulse to main pulse intensity ratio of 4 % and the delay time of 1.5 ns gave

the best result. With this delay time, measured x-ray laser signals at the forward and the backward direction showed that the narrow and strong x-ray lasing signal was obtained at the forward direction, while the weaker and much wider divergence beam was obtained at the opposite side. The peak of the time integrated x-ray laser intensity and the horizontal beam divergence was measured with the CCD detector coupled with the grazing incidence spectrometer as a function of the target length. The gain coefficients of the Ni-like Yb and Hf lasing lines were 6.6 cm^{-1} and 3.6 cm^{-1} which corresponded to the gain length product of 11 and 6, respectively. On the other hand, with the delay time of 600 ps and the prepulse to main pulse intensity ratio of 4 %, the gain coefficient of Yb laser was 1 cm^{-1}. Simultaneously, we have measured ionization balance such as Ni-like and Co-like ion abundance with a high resolution crystal spectrometer. Based on these results, we can estimate the suitable pumping condition for the saturated water window x-ray lasers. We also show the new pumping configurations to realize such a laser for high density plasma probing.

References

[1]H. Daido et al.,Phys. Rev. Lett. **75**, 1074 (1995).
[2] H. Daido et al., Opt. Lett. **21**, 958 (1996).
[3] H. Daido et al., Int. J. Mod. Phys.B**11**, 945 (1997).
[4] G-Y. Yoon et al., Appl. Phys. Lett. **72**, 2785 (1998).
[5] S. Wang et al., Jpn. J. Appl. Phys. **37**, L1234 (1998).
[6] H. Daido et al., J. Opt. Soc. Am. B**16**, 296 (1999).
[7] H. Daido et al, to be published in J. Opt. Soc. Am B.

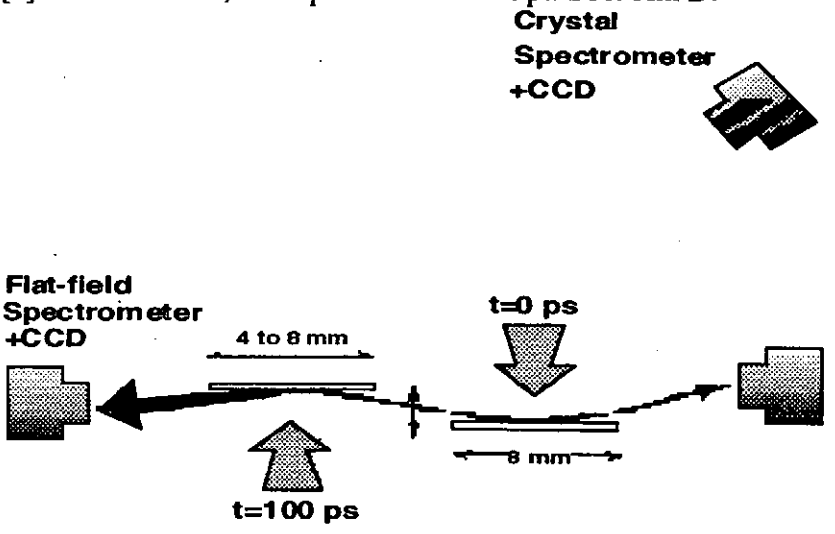

Fig. 1 Top view of the double target experiment with the x ray spectrometers. Arrows show the pumping lasers with appropriate time delay for traveling wave pumping.

Characterization of the soft x-ray source with elements in the fifth period and their compounds

Il Woo Choi, Huajing Tang, Susumu Yamagami, and Hiroyuki Daido,
Institute of Laser Engineering, Osaka University, 2-6 Yamada-oka, Suita Osaka 565-0871, Japan
Masayuki Suzuki
Department of Electric Engineering, Kinki University, 3-4-1 Kowakae, Higashi-Osaka, Osaka 577-0818, Japan

Abstract. Space-resolved soft x-ray spectra from laser produced plasmas of the pure metal and oxide compound targets of the fifth period elements such as tin and indium were measured and compared in the spectral range of 6 to 24 nm. The bandwidth and peak intensity of the unresolved transition array centered at 13.5-nm wavelength are dramatically changed with the position on the plasmas, rather than with the element purity(pure metal or oxide compound).

An ideal source for the soft x-ray projection lithography requires efficient x-ray generation in a narrow wavelength band where multilayer coated mirror can be fabricated to yield high reflectivity. Laser plasma sources produced by tin and antimony targets are regarded as an optimum choice at the 13-nm wavelength where Mo/Si multilayer mirrors have high reflectivity.[1] Narrow and intense quasi-continuum(unresolved transition array, UTA) overlaid on the recombination continuum is emitted from the tin plasma near 13.5 nm. Since oxide compounds(SnO_2 and SnO) of tin can be manufactured to be very fine particles with a few tens of nanometer size, a gas-mixed powder target of the oxides may be realized. Enhanced intensity and narrowing of the UTA were obtained with the oxide powders blowing off a gas valve filled with argon and xenon gases.[2] In this paper, we intend to investigate the physical mechanism on the enhancement and the narrowing, and thus measured space-resolved soft x-ray spectra from pure metal and its oxide plasmas of the fifth period elements.

Spectra were produced by focusing a Nd:YAG laser of 1064-nm wavelength with a maximum energy of 500 mJ in a 10-ns pulse width onto a planar target. Focusing power density on the target was changed in the range of 0.7 to 3.3×10^{11} W/cm^2 in order to study intensity dependence of the spectra. Oxide powers of tin and indium were glued on a double-sided tape and compressed by hand to form a slab target, and SnO_2 solid target coated on an aluminum substrate was also prepared. Space-resolved spectra along the target normal were measured using a flat-field soft x-ray spectrometer equipped with a toroidal mirror.[3, 4] Dependence of the emission spectra on the angle between observation axis and the target normal was also obtained using an additional spectrometer at a different measurement angle from the former. All the spectra were taken with a soft x-ray CCD, and only one shot of the laser pulse was sufficient for the detection.

The space-resolved spectral images and intensity distributions along the target normal are shown in Fig. 1 for the observation angle of 90° with respect to the target normal. The bandwidth and peak intensity of the UTA centered at 13.5-nm wavelength are dramatically changed with the position from the target surface, rather than with plasma purity(pure metal or its oxides). This UTA is due primarily to $4p^64d^N - 4p^64d^{N-1}4f$ (4d–4f) and $4p^64d^N - 4p^54d^{N+1}$ (4p–4d) transitions in the ion stages from Sn^{4+} to Sn^{13+}.[5] At shorter wavelengths the spectra contain additional weak UTA's from $4d^N - 4d^{N-1}5f$ and $4d^N - 4d^{N-1}6p$ transitions that produce weak bands of quasicontinua down to 6 nm,[6] especially in the pure tin spectra. The bandwidth of the UTA at 13.5 nm is very narrow near the target surface, and becomes wider with the position and finally merges into background continuum far away from the target surface. Intensities of the short-wavelength UTA's decrease with the position, whereas the long-wavelength shoulder of the 13.5-nm UTA increases in moving away from the target.

According to the atomic structure calculations performed by several authors,[5, 7, 8] because the 4p4f

and $4d^2$ orbitals have almost the same energy, the configurations $4p^64d^{N-1}4f$ and $4p^54d^{N+1}$ strongly mix. The configuration interaction causes the narrowing of the UTA, and also leads the weighted center of gravity to shift to shorter wavelength compared with those in the absence of the mixing. In the case of tin, the effect is complicated because the overlap of 4d and 4f increases as N decreases up to Sn^{9+} and configuration interaction effects are greatly reduced since the energy shift depends strongly on the dipole matrix element. The net result is that in the lower ion stages configuration interaction effects are less important and the extent of the emission is greater than for higher stages.[5] The effect is most noticeable on the long wavelength shoulder of the UTA. Since temperature and ion stage of plasmas decrease with the position from target surface due to plasma expansion, the configuration interaction becomes less effective and thus the bandwidth increases.

In conclusion, the emission properties of the tin UTA at 13.5-nm wavelength strongly depend on plasma conditions, and the variation can be investigated from the space-resolved measurement along the target normal. Detailed atomic structure calculation and plasma hydrodynamic simulation will be performed for further understanding of the mechanism.

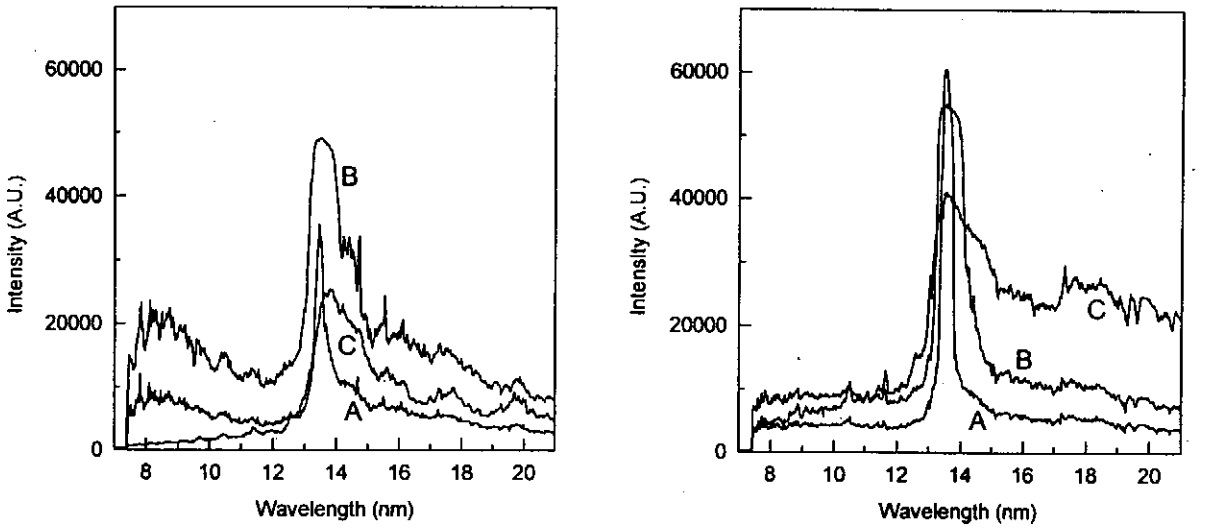

Fig. 1. Space-resolved intensity distributions of the soft x-ray emission from pure tin and its oxide plasma. (a) emission from the pure metal target and (b) emission from SnO_2 coating target, for the observation angle of 90° with respect to the target normal. In the intensity distributions, the position moves away from the target surface in going from A and then B to C lines : A to B line corresponds to 144 μm in distance, and B to C line to 240 μm.

References

[1] R. L. Kauffman et al., App. Opt. **32**, 6897 (1993).

[2] T. Matsui and N. Kogawa, Extended abstracts of the 46th spring meeting of the Japan society of applied physics and related societies, 722 (1999).

[3] I. W. Choi et al., App. Opt. **36**, 1457 (1997).

[4] H. Fiedorowicz et al., Opt. Comm. **163**, 103 (1999).

[5] G. O'Sullivan and R. Faulkner, Opt. Eng. **33**, 3978 (1994).

[6] W. Svendsen and G. O'Sullivan, Phys. Rev. A, **50**, 3710 (1994).

[7] P. Mandelbaum et al., Phys Rew. A **35**, 5051 (1987).

[8] J. Bauche et al., J. Phys. B : At. Mol. Phys. **20**, 1443 (1987).

Effects of electron-impact inner-shell ionization of Na-like ions on the linear polarization of the $(2p_{3/2}^{-1}3s)\,J = 1,2 \rightarrow 2p^6$ Se^{24+} X-ray lines

M.K. Inal[1], H.L. Zhang[2], and D.H. Sampson[3]

[1] *Institut des Sciences Exactes, Departement de Physique, B.P. 119, 13000 Tlemcen, Algeria*
[2] *Appl. Theor. and Comput. Phys. Div., Los Alamos National Laboratory, Los Alamos, NM 87545, USA*
[3] *Dept. of Astron. and Astrophys., The Pennsylvania State University, University Park, PA 16802, USA*

Abstract. The degree of linear polarization of the two X-ray lines $(2p_{3/2}^{-1}3s)\,J = 1,2 \rightarrow 2p^6$ emitted by Ne-like Se^{24+} ions collisionally excited by an electron beam has been calculated allowing for the process of inner-shell ionization of Se^{23+} ions. The required cross sections for excitation and ionization to individual magnetic sublevels were computed in a fully relativistic distorted-wave approximation. The inner-shell ionization is found to be almost unselective in populating the different $|M|$ sublevels of each upper level and its inclusion can result in a significant depolarization of the two lines.

1 Introduction

The linear polarization of X-ray line emission following collisions of highly charged ions with an electron beam has been the subject of numerous theoretical studies during the past 15 years [1-4]. Such studies are of great interest for applications in the modeling and diagnostics of hot laboratory and astrophysical plasmas [5] in which occur a non-thermal electron population with an anisotropic velocity distribution. The knowledge of X-ray line polarization is also of importance in EBIT experiments [6] for the interpretation of line intensity ratios.

Among the electron-ion collisional processes giving rise to the X-ray line emissions, only excitation [1,3,7-10] and dielectronic recombination [2,4,11] were treated in the previous polarization studies. The purpose of this paper is to allow for the process of inner-shell ionization, which could make a significant contribution to the population of excited levels particularly in non-thermal plasmas. Here we consider direct ionization of an internal $2p_{3/2}$ electron of the Na-like selenium ion in its ground level $(2p^6 3s)_{1/2}$, and focus on the influence of this process on the linear polarization of both the electric-dipole $(2p_{3/2}^{-1}3s)_1 \rightarrow 2p^6$ and the magnetic-quadrupole $(2p_{3/2}^{-1}3s)_2 \rightarrow 2p^6$ lines (labeled $3G$ and $3H$, respectively) emitted by Ne-like Se^{24+} ions.

2 Theory

Cross sections for excitation of Ne-like Se^{24+} ions from the ground level to individual magnetic sublevels of the $(2p_{3/2}^{-1}3s)_{1,2}$ levels were calculated by using the fully relativistic distorted-wave code of Ref. [7]. For inner-shell ionization of Na-like Se^{23+} ions from their ground level to the magnetic sublevels of the same levels the corresponding cross sections were computed in a fully relativistic distorted-wave method using the basic code of Ref. [12] modified analogously to the modifications for excitation given in Ref. [7].

For the Ne-like electric-dipole $J=1\rightarrow0$ and magnetic-quadrupole $J=2\rightarrow0$ lines of interest here observed at 90° with respect to the incident electron beam, the degree of linear polarization P is related to the populations N_M of the upper M-sublevels by $P = (N_k - N_1)/(N_k + N_1)$, where $k=0$ for $J=1\rightarrow0$ and $k=2$ for $J=2\rightarrow0$. In the present investigation we consider a low-density beam of electrons, such as found in EBIT devices. Moreover, only direct-excitation from the Ne-like $2p^6$ ground level and inner-shell ionization from the Na-like $2p^6 3s$ ground level are taken into account. In this case, N_M in Eq. (3) can be replaced with the combination $\sigma_M^e + r\sigma_M^i$ of cross sections for excitation σ_M^e and ionization σ_M^i to the M sublevel, r being the ratio of the Na-like ground-state density to the Ne-like ground-state density.

[1] E-mail : bel@ist.cerist.dz

3 Results

Table 1 shows the results of our calculations for both excitation and inner-shell ionization cross sections at incident electron energies between 190 and 800 Ry. It can be seen that the excitation process is highly selective in populating the magnetic sublevels of the J=1 level. The cross section ratio σ_0^e / σ_1^e between the M=0 and 1 sublevels can reach value of almost 4. For the J=2 level the M=1 sublevel is preferentially excited relative to M=2 by a factor less than ~1.5. However, for both J=1 and 2 levels there are insignificant differences of population between the magnetic sublevels due to inner-shell ionization.

Table 1: Cross sections (in units of 10^{-23} cm^2) for both excitation of Ne-like Se^{24+} ions from the ground level $(2p^6)_0$ (upper entries) and inner-shell ionization of Na-like Se^{23+} ions from the ground level $(2p^6 3s)_{1/2}$ (lower entries) to individual magnetic sublevels M of the two $(2p_{3/2}^{-1} 3s)_{1,2}$ levels for various incident electron energies ε. Calculated threshold energies for excitation ΔE and ionization I are also given.

Upper level	ΔE (Ry)	I (Ry)	M	ε (Ry) 190	250	400	800
$(2p_{3/2}^{-1} 3s)_1$	105.65	181.79	1	13.94 22.13	15.02 111.1	17.18 154.7	18.07 133.9
			0	54.95 22.63	56.36 114.5	51.19 164.0	35.40 140.6
$(2p_{3/2}^{-1} 3s)_2$	105.42	181.57	2	3.442 22.51	1.889 110.1	0.6584 150.8	0.1269 131.1
			1	5.334 23.12	2.915 114.0	0.9138 161.7	0.1339 138.9
			0	5.963 23.32	3.256 115.4	0.9988 165.4	0.1362 141.5

Table 2: Degree of linear polarization P (%) of the lines $3G$ (upper entries) and $3H$ (lower entries) of Se^{24+} ions for various incident electron energies ε and for differents values of the ratio r of the ground-level ion population Se^{23+}/Se^{24+}.

	ε (Ry) 190	250	400	800
0.00	59.5 -21.6	57.9 -21.4	49.7 -16.2	32.4 -2.7
0.05	57.7 -17.4	50.2 -7.6	40.9 -4.7	26.3 -2.9
0.10	56.0 -14.6	44.4 -5.2	34.9 -4.1	22.2 -2.9
0.20	52.8 -11.3	36.1 -3.6	27.2 -3.8	17.2 -2.9
0.50	45.2 -7.0	23.4 -2.5	17.0 -3.6	10.8 -2.9

The calculated degrees of linear polarization for the two lines $3G$ and $3H$ are presented in Table 2 for the four incident electron energies and for several values of the parameter r, the Se^{23+}/Se^{24+} abundance ratio. As seen, the inner-shell ionization process can lead to a significant depolarization of the lines.

Acknowledgements. One of us (MKI) gratefully acknowledges financial support of NIFS for his participation in the Seminar. The computational work was done on NERSC computers at Livermore, California.

References

[1] Inal M K and Dubau J 1987 *J. Phys. B* **20** 4221
[2] Inal M K and Dubau J 1989 *J. Phys. B* **22** 3329
[3] Reed K J and Chen M H 1993 *Phys. Rev. A* **48** 3644
[4] Shlyaptseva A S, Mancini R C, Neill P, and Beiersdorfer P 1999 *J. Phys. B* **32** 1041
[5] Fujimoto T and Kazantsev S A 1997 *Plasma Phys. Control. Fusion* **39** 1267
[6] Wong K L, Beiersdorfer P, Reed K J, and Vogel D A 1995 *Phys. Rev. A* **51** 1214
[7] Zhang H L, Sampson D H, and Clark R E H 1990 *Phys. Rev. A* **41** 198
[8] Inal M K and Dubau J 1993 *Phys. Rev. A* **47** 4794
[9] Zhang H L and Sampson D H 1995 *Phys. Rev. A* **52** 3827
[10] Fontes C J, Zhang H L, and Sampson D H 1999 *Phys. Rev. A* **59** 295
[11] Chen M H and Scofield J H 1995 *Phys. Rev. A* **52** 2057
[12] Zhang H L and Sampson D H 1990 *Phys. Rev. A* **42** 5378

Plasma Polarization Spectroscopy

Takeru Inoue*1, Akihiro Tanaka, Kazuki Kawakami, and Takashi Fujimoto

Department of Engineering Science, Faculty of Engineering, Kyoto University, Kyoto 606-01, Japan

Abstract. We have observed the polarization of impurity oxygen ion lines from the WT-3 tokamak at Kyoto University and estimated the velocity distribution of electrons in the plasma by comparing the experiment with the kinetic model calculation.

1. Experiment observations

The WT-3 tokamak at Kyoto University had major and minor radii of 0.65 m and 0.23 m, respectively, and the joule heating current was 60 kA in the toroidal magnetic field of 1.5 T.

The radiation from the central chord went through the viewing window, the five-mirror system to be focused onto the entrance slit to tailor the image of the plasma. Thus a thin beam of light (0.4 mm x 0.1 mm) was incident from the entrance slit on the calcite plate (5.4 mm thick) placed just behind the slit. The optic axis of the crystal was 30 degrees with respect to the surface normal. The π-light, the electric vector of which oscillated in the troidal direction, was the o-ray for the crystal, and the σ-light was the e-ray, so that it was displaced by the crystal vertically by about 0.5 mm. After dispersed by the grating these rays were focused onto the CCD detector surface.

Thus we obtained the polarization resolved spectra. Figure 1 shows an example of the image on the surface. These are the berylliumlike oxygen $3^3S(J=1)$ -$3^3P(J=0,1,2)$ lines. The weakest (1-0) line is never polarized and we used this line to calibrate the sensitivities of our detection system for different polarized components. we defined the intensity as $I = 2/3(I_\pi+2I_\sigma)$ and the longitudinal alignment as $A_L = (I_\pi-I_\sigma)/(I_\pi+2I_\sigma)$, where I_π and I_σ are, respectively, the intensities of the π- and σ-light.

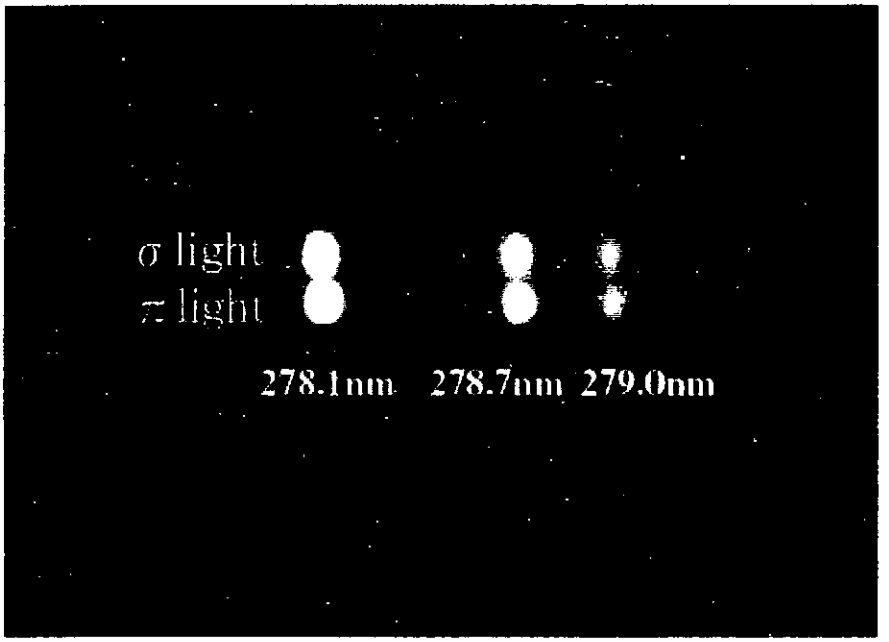

Figure 1. An example of the image on the CCD detector surface.

*1 E-mail : inoue@jasmine.kues.kyoto-u.ac.jp

We recorded the spectra in every 30 ms, and obtained I and A_L as shown in Fig. 2, where I (1-2) and I (1-1) have been normalized by I (1-0).

2. Population-alignment collisional-radiative (PACR) model

We estimated the velocity distribution of electrons by a kinetic model (PACR model). In the model, we assign the population and the alignment to each of the levels, and these quantities are connected by the cross sections or the rate coefficients. We calculated the populations and the alignments from the rate equations.

We assumed that the velocity distribution is expressed by different temperatures for the toroidal direction, T_t, and the poloidal direction, T_p.

Figure 3 shows a calculation result. The intensity ratio is consistent with the experiment. The longitudinal alignment at $\alpha = 10$ is roughly consistent with the experiment at 60 ms. The velocity distribution at $\alpha = 10$ is a very thin pancake like. The other experiment data, at 30 ms and 90 ms, cannot be explained within the present assumption.

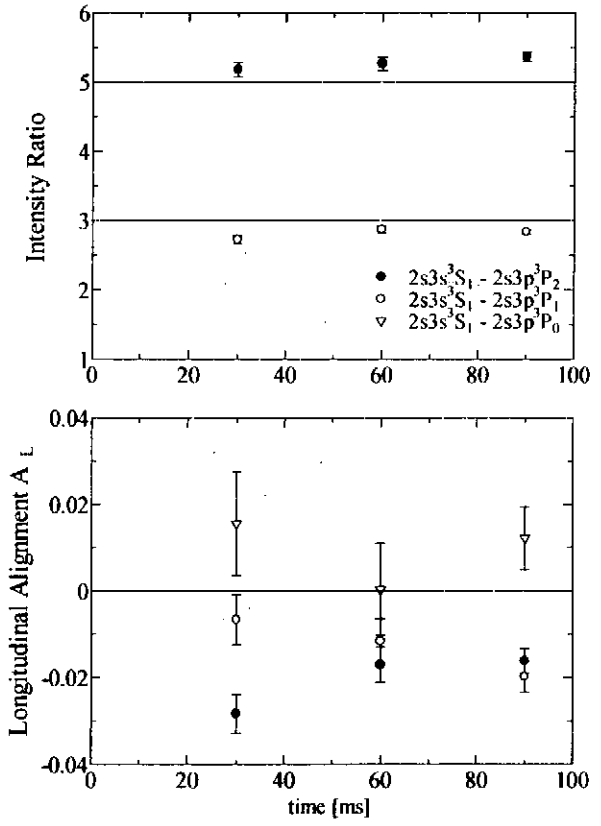

Figure 2. Intensity ratio and longitudinal alignment from the WT-3 tokamak. We can see polarization in J=2 to J=1 and J=1 to J=1.

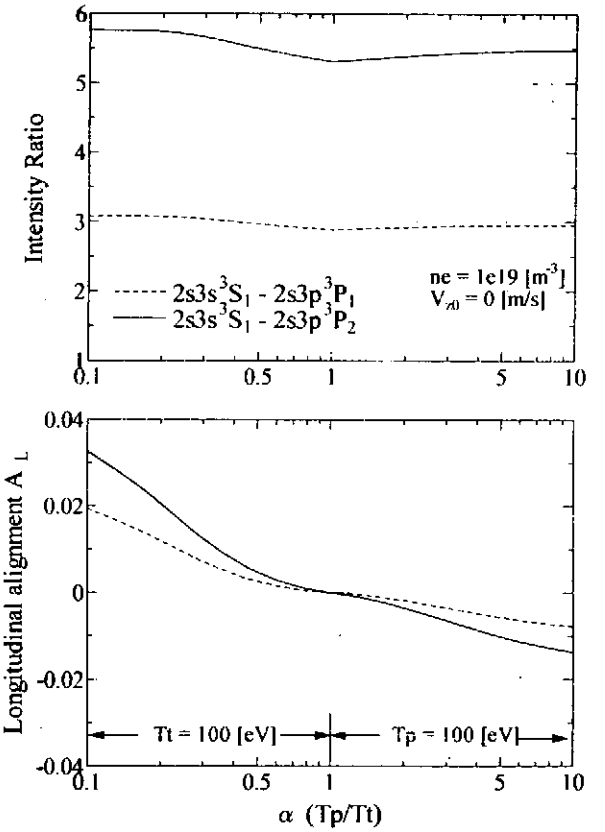

Figure 3. Intensity ratio and longitudinal alignment from kinetic model (PACR model).

References

[1] T.Fujimoto and Sergei A Kazantsev 1997 *Plasma Phys. Control. Fusion* **39** 1267

[2] M.Nakai 1999 *Thesis for the degree of Master*

Absolute Calibration of Space- and Time-Resolving Flat-Field Vacuum Ultraviolet Spectrograph for Plasma Diagnostics

Yuuji OKAMOTO, Masayuki YOSHIKAWA, Naohiro YAMAGUCHI [1)], Chikara WATABE, Teruo TAMANO, Eiichiro KAWAMORI and Kiyoshi YATSU

Plasma Research Center, Univ. of Tsukuba, Tsukuba, Ibaraki 305-8577, JAPAN

1) Toyota Technological Institute, 2-12-1 Hisakata, Tempaku, Nagoya 468-8511, JAPAN

Measurements of spectra in the wavelength range from the vacuum ultraviolet (VUV) to soft x-ray are important means to diagnose impurities in magnetically confined plasmas used in fusion plasma such as a GAMMA10 plasma. Recently, a space- and time-resolving flat-field grazing-incidence vacuum ultrarviolet spectrograph has been constructed for simultaneous observation of spatial, temporal and spectral distributions of plasma radiation in the wavelength range 150-1050 Å. The spatial image is realized by an optical system of an astigmatic pinhole camera, using a short entrance slit of limited height which provides spatial resolution and averration-corrected concave grating with variable groove spacing and image-intensified two-dimensional detector.

Figure 1 shows a schematic of the VUV spectrograph on the GAMMA10. It consists of an entrance slit of limited height (100μm × 2-6mm) which provides spatial resolution, an averration-corrected concave grating with variable grooves (Hitachi P/N001-0464) which give a flat-field spectral output plane, and an image-intensified two dimensional detector system. The specifications of the grating are that a radius of curvature is 500 mm, nominal groove density 1200g/mm, braze angle 3.08 ° and ruled area 48 × 48 mm^2, the incident angle 51°, and the effective braze wavelength about 600 Å. One can observe the upper half of the plasma with a field of view of about 25 cm diameter. The detector system consists of a MCP intensified image detector assembly (Hamamatsu F2814-23P, 50 × 50 mm^2) and two image recording cameras. One is an instant photographic camera and the other is a high speed solid state camera (Reticon MC9256) with a fast scanning controller (C.C.D. RS-9100). The frame rate with full image size, 256 × 256 pixels, can be changed from 4 to 106 frame/s.

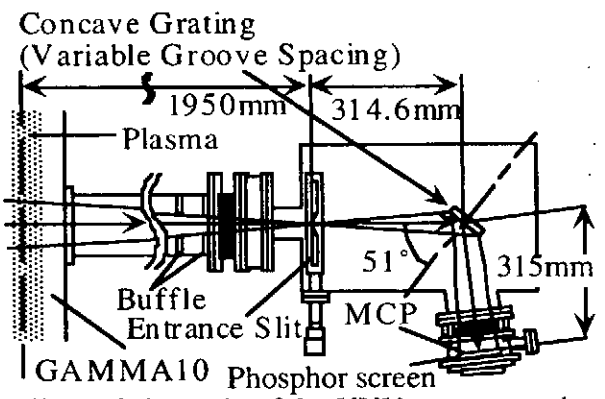

Fig.1 Schematic of the VUV spectrograph on the GAMMA 10

An absolute calibration experiment has been performed by using synchrotron radiations at the PF in KEK (BL-11C) [1]. The height of the entrance slit was 6 mm. The number of incident photons was measured just behind the entrance slit by using an XUV silicon photodiode which had already been absolutely calibrated. The output spectral image was recorded by using high speed solid state camera at 40 frame/s. The voltage of MCP was -1.2 kV and the voltage of phosphor screen was 2.6 kV. Measurements were repeated for incident S.R. beam wavelengths from 450 Å to 1050 Å at intervals of 50 Å at the central point of the grating along the groove direction. Output of the spectrograph was estimated by integrating intensity of whole space of recorded image. Efficiency of the spectrograph was obtained by deviding output of the spectrograph by a number of photons. Figure 2 shows a relative efficiency of the spectrograph as a function of wavelength. The sensitivity of the high speed solid state camera response against photon exposure was obtained. This experiments were carried out

under the S polarization of the spectrograph. The position of a peak (at nearly 550 Å) corresponds to the braze wavelength of the grating used in this spectrograph. We were able to observe the second order diffracted lights of wavelength range from 300 Å to 500 Å incident light in this spectrograph. It is noted that at the wavelengths above 900 Å, the sensitivity of second order diffracted light of lower wavelength is better than that of the first order diffracted light. To handle the spectrum at the wavelengths above 900 Å on plasma experiments, we must pay attention to the second order diffracted light and deduct the effect of second order diffracted light. At the wavelength under 900 Å, it is probably neglected the effect of second order diffracted light so that the reflect rate of Pt used as coating of the concave grating is quite low at the wavelengths under 400 Å.

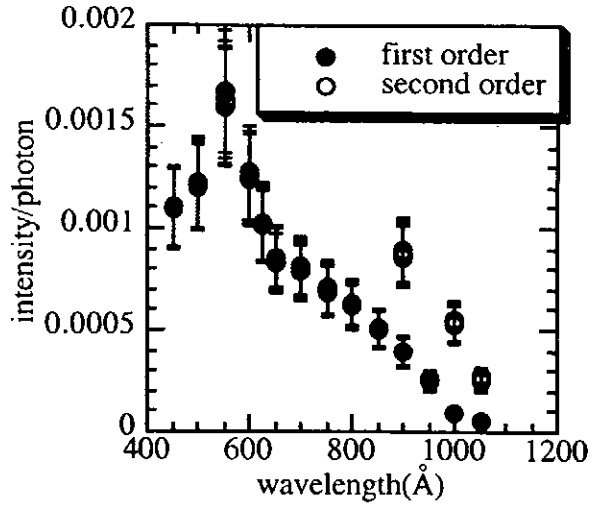

Fig.2 Sensitivity for wavelength

The VUV spectrograph has been placed in the central cell region of the GAMMA10. Plasma confinement is achieved not only by a magnetic mirror configuration but also by positive high potentials at the end regions. The plug potential is produced by means of ECRH at the plug/barrier region. The main plasma confined in the GAMMA10 is produced and heated by ICRF power deposition. Space- and time-resolved spectra have been obtained successfully in GAMMA10 experiments. Figure 3(a) shows the spectrum of the image at 10 cm radius taken by using the high speed camera and (b) show the spectrum at 10 cm radius after correction sensitivity of VUV spectrograph.

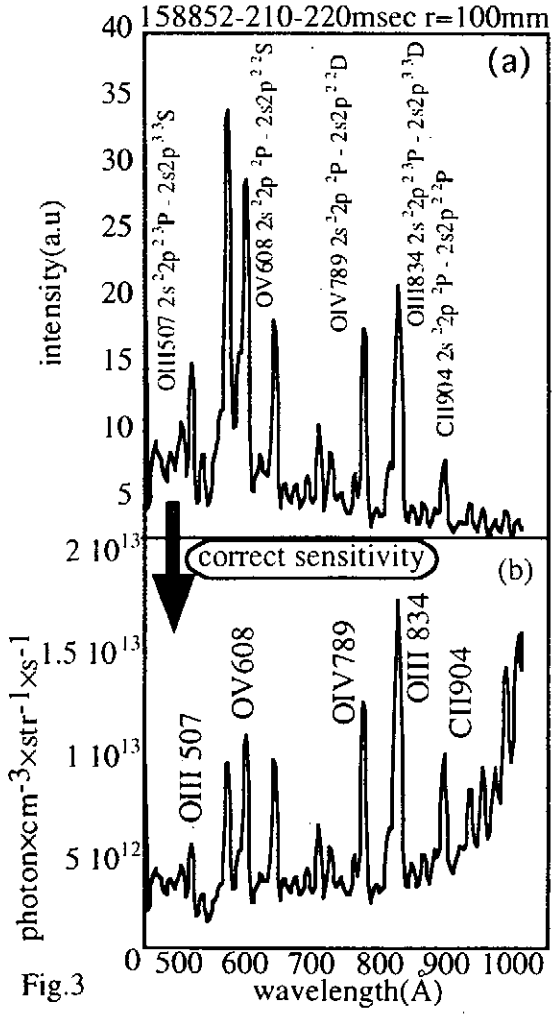

Fig.3

We analyzed a spatially and time resolved VUV spectrophotograph using the following procedure. First a brightness profile for a given wavelength interval was obtained from a space resolved spectral image after correction of the efficiency for the intensified system of the spectrograph and the sensitivity of spectrograph. This procedure was carried out along the wavelength range from 450 Å to 1050 Å, of course we must consider the effect of second order diffracted light. Next, the brightness profile of each wavelength was transformed to an Abel inverted profile. Then, each Abel inverted profile was reconstructed into a two-dimensional image. Thus, one can investigate the emissivity profile of each spectal source in a visual way from a spatially and time resolved VUV spectrograph.

Preference

1. Yoshikawa, M. , Yamaguchi, N. , Aota, T. , Ikeda, K. , Okamoto, Y. Yatsu, K . & Tamao, T. (1998). J.Synchrotron Rad. 5, pp.762-765

Spectroscopic study of Ti-like ions

H. Watanabe[1], C. Yamada[1,2], T. Fukami[2], D. Kato[1] and S. Ohtani[1,2]

[1] *Cold Trapped Ions Project, ICORP, Japan Science and Technology Corporation (JST), Axis Chofu 3F, 1-40-2 Fuda, Chofu, Tokyo 182-0024, Japan*
[2] *University of Electro-Communications, Chofu, Tokyo 182-8585, Japan*

Abstract. The magnetic dipole transition of $(3d^4)$ $^5D_2$-$^5D_3$ of Ti-like ions have been measured for Sb(Z=51), I(Z=53), Xe(Z=54), Cs(Z=55) and Ba(Z=56). The wavelengths of this transition were measured to be 470.24(3), 430.33(8) nm, 413.88(7) nm, 402.14(12) nm, 393.08(18) nm for Sb, I, Xe Cs and Ba, respectively.

Introduction. Feldman *et al.* [1] calculated wavelengths of the magnetic dipole transition of $(3d^4)$ $^5D_2$-$^5D_3$ of Ti-like ions for Z=42-92 by use of the multi-configuration Dirac-Fock method. Their result shows that these lines appear in the visible region and the wavelengths are stable with respect to change in Z. This feature is rather exceptional for an isoelectronic series, since it is common that wavelengths decrease with increase in Z. The wavelengths of this transition were measured for Xe, Ba, Nd and Gd [2,3,4]. The predicted Z dependence on wavelengths reproduces experimental results, however the absolute values of measured wavelengths are different from the prediction. We have measured wavelengths and compared with theoretical values for Sb, I, Xe, Cs and Ba. Some of the visible and near-UV lines of impurity ions have been used for the purpose of plasma diagnostics. These lines may serve as a probe for high temperature plasma in future fusion devices.

Experimental. We used Tokyo-EBIT [5] to produce and to trap highly charged Sb, I, Xe, Cs and Ba ions. A biconvex fused silica lens with a focal length of 153.8 mm (designed at 546.1 nm) was placed at 347 mm from the electron beam axis of the EBIT and at 265 mm from the entrance slit of a monochromator. The position of the monochromator was set on the optical axis defined by a laser beam and slightly adjusted by measurements of light from the EBIT. The monochromator was of the Czerny-Turner type (Jobin-Yvon HR320) with focal length of 320 mm and f number of 4.2. The grating of 600 grooves/mm and blazed at 800 nm was used in the second order for the I, Xe, Cs and Ba measurements, and that of 1200 grooves/mm and blazed at 400 nm was used for the Sb measurement. The entrance slit was set 100 μm. A liquid nitrogen cooled CCD camera (Princeton Instruments LN/CCD-1100-PB/VISAR) was placed in the focal plane of the monochromator. The CCD pixels had width of 24 μm, which corresponded to 0.055 nm in wavelength and were mounted in the 1100×330 array. The electron beam energy and current were typically about 2.2 keV and 25 mA, respectively. Accumulation of the signals was for

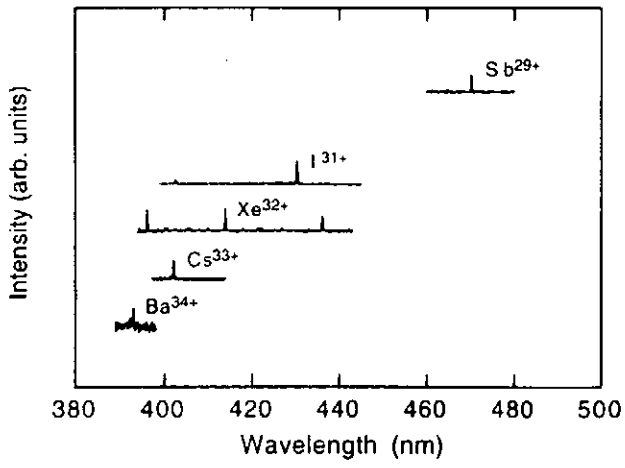

Fig. 1 The visible spectra of the highly charged Sb, I, Xe, Cs and Ba ions.

E-mail h_watana@ils.uec.ac.jp

1-7 hours depending on the signal intensity.

Result and discussion. The results are shown in figure 1. The wavelength scale was calibrated with light from low pressure discharge lamps (He, Ne, Ar, Kr, Xe and Hg). The light was introduced from a port opposite the monochromator. We determine the center of lines by fitting a gaussian function. The uncertainties considered are statistical uncertainty propagated by the fitting procedure and uncertainty originating from the wavelength calibration. Both the uncertainties are added in quadrature. The lines observed at 470.24(3), 430.33(8) nm, 413.88(7) nm, 402.14(12) nm, 393.08(18) nm are identified as $(3d^4)$ $^5D_2$-$^5D_3$ transition of Ti-like Sb, I, Xe, Cs and Ba ions, respectively. The line observed at 396.19(12) nm is $(3d^5)$ $^4G_{7/2}$- $^4G_{9/2}$ transition of V-like Xe ion according to Morgan *et al.* [2] and that at 436.15(8) nm is line from Kr-like Xe ion according to Crespo López-Urrutia *et al* [6]. The line at 402.60(9) nm is from lower charge state ion of I, since this line was observed at lower electron beam energy at which Ti-like ion line disappeared. In table 1 we summarize the experimental results for $(3d^4)$ $^5D_2$-$^5D_3$ of Ti-like ions together with previous results. Recently we calculated wavelengths of these lines by the multi-configuration Dirac-Fock method (GRASP92 code [7]). We also show this result together with that of Feldman *et al* [1]. For Xe and Ba the agreement between the experimental results is good. In figure 2 we compare the experimental results with theoretical ones. Theoretical results reproduce Z dependence of the experimental ones. However discrepancy of the result of Feldman *et al.* is rather large. Our theoretical result agree well with the experimental results. The error of the calculation is reduced less than 1%.

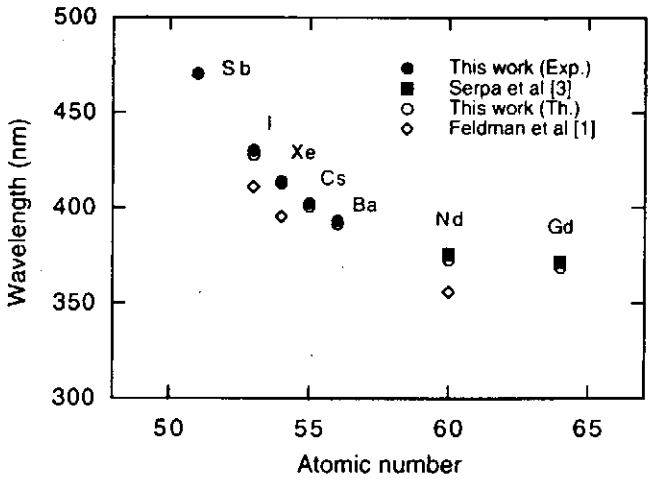

Fig. 2 Comparison between the experimental and theoretical wavelengths.

Table 1

	This work (Exp.)	This work (Th.)	Feldman et al [1]	Morgan et al [2]	Bieber et al [4]
Sb	470.24(3)	472.91			
I	430.33(8)	430.71	410.95		
Xe	413.88(7)	415.64	395.25	413.94(20)	
Cs	402.14(12)	402.85			
Ba	393.08(18)	393.65		393.24(20)	393.239(8)

[1] Feldman, U *et al*, J. Opt. Soc. Am. B **8**, 3 (1991)
[2] Morgan, C. A. *et al*, Phys. Rev. Lett. **74**, 1716 (1995)
[3] Serpa, F. G. *et al*, Phys. Rev. A **53**, 2220 (1996)
[4] Bieber, D. J. *et al*, Phys. Scr. **T73**, 64 (1997)
[5] Currell, F. J. *et al*, J. Phys. Soc. Jpn **65**, 3186 (1996)
[6] Crespo López-Urrutia, J. R. *et al*, "N-Division Experimental Physics Annual report", Lawrence Livermore National Laboratory, 26 (1995)
[7] Parpia, F. A. *et al*, Comp. Phys. Commu. **94**, 249 (1996)

THOMSON SCATTERING MEASUREMENT WITH THE TOKYO-EBIT

H.Kuramoto[1,*], T.Kinugawa[1], I.Yamada[2], C.Yamada[1,3] and S.Ohtani[1,3]

1 *Cold Trapped Ions Project, ICORP, JST, Chofu, Tokyo 182-0024, Japan*
2 *National Institute for Fusion Science, Toki, Gifu 509-5254, Japan*
3 *University of Electro-Communications, Chofu, Tokyo 182-8585, Japan*

We have observed Thomson scattering using the Tokyo-EBIT to measure the electron beam radius and to discuss the electron motion. A Doppler shift from the Thomson scattering spectrum was corresponded to calculation values. Also, we describe the device and report measurements of the electron beam diameter.

We have performed Thomson scattering measurements using the Tokyo-Electron Beam Ion Trap(EBIT). This measurement will give us important parameters of the EBIT. Especially, knowing the density profile of the electron beam is useful for the determination of absolute cross sections. Thomson scattering is a standard diagnostic for measuring the electron temperature and density profiles in fusion plasmas.

The instruments of this measurement consist of a YAG laser(532nm-CW, Verdy; Coherent) and a CCD camera(LN/CCD-1100PB; Princeton Instruments) for detection. Alignment of the laser is used by transit and alignment of a focus of CCD camera is used by a probe which has 1mm diameter. Especially, alignment of the laser is very difficult and important for getting a signal of the Thomson scattering. The laser light is injected on the upper window of the trap region and we detected the signal on the horizontal view port, that is 90 degree scattering lights. Typical conditions of the measurement are the laser power is 2W, exposure time of the CCD camera is 150 sec, beam energy is 15keV and beam current is 100mA. Also, we put a polarizer in front of CCD camera and performed experiment, that is electron beam on/off[1]. As these results, we concluded that the observed signal is the Thomson scattering.

We have also measured a Thomson scattering spectrum using a set of interference filters. Each filter has about 10nm FWHM. Figure 1 shows the results of this experiments. The solid curve are fitted with Gaussian profile. As in the figure, central wavelength of the spectrum is 427.46±1.67nm and the full width of half

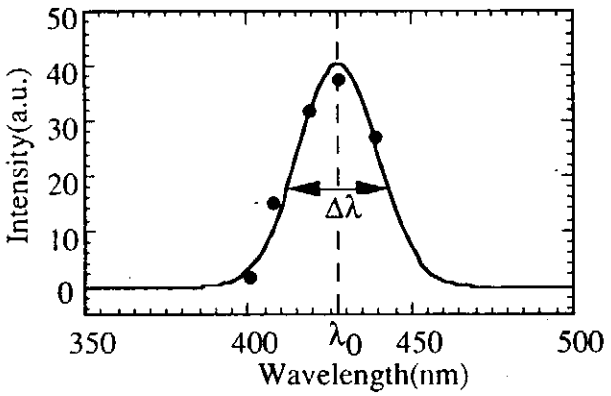

Figure 1: Thomson scattering spectral

*kuramoto@hci.jst.go.jp

maximum(FWHM) is 34.10nm. Here, the central wavelength on relativity is given by

$$\lambda_0 = \frac{\lambda_{laser}}{1 + v/c} \qquad (1)$$

where llaser is wavelength of laser light(532nm) and v is the velocity of an electron beam. c is the speed of light. From this equation, central wavelength of the Thomson scattering spectrum is calculated 428.03nm. This value is agreed with the experimental value. From $\Delta\lambda$, we can also obtain the width of energy is 1143eV. This value is too big. Therefore, this is for spiral motion of electron beam.

We have also measured electron beam radius using a lens with 10X magnification. This result is shown in the figure 2. The solid curve are fitted with Gaussian profile. As in the figure, we obtained 35.7±4.7μm, in good agreement with Herrmann theory prediction of r=33.1μm[2] and other EBIT experiments value of 33.9±1.2μm using X-ray pin-hole camera[3].

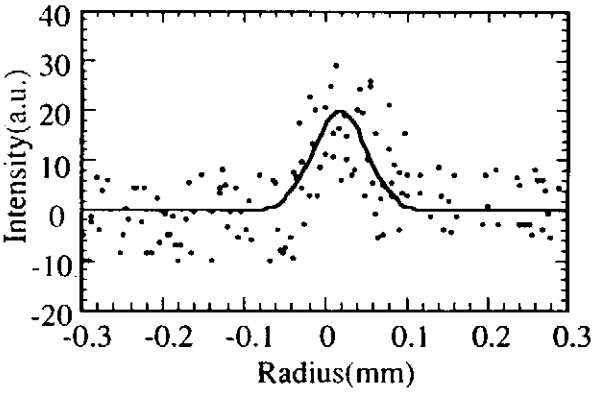

Figure 2: Beam image in a CCD camera.

We have measured the Thomson scattering with Tokyo-EBIT. From these results of experiments, we concluded that the getting signal is the Thomson scattering. Also, these results of the experiments are agree with theory.

References

[1] H.Kuramoto, et al., XXI ICPEAC FR043in sendai.

[2] G.Herrmann, J. Appl. Phys. 29, 127(1958).

[3] D.A.Knapp, et al., Nucl. Instr. and Meth. A334, 305(1993).

SPECTROSCOPY OF NEON INJECTED DISCHARGES IN THE RFX REVERSED FIELD PINCH

L. Carraro, K.B. Fournier[1], M. Mattioli, M.E. Puiatti, F. Sattin, P. Scarin, M. Valisa

Consorzio RFX - Corso Stati Uniti 4, 35127 Padova, Italy
[1]Lawrence Livermore National Laboratory, PO Box 808,L-41 Livermore, CA 94550, USA

Neon has been injected in the Reversed Field Pinch RFX (major radius R=2 m, minor radius a=0.46 m) during 0.8 MA plasma discharges in order to produce a peripheral radiative layer protecting the wall from peak power flux densities that may locally reach ~ 100 MW/m^2. This paper reports the observations of the Ne VI, Ne VII, Ne VIII lines emitted in the spectral range 6-100 nm, that have been simulated by a collisional-radiative atomic model coupled with a 1-dim impurity diffusion code [1].

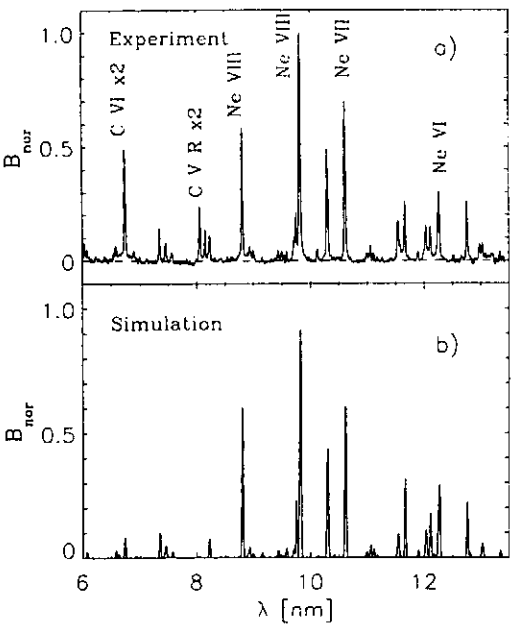

Fig. 1

The spectrum in the region 2-15 nm has been observed along a central line of sight by an extreme grazing incidence vacuum spectrometer equipped with two micro-channel-plate detectors, with a spectral resolution of ~ 0.02 nm (FWHM). The spectrometer has been relatively calibrated against an X-ray source at the K_α lines of O, N, C, B and Be, while it is absolutely calibrated by the branching ratio technique at the CV and CVI and O VII resonance line wavelengths. Fig. 1a shows the Ne spectrum, together with the intrinsic carbon lines, in the range 6-13.5 nm, obtained as the superposition of four spectra measured in similar discharges (n_e=4 10^{19} m^{-3}, T_e=210 eV). Several resonance lines from Ne VI, Ne VII and Ne VIII are emitted in the range 20-100 nm, where a flat-field quasi-grazing incidence spectrometer (SPRED) has been used to monitor the plasma emission (fig. 2a). An absolute calibration of the spectrometer has been obtained by the branching-ratio technique (for a limited number of wavelengths) and by comparing some experimental carbon and oxygen lines with their simulated values.

In the 1-dim impurity tranport code used to calculate the radial distributions of the impurity ions (C, O and Ne) the impurity fluxes are expressed as the sum of a diffusive and an inward convective term: $\Gamma_z = -D(r)\,\nabla\, n_z(r) - v(r)n_z(r)$. The diffusion coefficient D(r) and the convective velocity v(r) have been varied in order to simulate simoultaneously the intrinsic impurity behaviour (in terms of the ratio between C VI Ly_α and CV resonance line, of the C V G-ratio and of the O VII resonance line intensity) and the neon spectrum. The line intensities have been calculated by a collisional-radiative model where recently calculated neon photon emission coefficients are included [1,2]. Fig. 3 shows the radial profiles of

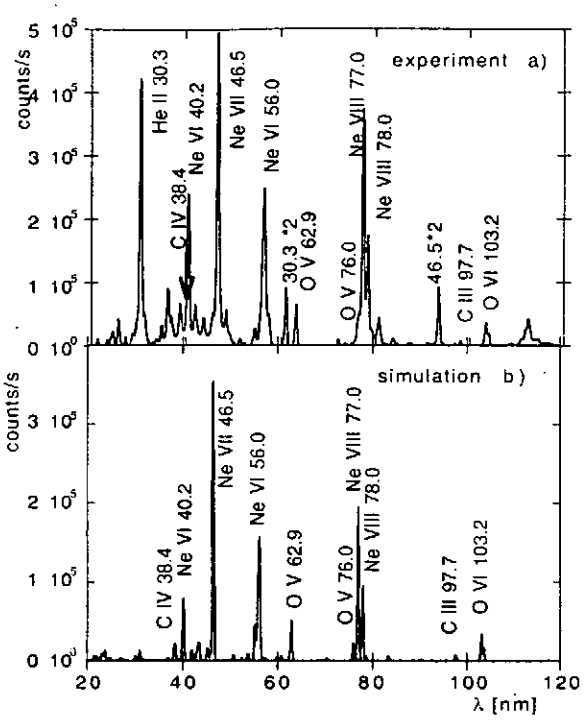

Fig. 2

the transport coefficients used to simulate the discharge corresponding to the spectra reported in figs.1a and 2a: near the edge D(r) decreases from 15 m^2/s to 1 m^2/s (a similar behaviour was also found for the main gas), while v(r) increases up to 30 m/s at about r/a=0.5. A C VI Ly_α / CV R ratio of 1.7 and a G-ratio of 0.53 have been obtained, in good agreement with the experimental values. The corresponding radial distribution of the neon ion populations is shown in fig.4. The impurity concentrations allowing the simulation of the absolute values of the emissivities and of the experimental plasma effective charge, total radiation and visible bremsstrahlung are of about 3% of the electron density for carbon and oxygen and 2% for neon. The final reconstructed spectra are shown in figs 1b and 2b, in comparison with the experimental ones. The flat radial profile of the neon density allows the reproduction of the ratio (~1.5) between the Ne VIII 9.8 nm and the Ne VII 10.6 nm line. Discharges at higher plasma electron densities and lower temperatures, corresponding to different ratioes between the Ne lines have also been simulated with similar transport parameters.

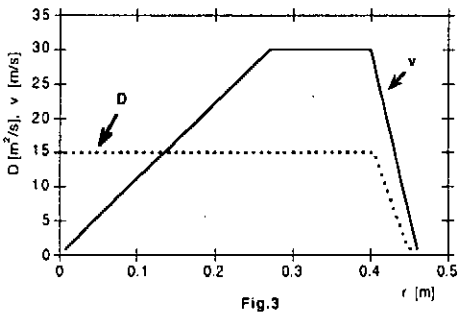

Fig.3

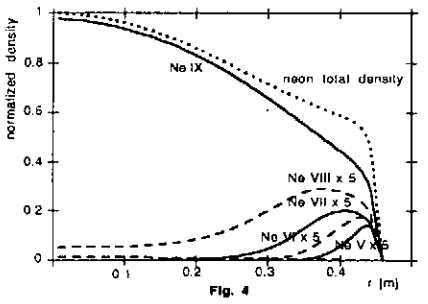

Fig. 4

[1] Mattioli M., et al., "Experimental and simulated neon spectra in the 10 nm range from tokamak and reversed field pinch plasmas", accepted for publication in Physical Review E.
[2] ADAS database: see ADAS user's manual JET report JET-IR (94) 06.

Ar Line Spectroscopy for Diagnostics of Implosion Stability

Yoshihiro Ochi[1], Mitsuhiro Fukao[1], Tohru Kawamura[1], Kazuhisa Fujita[1], Hiroaki Nishimura[1], Isamu Niki[1], Atsushi Sunahara[1], Hiroyuki Shiraga[1], Noriaki Miyanaga[1], Hiroshi Azechi[1], Hideaki Takabe[1], Kunioki Mima[1], Tatsuhiko Yamanaka[1], Sadao Nakai[2], Randolf Butzbach[3], Ingo Uschmann[3], and Echart Förster[3]

[1] *Institute of Laser Engineering, Osaka University, Suita 565-0871, Japan*

[2] *Department of Electronic, Information Systems, and Energy Engineering, Osaka University Suita 565-0871, Japan*

[3] *Institute of Optics and Quantumelectronics, Friedrich-Schiller University, Jena, Germany*

Abstract. In the direct-drive scheme of inertial confinement fusion (ICF), the hot spark formation is critically affected by laser non-uniformities and subsequent hydrodynamic instabilities. Stability analysis for balanced and unbalanced laser irradiation cases are described. Time- and space-resolved x-ray spectroscopic measurements were used for diagnostics. Experimental results were compared with post-processed hydro-code simulations by the aid of x-ray spectrum analysis code.

Fusion pellet implosions in direct-drive scheme were investigated by means of time- and space-resolved x-ray spectroscopic measurements. Fusion pellets filled with a deuterium fuel gas including a small amount of Ar dopant were directly irradiated with twelve beams of intense partially coherent light extracted from Gekko XII laser system. There were two types of implosion studies: First, experimental conditions were carefully chosen to provide implosions that were as stable as possible, these we refer to as the "balanced" case. Second, the energy balance was manipulated so that two specific beams, diametrically opposed to each other, had relative energy differences. This imposes additional low-modal non-uniformity on the pellet, and these experiments are called "unbalanced" cases. Time-, space-, and spectrally resolved x-ray measurements were made for diagnostics. An x-ray steak spectrograph (XSS) with a flat RbAP (100) crystal was used to observe temporal variation of the Ar K-shell emissions ranging from 2.9 to 4.2 keV. Time resolution was 10 ps and energy resolution including source extent was 6 eV at around the Ar^{16+} He-ß ($1s^2$-1s3p) line. A monochromatic x-ray framing camera (M-XFC) was used to provide monochromatic images of Ar^{16+} He-ß and Ar^{17+} Ly-ß (1s-3p) lines in five frames each. Spatial resolution was measured to be 10 μm and spectral resolution for He-ß and Ly-ß lines were respectively set to be 19.0 eV and 34.9 eV. Time resolution and frame interval were respectively 40 ps and 50 ps.

Experimental results were compared with one-dimensional hydrocode simulations, which were post-processed by the aid of x-ray spectrum analysis code RATION. Radiation transport along the line of sight is properly treated by using the opacities and the emissivities calculated by the code. Resultant temporal variations of the volume-integrated intensities of the Ar He-ß line are shown in Fig. 1 together with the experimental results from the XSS (Δ).

ochi@ile.osaka-u.ac.jp

Post-processed monochromatic He-ß images together with experimental results from the M-XFC are also shown in Fig. 2. The time origin was determined so that the onset of the experimental signal coincide with the simulations. Here t=0 corresponds to the time when the shock wave reached the center of the pellet. In the Fig. 1, a reasonable agreement is obtained between the experiment and the simulation for the balanced case, although the peak intensity is somewhat lower. In addition, the size of the emission region shown in Fig. 2 is close to the diameter of the imploded fuel in the simulation. These agreements conclusively suggest that the implosion dynamics are well replicated by the 1-D simulation. In another words, the experimental hot spark was a consequence of stable convergence. The lower peak intensity in experimental data may be caused by the remaining non-uniformity of the mode 6, originally existing in the Gekko XII system. On the other hand, for the unbalanced case, the temporal variations of He-ß line intensity and monochromatic images do not fit to the simulations; the signal disappears at early time of the compression and the size of it is much smaller than that of the simulation. It is concluded that the hot spark was not formed as the 1-D simulation predicts and was probably invaded with dense cold material from outer regions. More sophisticated analysis with 2-D simulation code are underway by imposing plausible velocity perturbations and displacements at the ablation front. This will provide us much useful information to proceed the ICF research to a next step.

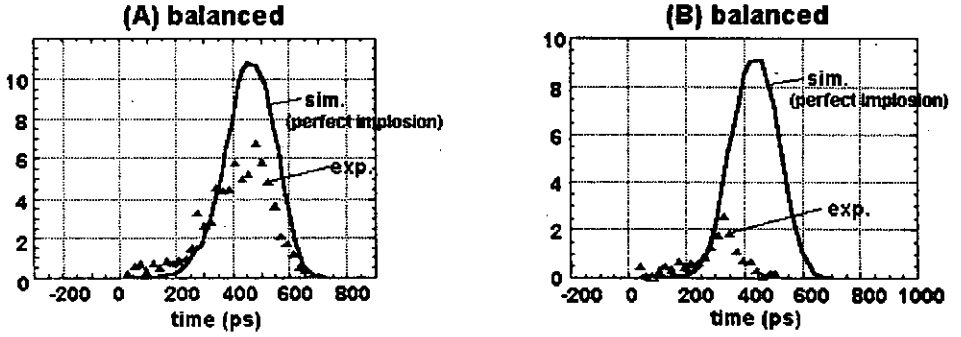

Fig. 1 Temporal variations of the volume-integrated intensities of the Ar He-ß line

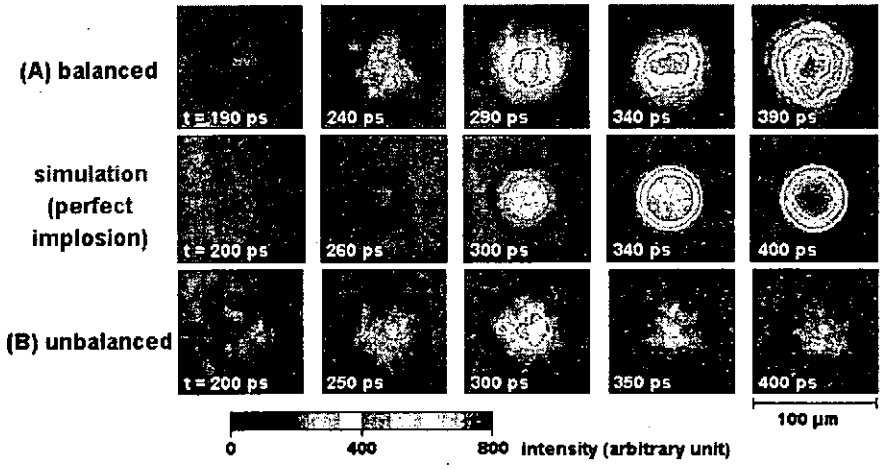

Fig. 2 Temporal variations of the monochromatic Ar He-ß images

X-ray spectroscopy of highly charged neonlike ions at the Tokyo electron beam ion trap

Nobuyuki Nakamura[1], Daiji Kato[1] and Shunsuke Ohtani[1,2]
[1]Cold Trapped Ions Project, ICORP, JST, Chofu, Tokyo 182-0024
[2]The University of Electro-Communications, Chofu, Tokyo 182-8585

Since the neonlike sequence has closed shell structure, its abundance in hot plasmas is high for a wide range of plasma parameters. Therefore, the neonlike sequence can be widely used for many kinds of applications, such as X-ray lasers and plasma diagnostics. For these applications, systematic studies of transition wavelengths, oscillator strengths and collision strengths in neonlike ions are strongly needed. In this paper, we present systematic wavelength measurements for X-ray transitions from excited states with strong configuration mixing among $(2p_{3/2}^{-1}3d_{5/2})_{J=1}$, $(2p_{3/2}^{-1}3d_{3/2})_{J=1}$ and $(2p_{1/2}^{-1}3s)_{J=1}$ to the ground states in neonlike Sb (Z=51), I (53), Cs (55) and Ba (56) ions. The experimental wavelengths are compared to the theoretical values calculated with the multiconfigurational Dirac-Fock (MCDF) method.

The measurements were made with a flat crystal spectrometer on the Tokyo electron beam ion trap[1]. The X-ray transition excited by a 60 μm-diam electron beam was observed with a flat crystal spectrometer. The spectrometer consisted of a flat LiF (200) crystal and a position sensitive proportional counter (PSPC). In the present observations, the crystal was placed at 620 - 730 mm away from the center of the trap and the PSPC at 460 - 740 mm away from the crystal. The effective volume of the PSPC was 100x30x4 mm^3 in which 4 atmospheric pressure of PR gas (90 % Ar + 10% CH_4) was filled. Resolution in position for the present PSPC was typically about 300 μm. The spectrometer was operated in vacuo (~10^{-7} torr) to avoid absorption by air. A beryllium foil with a thickness of 50 μm was used to separate the vacuum of the EBIT (~10^{-9} torr) from the spectrometer.

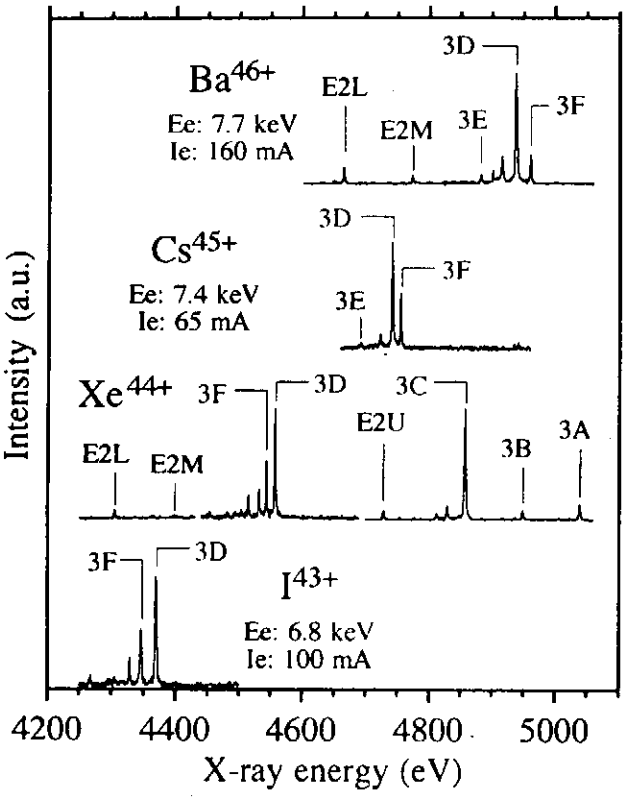

Figure 1. X-ray spectra from neonlike I, Xe, Cs and Ba. The notations used by Beiersdorfer et al. [2] are indicated in the figure. Ee and Ie represent the electron energies and the currents, respectively, at which the spectra were obtained. For neonlike Xe, three spectra (4250-4430, 4440-4690 and 4700-5060 eV) were observed individually. It is noted that intensity ratio between different spectra cannot be compared.

Figure 1 shows the X-ray spectra from neonlike I, Xe, Cs and Ba ions. It is clearly demonstrated in the figure that the $3D$ ($(2p_{3/2}^{-1}3d_{5/2})_{J=1}\rightarrow 2p^6$) and $3F$ ($(2p_{1/2}^{-1}3s)_{J=1}\rightarrow 2p^6$) lines become close, change positions and then become far again as the atomic number increases. To determine wavelengths for neonlike I, Cs and Ba ions, the wavelengths for the same transitions in neonlike Xe ions which were determined experimentally in the

previous work[2] were used as references. Wavelengths for neonlike Sb are determined using transitions in heliumlike Ar as references, though the spectra for neonlike Sb and heliumlike Ar are not shown in the figure.

The present experimental wavelengths are plotted in figure 2 for $3D$, $3E$ ($(2p_{3/2}^{-1}3d_{3/2})_{J=1}\rightarrow 2p^6$) and $3F$ together with the present theoretical results calculated with the MCDF method. For the experimental values for neonlike Xe (Z=54) and La (57), the values obtained by Beiersdorfer *et al.* [2] are used in the plot. Agreement between the experiments and the theory is very well as seen in the figure. It is noted that both of the experimental and the theoretical results clearly indicate that the two levels get close each other around Z=55 but avoid to degenerate. It suggests that they are coupled through strong mixing of electronic configurations. On the other hand, the theoretical results show that repulsion between $3E$ and $3F$ at Z~51 is weak compared to that between $3D$ and $3F$ at Z~55. To investigate this difference in more detail, systematic studies especially for Z~50 are on going.

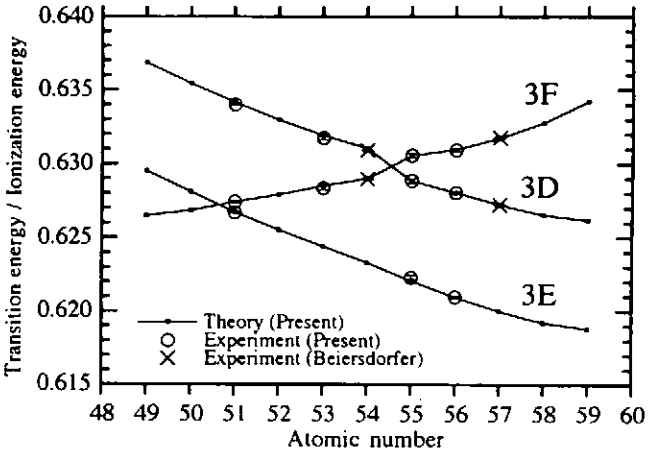

Figure 2. Experimental and theoretical transition energies for 3D, 3E and 3F. Solid lines represent the present theoretical values, open circles the present experimental values, and crosses the experimental values obtained by Beiersdorfer et al. [2]

---

[1] N. Nakamura *et al.*, Rev. Sci. Instrum. 69 (1998) 694

[2] Beiersdorfer *et al.*, Phys. Rev. A 37 (1988) 4153

Applications of inner-shell ionization driven by high intensity laser

K. Moribayashi[†], A. Sasaki[†], Y. Ueshima[†], and T. Tajima[†,‡]

[†] Advanced Photon Research Center, Japan Atomic Energy Research Institute, 25-1, Mii-minami-cho, Neyagawa-shi, Osaka, 572-0019, Japan

[‡] Department of Physics and Institute for Fusion Studies, University of Texas at Austin, Austin, Texas 78712, USA

An application of inner-shell ionization processes driven by high intensity laser is considered. For an inner-shell ionization x-ray laser, detailed requirements such as intensity of laser, density of target, for an experiment is shown. Furthermore, a multi-inner-shell ionization x-ray laser with various wavelengths are suggested.

We have suggested high-brightness short-pulse x-ray sources driven by high intensity lasers: Larmor x-rays are generated from the acceleration of electrons in the laser electromagnetic fields[1]. We also have shown the high harmonic generation resulting from the interaction of high intensity laser with a thin foil. With the use of high brightness x-rays as a pump source, we have also suggested inner-shell ionization and hollow atom x-ray lasers[2. 3]. In this paper we study an application of multi-inner-shell ionization processes pumped by the high-brightness x-rays. We have considered some applications, that is, (i)inner-shell ionization x-ray laser, (ii)x-ray measurement for ultrafast chemical reactions, (iii) measurement for hollow atom spectra, and (iv)hollow atom x-ray laser. We showed experimental classes for inner-shell ionization and hollow atom x-ray lasers and x-ray measurement of ultrafast chemical reactions in Ref.[2]

In the inner-shell ionization x-ray laser, we have showed that Larmor x-rays are suitable as a x-ray pumping source[3]. Their peak intensity and energy spectrum are appropriate for inner-shell ionization. As soon as the high-intensity (10^{20} W/cm^2, $a_0 \sim 5$) short-pulse (100 fs) laser irradiates the plasma with n_e=3×10^{21}cm^{-3}, R_s=5 μm, and R_L=90 μm, the high brightness (10^{13} W/cm^2) short-pulse (100 fs) Larmor x-rays with E_{pk}=100 eV are emitted. By using Larmor x-rays for an x-ray pump source and Mg vapor with 10^{19} cm^{-3} density for a target, an inner-shell ionization x-ray laser with large Γ ($\sim$300 cm^{-1}) may be realized.

Figure 1 shows the total photon number (N_p) for the wavelength with the intensity of I=10^{10}, 10^{13}, and 10^{15} W/cm^2 of Larmor x-rays. The target material is sodium vapor with the density of 10^{17}/cm^2. From the single inner-shell excited state, N_p remains

nearly constant for different intensity I. On the other hand, from hollow atoms, N_p increases as I becomes larger. We also suggested that with use of multi-inner-shell ionization processes, an x-ray laser with various wavelengths is emitted. This may come from the fact that x-rays with a new wavelength are produced whenever an inner-shell ionization process occurs. Fig.2 shows the gain vs. times. The gain of about 10/cm for all wavelengths is estimated.

References

[1] Y.Ueshima *et al.*, Laser Part. Beams, to be published in 1999.

[2] K. Moribayashi, A. Sasaki, and T. Tajima, Phys.Rev.A, **58**, 2007 (1998).

[3] K. Moribayashi, A. Sasaki, and T. Tajima, Phys.Rev.A, **59**, 2732 (1999).

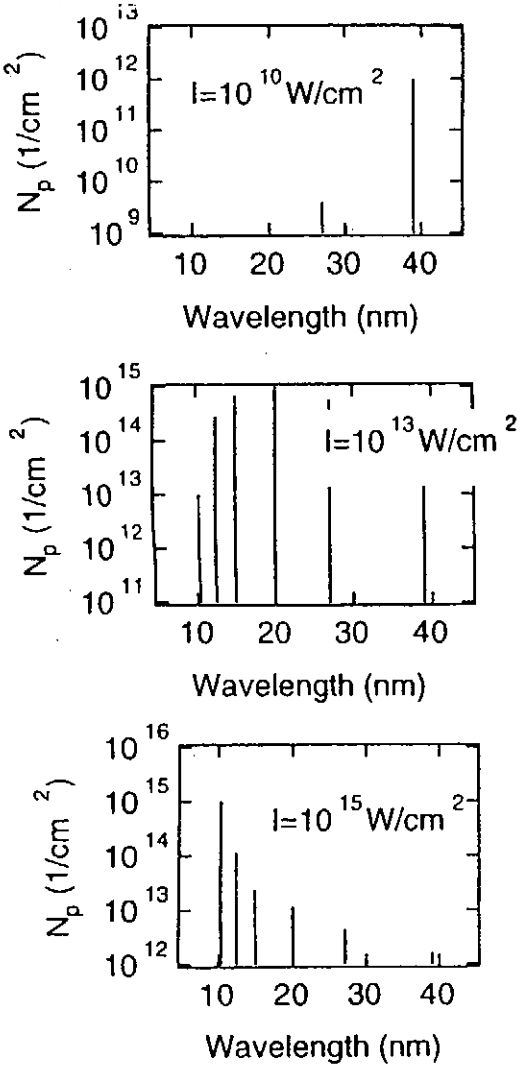

Fig.1

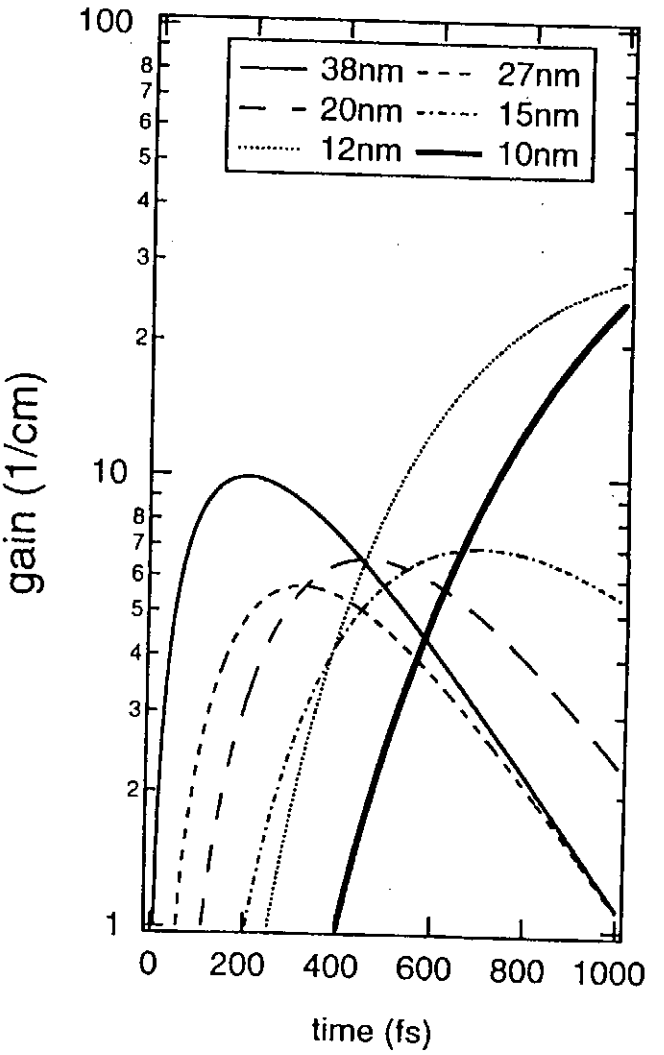

Fig.2

Theoretical Study of Spectral Resolved Opacity in Plasmas

Jun Yan*[1], Yi-Zhi Qu♯, and Jia-Ming Li*,♯

[1] *Center of Atomic and Molecular Sciences, Department of Physics, Tsinghua University Beijing 100084, China*
♯*Institute of Physics, Chinese Academy of Sciences P.O. Box 603-22, Beijing 100080, China*

1 Introduction

The radiative properties of hot dense plasmas produced by laser irradiation play an important role in studies of inertial confinement fusion(ICF) and X-ray lasers. They are also used extensively to diagnose laser-produced plasmas. In recent years, with the development of high precision diagnostic techniques[1], experimental measurements can provide bench mark data to test the validity of LTE opacity codes. Theoretical simulations for the absorption and emission spectra of laser-produced plasmas require a huge number of atomic data. Using the detailed configuration accounting(DCA) with the term structures treated by the unresolved transition array(UTA) model[2], we present a method[3] to calculate the transmission spectra for high-power laser-produced plasmas. Due to our fully relativistic treatment, incorporated with the quantum defect theory to handle the huge number of transition arrays from many configurations with high principal quantum number, we can calculate the opacities for any middle- and high-Z plasmas with much less computational efforts. We also can conveniently identify the dominant configurations and the detailed features of transition arrays, which are very helpful for the diagnostic of the plasma conditions.

2 Theoretical Method

The fraction of incident radiation transmitted through the plasma is given by

$$F(\hbar\omega) = \frac{I(\hbar\omega)}{I_0(\hbar\omega)} = exp(-\alpha(\hbar\omega)L), \tag{1}$$

where $\alpha(\hbar\omega)$ is the coefficient of absorption and can be written as[3]

$$\alpha(\hbar\omega) = \sum_i \left[\sum_{c,c'} N_{i,c}\sigma^{bb}_{i,c,c'}(\hbar\omega) + \sum_c N_{i,c}\sigma^{bf}_{i,c}(\hbar\omega) \right] + N_e\sigma^{ff}(\hbar\omega), \tag{2}$$

where i indicates the ionic stage, $N_{i,c}$ is the number of ions of configuration c per unit volume, N_e is the number of electrons per unit volume, which can be calculated by solve the Boltzmann-Saha equations[3] for the case of LTE plasmas and rate equations[4] for the non-LTE case. $\sigma^{ff}(\hbar\omega)$ is the free-free absorption cross section, which can be calculated by the simple Kramers formula with Gaunt factor or exact numerical methods with atomic self-consistant potentials[5]. $\sigma^{bb}_{i,c,c'}(\hbar\omega)$ is the photoexcitation cross section from configuration c to c', $\sigma^{bf}_{i,c}(\hbar\omega)$ is the total photoionization cross section from all subshells of configuration c. $\sigma^{bb}_{i,c,c'}(\hbar\omega)$ and $\sigma^{bf}_{i,c}(\hbar\omega)$ can be calculated with different kinds

[1] E-mail : jyan@cams.tsinghua.edu.cn

of method[3]. According to QDT, the photoexcitation and photoionization processes can be treated in an unified manner. The infinite bound and adjacent continuum states with the same angular momentum and parity can form a channel. Within a channel, the energy-normalized matrix element varies smoothly across the ionization threshold. Therefore, with several benchmark points, the relevant transition matrix elements from an initial state to the final channel can be obtained conveniently by interpolation.

3 Results and discussion

Based on the method described above, we have developed a computer code to calculate opacity for middle- and high-Z plasmas. In order to test the accuracy of our method, we calculate the transmission spectra of Ge plasma with $k_BT = 38eV$ and an ion density of $0.012g/cm^3$[1]. The SCF energy levels database are use to investigate and produce all important configurations included in the opacity calculation firstly. Figure 1 shows our simulation results of the Ge transmission spectra, as well as the experimental measurements and the numerical simulation of STA method[1] for comparision. Our theoretical results are in general agreement with the experimental data and the simulation of STA. We also trace out the originality of the transmission spectra structure, which are labelled in Fig. 1. Here it should be noticed that the self-consistant potential are used in our calculation without any adjustment. Therefore, our method (DCA/UTA, the atomic data calculated by self-consistant potential) can provide LTE opacity data with adequate accuracy.

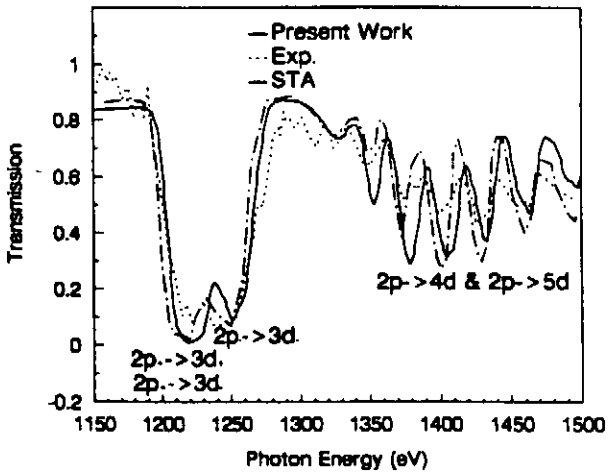

Comparison of the transmission spectra for Ge. Solid line: present results (DCA/UTA); dot-dashed line: STA results[1] ; dotted line: experimental data[1].

References

[1] T.S. Perry, K. S. Budil, R. Cauble, et al., J. Quant. Spectrosc. Radiat. Transfer 1995,**54**: 317-324.

[2] C. Bauche-Arnoult and J. Bauche, Phys. Rev. 1979, **A20**: 2424-2439; Phys. Rev. 1982, **A25**: 2641-2646; Phys. Rev. 1984, **A30**: 3026-3032; Phys. Rev. 1985, **A31**: 2248-2259.

[3] Jun Yan, Yi-Zhi Qu, and Jia-Ming Li, High Power Laser and Particle Beams **11**, 65(1999).

[4] Jian-Guo Wang, Jia-Ming Li, High Power Laser and Particle Beams (in chinese), **9**, 34(1997)

[5] C.M.Lee(Jia-Ming Li), Lynn Kissel and R. H. Pratt, Phy. Rev. **A13**, 1714(1976); C. M. Lee(Jia-Ming Li), R. H. Pratt and H. K. Tseng Phy.Rev. bf A16, 2169(1977).

Ionization processes in overdense plasmas produced by subpicosecond pulse lasers

ZHIDKOV Alexei, SASAKI Akira, TAJIMA Toshiki
Advance Photon Research Center, JAERI
25-1 Mii-minami-cho, Neyagawa-shi, Osaka 572-0019, Japan

Recently, plasmas produced in ultra intense short-pulse laser irradiated solid targets became objects for experimental study [1,2]. Such plasmas can be ultimate coherent VUV and incoherent multi-keV X-ray sources [3], γ-ray [4] and positron [5] sources, and also multi-MeV multiple-charged ion emitters [6].

The laser absorption rate, dynamics and kinetics of plasmas irradiated by intense laser light are strongly dependent on plasma ionization. In the case of slab targets, plasma parameters as the electron density and temperature are dominated by the heat transfer into the plasma [7] while in the case of foils, they are steered by the emission of energetic ions. In the present paper we study the effect of transient plasma ionization, including collisional, optical and plasma-induced field ionization, on multiple-charged-ion emission from thin targets and consequent effect of the ion emission on plasma parameters after the laser pulse.

Usually in long pulse (>100 ps) laser-produced plasmas, electron inelastic collisions dominate the ionization. In the slab targets, in spite of hot electrons, produced by the intense pulse laser, cannot ionize plasma efficiently, the electrons from the return current, which compensates the direct current of hot electrons, having much less energy collisionally ionize the plasma. The Ohmic heating due to the return current, which is determined by plasma ionization, along with inelastic collisions is the main channel of electron energy loss [7]. However, in the case of thin targets irradiated by an ultra-intense pulse laser, the plasma electron lose their energy to ion acceleration because of the heat transfer and radiation reduced. Moreover, in such a plasma, being overheated rapidly up to 100 keV, highly charged states are not produced within the pulse duration because the collisional ionization time increase as $I_Z T_e^{1/2}$. Since the rate of collisional ionization is proportional to the density, the ionization occurs only in high density bulk plasma before the expansion which also lead to a rapid decrease of the rate. In the corona plasma the rate is negligibly small. In the case of an intense pulse laser the optical field ionization (OFI) gets important in the plasma on the front surface of a foil. Ions are continuously ionized by the laser. On the other hand, we find that in the rear surface the field ionization becomes significant if the thickness of the foil is less than the hot electrons excursion length. The hot electrons accelerated inward the bulk plasma by the ponderomotive force produce the electrostatic field on the foil surface. This field can be as strong as the laser [8] providing efficient field ionization.

We apply a relativistic particle-in-cell method including plasma ionization in the framework of the average ion model to simulate the dynamics and kinetics of the multiple-charged ion plasma produced from an intense-pulse laser irradiated thin target. The details of the method can be found in Ref. [6-8].

The effect of optical and plasma induced field ionization is shown in Fig.1 for Al and Ti foils. The four regions in the plasma can be recognized in Fig.1a: skin layer, plasma bulk, rear and front of the foil. In the skin layer both the OFI and collisional ionization are important while in the plasma bulk the collisional ionization is dominant leading to an uniform spatial charge distribution, Al^{+9}. Ions accelerated backwardly, to the laser beam, are further ionized by the laser field up to Al^{+10}- Al^{+13} states. In the rear side of the foil, the significant plasma ionization is produced by the hot electron induced field. As the field strength is weaker than that of the laser, the ionization is slower. If the field ionization is excluded, the distribution of ion charges is dominated by collisional ionization which has a smaller rate in the plasma. The collisional ionization rate in the plasma bulk of a Ti foil, in contrast to a Al foil, is faster than the field

ionization rate because of higher electron density. However, the field ionization significantly increases charges of accelerated ions up to Ti^{+15}-Ti^{+16}. The ions are not fully ionized (z=22) even in the bulk plasma because of a collisional ionization rate decrease with the plasma temperature.

The temporal evolution of the plasma parameters after the laser pulse is shown in Fig.2 for 100 nm Al foil. Being heated by the laser up to 20 keV, the plasma electrons rapidly convert their energy to ions. The electron temperature significantly decreases already after 0.25 ps. At t=0.75 ps more than 95% of laser energy absorbed by electrons is converted to ions. Due to rapid expansion the Al plasma does not reach the full ionized state even in the bulk.

References

1. G.Malka, J.L.Miquel, Phys. Rev. Lett. 77, 75 (1996)
2. R. Shepherd, R.More, R.Young et. al., JQSRT 58, 911 (1997)
3. J.Yu.Jiang, J.C.Kieffer, A.Krol, Phys.Plasmas 6, 1319(1999)
4. E.P.Liang, S.C.Wilks, M.Tabak, Phys. Rev. Lett. 81, 4887 (1999)
5. P.A.Norreys, M. Santala, E.Clark, et al., Phys. Plasmas 6, 2150 (1999)
6. A.Zhidkov, A.Sasaki, T.Tajima et al., to appear in Phys. Rev.E (1999)
7. A Zhidkov, A.Sasaki, Phys. Rev. E57, (1999)
8. A.Zhidkov, A.Sasaki, T.Tajima, JPFR, 75, (1999)

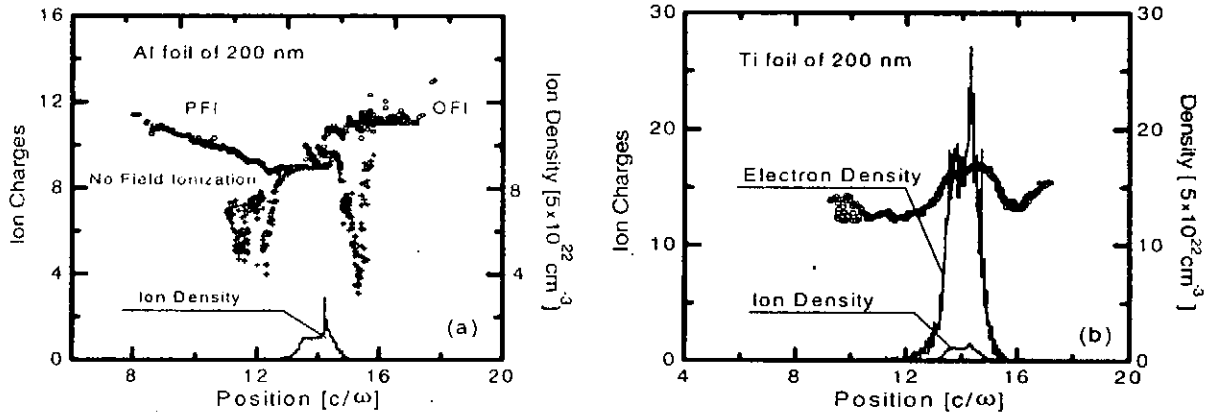

Fig.1 The spatial distribution of ion charges in an Al (a) and Ti (b) foils after 100 fs of the irradiation by a laser pulse with $I=4\times10^{19}$ W/cm^2 and λ=800 nm.

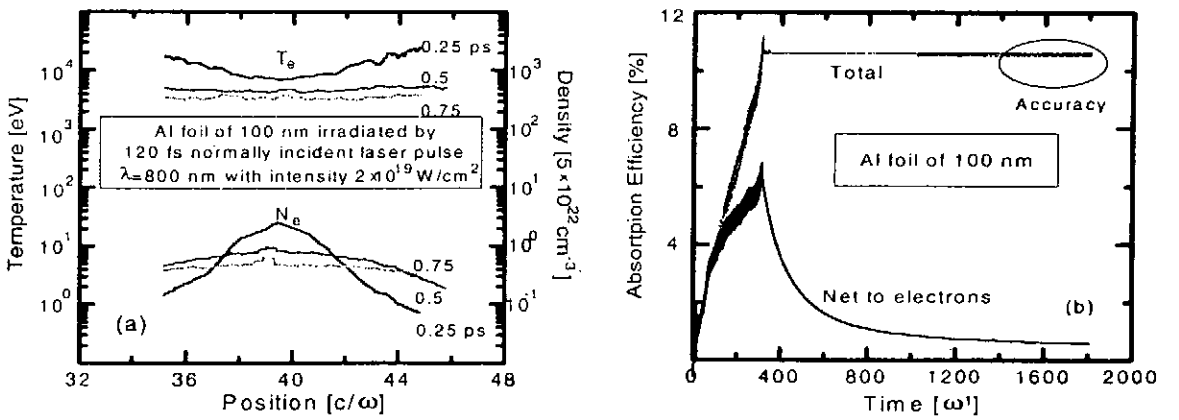

Fig.2 The temporal evolution of plasma parameters (a) and absorption efficiency (b) of 100 nm Al foil irradiated by 120 fs pulse laser with $I=2\times10^{19}$ W/cm^2 and λ=800 nm.

A theoretical study on high harmonic generation

Baek Il Nam[1], Young Soon Kim[1], and Moon-Gu Baik[2]

[1] *Dept. of Physics, Myong Ji University, Yong-In 449-728, Korea*
[2] *Dept. of Physics, Kyungwon University, Songnam 461-701, Korea*

Abstract. We study influences of an atomic potential and the shape of external laser pulse on high harmonic generation(HHG) by solving 1-D Schrödinger equation with a model potential that satisfies scaling property. We see how harmonic spectrum is affected by potential depth, especially by considering a deeply bound ground state of which the tunneling probability is very small. We perform Fourier transform of the input laser fields of several forms to see how external field without atomic potential influences HHG. We find that a rectified sine-squred pulse, albeit artificial, generates even orders of harmonics without atomic potential while it produces both even and odd orders of harmonics in the presence of atomic potential.

1 Introduction

HHG is now relatively well understood both experimentally and theoretically. In theory, the semiclassical "recollision" picture explains most of the important experimental features including a plateau and a cutoff [1, 2]. However these general features are reproducible even in the two-state model where no ionization occurs [3]. This is mainly because the atomic potential is less important than the external electric field for highly energetic electrons which can produce higher order harmonics. However the atomic potential is not negligible for lower order harmonics and it can be an important factor in this region [4].

We present the calculation results of HHG spectra for various atomic and laser parameters to study the differences between the effects by atomic potential and by external field.

2 Results and discussion

Solving time dependent Schrödinger equation(TDSE) is now the most common numerical method for studying HHG. We also solve TDSE using the 1-D soft-core model potential:

$$V(x) = \frac{-Z}{\sqrt{(a^2/Z^2) + x^2}},$$

where Z is an atomic number and a is a parameter that determines the energies of the eigenstates; a set of parameters $\{Z = 1, a^2 = 2\}$ supports the ground state energy at -0.5 a.u. as in the hydrogen atom. The form of the above potential is chosen to satisfy the scaling property. We calculate HHG spectra for $Z = 1, 2,$ and 3 for external laser pulse with sine-squred envelop. The results are almost identical, which implies the validity of this calculation.

For $Z = 2$ or 3 but with fixed laser parameters (for example, $\lambda = 527$ nm, $I = 5.5 \times 10^{15}$ W/cm^2) we see suppression of HHG spectrum in the lower order harmonics followed by the spurious but reproducible rising of higher order harmonics. We are not sure at this time of this result even though it resembles harmonic spectrum of He^+ by

[1]E-mail : binam@qopts.myongji.ac.kr

J. B. Watson *et al.* [5] Note that this is not the region where the "recollision" picture is applied.

We also calculate HHG for half wave rectifier and full wave rectifier that have only even orders components except the fundamental frequency when it is Fourier transformed. Fig. 1 (a) shows the shape of the half wave rectifier of sine-squared pulse. Then the averaged position of electron shifts to one side, opposite to the shape of this pulse. Fig. 1 (b) is the spectrum calculated from the dipole acceleration. where both even and odd order harmonics are shown in the lower orders while only even orders peaks are shown for the higher orders, that is nothing but the result from the external field only. We may suggest that we can generate not only odd orders of harmonics but even orders of harmonics once we know how to shift average position of the electron cloud.

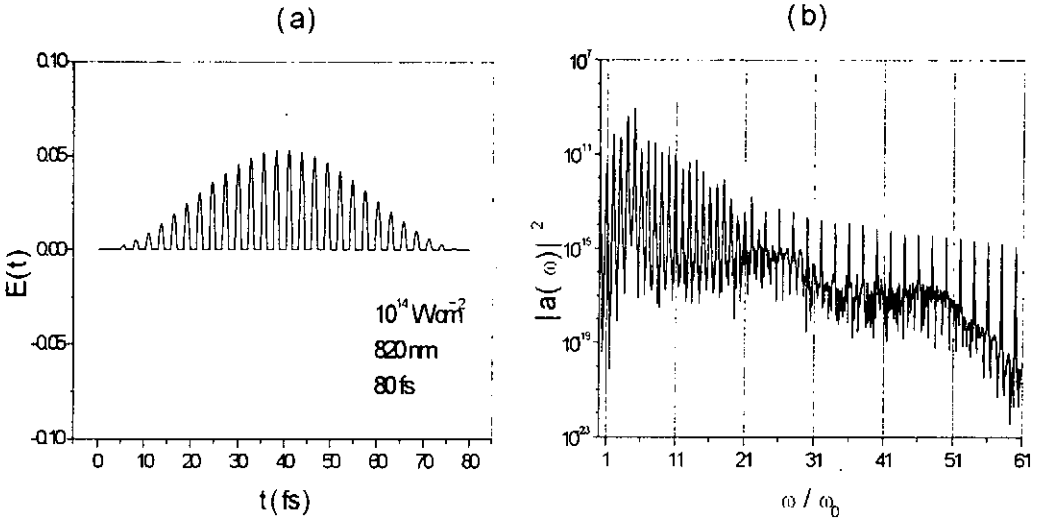

Figure 1: (a) half wave rectifier of sine-squared pulse (b) harmonic spectrum.

References

[1] J. L. Krause, K. J. Schafer, and K. C. Kulander, Phys. Rev. Lett. **68** 3535 (1992)

[2] P. B. Corkum, Phys. Rev. Lett. **71** 1994 (1993)

[3] F. I. Gauthey, B. M. Garraway, and P. L. Knight, Phys. Rev. A **56** 3093 (1997)

[4] C. F. de Morisson Faria, M. Dörr, and W. Sandner. Phys. Rev. A **58** 2990 (1998)

[5] J. B. Watson, A. Sanpera, and K. Burnett, Phys. Rev. A **51** 1458 (1995)

Gain characteristics of innershell L_2-M_1 transition in Ti

D. Kim[1], S. H. Son[1], J. H. Kim[1], C. Toth[2] and C. P. J. Barty[2]

[1] *Physics Department, POSTECH, Pohang, Kyungbuk 790-784, KOREA*
[2] *Inst. of Nonlinear Science, Univ.of California, San Diego, CA 92093-0339*

Abstract. X-ray laser schemes are described in which the Coster-Kronig Auger-process is the dominant lower level decay mechanism. Such systems have inherently short lower level lifetimes and it is shown that under certain conditions they can be inverted with excitation by energetic electrons as well as X-rays.

1. Introduction

The recent advances in 10-fs-range, high-peak-power lasers have renewed interest in developing keV X-ray lasers based on inner-shell atomic transitions[1-8]. If it were possible to create an inner-shell population inversion via atomic processes involving electrons only, then photo-ionization pumped X-ray laser schemes based on the same transitions would be less sensitive to secondary electron collisional filling of the lower state, require less demanding X-ray pumping conditions, and result in inversions which could be maintained longer, compared to equivalent photo-inner-shell ionization pumping schemes for K_L transition. Coster-Kronig or super Coster-Kronig decay can be significantly larger than those of the next deeper vacancy states, i.e. the potential upper state of a lasing transition. As pointed out in Ref. 4 and 5, for selected states in numerous atomic systems in which the lower state decay is mediated by Coster-Kronig or Super-Coster-Kronig decay while the upper state is not, a transient, femtosecond time-scale inversion can be achieved. As mentioned above, photo-ionization pumped inner-shell X-ray laser schemes using these transitions will benefit from this concept because the additional rate out of the lower state can overcome secondary filling processes.

2. Pumping by electrons

For appropriately chosen atomic species and transitions, the population inversion between inner-shell hole states can be created by electron collisional ionization only – a situation which has previously been considered impossible. We have reviewed radiative and non-radiative decay rates from inner-shell vacancies in elements up to Z=90 .To study the population dynamics, we have numerically solved the rate equations for the populations of the states of interest when neutral atoms are ionized by a short, intense electron pulse. Computer simulations show that among these transitions the L_2M_1 transition for Z=22 to 32 is the most robust to detrimental collisional processes. Transient population inversion with a maximum value of 2.4×10^{19} cm^{-3} at 3.09 nm wavelength in Ti could be achieved for an electron pulse of 5 fs (Figure 1).

3. Pumping by photons

Photo-ionization inner-shell pumping schemes will also benefit from the usage of this type of transition. To investigate the performance of the gain on the L_2M_1 transition by photo-pumping, a population kinetics code has been developed. Populations are calculated only for the single

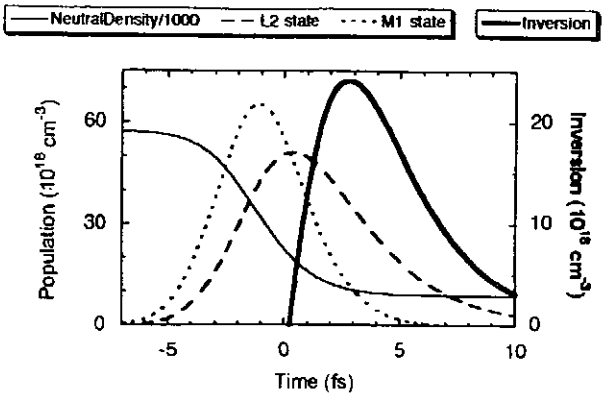

Fig. 1 pumping with a 5 fs electron pulse. Solid density of 6×10^{22} cm^{-3} for titanium and density of 10^{21} cm^{-3}.

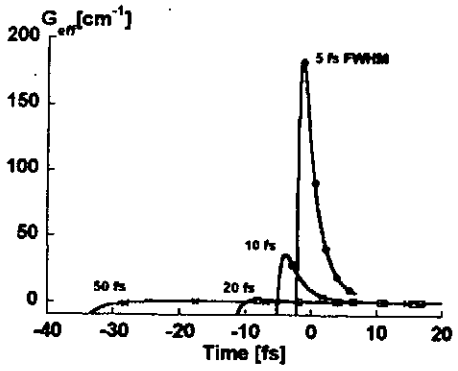

Fig. 2. Pumping with photons. Monochromatic flux at 470eV of electron 1.4x 10^{18} photons / cm^2.

vacancy states. Double vacancy states are considered to include the decay channels from the single vacancy states such as photo-ionization, electron collisional ionization, Auger and Coster-Kronig and to calculate the electron energy distribution. Radiation source is a monochromatic or black-body source. In the case of monochromatic source, the Gaussian pulse shape of an incoming photon flux is assumed. The calculations were done for the case of Ti. G_{eff} is the difference between the gain on the L_2M_1 transition due to inversion and absorption on L_2M_1 due to neutrals: $G_{eff} = G_{inv} - G_{abs}$ (absorption by neutral). Figure 2 shows that the effective gain changes dramatically when the pulse duration (FWHM) is below 20 fs. This calculation is done for monochromatic source at 470eV and the total photon flux delivered at 1.4x 10^{18} photons / cm^2.

Acknowledgments

This work has been supported in part by Basic Science Research Institute (BSRI 98-2439).

References

[1] S. J. Moon and D. C. Eder, Phys. Rev. A **57**, 1391 (1998).
[2] K. Moribayashi, A. Sasaki, and T. Tajima, Phys. Rev. A **58**, 2007(1998).
[3] Y. Li, H. Schillinger, C. Ziener, R. Sauerbrey, Opt. Comm. **144**, 118 (1997).
[4] C. P. J. Barty, T. Guo, C. Le Blanc, F. Ráksi, C. Rose-Petruck, J. Squier, B. C. Walker, K. R. Wilson, V. V. Yakovlev, and K. Yamakawa, in *X-ray lasers 1996*, IOP Conf. Series **151**, 282 (1996).
[5] D. Kim, C. Toth, and C. P. J. Barty, Phys. Rev. A **59**, R4129 (1999).
[6] S. Meyer, T. Menzel, B. Wellegehausen, P. -X. Lu, S. Insam, and E. Fill, in *X-ray lasers 1996*, IOP Conf. Series **151**, 173 (1996).
[7] G. L. Strobel, R. A. London, D. C. Eder, Applied Phys. B **60**, 513 (1995).
[8] H. Kapteyn, Applied Optics **31**, 4931 (1992).

Collective Effects in the Transient Plasma formed by Multiphoton Ionization of Deuterium Atoms by a Pulsed Laser Beam

B. Shortt[1], F. Giammanco[2], P. J. M. van der Burgt[1], and R. W. O'Neill[1]

[1] *Dept. of Experimental Physics, National Univ. of Ireland, Maynooth, Co. Kildare, Ireland*
[2] *Department of Physics, University of Pisa, 56126 Pisa, Italy*

Abstract. A transient laser plasma is formed by multiphoton ionization of deuterium atoms with a pulsed laser beam. A laser beam of 243 nm is used, so that the photoionization is resonant with the metastable 2s state of deuterium. Collective effects in the plasma affect the spatial and temporal distribution of the photo-electrons and the ions. Measurements of the time-dependent yields of ions and of metastable atoms are compared with a fluid-dynamics model based on the Boltzmann transport equations.

1 Introduction

This project involves a study of the transient plasma produced by three-photon ionization of deuterium atoms. We use a pulsed laser beam with the wavelength tuned to 243 nm, pulsewidth 13 ns, and maximum intensity 200 MW/cm^2, produced by an excimer-pumped dye laser (Lambda Physik LEXTRA + LPD 3002). Inside a vacuum chamber the laser beam is crossed with a beam of deuterium atoms produced by a radio-frequency discharge source. Atoms that simultaneously absorb two photons are excited to their metastable 2s state, which can be ionized if a third photon is absorbed.

An extraction electric field is turned on in the interaction region, so that the ions are accelerated towards the ion detector, and the metastable atoms are quenched. When quenched the metastable atoms decay by emission of a Lyman-alpha photon which is detected by a photon detector. A detailed description of the experiment is given in [1].

At high laser intensities many atoms are ionized during the laser pulse, and a transient plasma of photo-electrons and ions is formed at the spot where the laser beam intersects the atomic beam. During and shortly after the laser pulse collective effects depending on the mutual interaction of the electrons and the ions affect the spatial and temporal distribution of the ions. As a result the time-dependent yields of ions and of metastable atoms are modulated by the interplay of two processes: (i) the multiphoton ionization of the atoms, and (ii) the collective effects in the plasma.

Multiphoton ionization of deuterium presents an ideal situation for the study of this interplay. Deuterium is almost the lightest element and therefore deuterium ions are very susceptible to the collective field, and the near-degeneracy of the 2s and 2p states makes that the resonant multiphoton ionization is affected by the Stark mixing of the 2s and 2p states in the collective field.

2 Theoretical model

The space-time behaviour of the ions and the electrons produced in the multiphoton process is modelled by using a fluid-dynamics description [2] of the coupled motion of the ions and electrons based on the Boltzmann transport equations. This model includes the production of ions and electrons by photoionization during the laser pulse. The motions of ions and electrons are calculated in a perpendicular intersection of the laser beam and assuming radial

symmetry around the axis of the laser beam. Although this approximation is strictly valid only in the absence of the extraction field, the model reproduces the observed features of the measurements very well.

We are presently working on improvements in the theoretical model. In [1] rate equations were used to describe the photoionization process. The present model incorporates a four-level density matrix description of the atom in the laser field. This formalism includes the $1s_{1/2}$, $2s_{1/2}$, $2p_{1/2}$ and $2p_{3/2}$ levels, the Rabi frequency for the two-photon transition [3], the 2s-2p Stark coupling due to the collective field, the AC Stark shifts, and Lyman-alpha decay. In the present model the fluid equations describing the space-time evolution of the electron and ion densities are solved simultaneously.

3 Experimental results

In the experiment (see [1]) the ion yield, ion time-of-flight spectra and the Lyman-alpha signal vs. time are measured as a function of laser intensity. Each set of experimental measurements is performed twice, once with the extraction field present during the laser pulse, and once with the extraction field switched on shortly immediately after the laser pulse. All measurements are compared with theoretical calculations.

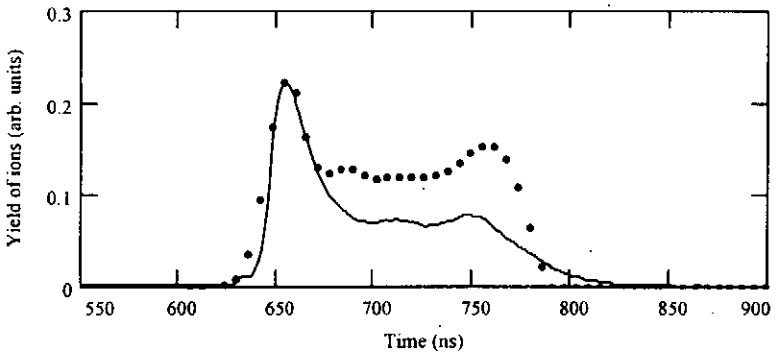

Figure 1: A measured ion time-of-flight spectrum — compared with a calculated profile ···. The collective effects in the laser plasma are the cause of the width of the profile and the modulations in the ion yield (see text). The theoretical profile does not take into account the finite opening angle of the ion detector.

Figure 1 shows a typical ion time-of-flight spectrum (laser intensity 195 MW/cm^2, extraction field present during the laser pulse). Both the early arrival of the ions in the first peak and the width of the profile are the result of collective effects. In the absence of collective effects at very low laser intensities only a single ion peak is observed at 670 ns. The modulations in the ion yield are due to the coupled motion of the electrons and the ions in the plasma. The calculated profile shows similar oscillations; they are only obtained by including a full description of the electron motion into the plasma model.

Measurements are in progress to observe ion and metastable yields as a function of the laser intensity, the target density, and the laser wavelength near the two-photon resonance.

References

[1] Bowe P, Giammanco F, O'Neill R W, van der Burgt P J M, and Slevin J A 1998 *Phys. Rev. A* **58** 1389
[2] Giammanco F 1989 *Phys. Rev. A* **40** 5171
[3] Holt C R, Raymer M G, and Reinhardt W P 1983 *Phys. Rev. A* **27** 2971

Atomic and Molecular Data Activities at NDC/JAERI

Toshizo Shirai
Nuclear Data Center (NDC), Japan Atomic Energy Research Institute (JAERI)
Tokai-mura, Ibaraki 319-1195, Japan

The NDC/JAERI is a member of the international atomic and molecular (A+M) data center network for fusion, coordinated by the International Atomic Energy Agency. In this poster we introduce our Evaluated Atomic and Molecular Data Library (JEAMDL) developed in collaboration with the JAERI Research Committee on A+M Data and with researchers of ORNL and NIST under the US-Japan fusion cooperation program. JEAMDL comprises databases of collision cross section data and of spectroscopic data. We briefly summarize these two databases below.

Collision Cross Section Database

The data compilations published so far as the JEAMDL series for fusion research are for charge transfer of hydrogen atoms and ions colliding with gaseous atoms and molecules [1] and metal vapors [2], for state-selective-electron capture in collisions of C^{6+} and O^{8+} with atomic hydrogen [3], and for collisions of H, H_2, He, and Li atoms and ions with atoms and molecules [4]. In order to facilitate the extraction of numerical data, analytical least-squares fits has been made to the recommended cross sections. The functional forms used for analytic expressions are those proposed by Green and McNeal [5] semi-empirically and modifications of them. The use of such expressions allows one not only to interpolate but also extrapolate the data to some extent in contrast to polynomial fits. All the results for 603 kinds of collision processes are available from a homepage of the NDC/JAERI (http://wwwndc.tokai.jaeri.go.jp/JAEMDL/index.html) (see also the figure at the bottom).

Semi-empirical scaling formulas were obtained of the cross sections for single-electron capture [6] and ionization [7] in collisions of multiply charged ions with H, H_2, and He. However, more accumulation of experimental data are needed to establish the low-energy behavior of the cross sections.

Recently, analytic expressions have been made of the cross sections for many different processes in collisions of H^+, H_2^+, H_3^+, H, H_2, and H^- with hydrogen molecules in the energy range below 100 keV [8] by using the recommended data of Phelps [9]. The data compilations of collision processes of molecules (hydro-carbon, H_2O, CO, CO_2) by electron impacts [10] will be revised with recent experiments in 1990 through 1998. Analytic expressions to the recommended data will be given also.

Spectroscopic Database

Critically evaluated data for energy levels, transition energies, ionization energies, and oscillator strengths, both observed and calculated, are tabulated for the elements Ti, V, Cr, Mn, Fe, Co, Ni, Cu, Kr, and Mo [11], which are of special importance for fusion research. These tables include data for all stages of ionization from Ca-like through H-like spectra. About 20,000 transitions are covered by this database. Short reviews of the line identifications are given for each stage of ionization. Grotrian diagrams were already published in a series of JAERI-Data/Code [12] and are now available on request.

A similar data compilation will be published soon for these spectroscopic quantities for neutral and all stages of ionization of Argon (Ar I through Ar XVIII) and Gallium (Ga I through Ga XXXI). The tungsten compilation is now in progress.

References

[1] Y. Nakai, T. Shirai, T.Tabata, and R. Ito, Atom. Data Nucl. Data Tables 37, 69 (1987).

[2] T. Tabata, R. Ito, Y. Nakai, T. Shirai, M. Sataka, and T. Sugiura, Nucl. Instr. Meth. B31, 375 (1988).

[3] R. K. Janev, R. A. Phaneuf, H. Tawara, and T. Shirai, Atom. Data Nucl. Data Tables 55, 201 (1993).

[4] R. Ito, T. Tabata, T. Shirai, and R.A. Phaneuf, JAERI-M 93-117, JAERI-Data/Code 94-005, JAERI-Data/Code 95-008, and JAERI-Data/Code 96-024.

[5] A.E.S. Green and R.J. McNeal, J. Geophys. Res. 76, 133 (1971).

[6] Y. Nakai, T. Shirai, T. Tabata, and R. Ito, Phys. Scr. T28, 77 (1989).

[7] T. Tabata, R. Ito, T. Shirai, Y. Nakai, H.T. Hunter, and R.A. Phaneuf, At. Plasma-Mater. Interact. Data Fusion Vol. 2, 91 (1992).

[8] T. Tabata and T. Shirai, Atom. Data Nucl. Data Tables, (1999) submitted.

[9] A.V. Phelps, J. Phys. Chem. Ref. Data 19, 653 (1990).

[10] H. Tawara, Y. Itikawa, H. Nishimura, H. Tanak, and Y. Nakamura, NIFS-Data-6 (1990); H. Tawara, NIFS-Data-19 (1992).

[11] T. Shirai, J. Sugar, W.L. Wiese, and A. Musgrove, Monograph 8, J. Phys. Chem. Ref. Data (1999) in print.

[12] T. Shirai, J. Sugar, and W.L. Wiese, JAERI-Data/Code-97-022 to -031.

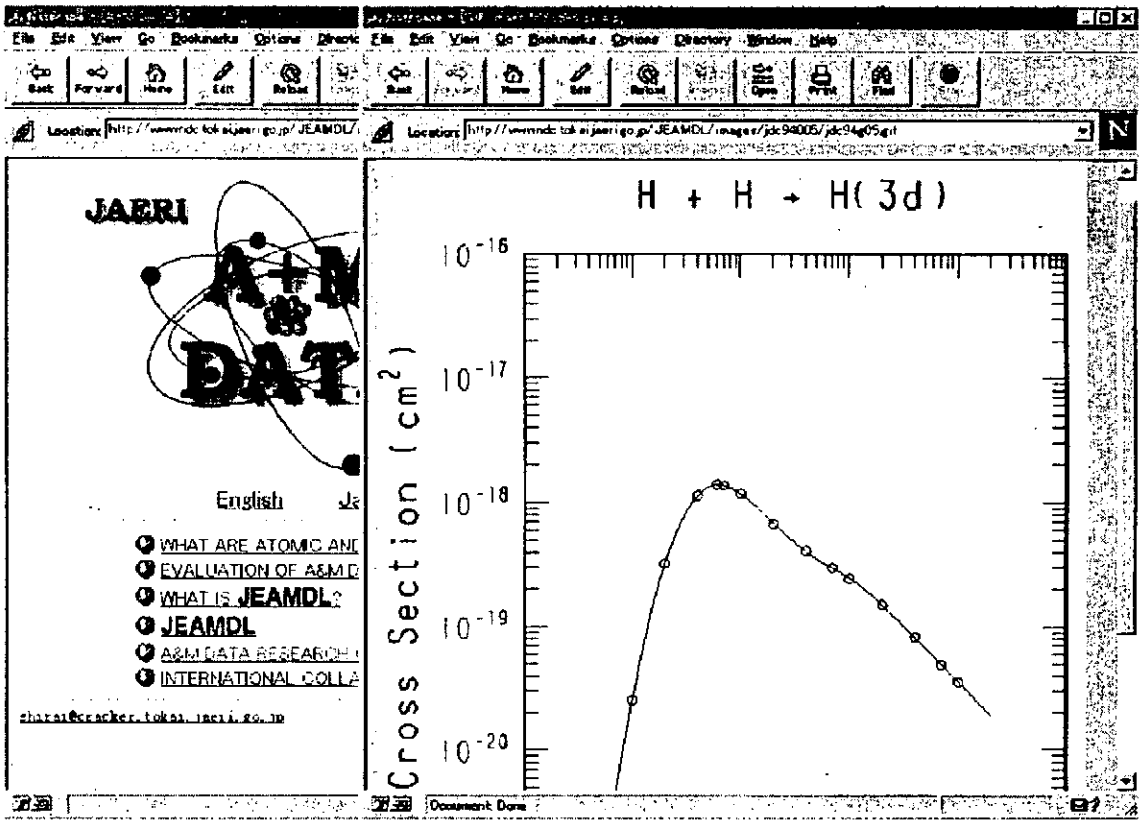

Homepage (http://wwwndc.tokai.jaeri.go.jp/JEAMDL/index.html) for atomic and molecular data at the NDC/JAERI.

Apparent Wavelength Shifts of H-like Ions Caused by the Spectral Fine Structure Observed in CHS Plasmas

Shin Nishimura, Katsumi Ida, and CHS Group

National Institute for Fusion Science, Toki 509-5292, Japan

Abstract. The effect of the spectral fine structure of H-like ions on the plasma rotation measurements was investigated using the 'bidirectional' viewing of the charge exchange excited CVI lines. The wavelength given by a single Gaussian fitting shows the apparent wavelength shifts of $\Delta\lambda$ ~0.01 Å depending the ion temperatures in the range of ~100eV.

1 Introduction

The spectroscopic measurements of plasma rotations are widely used to measure radial electric fields in magnetically confined plasmas. For the precise measurement of Doppler shifts in the rotation velocity range of a few km/s[1,2], there are several problems that come from the mechanical wavelength offset in spectrometers and so on. The best approach to measure the absolute value of Doppler shifts canceling the wavelength offset is the bidirectional viewing (simultaneous two viewing along opposite viewing directions)[3]. The results of charge exchange spectroscopy(CXS)[4] using this method in the Compact Helical System(CHS) clarified another problem which comes from the spectral fine structure of hydrogen-like ions.

In this paper, the observed effect of the fine structure on the plasma rotation measurements is presented. CHS is a Heliotron/Torsatron type helical torus with the major radius of R=1m, the averaged minor radius of a=0.2m and the magnetic field strength of <2T. Charge exchange excited spectral lines from the heating neutral beam (<40kV, <1MW) are used for the spectroscopic measurements of the ion temperature and the poloidal rotation. The measurement system has two fiber arrays viewing the plasma from upper and lower ports simultaneously at the vertically elongated section (port 7D and 7U), and the average of the wavelength measured from both sides gives the wavelength without Doppler shifts ($\Delta\lambda = 0$). And it uses one more fiber array to measure the background radiation at another vertically elongated section (port 8D). All of these fibers (90ch) are connected to the entrance slit of a spectrometer and the diffraction image is detected by a CCD camera with an image intensifier.

2 Results and Discussions

The hydrogen-like ions created by the charge exchange reaction of the beam neutrals and the fully ionized plasma ions have the splitting of energy levels due to a relativistic effect expressed in the formula

$$E(n,j) = -\frac{Z^2 Ry}{n^2}\left[1 + \frac{(\alpha Z)^2}{n}\left(\frac{1}{j+1/2} - \frac{3}{4n}\right)\right]$$

where, n is principal quantum number, j is total angular momentum, Z is nuclear charge, R_y is Rydberg constant and α is fine structure constant (=1/137). The sub-level populations that determine the intensity ratio of fine structure components can be assumed to be proportional to statistical weights $2(2l+1)/n^2$ based the collisional l-mixing model[4]. Figure 1 shows the example of observed spectral profiles of the CVI line(Δn=7-6, λ=3434 Å) and the fine structure pattern calculated with this assumption. The fitting with the super-position of fine structural components with Doppler broadening shows better agreement with the measured

E-mail : shin@nifs.ac.jp

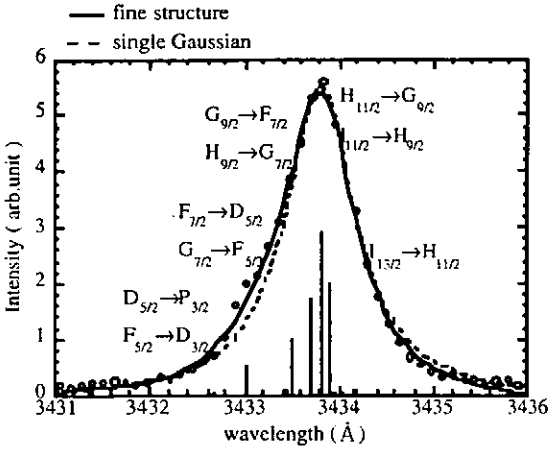

Figure 1:Spectral profile of the CVI line(Δn=7-6).

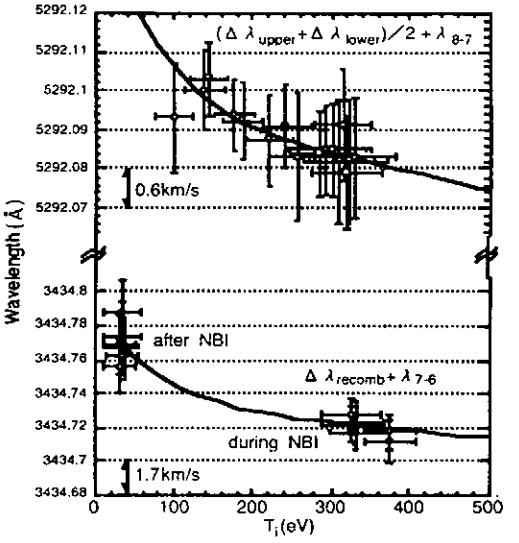

Figure 2: Apparent wavelength.

spectrum than the fitting with single Gaussian profile. The red-side/blue-side asymmetry of the spectral pattern causes the ion temperature (i.e. Doppler width) dependence of the the center wavelength for the half-maximum of spectral profiles. The solid curves in Figure 2 show the center wavelength for the half-maximum of calculated spectral profiles. They shifts to the red side with decreasing ion temperature and total shift in the ion temperature range of hundreds eV corresponds to the velocity error of a few km/s.

The wavelength shifts given by a least square fitting of single Gaussian profile to the measured Doppler broadened CVI spectral lines in visible range(Δn=8-7, λ =5290 Å and Δn=7-6, λ =3434 Å) show apparent shifts, not due to the real Doppler shifts, depending on the ion temperatures. These apparent shifts can be distinguished from the real Doppler shifts by the bidirectional viewing. The Δn=8-7 line observed in the plasma having the center ion temperature of $T_i(0)$=330eV shows red-side shifts in the peripheral region with the ion temperature of $T_i(r\sim a)$=100eV. The wavelength of the line without the Doppler shift is given by the 'average' of the measured 'wavelength' at the upper and lower viewing ports ($\Delta\lambda_{upper}+\Delta\lambda_{lower})/2+\lambda_{8-7}$, where λ_{8-7} is taken to be 5292.082 Å. The Δn=7-6 line observed in the after-glow phase of NBI heated plasma also shifts to red-side compared to the NBI heated phase. The wavelength of this line is given by $\Delta\lambda_{recomb}+\lambda_{7-6}$, where $\Delta\lambda_{recomb}$ is the wavelength jump from the NBI phase to the after-glow recombining phase and λ_{7-6} is taken to be 3434.72 Å. Open circles in Figure 2 show these measured wavelength. The observed dependence on the ion temperature can be explained by the prediction from the fine structure calculation.

References

[1] K.Kondo, H.Zushi, S.Nishimura, et al., Rev. Sci. Instrum. **59**, 1533(1988).

[2] K.Ida, et al., Phys. Fluids **B 3**, 515(1991) and **B 4**, 1360(1992).

[3] A.R.Field, G.Fussmann, et al., Nucl. Fusion **32**, 1191(1992).

[4] R.J.Fonck, D.S.Darrow and K.P.Jaehnig, Phys. Rev. **A 29**, 3288(1984).

Spectra of Neutral Carbon for Plasma diagnositics

J.G. Wang[1], M. Kato, and T. Kato

National Institute for Fusion Science, Toki 509-5292, Japan

1 Introduction

In the magnetic controlled fusion research, the impurity atoms and ions play an important role for plasma cooling, meanwhile, the radiation also contains the information on the nature of plasma, and the spectroscopy of the radiation can be used to measure the plasma parameters.

Recently, Sergeev et al[1] have perfomed carbon pellet experiments on W-7AS, and observed several CI lines. The situation of the pellet cloud plasma may change from the cold dense plasma (with cloud density $n_{CL} \sim 10^{15} - 10^{17} cm^{-3}$ and cloud temperature $T_{CL} \sim 1 - 50eV$) to hot ambient plasma (with electron density $n_e \sim (0.5 - 10)10^{13} cm^{-3}$ and temperature $T_e \sim 100 - 3000eV$). In so large varied condition, the CR model is needed to calculate the spectra, in which both ionizing and recombining plasma should be included. In this article, using the CR model including 79 states with the principal quatumn number $n \leq 6$ and $l \leq 4$, we calculate the line spectra and line intensity ratios in the ionizing and recombining plasma.

2 Rate equation

The population densities of the i-th state of carbon atoms, n(i), is described by the following rate equation:

$$\frac{dn(i)}{dt} = \{\sum_{j \neq i} n_e C_{ji} n(j) + \sum_{j>i} A_{ji} n(j)\} - \{\sum_{j \neq i} n_e C_{ij} n(i) + \sum_{j<i} A_{ij} n(i)\} - \sum_k n_e S_{ik} n(i) + \sum_k n_e \alpha_{ki} n_+(k), \quad (1)$$

where n_e is the electron density and $n_+(k)$ is the population density in the k-th state of a singly charged ion. The electron impact excitation and ionization, spontaneous radiation, radiative recombination, dielectronic recombination and three-body recombination processes are included in our caculation. According to the method of the quasi-steady-state solution [2], the population of excited states can be divided into two components, which are called the recombining plasma and the ionizing plasma, respectively.

3 Atomic data

The collisional excitation rate coefficients for $n \leq 4$ are calculated by R-matrix[3], and others are calculated by Mewe's semi-empirical formula[4] using the oscillator strength f_{ij} and excitation energy E_{ij}[5]. Electron impact ionization rate coefficients are estimated by Lotz's empirical formula. Radiative recombination rate coefficient is obtained

[1]E-mail : wang@nifs.ac.jp

by detailed balance from the photoionization cross sections[6]. Dielectronic recombination rate coefficient is calculated by Cowan's code[7].

4 Results and discussion

In our calculation, we found when $T_e > 2$ eV, the collisional-radiative ionization rate coefficients are much larger than the collisional-radiative recombination rate coefficients, in the equilibrium or near-equalibrium region, the ionizing process dominates the recombining process; when $T_e < 0.8$ eV, the collisional-radiative recombination rate coefficients are much larger than the collisional-radiative ionization rate coefficients, the recombining process dominate over the ionizing process; when $0.8eV < T_e < 2eV$, no process dominates and it is the mixing of the ionizing and recombining processes. In different parameter range, the different transition lines should be choosed to measure the plasma parameters, because they have different dependences on the plasma parameters. As an example, we plot the spectra between 100-200 nm for the ionizing and recombining plasma as shown in Fig.1.

References

[1] V. Sergeev et al., private communication, 1998.

[2] T. Fujimoto, J. Phys. Soc. Jpn. **47** (1979) 265; **47** (1979) 272; **49** (1980)1561.

[3] K.M. Dunseath et al., JET Order No:JP2/11566(1993); W.C. Fon et al., JET Order No:JP2/11566(1994)

[4] Mewe R., Astron. Astrophys. **20** (1972) 215.

[5] G.A. Victor and V. Escalante, Atomic Data and Nuclear Data Tables **40** (1988)203.

[6] R. E. H. Clark et al., Atomic Data and Nucl. Data Tables **34** (1986) 415.

[7] U. Safronova and T. Kato, J. Phys. **B 31** (1998)2501.

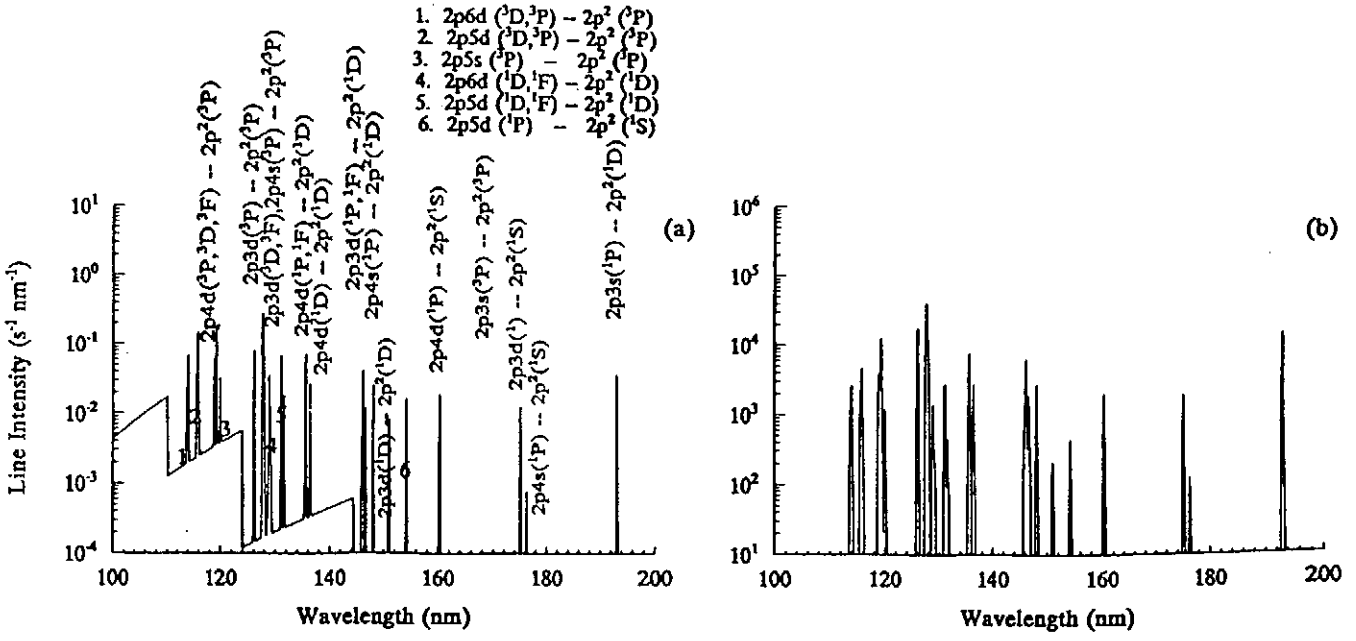

Fig.1 Spectra of neutron carbon. (a). the recombining plasma at $T_e = 0.8eV$ and $n_e = 10^{12}cm^{-3}$; (b). the ionizing plasma at $T_e = 10eV$ and $n_e = 10^{12}cm^{-3}$

Electron capture cross sections of low energy highly charged ions in collisions with alkali atoms

Kazumoto Hosaka, Hiroyuki Tawara, Ichihiro Yamada, Hiroyuki A. Sakaue, Nobuyuki Nakamura, Shunsuke Ohtani, Hirofumi Watanabe, Atsunori Danjo, Masahiro Kimura, Atsushi Matsumoto, Makoto Sakurai and Masuhiro Yoshino

National Institute for Fusion Science, Toki 509-5292, Japan

Abstract

We have determined the absolute total cross sections for electron capture between slow, highly charged ions and alkali targets under single collision conditions. It is found that these cross sections increase as the charge of the projectile ions increases. On the other hand, the cross sections are about one third of values expected from a scaling law previously proposed for rare gas atoms, which is based on the extended classical over barrier model.

The electron capture processes in collisions of slow, highly charged ions with neutral atoms and molecules are of great importance not only in basic atomic physics but also in applied fields such as fusion plasmas and astrophysics. In such processes, several electrons are simultaneously transferred into multiply excited states of highly charged ions with significantly large cross sections (the following process (1)), and finally the product ions are stabilized through ejection of electron(s) or photon(s) (process (2)),

$$A^{q+} + B \rightarrow A^{(q-j)+*} + B^{j+} \qquad (1)$$

$$\rightarrow A^{(q-i)+} + B^{j+} + (j-i)e + n(h\nu) \qquad (2)$$

where j and i are the number of electrons initially transferred from target and the final number of electrons captured into projectile ions. The cross sections for the processes (1) and (2) are defined as σ^{j}_{q} and $\sigma^{j}_{q,q-i}$, respectively. Previously we measured the electron capture cross sections in collisions of highly charged ions with rare gas atoms[1],[2], and then proposed a scaling law for representing the charge capture processes systematically[3], which is based on the extended classical over barrier model. Furthermore, we have already found that this scaling law proposed for rare gas atoms can also reproduce our measured data for molecular targets[4], as well.

In this paper, we report the experimental results of the absolute total electron capture cross sections in $1.5\times q$ keV I^{q+} (q=10-30) + alkali atom (Na, Rb, Cs) collisions. Furthermore, we compare the present alkali atoms data with our scaling law.

The absolute total electron capture cross sections have been measured using the initial growth-rate method combined with the retardation technique. The same experimental set-up as that of

Tawara *et al.*(1985)[5] is used and here we briefly describe the main features of the present measurements. The alkali metal atom targets are generated through an oven whose temperature is controlled by a programmable controller within ± 0.1℃. The target densities are estimated from the oven temperature measured by thermocouples. To determine the growth rates of the charge changed $I^{(q-i)+}$ (i>1) ions, the retarding voltage was fixed. The linear growth curves of the count rates of these ions were obtained as a function of the alkali target density which was sufficiently low to ensure the single collision conditions. From the observed growth curve, the total cross sections ($=\Sigma_{i>1}\sigma_{q,q-i}$) were determined.

It is shown that the electron capture cross sections of low energy highly charged ions in collisions with alkali atoms increase as the charge of the projectile ions increases as expected. The observed electron capture cross sections for alkali atoms roughly follow a line which is in proportion to q/I_P^2, where I_P is the ionization energy of the target atom (Fig. 1) but are found to be about one third values expected from the scaling law[3]. This difference can be due to the effective number of electrons, mostly in the outer-most shells, which contributes to the electron transfer processes. It should be noted that the electron capture cross sections for alkali atoms are reproduced well with the classical trajectory Monte Carlo simulations(see the solid line in Fig.1). In order to understand electron capture processes in details, more systematic studies using other targets such as alkali-earth atom targets are planned.

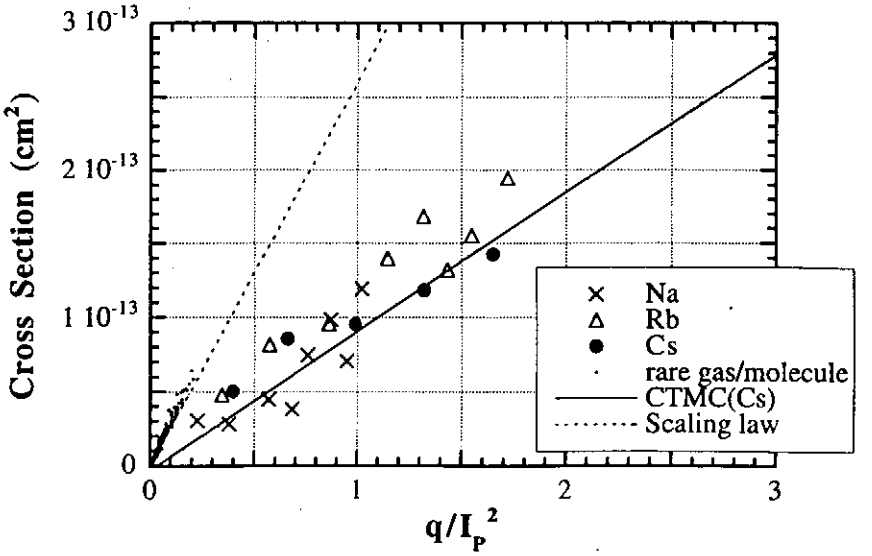

Fig1. Comparison between experimental data and a scaling law for electron capture cross sections.

References
[1] I. Yamada et al., J. Phys. **B28** (1995) L9.
[2] N. Nakamura et al., J. Phys. **B28** (1995) 2959.
[3] M. Kimura et al., J. Phys. **B28** (1995) L643.
[4] K. Hosaka et al., Phys. Scripta **T73** (1997) 273.
[5] H. Tawara et al., J. Phys. **B18** (1985) 337.

HIGH RESOLUTION X-RAY SPECTROMICROSCOPY OF LASER PRODUCED PLASMAS

A.Ya. Faenov

Multicharged Ions Spectra Data Center of VNIIFTRI (MISDC), Mendeleevo, Moscow region, 141570 Russia

In recent years new classes of X-ray spectroscopic instruments possessing both dispersive and focusing properties have been manifactured. Their principal advantage over more traditional instruments is that they combine very high luminosity with high spatial resolution, while preserving the highest possible spectral resolution of their dispersive elements. These instruments opened up the registration of plasmas in new regimes and surroundings. The measurements delivered new information about the properties of even previously studied traditional plasma objects (e.g. ns-laser produced plasmas). Also the detailed investigation of relatively new plasma laboratory sources with very small dimensions and low energy content (e.g. mJ fs-laser pulses) became possible.

The purpose of this report is to give a short review of the experimental and theoretical results obtained in the past few years by MISDC research team in the field of X-ray spectroscopy of a laser-produced plasma. Experimental spectra have been obtained at various laser installations with nanosecond, subnanosecond, picosecond and subpicosecond pulses interacting with solid, gaseous or cluster targets in collaborations with research teams from Russia, USA, Germany, France, Poland, Belgium, Italy, China and Israel. Practically all results have been obtained with the help of spectrographs with spherically bent mica crystals operating in FSSR-1D, 2D shemes.

I. LASER-PRODUCED PLASMA OF SOLID TARGETS.

Plasma created by nanosecond and subnanosecond laser pulses.

New X-ray spectroscopic techniques have allowed us even by using this traditional plasma source to obtain more accurate data on the wavelengths of the number of X-ray spectral lines and ionization potentials of multicharged ions, to observe (and to identify) the number of new lines (mainly, dielectron satellites to resonance transitions in H-, He- and Ne-like ions and radiative transitions from the Rydberg states of multicharged ions), and also to use X-ray spectroscopy methods for diagnosing of this plasma and for determining its spatial structure.

Space resolved spectra originating from plasma regions placed very close to the target showed up with rather unusual character: enough broad emission structures near the usual position of the resonance lines. It was shown that such kind of spectra does practically contain no resonance lines and consists mainly of high-n dielectronic satellite lines excited by the following mechanisms: (a) three body recombination to excited states and the subsequent formation of double excited levels from which dielectronic satellite spectra originate; (b) inner-shell excition from excited states; (c) dielectronic capture from excited states and (d) charge exchange processes from the residual gas.

We used X-ray spectroscopy also to study fast ion production in a plasma created by nanosecond lasers with different wavelengths (0.308 μm, 0.8 μm, 1.06 μm and 10.6 μm). It have been shown that interaction of laser radiation with solids leads to generation of fast multicharged ions (with energy up to several MeVs) even at moderate values of laser fluxes 10^{12}-10^{13} W/cm^2.

Plasma created by picosecond and subpicosecond laser pulses.

Our experiments have shown that the spectral features of this radiation depend sharply on the laser pulse contrast, i.e. on the pulse to prepulse intensity ratio. When the contrast is low the spectra of picosecond laser plasma is similar to that observed earlier in the same wavelength region with longer pulse lasers. The experiments carried out with femtosecond laser characterized by super high contrast of order 10^{11} revealed a new type spectra characterized by a more pronounced quasi-continuous spectral distribution which merges with the main reference lines. A physical reason for such drastic spectral restructuring could be naturally attributed to a difference in the mechanisms for plasma production. The absence of preplasma leads to a direct interaction of the ultra-short laser pulse with the solid substance resulting in the formation of plasma with much higher electron densities. At such densities numerous lines not developed at the coronal conditions become dominant in the spectrum.

The above discussed new excitation mechanism for dielectronic satellites are essential for the interpretation of X-ray spectra. Moreover, the radiation generated at high electron densities from multicharged hollow ions, i.e. ions with an empty K-shell have been observed. The presence of hollow ions is a manifestation of super high densities leading to the total breakdown of coronal conditions in these plasmas.

II. LASER-PRODUCED PLASMA OF GASEOUS TARGETS.

Plasma created by nanosecond laser pulses.

We have used the interaction of nanosecond laser pulses with a gas-puff mainly to obtain new spectral data on multicharged O, F, Ar, Kr, and Xe ions. For these elements the precision measurements of wavelengths for resonance Rydberg series of two-electron ions have been made and the complex satellite structures have been investigated. We have used also X-ray spectroscopy to determine the spatial distribution of laser gas puff plasma parameters, in particular it has been shown that in some cases the plasma channel is formed when nanosecond laser pulse interact with dense gaseous target.

Plasma created by subpicosecond laser pulses.

High resolution soft X-ray spectra of field ionized H-like nitrogen have been observed for the first time by irradiating the gas target by means of a 70 fs laser pulse with ultrahigh intensity. Very broad emission structures have been observed at the position of usual resonance lines. We proposed the generation of autoionizing levels in hollow nitrogen atoms which seriously blend with usual resonance lines. Atomic data calculations and spectral modeling demonstrate the big role of transitions from Rydberg autoionizing levels in the case of cold dense plasma.

III. LASER-PRODUCED PLASMA OF CLUSTER TARGETS.

In the last years a new class of targets, occupy average position between solids and rarefied gas has appear. It is so called cluster targets, i.e. gaseous beams, in which there are conglomerations consisting of significant numbers of molecules and having solid density at sizes 100-1000 nm. Such targets, on the one hand, possess all practical value of gaseous ones (manageability, the simplicity of replacement, good reproducibility etc.), and on the another hand, enable the analyses of all processes, characteristic for the high density targets.

First experiments show that X-ray spectroscopy methods can be successfully used for the systematic recording of the large volume of experimental information on the physical processes occurring in such kind of plasma. For example, transitions from Rydberg states of OVII,VIII and Ar XVII ions have been observed. It has been shown, that at the interaction of femtosecond laser pulses with CO_2 and Ar clusters the plasma contains ions (relative concentration about 10^{-2}-10^{-3}) with energies 0.1-1 MeV.

Density structure of the surface of Coulomb liquid and solid

Yasuyo Morita[1] and Shuji Kiyokawa[2]

[1] *Institute of Laser Engineering,Osaka University, Osaka 565-0871, Japan*
[2] *Dept. of Physics, Nara Women's University, Nara 630-8506, Japan*

Abstract. We present the results of Monte Carlo simulations for the inhomogeneous strongly coupled plasma, and report the observation of the transition in multilayer of ion density profile because of the correlation of the electron potential wall.

I. Introduction

Recently, the inhomogeneous one-component plasma (ocp) has proved a useful system for investigating liquid metal surfaces. The computer experiments have been carried out for the surface properties using the sphere model [1] and the slab model [2][3]. We apply this system for a model of surface of strongly coupled plasmas, where taken into account of the effect of electron polarization. In order to obtain thermal equilibrium properties, we carry out Monte Carlo simulation for ion system, simultaneously solving Schrödinger equation for electron system.

II. Theory

As shown in Fig 1, we consider a charge neutral system consist of N_i particles of charge $Z_a e$ and electrons, that form is regular prism of width L and infinite height,(though it seems to be finite in figure). Our model of the inhomogeneous plasma is ensemble of the above systems and is called the slab, therefore, we have only to simulate regular prism system under periodic boundary condition with period L.

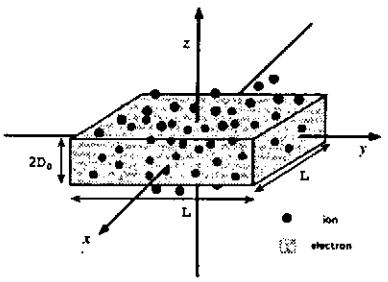

(Fig.1)
There are infinite number of regular prisms in the direction of x and y. The slab system has two surfaces perpendicular to z axis. Filled circles show ions, and the shaded area corresponds to electrons.

We assumed that the electrons responded to the thermal averaged distribution of ion density,

$$\rho_i(z) = \left\langle \frac{1}{L^2} \sum_{\ell=1}^{N_i} \delta(z - z_\ell) \right\rangle_{thermal} . \tag{1}$$

Where $< \cdots >_{thermal}$ shows the value in the thermodynamic equilibrium.
Therefore, electron density is determined as follows,

$$\left(-\frac{\hbar^2}{2m} \nabla^2 + v_{eff}(z) \right) \phi_n(z) = \varepsilon_n \phi_n(z), \tag{2}$$

[1]E-mail : ymorita@ile.osaka-u.ac.jp

$$v_{eff}(z) = \int_{-\infty}^{\infty} 2\pi Z_a e^2 |z - z'| \rho_i(z') dz' - \int_{-\infty}^{\infty} 2\pi e^2 |z - z'| \rho_e(z') dz' + v_{xc}(z), \tag{3}$$

v_{xc} is the exchange and correlation potential energy.

$$\rho_e(z) = \frac{2}{L^2} \sum_{\boldsymbol{k},n} f_{\boldsymbol{k},n} \phi_n(z)^2 \quad , f_{\boldsymbol{k},n} : \text{Fermi distribution function.} \tag{4}$$

The ion-ion effective interaction potential is

$$V_{ii} = \frac{(Z_a e)^2}{2} \sum_{\ell \neq \ell'} v_{ew}(\boldsymbol{R}_\ell - \boldsymbol{R}_{\ell'}) + \frac{2\pi e^2}{L^2} \sum_{\ell=1}^{N_i} \int_{-\infty}^{\infty} Z_a |z - z_\ell| \rho_e(z) dz. \tag{5}$$

v_{ew} is called the ewald potential which is constructed by summing up interactions with all the periodic images. We assumed that kinetic energy of electron system doesn't depend on a spacial configuration of ions.

III. Results

Fig.2 shows density profiles obtained for ion chareg $Z_a = 6$, electron average density $\bar{n}_e = 1.0 \times 10^{20}\text{cm}^{-3}$. For couping constant $\Gamma = 10$, ion density $\rho_i(z)$ expanded forward z-direction, while for $\Gamma = 20, 30$, it was observed multilayer of ion density profile, where the interval of layers is about 1.6 times of ionsphere radius. The cause of the multilayer is the correlation with the potential wall of electrons. We think that the transition in multilayer of density profile will occur for a certain value of Γ between 10 and 20.

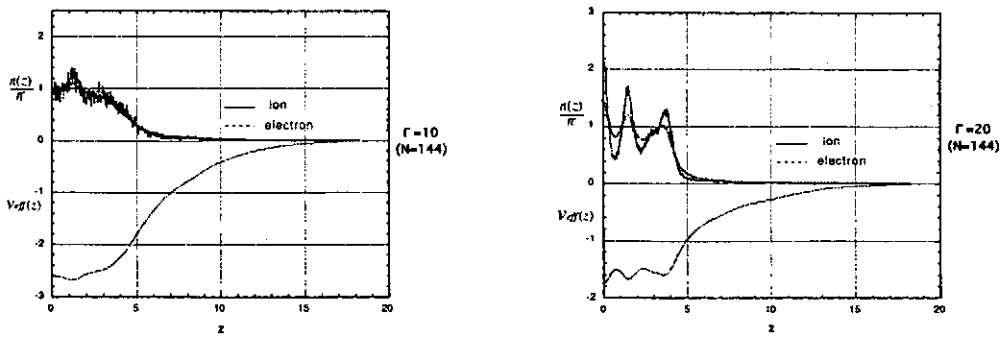

(Fig.2)
The value of horizontal axis, z ,is the distance from the xy-plane in the unit of the ion sphere radius. Full curve and broken curve of positive region show the density profile of ion and electron respectively. Broken curve of negative region shows the effective potential for electron.

Acknowledgements. The authors thanks Dr J. Chihara and Professor H. Totsuji for their continuous encouragement and useful conversations about this work.

References

[1] Badiali J.P., Rosinberg M.L., Levesque D and Weis J.J. 1983 J. Phys. C**16** 2183
[2] Totsuji H 1986 J. Phys. C**19** L573
[3] Ishida A, Hasegawa M and Watabe M 1987 J. Phys. C**20** L599

Computational Study of Laser Imprint Mitigation with X-Ray Radiation Using an Integrated Code

Naofumi Ohnishi[1], Hideo Nagatomo, Hideaki Takabe, Hiroaki Nishimura, Masaharu Nishikino, Hiroyuki Shiraga, and Tatsuhiko Yamanaka

Institute of Laser Engineering, Osaka University, Osaka 565-0871, Japan

Abstract. The initial imprint of density perturbation due to spatial nonuniformity of laser intensity is one of the most important issues in laser fusion research. The imprint mitigation scheme by use of soft x-ray radiation has been proposed to reduce the laser nonuniformity through the thermal conduction region. We present the results of two-dimensional simulation concerning this issue using our integrated code.

1 Introduction

In laser fusion, the initial imprint of perturbation to a target due to spatial nonuniformity of laser intensity is critical issue, since it becomes a seed of hydrodynamic instability which will prevent the spherical implosion. The laser energy is absorbed in the vicinity of the cut-off density and the absorbed energy is transported to the ablation surface by the electron thermal conduction. Therefore, a nonuniformity of the absorbed energy is expected to be suppressed through the thermal conduction region[1]. The width of this region is so called a stand-off distance, D_{AC}.

The external x-ray preirradiation scheme[2] has been proposed to suppression the laser imprint with x-ray radiation. In this scheme, the target is irradiated by x-ray before laser incidence, so that the preformed plasma is uniform. This preformed plasma forms a stand-off distance before laser irradiation.

2 Numerical Methods

We have been developing the integrated code ILESTA-2D[3] for laser fusion and related physics, numerical scheme of which is based on two-dimensional arbitrary Lagrangian Eulerian (ALE). This code includes the various physical processes of laser fusion to simulate the implosion. In our calculations, hydrodynamics, laser absorption, thermal conduction, radiation energy transport, opacity, and realistic EOS are consistently treated.

The radiation energy transport is calculated by the multi-group diffusion approximation with an Eddington factor. A tabulated opacity based on the averaged ion model is used.

3 Results and Discussion

As schematically shown in Fig. 1, the x-ray source is emitted from Au foil located at a distance of 1.8mm from the target and the foil is irradiated by the laser of 0.53μm wavelength and intensity 5.3×10^{13}W/cm^2. Time evolution of the radiation is calculated

[1]E-mail : ohnishi@ile.osaka-u.ac.jp

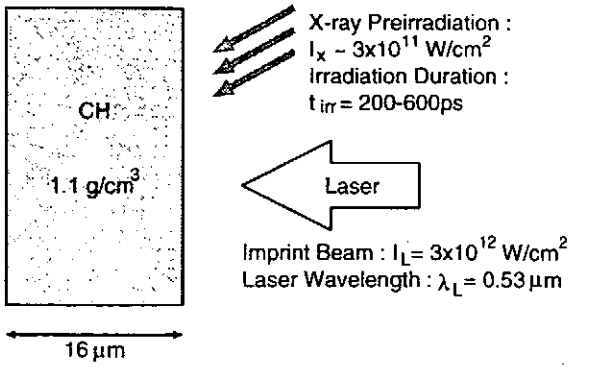

Figure 1: Simulation condition of the x-ray preirradiation scheme.

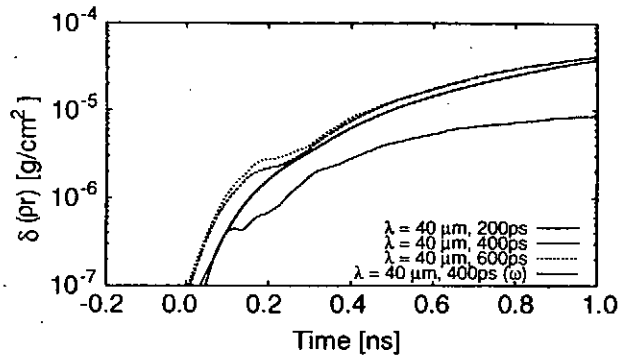

Figure 2: Time evolution of the areal density perturbation $\delta(\rho r)$ of the target

by one-dimensional code ILESTA-1D[4] and is used as the input for the outer boundary of two-dimensional calculation.

The spatial nonuniformity is assumed to be sinusoidal with $\delta I/I = 10\%$ and its wavelength, $\lambda = 40\mu$m. We can see that the dependency of the areal density perturbation on the x-ray irradiation duration is weak as shown in Fig. 2. This is because the stand-off distance is rather independent of the irradiation duration. On the other hand, the stand-off distance is enhanced when longer wavelength laser of $\lambda_L = 1.06\mu$m is used, and the imprint mitigation is seen in the two-dimensional calculation.

In the corresponding experiments at ILE[2], the nonuniform irradiance mitigation has been found more clearly. One of the reasons of the disagreement is that the emission spectra from Au foil are not sufficiently accurate in ILESTA-1D code[5]. Since the opacity calculations by non-LTE treatment for the emission spectra from high-Z material depend on the atomic model, we should improve them for detailed calculation.

4 Conclusion

We present the results of two-dimensional simulation of laser imprint mitigation scheme by use of x-ray radiation. It is found that the preformed plasma created by the x-ray source cannot directly suppress density perturbation due to laser nonuniformity. It is important that we seek the condition of keeping the long stand-off distance during nonuniform laser irradiation.

References

[1] M. H. Emery, J. H. Orens, J. H. Gardner, and J. P. Boris, Phys. Rev. Lett. **48**, 253 (1982).

[2] H. Shiraga, H. Azechi, Y. Kato, K. Mima, N. Miyanaga, M. Murakami, M. Nakai, S. Nakai, K. Nishihara, H. Nishimura, T. Norimatsu, K. Shigemori, H. Takabe, M. Takagi, T. Yamanaka, T. Endo, and C. Yamanaka, in Proceedings of the 16th IAEA Fusion Energy Conference, Montreal, Canada, 7–11 October, 1996, Paper IAEA-CN-64/B2-4 (International Atomic Energy Agency, Vienna, 1996).

[3] H. Nagatomo, H. Takabe, N. Ohnishi, S. Kato, and K. Mima, Fusion Eng. Des. **44**, 187 (1999).

[4] H. Takabe, T. Nishikawa, J. Quant. Spectrosc. Radiat. Transfer **51**, 379 (1994).

[5] H. Nishimura, H. Takabe, K. Kondo, T. Endo, H. Shiraga, K. Sugimoto, T. Nishikawa, Y. Kato, and S. Nakai, Phys. Rev. A **43**, 3073 (1991).

The use of an Electron Beam Ion Trap (EBIT) to measure electron impact ionisation cross-sections for highly charged argon ions.

E Sokell, F J Currell, H Watanabe and S Ohtani.

The University of Electro-Communications, Chofu, Tokyo, 182-8285, Japan.
Cold Trapped Ions Project, ICORP, JST, Axis Chofu 1-40-2, Tokyo, 182-0024, Japan.

Abstract.

A new technique for measuring electron impact ionisation cross-sections using an EBIT is presented. The method involves determining the charge distribution of ions extracted from the trap after well defined confinement times. Analysis of the onsets for the appearance of particular charge states in the trap gives ionisation rates which may be converted, under appropriate conditions, to relative cross-sections without theoretical input. The method has been used to make measurements for Ar^{15+}, Ar^{16+} and Ar^{17+}.

Introduction.

The process of electron impact ionisation is important in the field of atomic collision physics from both pure and applied perspectives. Measurements of these cross-sections provide important tests of our understanding of a range of fundamental physical processes and also provide vital information for databases used by the plasma physics community. Although a large number of high quality measurements have been performed for ions of low charge states ($Z < 10$) [1], experimental data is much less abundant for highly charged ions where low cross-sections make their measurement difficult. Electron Beam Ion Traps (EBITs) are one class of device which are appropriate for such studies and ionisation cross-sections have already been measured by utilising the equilibrium condition in an EBIT [2]. Here a different method for determining cross-sections, which works at times shortly after the appearance of ions of a particular charge state, will be described. The method provides relative cross-sections without theoretical input. The principal of this "onset" method bears some resemblance to work carried out at an Electron Beam Ion Source [3] the results from which are in good agreement with subsequent cross-beam measurements [1].

Principal.

At a given time the charge distribution within an EBIT can be described by a series of coupled rate equations which include the processes that are thought to be the most significant within the trap [4]. However, at times shortly after the appearance of ions of charge state q+1 the rate of increase of this species depends only on the number of ions of charge state q and the rate of ionisation from this charge state (R_q^I).

$$\frac{dN_{q+1}}{dt} = R_q^I N_q$$

This relationship is valid in the time regime when the ions produced by ionisation have not been in the trap long enough to undergo a subsequent reaction, for example ionisation or charge exchange. A simultaneous measurement of the rate of increase dN_{q+1}/dt and the number of ions of the lower, feeder, charge state, N_q, will give the ionisation rate, provided the efficiency for detecting ions of adjacent charge states is the same. These two quantities can be determined by measuring the charge distribution within the trap as a function of the confinement time. The rate of ionisation is related to the cross-section (σ_q^I);

$$R_q^I = \frac{I}{e \pi r^2} \sigma_q^I f_q$$

where I is the electron beam current, r the beam radius and f_q represents the overlap of ions of charge state q with the electron beam. If the ions are inside the electron beam $f_q = 1$ [5] and the beam radius does not change as a function of the electron impact energy, these rates can be directly converted to relative cross-sections.

Experimental.

The experimental arrangement is shown below. The potential applied to the central drift tube is controlled such that the trap is emptied after well defined, increasing, confinement times. A typical *time cycle* might include confinement times ranging from ~10 ms to ~100 ms. The ions leaving the trap are forced, by assymetric potentials applied to the outer drift tubes, to travel into the ion beam line.. Ions arriving at a position sensitive detector placed after the charge analysing magnet are recorded as a function of their position on the detector, the analysing magnetic field and their position in the *time cycle*. All ions including those escaping from the trap are detected so that these experiments also provide information about the physics of the trap, such as the temperature of the ions. After one *time cycle* has been completed the current in the magnet is altered and the cycle repeated. In this manner all of the charge states of interest are covered. In order to extract the ionisation rates from the data, spectra giving the charge state distribution as a function of position in the *time cycle* are constructed. Onsets for the appearance of the significant charge states and the ionisation rates are subsequently found from these spectra. This experimental method has been implemented at the Tokyo EBIT and results for ionisation cross-sections for Ar^{15+}, Ar^{16+} and Ar^{17+} are presented elsewhere in these proceedings [5].

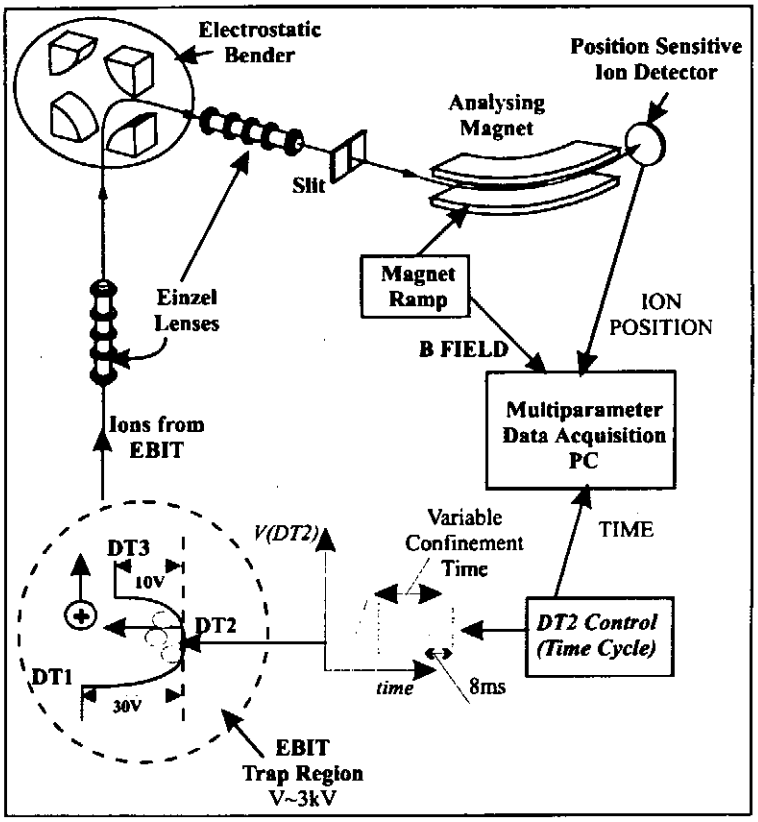

Conclusion.

A new technique for utilising EBITs for determining electron impact ionisation cross-sections in highly charged ions has been implemented at the Tokyo EBIT. A body of experimental results has bee obtained for highly charged Argon. The program is on going, the present goals being to extend the relative cross-section measurements to higher Z systems and to attempt to make absolute measurements.

References:

[1] Aichele K *et al* 1998 J. Phys. B. At. Mol. Opt. Phys. **31** 2369.

[2] Marrs R E, Elliot S R and Schofield J H 1997 Phys. Rev. A. **56** 1338.

[3] Donets E D and Ovsyannikov V P 1981 Sov. Phys. JETP **53** 466.

[4] Penetrante B M *et al* 1991 Phys. Rev. A. **43** 4861.

[5] Currell F J 1999 ISAPP T11 Measurement of Electron Impact Ionisation Cross-Sections in Highly Charged Ions.

Electron Capture Processes in Rb for He^- Formation

M. Sasao, M. Nishiura[1], A. Taniike[2], and M. Wada[3]

National Institute for Fusion Science, Toki, Gifu-509-52, Japan

[1] *The Graduate University for Advanced Studies, Toki, Gifu-509-52, Japan*

[2] *Dept. of Nuclear Eng.,Kobe Univ. of Mercantile Marine, Kobe 658, Japan*

[3] *Dept. of Electronics, Doshisha Univ., Tanabe, Kyoto-610-03, Japan*

Abstract

The electron capture process of He^+ into one-electron excited states of a He atom has been studied in prospect of subsequent He^- formation. Present work shows the experimental results of spectroscopic measurement in a Rb charge exchange cell when a low energy He^+ beam of 2 – 10 keV was injected. The ratio of emission lines decaying into triplet states to those into singlet is increased as the impact energy of He^+ increases. The results are compared with theoretical calculation using Smirnov method.

1 INTRODUCTION

Development of a high energy He^0 beam generated from a He^- is considered to be important on magnetic fusion experiments[1]. The surface production rate from a low work function surface has been experimentally studied and it was found being nearly zero [2]. It is also known that He^- can not be produced through a volume process. On the other hand, He^- has been produced via a two-step electron capture process in an alkali metal gas cell, such as Li, Na, Mg, K, Rb, or Cs [3,4]. In this process, intermediate states of a He atom play an important role, because a long-life, 10 – 300 μs, He^- (^4Pj) is produced effectively only through its metastable triplet state.

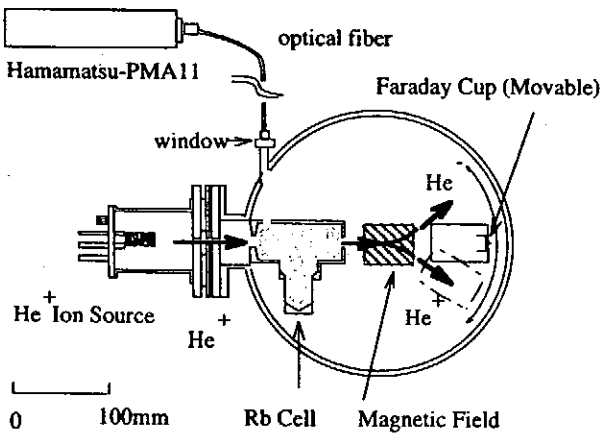

Figure 1: Schematic View of Experimental Arrangement

2 EXPERIMENTAL ARRANGEMENT

A schematic diagram of the experimental arrangement is shown in Fig. 1. A helium plasma is generated in an 8.5 cm-diam 10 cm-long compact multicusp ion source, which can be operated in a DC mode with discharge current up to 15 A. A He^+ beam is formed with a 6 mm-diam three-electrode-extraction-structure. The beam passes through the 1.5 cm-daim entrance aperture of the charge exchange cell located about 6 cm downstream. The main body of the charge exchange cell and the alkali metal reservoir are independently heated to control the temperature distribution so as to reduce the drain of metal vapor out of the cell. The temperature of the reservoir and that of the charge exchange cell are monitored with choromel-alumel thermocouples. To achieve high conversion efficiency, Rb was chosen as the charge exchange gas. Line spectrum from the cell, such as the Rb-D lines and HeI lines are measured using an optical fiber bundle and a Hamamatsu-PMA-011 which covers the 301-801 nm range with 0.48 nm resolution.

One of measured spectra is shown in Fig. 2. HeI lines decaying into triplet and singlet states of n=2 from n=3 states are shown. The line intensity ratio of $^3D(n=3)/^1D(n=3)$ decaying into each $^1P(n=2)$ state is plotted in Fig. 3. It increases as the incident beam energy is raised, together with the conversion ratio of He^+ to He^- [3].

3 PARTIAL CROSS SECTIONS

In order to understand the beam energy dependence of the triplet/singlet ratio, partial cross sections of He^{+} into He^{*}(nl) are calculated using an inter-molecular potential of long range force in near resonance[5]. The charge transfer occurs in the region of R_c. where the coupling matrix relates to the potentials as follows.

$$H_{12} = \frac{1}{2}\left|V_1(R_c) - V_2(R_c)\right| = \frac{1}{2}\Delta V(R_c)$$

$$H_{12} = \sqrt{I_1}\cdot\sqrt{I_2}R^{*}e^{-0.86R^{*}}$$

$$R^{*} = \frac{1}{2}(\alpha+\gamma)R$$

$$\frac{1}{2}\alpha^2 = I_1, \frac{1}{2}\gamma^2 = I_2$$

Here I_1 and I_2 are the effective ionization potentials of reactant(Rb^{0}) and product(He^{*}). The cross section can be calculated using the Smirnov method.

$$Q = 4\pi R_c^2\left(1-\frac{V_1(R_c)}{E}\right)\int_1^{\infty}\frac{dx e^{-\delta x}}{x^3\left(1+e^{-\delta x}\right)^2}$$

Where the reduced velocity δ^{-1} can be estimated by

$$\delta^{-1} = \frac{2\hbar\lambda v_0}{\pi\Delta V(R_c)}$$

In the Fig. 3 is also shown the calculated ratio of the partial cross section $\sigma(^3D\ (n=3))$ to $\sigma(^1D(n=3))$. Assuming the radiation decay rate A(D(n=3)->P(n=2)) are same for the triplet and singlet systems, the energy dependence of measured line intensity ratio shown in Fig. 3 can be explained by the ratio of partial cross sections.

4 CONCLUSION

For He production, it is important to form the He metastable sate, $^3S(n=2)$. The He can also be formed through the electron capture to $^3S(n=3)$, $^3P(n=3)$, $^3D(n=3)$ states which are decaying into the metastable sate, $^3S(n=2)$. . Calculated partial electron capture cross sections well explain the energy dependence of measured line intensity ratio of $^3D(n=3),/^1D(n=3)$, and $^3S(n=3),/^1S(n=3)$.,

References

[1] D.E.Post et al., Fusion Tech. 1 (1978), 355 M.Sasao et al., Fusion Tech. 10 (1986), 236

[2] M.Sasao et at, Rev. Sci. Instrum. 69-2 (1998) 974

[3] M.Sasao et at, Rev. Sci. Instrum. 69-2 (1998) 974

[4] R.J. Girnius et at, Nucl. Instrum. Methods, 137 (1976) 373.

[5] R.E.Olson and R. Smith, Phys. Rev. A 7-5, 1530 (1973).

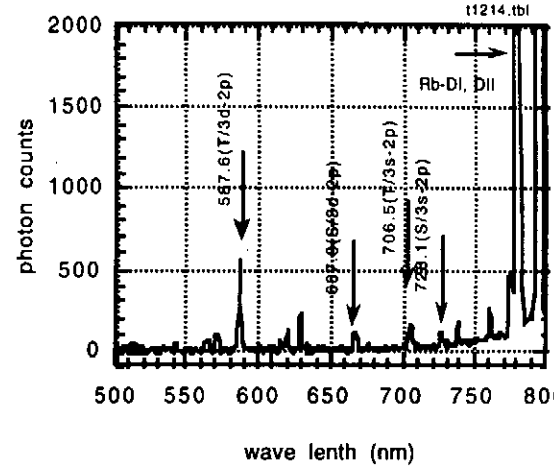

Figure 2: Measured spectrum in the Rb cell.

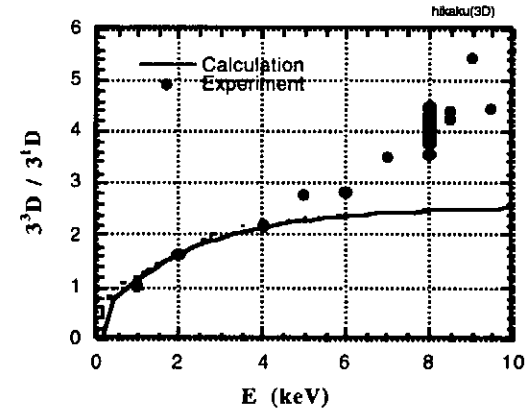

Figure 3: Comparison of partial electron capture cross sections with measured line intensity ratio of $^3D(n=3)/^1D(n=3)$

International Seminar on Atomic Processes in Plasmas
ISAPP July 29 - 30 1999
National Institute for Fusion Science
Toki, Japan

Program

July 28 (WED)

16:00-20:00 Early registration
Get-together-party

July 29 (THU)

8:30 Registration
Poster display preparation

9:30 Opening

Chairperson *Y. Itikawa*

9:30 - 9.35 Welcome Address by M. Fujiwara (Director General, NIFS)

9:35 - 9:55 T. Kato
T-1. Atomic processes in plasmas

Session I Atomic database, Atomic Code and Collisional - Radiative Models

Chairperson *H. Takabe*

9:55 - 10:20 H. Summers
T-2. An atomic data and analysis structure for interpreting fusion plasmas

10:20 - 10:45 M. Klapisch
T-3. SCROLL, a collisional-radiativemodel with superconfigurations

10:45 - 11:10 R. More
T-4. Non-Equilibrium Atomic Processes in Dense Plasmas

11:10 - 11:40 coffee

Chairperson *K. Aggarwal*

11:40 - 12:00 I. Murakami
T-5. Atomic database systems

Session II Electron- Ion Collisions

12:00 - 12:25 A. Pradhan
T-6. Recent Theoretical Studies on Excitation and Recombination
12:25 - 12:50 P. Beiersdorfer
T-7. Recent Livermore Excitation and Dielectronic Recombination Measurements for Fusion and Astrophysical Line Diagnostics
12:50 - 13:15 R. Schuch
T-8. Experimental recombination rates for highly charged ions in plasmas

13:15 - 14:30 Lunch (NIFS cafeteria)

Chairperson *S. Nakazaki*
14:30 - 14:55 Y.K. Kim
T-10. Theory of Ionization for Atoms and Molecules
14:55 - 15:20 F. Currell
T-11. Measurement of Electron Impact Ionisation Cross Sections for Highly Charged Ions

Session III LHD at NIFS

15:20 - 15:45 S. Sudo
T-12. Overview of LHD Diagnostics

15:45 - 16:10 Coffee

Chairperson *S. Ohtani*
16:10 - 18:00 Poster Session

The NIFS cafeteria is open 17:30 - 19:00

19:00 - 20:00 LHD tour (optional)

20:30 Public Bus from Institute to Tajimi station

July 30 (FRI)

Session IV Ion- Ion/Atom Collisions

Chairperson *H. Winter*

9:00 - 9:25 P. Krstic

T-13. Elastic collisions and related transport processes in cold hydrogen plasmas

9:25 - 9:50 E. Salzborn

T-14. Ion-ion collisions

Seesion V Molecular processes in plasmas

Chairperson *S.C. Mukherjee*

9:50 - 10:15 R.K. Janev

T-15. Molecular processes in divertor plasmas

10:15 - 10:40 N. Ohno

T-16. Plasma Detachment with Molecular Processes in Divertor Plasmas

10:40 - 11:10 coffee

Session VI Panel discussion on International Data Center collaboration

Chairperson *R.K. Janev*

11:10 - 12:50

NIFS, JAERI(Shirai), NIST(Y.K.Kim), ORNL(P. Krstic),
IAEA(R. Janev), U.K.(H. Summers),
Russia(A. Faenov), Korea(Y.J.Rhee), China(Yan Jun)

12:50 Photo

12:50 - 14:20 Lunch (NIFS cafeteria)

Session VII Plasma spectroscopy, Impurity radiation loss

Chairperson *D.E. Kim*

14:20 - 14:25 H. Kubo

T-17. Spectroscopic Study of JT-60U Divertor Plasma

14:25 - 15:10 T. Kawachi

T-18. Atomic processes involving doubly excited levels in a low temperature dense plasma - recombination x-ray laser -

15:10 - 15:50 coffee

Chairperson *A. Shlyaptseva*

15:50 - 16:15 K. Koyama

T-19. Spectroscopic Study of Astrophysical Plasmas

16:15 - 16:40 T. Fujimoto

T-20. Plasma Polarization Spectroscopy

16:40 Concluding

17:00 Bus from NIFS to Yamagami Spa

18:00 - 20:30 Party at "Yamagami Spa"

21:00 Bus from Yamagami to NIFS or Tajimi station

Poster Presentations

P-1. Winter, Hannspeter

"Database for inelastic collisions of Lithium atoms with electrons, protons and multiply charged ions"

P-2. Safronova, Ulyana I.

"Relativistic many-body calculations of excitation energy and radiative transition probabilities for many-electron ions"

P-3. Kato, Daiji

"Magnetic-Dipole Transitions between Ground-State Fine-Structure Levels of Ti-like Highly Charged Ions"

P-4. Bureyeva, Lyudmila

"Model Electron Density Approximations for Electron Radiative Transitions in the Field of Complex Ions"

P-5. Nishikawa, Takeshi

"Atomic modeling based on semiclassical theory"

P-6. Sasaki, Akira

"Detailed atomic model of short pulse laser pumped X-ray lasers"

P-7. Koike, Fumihiro

"Application of Atomic Structure Code for Precision Plasma Diagnostics"

P-8. Aggarwal, Kantim

"Electron Impact Excitation of Gd XXXVII and Electron Impact Excitation of Fe XXI"

P-9. Safronova, Ulyana I.

"Doubly and triply excited states for different plasma source"

P-10. Safronova, Ulyana I.

"Dielectronic recombination rate coefficients to the Excited states of Be-like ions"

P-11. Teng, Huaguo

"Electron-impact single ionization of K^{10+} and Kr^{11+} ions"

P-12. KIM, Yong-Ki

"Differential Ionization Cross Sections for Rare Gases"

P-13. Kagawa, Takashi

"Relativistic theory of electron-impact excitation of highly-charged ions"

P-14. Nakazaki, Shinobu and Kimura Eiji,

"Relativistic calculation of electron impact excitation rate coefficients in helium-like ions"

P-15. Berrington, Keith

"R-matrix calculations on electron-ion processes"

P-16. Schippers, Stefan

"Dielectronic recombination rates for iron L-shell ions from storage ring experiments"

P-17. Lindroth, Eva

"Accurate calculations of Dielectronic Recombination Resonances."

P-18. Roy, Amulya C.

"Singly differential cross section for $H(e,2e)H^+$ reaction process"

P-19. Sato, Kuninori

"VUV Emission Characteristics during NBI Experiment in LHD"

P-21. Mukherjee, S.C.,

"Ionization cross sections of state selective atomic hydrogen by impact of fully stripped ion"

P-22. Reid, Robert H. G.

"Proton-Impact Excitation of Lithium-like Ions"

P-23. Shibata, Takemasa,

"Symmetric charge transfer of rare earth element"

P-24. Kim, Sun Kook

"Monte-Carlo Particle-In-Cell Simulation of the charge-exchange process between Sm and Sm^+"

P-25. Toyoda, Hirotaka

"Cross Section Measurement of Electron Impact Dissociation into Neutral Radicals from SF6 and C3HF7O"

P-26. Sakimoto, Kazuhiro

"Dissociation in atom and diatom collisions"

P-27. Takagi, Hidekazu

"Dissociative recombination and dissociative excitation of H^{2+}"

P-28. Shlyaptseva, Alla S.

"The Application of X-Ray Line Polarization Plasma Spectroscopy for the Study of Atomic Processes"

P-29. Yoshikawa, Masayuki

"Impurity Diagnostics on the GAMMA 10 Tandem Mirror"

P-30. Bing-Jia, Xiao

"Spectroscopic Study of Plasma in Low temperatures"

P-31. Daido, Hiroyuki

"Experimental characterization of laser-produced plasmas for intense soft x-ray lasers"

P-32. Choi, Il Woo

"Characterization of the Soft X-ray Source with Elements in the Fifth Period and Its Compounds"

P-33. Tohyama, Yusuke

"X-Ray Spectroscopy of High Intense Laser-Produced Plasmas using a Focusing Toroidal Crystal Spectrometer"

P-34. Inal, Mokhtar K.

"Effects of electron-impact inner-shell ionization of Na-like ions on the linear polarization of the $2p^5$ 3s J=1,2 - $2p^6$ Se^{24+} X-ray lines"

P-35. Inoue, Takeru

"Plasma Polarization Spectroscopy"

P-36. Okamoto, Yuuji

"Absolute Calibration of Space and Time-Resolving Flat- Field Vacuum Ultraviolet Spectrograph for Plasma Diagnostics"

P-37. Watanabe, Hirofumi

"Spectroscopic study of Ti-like ions"

P-38. Kuramoto, Hideharu

"Thomson scattering measurement with the Tokyo-EBIT."

P-39. Sattin, Fabio

"Spectroscopy of Neon injected discharges in the RFX reversed field pinch"

P-40. Ochi, Yoshihiro

"Ar line spectroscopy for diagnostics of implosion stability"

P-41. Nakamura, Nobuyuki

"X-ray spectroscopy of highly charged neon like ions at the Tokyo electron beam ion trap"

P-42. Moribayashi, Kengo

"Applications of inner-shell ionization processes driven by high intensity laser"

P-43. Yan, Jun

"Theoretical study of Spectral Resolved Opacity in Plasmas"

P-44. Zhidkov, Alexei

"Ionization processes in overdense plasmas produced by subpicosecond pulse lasers"

P-45. Kim, Young Soon; Nam, Baek-Il, and Baik, Moon-Gu

"A theoretical Study on High Harmonic Generations"

P-46. Kim, Dong-Eon

"Gain characteristics of innershell L2-M1 transition in Ti."

P-47. van der Burgt, Peter J. M.

"Collective effects in the transient plasma formed by multiphoton ionization of deuterium atoms by a pulsed laser beam"

P-48. Wei YU

"A classical model for high-harmonic generation from a rare gas"

P-49. Shirai, Toshizo

"A+M Data Activities at JAERI Nuclear Data Center"

P-50. Nishimura, S., Ida, K. and CHS group

"Apparent wavelength shift of H-like ions cuased by the spectral fine structure observed in CHS plasmas"

P-51. Wang, J.-G., Kato, M. and Kato, T.

"Carbon Spectra for Diagnostic of Plasma Temperature and Density"

P-52. Hosaka, K., Tawara, H., Yamada, I., Sakaue, H. A., Nakamura, N., Ohtani, S., Watanabe, H., Danjo, A., Kimura M., Matsumoro, A., Sakurai, M., and Yoshino M.

"Electron capture cross sections of low energy highly charged ions in collision with atoms and molecules"

P-53. Faenov, A.

"High-resolution X-ray spectroscopy of laser-produced plasma"

P-54. Morita, Yasuyo

"Density structure of the surface of Coulomb liquid and solid"

P-55. Ohnishi, Naofumi

"Computational study of laser imprint mitigation with X-ray radiation using integrated code in ICF targets"

P-56. Sokell, Emma J.

"THE USE OF AN ELECTRON BEAM ION TRAP (EBIT) TO MEASURE ELECTRON IMPACT IONISATION CROSS-SECTIONS FOR HIGHLY CHARGED ARGON IONS"

P-57. Sasao, Mamiko

"Electron Capture Processes in Rb for He- production"

International Seminar on Atomic Processes in Plasmas, July 29-30, 1999, at NIFS, Toki, Japan: Participant List 1

Name	Affiliation	Address	Country		Email address
Aggarwal, Kanti M.	Dept. of Pure & Applied Physics, The Queen's University of Belfast	BELFAST BT7 1NN, Northern Ireland	UK	Phone: +44-1232-273239 Fax: +44-1232-438918	K.Aggarwal@qub.ac.uk
Akimoto, Fumie	Dept. of Physics, Nagoya University,	Furo-cho, Chikusa-ku, Nagoya, 464-8602,	Japan	Phone: +81-52-789-2917 Fax: +81-52-789-2919	akimoto@u.phys.nagoya-u.ac.jp
Baik, Moon-Gu	Dept. of Physics, Kyungwon University	Songnam-shi, Kyonggi-do, 461-701	Korea	Phone: +82-342-750-5490 Fax: +82-342-750-5389	mgbaik@mail.kyungwon.ac.kr (justin00@unitel.co.kr)
Beiersdorfer, Peter	Lawrence Livermore National Laboratory	1000 East Ave., Livermore, CA 94550	USA	Phone: +1-925-423-3985 Fax: +1-925-422-5940	beiersdorfer@llnl.gov
Berrington, Keith	School of Science and Mathematics, Sheffield Hallam University,	Sheffield S1 1WB	UK	Phone: +44 114 225 4933 Fax: +44 114 225 3066	k.berrington @ shu.ac.uk
Bing-Jia, Xiao	Dep.of Quantum Engi. and System Sciences, Faculty of Engineering, The University of Tokyo,	7-3-1, Hongo Bunkyo-ku, Tokyo	Japan	Phone: +81-3-3812-2111 Fax: +81-3-5800-6860	bjxiao@flanker.q.t.u-tokyo.ac.jp
Bureyeva, Lyudmila	Scientific Council on Spectroscopy of the RAS	Leninski Pr. 53 Moscow, 117924	Russia	Phone: +7-095-1351420 Fax: +7-095-1326508	bureyeva@sci.lebedev.ru
Choi, Il Woo	Institute of Laser Engineering Osaka University	2-6 Yamada-oka, Suita, Osaka 565-0871	Japan	Phone: +81-6-6879-8751 Fax: +81-6-6877-4799	choi@ile.osaka-u.ac.jp
Chung, Young Min	Pohang Accelerator Laboratory, POSTECH	San31, Hyoja-dong, Pohang, 790-784	Korea	Phone: +82-562-279-1534 Fax: +82-562-279-1599	ychung@postech.ac.kr
Currell, F.	Univ. of Electro-Communication	1-5-1 Chofugaoka , Chofu,Tokyo, 182-8585	Japan	Phone: Fax:	fred@falcon.fedu.uec.ac.jp
Daido, Hiroyuki	Institute of Laser Engineering Osaka University	2-6 Yamada-oka, Suita, Osaka 565-0871	Japan	Phone: +81-6-6879-8766 Fax: +81-6-6877-4799	daido@ile.osaka-u.ac.jp

Name	Affiliation	Address	Country		Email address
Daniel, Romanos	DAMTP Cambridge University	Silver street, Cambridge, Cambridgeshire	UK	Phone: +44 (0)7957471274 Fax: +44 (0)1223 337918	rd10011@hermes.cam.ac.uk
Faenov, Anatoly	Multicharged Ion Spectral Data Center of Natl. Inst. Phys.-Tech. Radiotechnical Measurements	Mendeleevo, Moscow region, 141570	Russia	Phone: +7-095-535-91-35 Fax: +7-095-535-73-86	faenov@yahoo.com
Fujima, Kazumi	Yamanashi Univ.	4-3-11 Takeda Kofu, Yamanashi 400-8511	Japan	Phone: +81-552-20-8587 Fax: +81-552-20-8587	rose@mail.yamanashi.ac.jp
Fujimoto, Takashi	Dept. of Enginnering Phys. and Mech. Kyoto Univ.	Sakyo, Kyoto 606-8501	Japan	Phone: +81-75-753-5211 Fax: +81-75-771-7286	a53080@sakura.kudpc.kyoto-u.ac.jp
Fujita, Junji	Daido Institute of Technology	2-21 Daido-cho, Minami-ku, Nagoya 457-8531	Japan	Phone: +81-52-611-0513 Fax: +81-52-612-5653	fujita@daido-it.ac.jp
Fujita, Kazuhisa	Institute of Laser Engineering Osaka University	2-6 Yamada-Oka, Suita, Osaka 565-0871	Japan	Phone: +81-6-6879-8777 Fax: +81-6-6877-4799	kfujita@ile.osaka-u.ac.jp
Fukao, Mitsuhiro	Institute of Laser Engineering Osaka University	2-6 Yamada-oka, Suita, Osaka 565-0871	Japan	Phone: +81-6-6879-8777 Fax:	mfukao@ile.osaka-u.ac.jp
Furuzawa, Akihiro	Dept. of Physics, Nagoya University,	Furo-cho, Chikusa-ku, Nagoya, 464-8602,	Japan	Phone: +81-52-789-2920 Fax: +81-52-789-2919	furuzawa@u.phys.nagoya-u.ac.jp
Hahn, Yukap	Physics of Conneticut University of Connecticut	Sotrrs, CT 06269	USA	Phone: +1-(860)486-4469,- Fax: +1-(860)486-3346	hahn3@uconnvm.uconn.edu
Hayashi, Makoto	Gaseous Electronics Institute	4-15-14-503 Sakae, Naka-ku, Nagoya 460-0008	Japan	Phone: +81-52-243-2314 Fax: +81-52-243-2314	
Hosaka, Kazumoto	National Institute for Fusion Science	322-6 Oroshi-cho Toki, 509-5292	Japan	Phone: +81-572-58-2257 Fax: +81-572-58-2628	hosaka@nifs.ac.jp

Name	Affiliation	Address	Country		Email address
Ida, Katsumi	National Institute for Fusion Science	322-6 Oroshi-cho Toki, 509-5292	Japan	Phone: +81-572-58-2182 Fax: +81-572-58-2619	ida@nifs.ac.jp
Inal, Mokhtar K.	Institut des Sciences Exactes Department de Physique University A. Belkaid	B.P. 119 Bel-Horizon, 13000 Tlemcen	Algeria	Phone: +213-720-33-44 Fax: +213-720-30-30	BEL@ist.cerist.dz
Inoue, Takeru	Department of Engineering Physics and Mechanics Kyoto University	Sakyo,Kyoto 606-8501	Japan	Phone: +81-75-753-4860 Fax:	inoue@jasmine.kues.kyoto-u.ac.jp
Itikawa, Yukikazu	Institute of Space and Astronautical Science	2-1-1 Yoshinodai, Sagamihara	Japan	Phone: +81-42759-8205 Fax: +81-42759-8209	itikawa@pub.isas.ac.jp
Janev, Ratko K.	Research Centre for Energy Macedonian Academy of Sciences and Arts	Bulevar K. Misirkov, 2; P.O. Box 428 91000 Skopje	Macedonia	Phone: Fax:	janev@ripcrs02.iaea.or.at
Kagawa, Takashi	Department of Physics, Nara Women's University	Department of Physics, Nara Women's University, Nara 630-8506	Japan	Phone: +81-742-20-3375 Fax: +81-742-20-3377	kagawa@cc.nara-wu.ac.jp
Kato, Daiji	Cold Trapped Ions Project, Japan Science and Technology Co.	Axis-Choufu Bldg. 3F, 1-40-2 Fuda, Choufu, Tokyo 182-0024	Japan	Phone: +81-424-83-1094 Fax: +81-424-83-1409	kato@hci.jst.go.jp
Kato, Takako	Data and Planning Center, National Institute for Fusion Science	322-6 Oroshi-cho Toki, 509-5292	Japan	Phone: +81-572-58-2265 Fax: +81-572-58-2628	takako@nifs.ac.jp
Kawachi, Tetsuya	Advanced Photon Research Center, Japan Atomic Energy Research Institute	Tokai-mura, Naka-gun, Ibaraki, 319-1195	Japan	Phone: +81-29-282-6383 Fax: +81-29-282-6704	kawachi@hikari.tokai.jaeri.go.jp
Kawamura, Takaichi	National Institute for Fusion Science	322-6 Oroshi-cho Toki, 509-5292	Japan	Phone: +81-572-58-2229 Fax: +81-572-58-2628	kawamura@nifs.ac.jp
Kawamura, Tohru	Institute of Laser Engineering Osaka University	2-6 Yamada-oka, Suita, Osaka 565-0871	Japan	Phone: +81-6-6879-8741 Fax: +81-6-6877-4799	tohru@ile.osaka-u.ac.jp

Name	Affiliation	Address	Country		Email address
Kim, Dong-Eon	Physics Department, Pohang University of Science and Technology	San 31 Hyoja-Dong Namku Pohang, Kyungbuk 790-784	Korea	Phone: +82-562-279-208 Fax: +82-562-279-3099	kimd@vision.postech.ac.kr
Kim, Sun Kook	Lab for Quantum Optics, Korea Atomic Energy Research Institute	P.O.Box 105, Yusung, Taejon 305-600	Korea	Phone: +82-42-868-8379 Fax: +82-42-861-8292	skkim4@nanum.kaeri.re.kr
Kim, Yong-Ki	National Inst. of Standards & Technology,	Gaithersburg, MD 20899-8423	USA	Phone: +1-301-975-3203 Fax: +1-301-990-1350	yong-ki.kim@nist.gov
Kim, Young Soon	Department of Physics, Myongji University	Yong-In, 449-728	Korea	Phone: +82-335-330-6169 Fax: +82-335-335-9533	yskim@wh.myongji.ac.kr
Kimura, Eiji	Department of Materials Science, Faculty of Engineering, Miyazaki University	1-1, Gakuen Kibanadai-Nishi, Miyazaki 889-2192	Japan	Phone: +81-985-58-7366 Fax: +81-985-58-7376	eiji@phys.miyazaki-u.ac.jp
Klapisch, Marcel	ARTEP, inc.	Naval Research Laboratory, code 6730, 4555 Overlook Ave, SW, Washington, DC 20375	USA	Phone: +1-202-404-7802 Fax: +1-202-767-0046	klapisch@this.nrl.navy.mil
Kobayashi, Kazuki	University of Tokyo	7-3-1 Hongo, bunkyo-ku, Tokyo 113	Japan	Phone: +81-3-5841-6970 Fax: +81-3-3818-3455	kazuki@duke.q.t.u-tokyo.ac.jp
Koike, Fumihiro	School of Medicine, Kitasato University	Kitasato 1-15-1 Sagamihara Kanagawa 228-8555	Japan	Phone: +81-42-778-8029, Fax: +81-42-778-8441	koikef@kitasato-u.ac.jp
Kondo, Yoshitaka	Daido Institute of Technology	Daido-cho 2-21, Minamiku, Nagoya	Japan	Phone: +81-52-611-0513 Fax: +81-52-612-5653	kondo@daido-it.ac.jp
Koyama, Katsuji	Department of Physics, Kyoto-U.	Kitashirakawa, Sakyo-ku, Kyoto	Japan	Phone: +81-75-753-3833 Fax: +81-75-753-3799	koyama@cr.scphys.kyoto-u.ac.jp
Krstic, Predrag S	Physics Division, Oak Ridge National Laboratory	P.O. Box 2008, Oak Ridge, TN 37831-6372	USA	Phone: +1-423-574-4701 Fax: +1-423-574-4745	krstic@mail.phy.ornl.gov

Name	Affiliation	Address	Country		Email address
Kubo, Hirotaka	Naka Fusion Research Establishment, Japan Atomic Energy Research Institute	801-01 Mukoyama, Naka-machi, Naka-gun, Ibaraki-ken, 311-0193	Japan	Phone: +81- 29 270 7343 Fax: +81- 29 270 7419	kubo@naka.jaeri.go.jp
Kumar, Vijay	Physical Resarch Laboratory,	Navrangpura Ahmedabad-380009	India	Phone: +91-79-6462129 Fax: +91-79-6301502	vkumar@prl.ernet.in
Kuramoto, Hideharu	Japan Science and Technology Corporation	Axis Chofu 3F, 1-40-2 Fuda, Chofu, Tokyo 182-0024,	Japan	Phone: +81-424-83-1094 Fax: +81-424-83-1409	kuramoto@hci.jst.go.jp
Lee, Hae June	Pohang Univ. of Sci. & Techn.	San 31, Hyoja, Pohang 790-784	Korea	Phone: +82-562-279-5518 Fax: +82-562-279-3099	leehj@postech.ac.kr
Lee, Jae Koo	Pohang Univ. of Sci. and Techn.	San-31 Hyoja, Pohang 790-784	Korea	Phone: +82-562-279-2083 Fax: +82-562-279-3099	jkl@postech.ac.kr
Lepson, Jaan K	Space Sciences Laboratory, Univ. of California	Berkley, CA 94550	USA	Phone: Fax:	lepson @ssl.berkely.edu
Lindroth, Eva	Atomic Physics, Stockholm University	FrescativÁ»en 24, S-104 05 Stockholm	Sweden	Phone: +46 8 16 10 18 Fax: +46 8 15 86 74	lindroth@atom.msi.se
Mangina, Rao VVS	Thermosciences Institute NASA-Ames Researh Center	MS 229-1, NASA-Ames Research Center, Moffett Field, CA 94035, USA	USA	Phone: +1-650-604-2887 Fax: +1-650-604-0484	rmangina@mail.arc.nasa.gov
More, Richard M.	National Institute for Fusion Science	322-6 Oroshi-cho Toki, 509-5292	Japan	Phone: +81-572-58-2262 Fax: +81-572-58-2628	more@nifs.ac.jp
Moribayashi, Kengo	Japan Atomic Energy Research Institute	25-1, Mii-minami-cho, Neyagawa, Osaka 572-0019	Japan	Phone: +81-720-31-0709 Fax: +81-720-31-0596	kengo@apr.jaeri.go.jp
Morita, Yasuyo	Institute of Laser Engineering Osaka University	2-6 Yamada-oka, Suita, Osaka 565-0871	Japan	Phone: +81-6-6879-8742 Fax: +81-6-6877-4999	ymorita@ile.osaka-u.ac.jp

Name	Affiliation	Address	Country		Email address
Mukherjee, S. C.	Indian Association for the Cultivation of Science	Jadavpur, Calcutta 700 032	India	Phone: +91-33-473-4971 Fax: +91-33-473-2805	tpscm@mahendra.iacs.res.in
Murakami, Izumi	Data and Planning Center, National Institute for Fusion Science	322-6 Oroshi-cho Toki 509-5292	Japan	Phone: +81-572-58-2264 Fax: +81-572-58-2628	mizumi@nifs.ac.jp
Nakamura, Nobuyuki	Cold Trapped Ions Project, Japan Science and Technology Corporation	Axis Chofu 3F, 1-40-2 Fuda, Chofu, Tokyo 182-0024	Japan	Phone: +81-424-83-1094 Fax: +81-424-83-1409	nakamura@hci.jst.go.jp
Nakashima, Ken'ichi	Institute of Laser Engineering Osaka University	2-6 Yamada-oka, Suita, Osaka 565-0871	Japan	Phone: +81-6-879-8742 Fax: +81-6-877-4799	knakashi@ile.osaka-u.ac.jp
Nakazaki, Shinobu	Department of Materials Science, Faculty of Engineering, Miyazaki University	1-1, Gakuen Kibanadai-Nishi, Miyazaki 889-2192	Japan	Phone: +81-985-58-7366 Fax: +81-985-58-7376	shinobu@phys.miyazaki-u.ac.jp
Nam, Baek Il	Department of Physics, Myong Ji University	38-2 Nam-dong, Yongin 449-728	Korea	Phone: +82-335-337-2352 Fax: +82-335-335-9533	binam@wh.myongji.ac.kr
Namba, Chusei	National Institute for Fusion Science	322-6 Oroshi-cho Toki, 509-5292	Japan	Phone: +81-572-58-2263 Fax: +81-572-58-2628	namba@nifs.ac.jp
Namba, Shinichi	Nagoya university	322-6 Oroshi-cho Toki, 509-5292	Japan	Phone: +81-572-58-2222 ex Fax: +81-572-58-2624	snamba@nifs.ac.jp
Nishikawa, Takeshi	Dep't Electrical and Electronic Eng., Okayama University	3-1-1, Tsushima-naka, okayama 700-8530	Japan	Phone: +81-86-251-8140 Fax: +81-86-251-8261	nisikawa@elec.okayama-u.ac.jp
Nishimura, Hiroaki	Institute of Laser Engineering Osaka University	2-6 Yamada-oka, Suita, Osaka 565-0871	Japan	Phone: +81-6-6879-8772 Fax: +81-6-6877-4799	nishimu@ile.osaka-u.ac.jp
Nishimura, Shin	National Institute for Fusion Science	322-6 Oroshi-cho Toki, 509-5292	Japan	Phone: +81-572-58-2183 Fax: +81-572-58-2619	shin@nifs.ac.jp

Name	Affiliation	Address	Country		Email address
Ochi, Yoshihiro	Institute of Laser Engineering Osaka University	2-6 Yamada-oka, Suita, Osaka 565-0871	Japan	Phone: +81-6-6879-8777 Fax: +81-6-6877-4799	ochi@ile.osaka-u.ac.jp
Ohnishi, Naofumi	Institute of Laser Engineering Osaka University	2-6, Yamada-oka, Suita, Osaka, 565-0871	Japan	Phone: +81-6-879-8742 Fax: +81-6-877-4799	ohnishi@ile.osaka-u.ac.jp
Ohno, Noriyasu	Nagoya Univ.	Furo-cho, Chikusa-ku, Nagoya 464-8603	Japan	Phone: +81-52-789-3145 Fax: +81-52-789-3944	ohno@ees.nagoya-u.ac.jp
Ohtani, Shunsuke	Univ. of Electrocommunications	1-5-1 Chofugaoka, Chofu, Tokyo 182-8585	Japan	Phone: +81-424-43-5446 Fax: +81-424-85-8960	ohtani@ils.uec.ac.jp
Okamoto, Yuuji	Plasma Research Center, Tsukuba Univ.	1-1-1 tenoudai, Tsukuba, Ibaraki 300-3261	Japan	Phone: +81-298-53-7465 Fax: +81-298-53-6202	okamoto@prc.tsukuba.ac.jp
Ono, Kouichi	Kyoto University	Yoshida-Honmachi, Sakyo-ku, Kyoto 606-8501	Japan	Phone: +81-75-753-5793 Fax: +81-75-753-5980	ono@eddie.kuaero.kyoto-u.ac.jp
Pradhan, Anil K	Dept. of Astronomy, The Ohio State University	174 W. 18th Ave., Columbus, OH 43210-1106	USA	Phone: +1-614-292-5850 Fax: +1-614-292-2928	pradhan.1@osu.edu
Reid, Robert H. G.	Dept. of Applied Maths and Theor. Physics Queen's University	Belfast BT7 INN	UK	Phone: +44-1232-273168 Fax: +44-1232-239182	r.reid@qub.ac.uk
Rhee, Yong-Joo	Laboratory for Quantum Optics, Korea Atomic Energy Research Institute	P.O.Box 105 Yusong, Taejon, 305-600	Korea	Phone: +82-42-868-2935 Fax: +82-42-861-8292	yjrhee@nanum.kaeri.re.kr
Roy, Amulya C.	Department of Physics University of Kalyani	Kalyani 741235	India	Phone: +91-33-5828750 Fax:	amulya@klyuniv.ernet.in
Safronova, Ulyana I.	Department of Physics University of Notre Dame	225 Nieuwland Science Hall, Notre Dame, Indiana 46656	USA	Phone: +1-219-631-5952 Fax: +1-219-631-4008	usafrono@darwin.helios.nd.edu

Name	Affiliation	Address	Country		Email address
Saka, Takashi	Daido Institute of Technology	2-21 Daido-cho, Minami-ku, Nagoya 457-8531	Japan	Phone: +81-52-611-0513 Fax: +81-52-612-5653	saka@daido-it.ac.jp
Sakaue, Hiroyuki	National Institute for Fusion Science	322-6 Oroshi-cho Toki, 509-5292	Japan	Phone: +81-572-58-2176 Fax: +81-572-58-2619	sakaue@nifs.ac.jp
Sakimoto, Kazuhiro	Institute of Space & Astronautiucal Science	Yoshinoda 3-1-1, Sagamihara 229-8510	Japan	Phone: +81-42-779-8207 Fax: +81-427-59-8440	sakimoto@pub.isas.ac.jp
Salzborn, Erhard	Institut fuer Kernphysik, University of Giessen	Leihgesterner Weg 217, D-35392 Giessen	Germany	Phone: +49-641-99-15100 Fax: +49-641-99-15109	salzborn@strz.uni-giessen.de
Sasaki, Akira	Kansai Research Establishment, Japan Atomic Energy Research Institute	25-1 Miiminami-cho, Neyagawa-shi, Osaka 572-0019	Japan	Phone: +81-720-31-0709 Fax: +81-720-31-0596	sasaki@apr.jaeri.go.jp
Sasao, Mamiko	National Institute for Fusion Science	322-6 Oroshi-cho Toki, 509-5292	Japan	Phone: +81-572-58-2185 Fax: +81-572-58-2619	sasao@nifs.ac.jp
Sato, Kuninori	National Institute for Fusion Science	322-6 Oroshi-cho Toki, 509-5292	Japan	Phone: +81-572-58-2238 Fax: +81-572-58-2624	kuninori@ms.nifs.ac.jp
Sattin, Fabio	Consorzio RFX	Corso Stati Uniti 4, I-35125 Padova	Italy	Phone: +39 049 8295030 Fax: +39 049 8700718	sattin@igi.pd.cnr.it
Schippers, Stefan	Institut fuer Kernphysik Strahlenzentrum der Justus-Liebig-Universitaet,	Leihgesterner Weg 217, 35392 Giessen	Germany	Phone: +49-641-15203 Fax: +49-641-15009	Stefan.E.Schippers@strz.uni-giessen.de
Schuch, Reinhold H	Stockholm University	Frescativ 24, S-10405 Stockholm	Sweden	Phone: +46 8 161046 Fax: +46 8 158674	schuch@msi.se
Shibata, Takemasa	Japan Atomic Energy Research Institute	Tokai-mura, Ibaraki-ken, 319-1195	Japan	Phone: +81-29-282-5918 Fax: +81-29-282-5572	mojun@popsvr.tokai.jaeri.go.jp

Name	Affiliation	Address	Country		Email address
Shirai, Toshizo	Japan Atomic Energy Research Institute	Nuclear Data Center, JAERI, Tokai-mura, Ibaraki 319-1195	Japan	Phone: +81-29-282-6087 Fax: +81-29-282-5766	shirai@ndc.tokai.jaeri.go.jp
Shlyaptseva, Alla S.	University of Nevada	Physics Dep. 1220 University of Nevada, Reno, NV89557-0058	USA	Phone: +1-775-784-4734 Fax: +1-775-784-1398	alla@physics.unr.edu
Sokell, Emma J	IRSAMC, Universite Paul Sabatier	118 Route de Narbonne, 31062, Toulouse.	France	Phone: + 33 5 61 55 64 02 Fax: + 33 5 61 55 83 17	emma@yosemite.ups-tlse.fr
Sudo, Shigeru	National Institute for Fusion Science	322-6 Oroshi-cho Toki, 509-5292	Japan	Phone: +81-572-58-2225 Fax: +81-572-58-2624	sudo@LHD.nifs.ac.jp
Summers, Hugh P.	University of Strathclyde, Department of Physics and Applied Physics	107 Rottenrow, Glasgow ,G4 0NG	UK	Phone: +44-141-548-4196 Fax: +44-141-552-2891	summers@phys.strath.ac.uk
Sunahara, Atsushi	Institute of Laser Engineering Osaka University	2-6 Yamada-oka, Suita, Osaka 565-0871	Japan	Phone: +81-6-6879-8742 Fax: +81-6-6877-4799	suna@ile.osaka-u.ac.jp
Takabe, Hideaki	Institute of Laser Engineering Osaka University	2-6 Yamada-oka, Suita, Osaka 565-0871	Japan	Phone: +81-6-6879-8731 Fax: +81-6-6877-4799	takabe@ile.osaka-u.ac.jp
Takagi, Hidekazu	School of Medicine, Kitasato University	1-15-1 Kitasato, Sagamihara	Japan	Phone: +81-42-778-8447 Fax: +81-42-778-8441	takagi@kitasato-u.ac.jp
Takahashi, Nobuyuki	Kanto Technical Institute, Kawasaki Heavy Industries, Ltd.,	118 Futatsuzuka, Noda, Chiba, 278-8585	Japan	Phone: +81-471-24-0466 Fax: +81-471-24-5917	takahashi_n@khi.co.jp
Tanaka, Akihiro	Dep. of Engineering Physics and Mechanics, Kyoto University	Sakyo, Kyoto 606-8501	Japan	Phone: +81-75-753-4860 Fax: +81-75-771-7286	tanaka@jasmine.kues.kyoto-u.ac.jp
Teng, Huaguo	Strahlenzentrum, Institut fuer Kernphysik	Leihgesterner Weg 217, D-35392, Giessen	Germany	Phone: +49-641-99-15216 Fax: +49-641-99-15009	huaguo.teng@strz.uni-giessen.de

Name	Affiliation	Address	Country		Email address
Tohyama, Yusuke	Institute of Laser Engineering Osaka Univ.	2-6 Yamada-oka Suita Osaka, 565-0871	Japan	Phone: +81-6 - 6879 - 8751 Fax: +81-6 - 6877 - 4799	ytohyama@ile.osaka-u.ac.jp
Toyoda, Hirotaka	Department of Electrical Engineering, Nagoya University	Furo-cho, Chikusa-ku, Nagoya 464-8603	Japan	Phone: +81-52-789-4698 Fax: +81-52-789-3150	toyota@nuee.nagoya-u.ac.jp
van der Burgt, Peter	Dep.of Experimental Physics, National University of Ireland, Maynooth	Maynooth, Co. Kildare	Ireland	Phone: +353-1-708-3782 Fax: +353-1-708-3313	peter.vanderburgt@may.ie
Wallbank, Barry	Dept. of Physics, St. Francis Xavier University,	P.O. Box 5000, Antigonish, Nova Scotia, B2G 2WS	Canada	Phone: +1-902-867-2301 Fax: +1-902-867-2414	bwallban@stfx.ca
Wang, Jianguo	National Institute for Fusion Science	322-6 Oroshi-cho Toki, 509-5292	Japan	Phone: +81-572-58-2257 Fax: +81-572-58-2628	wang@nifs.ac.jp
Watanabe, Hirofumi	Japan Science and Technology Corporation	Fuda 1-40-2, Choufu-shi, Tokyo, 182-0024	Japan	Phone: +81-424-43-5709 Fax: +81-424-85-8960	h_watana@ils.uec.ac.jp
Winter, Hannspeter	Institut feur Allgemeine Physik, TU Wien	Wiedner Hauptstrasse 8-10 A-1040 Wien	Austria	Phone: +43-1-58801-13410 Fax: +43-1-58801-13499	winter@iap.tuwien.ac.at
Yan, Jun	Center of Atomic and Molecular Sciences, Dept. of Phys. Tsinghua Univ.	Beijing 100084	China	Phone: +86-10-62788597 Fax: +86-10-62562605,	jyan@cams.tsinghua.edu.cn
Yoshikawa, Masayuki	University of Tsukuba	1-1-1 Tennodai, Tsukuba, Ibaraki 305-8577	Japan	Phone: +81-298-53-6236 Fax: +81-298-53-6202	yosikawa@prc.tsukuba.ac.jp
Yu, Wei	Shanghai Institute of Optics and Fine Mechanics	P.O. Box 800-211, Shanghai 201800	China	Phone: +86-21-59534890 Fax: +86-21-59528812	weiyu@mail.shcnc.ac.cn
Zhidkov, Alexei	Advanced Photon Research Center, JAERI	25-1, Mii-minami-cho, Neyagawa-shi, Osaka, 572-0019	Japan	Phone: +81-720-31-1095 Fax: +81-720-31-0596	zhidkov@apr.jaeri.go.jp

Publication List of NIFS-PROC Series

NIFS-PROC-1 "*U.S.-Japan on Comparison of Theoretical and Experimental Transport in Toroidal Systems Oct. 23-27, 1989*", Mar. 1990.

NIFS-PROC-2 "*Structures in Confined Plasmas –Proceedings of Workshop of US-Japan Joint Institute for Fusion Theory Program–* "; Mar. 1990

NIFS-PROC-3 "*Proceedings of the First International Toki Conference on Plasma Physics and Controlled Nuclear Fusion –Next Generation Experiments in Helical Systems– Dec. 4-7, 1989*" Mar. 1990

NIFS-PROC-4 "*Plasma Spectroscopy and Atomic Processes –Proceedings of the Workshop at Data & Planning Center in NIFS–*"; Sep. 1990

NIFS-PROC-5 "*Symposium on Development of Intensed Pulsed Particle Beams and Its Applications February 20 1990*"; Oct. 1990

NIFS-PROC-6 "*Proceedings of the Second International TOKI Conference on Plasma Physics and Controlled Nuclear Fusion , Nonlinear Phenomena in Fusion Plasmas -Theory and Computer Simulation-*"; Apr. 1991

NIFS-PROC-7 "*Proceedings of Workshop on Emissions from Heavy Current Carrying High Density Plasma and Diagnostics*"; May 1991

NIFS-PROC-8 "*Symposium on Development and Applications of Intense Pulsed Particle Beams, December 6 - 7, 1990*"; June 1991

NIFS-PROC-9 "*X-ray Radiation from Hot Dense Plasmas and Atomic Processes*"; Oct. 1991

NIFS-PROC-10 "*U.S.-Japan Workshop on "RF Heating and Current Drive in Confinement Systems Tokamaks" Nov. 18-21, 1991*, Jan. 1992

NIFS-PROC-11 "*Plasma-Based and Novel Accelerators (Proceedings of Workshop on Plasma-Based and Novel Accelerators) Nagoya, Japan, Dec. 1991*"; May 1992

NIFS-PROC-12 "*Proceedings of Japan-U.S. Workshop P-196 on High Heat Flux Components and Plasma Surface Interactions for Next Devices*"; Mar. 1993

NIFS-PROC-13 「NIFS シンポジウム
「核燃焼プラズマの研究を考える－現状と今後の取り組み方」
1992 年 7 月 15 日、核融合科学研究所」1993 年 7 月
NIFS Symposium "Toward the Research of Fusion Burning Plasmas -Present Status and Future strategy-", 1992 July 15, National Institute for Fusion Science"; July 1993 (in Japanese)

NIFS-PROC-14 "*Physics and Application of High Density Z-pinches*", July 1993

NIFS-PROC-15 岡本正雄、講義「プラズマ物理の基礎」
平成 5 年度 総合大学院大学1994 年 2 月
M. Okamoto,
*"Lecture Note on the Bases of Plasma Pysics"Graduate University for Advanced Studies*Feb. 1994
(in Japanese)

NIFS-PROC-16 代表者 河合良信
平成 5 年度 核融合科学研究所共同研究
研究会報告書「プラズマ中のカオス現象」
*"Interdisciplinary Graduate School of Engineering Sciences" Report of the meeting on Chaotic Phenomena in Plasma*Apr. 1994 (in Japanese)

NIFS-PROC-17 平成 5 年度 NIFS シンオジウム報告書
「核融合如開発研究のアセスメント」平成 5 年 11 月 29 日-30 日 於 核融合科学研究所
"Assessment of Fusion Reactor Development" Proceedings of NIFS Symposium held on November 29-30, 1993 at National Insitute for Fusion Science" Apr. 1994(in Japanese)

NIFS-PROC-18 "*Physics of High Energy Density Plasmas Produced by Pulsed Power*" June 1994

NIFS-PROC-19 K. Morita, N. Noda (Ed.),

"*Proceedings of 2nd International Workshop on Tritium Effects in Plasma Facing Components at Nagoya University, Symposion Hall, May 19-20, 1994*", Aug. 1994

NIFS-PROC-20 研究代表者 阿部 勝憲 (東北大学・工学部)
所内世話人 野田信明
平成6年度 核融合科学研究所共同研究〔研究会〕「金属系高熱流束材料の開発と評価」成果報告書
K. Abe and N. Noda (Eds.),
"Research and Development of Metallic Materials for Plasma Facing and High Heat Flux Components" Nov. 1994(in Japanese)

NIFS-PROC-21 世話人:森田 健治(名大工学部)、金子 敏明(岡山理科大学理学部)
「境界プラズマと壁との相互作用に関する基礎過程の研究」研究会報告
K. Morita (Nagoya Univ.), T. Kaneko (Okayama Univ. Science)(Eds.)
"*NIFS Joint Meeting "Plasma-Divertor Interactions" and "Fundamentals of Boundary Plasma-Wall Interactions" January 6-7, 1995 National Institute for Fusion Science*" Mar. 1995 (in Japanese)

NIFS-PROC-22 代表者 河合 良信
プラズマ中のカオス現象
Y. Kawai,
"*Report of the Meeting on Chaotic Phenomena in Plasma, 1994*" Apr. 1995 (in Japanese)

NIFS-PROC-23 K. Yatsui (Ed.),
"*New Applications of Pulsed, High-Energy Density Plasmas*", June 1995

NIFS-PROC-24 T. Kuroda and M. Sasao (Eds.),
"*Proceedings of the Symposium on Negative Ion Sources and Their Applications, NIFS, Dec. 26-27, 1994*", Aug. 1995

NIFS-PROC-25 岡本 正雄
新古典輸送概論(講義録)
M. Okamoto,
"*An Introduction to the Neoclassical Transport Theory" (Lecture note)*, Nov. 1995 (in Japanese)

NIFS-PROC-26 Shozo Ishii (Ed.),
"*Physics, Diagnostics, and Application of Pulsed High Energy Density Plasma as an Extreme State*", May 1996

NIFS-PROC-27 代表者 河合 良信
プラズマ中のカオスとその周辺非線形現象
Y. Kawai ,
"*Report of the Meeting on Chaotic Phenomena in Plasmas and Beyond, 1995*", Sep. 1996 (in Japanese)

NIFS-PROC-28 T. Mito (Ed.),
"*Proceedings of the Symposium on Cryogenic Systems for Large Scale Superconducting Applications*", Sep. 1996

NIFS-PROC-29 岡本 正雄
講義「核融合プラズマ物理の基礎 - I」
平成8年度 総合研究大学院大学 数物科学研究科 核融合科学専攻 1996年10月
M. Okamoto
"*Lecture Note on the Fundamentals of Fusion Plasma Physics - I" Graduate University for Advanced Studies;* Oct. 1996 (in Japanese)

NIFS-PROC-30 研究代表者 栗下 裕明(東北大学金属材料研究所)
所内世話人 加藤 雄大
平成8年度核融合科学研究所共同研究「被損傷材料の微小体積強度評価法の高度化」研究会 1996年10月 9日 於:核融合科学研究所
H. Kurishita and Y. Katoh (Eds.)
NIFS Workshop on Application of Micro-Indentation Technique to Evaluation of Mechanical Properties of Fusion Materials, Oct. 9, 1996, NIFS ; Nov. 1996 (in Japanese)

NIFS-PROC-31 岡本 正雄
講義「核融合プラズマ物理の基礎 - II」
平成8年度 総合研究大学院大学 数物科学研究科 核融合科学専攻 1997年4月
M. Okamoto
"*Lecture Note on the Fundamentals of Fusion Plasma Physics - II" Graduate University for Advanced*

Studies; Apr. 1997 (in Japanese)

NIFS-PROC-32 代表者　河合　良信
平成8年度　核融合科学研究所共同研究　研究会報告「プラズマ中のカオスとその周辺非線形現象」
Y. Kawai (Ed)
Report of the Meeting on Chaotic Phenomena in Plasmas and Beyond, 1996; Apr. 1997 (mainly in Japanese)

NIFS-PROC-33 H. Sanuki,
Studies on Wave Analysis and Electric Field in Plasmas; July 1997

NIFS-PROC-34 プラズマ対向機器・PSI・熱・粒子制御合同研究会報告
平成9年6月27日（金）9:00～16:20　核融合科学研究所・管理棟4F第1会議室
1997年　10月
T. Yamashina (Hokkaido University)
Plasma Facing Components, PSI and Heat/Particle Control June 27, 1997, National Institute for Fusion Science T. Yamashina (Hokkaido University) ; Oct. 1997 (in Japanese)

NIFS-PROC-35 T. Watari,
Plasma Heating and Current Drive; Oct. 1997

NIFS-PROC-36 T. Miyamoto and K. Takasugi (Eds.)
Production and Physics of High Energy Density Plasma; Production and Physics of High Energy Density Plasma; Oct. 1997

NIFS-PROC-37 (Eds.)T. Fujimoto, P. Beiersdorfer,
Proceedings of the Japan-US Workshop on Plasma Polarization Spectroscopy and The International Seminar on Plasma Polarization Spectroscopy January 26-28, 1998, Kyoto; June 1998

NIFS-PROC-38 (Eds.) Y. Tomita, Y. Nakamura and T. Hayashi,
Proceedings of the Second Asian Pacific Plasma Theory Conference APPTC '97, January 26-28, 1998, Kyoto; Aug. 1998

NIFS-PROC-39 (Ed.) K. Hirano,
Production, Diagnostics and Application of High Energy Density Plasmas; Dec. 1998

NIFS-PROC-40 研究代表者　加古　孝（電気通信大学）
所内世話人　渡辺　二太
平成10年度核融合科学研究所共同研究 研究会「プラズマ閉じ込めに関連する数値計算手法の研究」
Ed. by T. Kako and T. Watanabe
Proceeding of 1998-Workshop on MHD Computations "Study on Numerical Methods Related to Plasma Confinement Apr. 1999

NIFS-PROC-41 (Eds.) S. Goto and S. Yoshimura,
Proceedings of The US-Japan Workshop and The Satellite Meeting of ITC-9 on Physics of High Beta Plasma Confinement in Innovative Fusion System, Dec. 14-15, 1998, NIFS, Toki; Apr. 1999

NIFS-PROC-42 (Eds.) H. Akiyama and S. Katsuki,
Physics and Applications of High Temperature and Dense Plasmas Produced by Pulsed Power; Aug. 1999

NIFS-PROC-43 (Ed.) M. Tanaka,
Structure Formation and Function of Gaseous, Biological and Strongly Coupled Plasmas; Sep. 1999

NIFS-PROC-44 (Eds.) T. Kato and I. Murakami,
Proceedings of the International Seminar on Atomic Processes in Plasmas, July 29-30, 1999, Toki, Japan; Jan. 2000